



HAL
open science

On the surface structures and catalytic properties of Al-based intermetallics

Corentin Chatelier

► **To cite this version:**

Corentin Chatelier. On the surface structures and catalytic properties of Al-based intermetallics. Materials Science [cond-mat.mtrl-sci]. Université de Lorraine, 2020. English. NNT : 2020LORR0230 . tel-03254779

HAL Id: tel-03254779

<https://hal.univ-lorraine.fr/tel-03254779>

Submitted on 9 Jun 2021

HAL is a multi-disciplinary open access archive for the deposit and dissemination of scientific research documents, whether they are published or not. The documents may come from teaching and research institutions in France or abroad, or from public or private research centers.

L'archive ouverte pluridisciplinaire **HAL**, est destinée au dépôt et à la diffusion de documents scientifiques de niveau recherche, publiés ou non, émanant des établissements d'enseignement et de recherche français ou étrangers, des laboratoires publics ou privés.



AVERTISSEMENT

Ce document est le fruit d'un long travail approuvé par le jury de soutenance et mis à disposition de l'ensemble de la communauté universitaire élargie.

Il est soumis à la propriété intellectuelle de l'auteur. Ceci implique une obligation de citation et de référencement lors de l'utilisation de ce document.

D'autre part, toute contrefaçon, plagiat, reproduction illicite encourt une poursuite pénale.

Contact : ddoc-theses-contact@univ-lorraine.fr

LIENS

Code de la Propriété Intellectuelle. articles L 122. 4

Code de la Propriété Intellectuelle. articles L 335.2- L 335.10

http://www.cfcopies.com/V2/leg/leg_droi.php

<http://www.culture.gouv.fr/culture/infos-pratiques/droits/protection.htm>



THÈSE

présentée et soutenue publiquement le 15 décembre 2020

pour l'obtention du

Doctorat de l'Université de Lorraine

(mention Sciences des Matériaux)

par

CORENTIN CHATELIER

On the surface structures and catalytic properties of Al-based intermetallics

Composition du jury :

<i>Président :</i>	Dr. Sylvain RAVY	Directeur de Recherche, LPS, CNRS
<i>Rapporteurs :</i>	Dr. Céline CHIZALLET Dr. Holger MEYERHEIM	Chef de projet, IFPEN Directeur de Recherche, MPI Halle
<i>Examineurs :</i>	Dr. Sébastien LEBÈGUE Dr. Christine MOTTET Dr. Marie-Ingrid RICHARD	Directeur de Recherche, LPCT, CNRS Directrice de Recherche, CINaM, CNRS Chercheur, CEA
<i>Invités :</i>	Pr. Yves GARREAU Dr. Laurent PICCOLO	Professeur, Université de Paris, MPQ, SOLEIL Chargé de Recherche, IRCELYon, CNRS
<i>Directrice :</i>	Pr. Émilie GAUDRY	Professeure, Université de Lorraine, IJL
<i>Co-directeur :</i>	Dr. Alessandro COATI	Responsable de ligne, SOLEIL

Remerciements

Dans un premier temps, je souhaite remercier les membres du jury de soutenance : Céline Chizallet et Holger Meyerheim, pour le temps qu'ils ont consacré à la lecture consciencieuse de mon manuscrit et pour leurs retours pertinents et constructifs; Sébastien Lebègue, Christine Mottet et Marie-Ingrid Richard, pour toutes les discussions que nous avons eu; et enfin Sylvain Ravy, qui a accepté de présider cette soutenance.

Je remercie Jean Daillant, Éric Gaffet et Thierry Belmonte pour leurs accueils dans leurs laboratoire au cours de ces trois dernières années. Je tiens aussi à remercier à cet endroit la Région Grand-Est et le Synchrotron SOLEIL pour leurs financements respectifs de ma thèse, ainsi que les centres de calculs Occigen (CINES), Cobalt (TGCC) et Explor (Université de Lorraine) pour leurs ressources HPC.

Cette thèse n'aurait rien été sans ses directeurs. Un immense merci à Émilie et Alessandro pour ces trois dernières années passées sous vos directions et conseils. Concilier les calculs théoriques et les expériences n'était pas une mince affaire, et ce fut parfois difficile, mais vous avez toujours été là pour m'accompagner. Merci Émilie de m'avoir initié à cette superbe théorie qu'est la DFT, de m'avoir fait confiance tout au long de cette thèse, et de m'avoir autorisé certaines libertés scientifiques tout en me guidant judicieusement. Merci Alessandro de m'avoir accueilli si chaleureusement dans le monde du rayonnement synchrotron et de la diffraction de surface, de m'avoir laissé les reines de la ligne pendant de nombreux temps de faisceau, et ce malgré ma malchance avec les équipements qui planait constamment au dessus de ma tête. J'espère que l'avenir nous réservera de belles et fructueuses collaborations scientifiques.

Quelques mentions spéciales à présent. Si Émilie et Alessandro ont été mes encadrants officiels durant ces trois années de thèse, j'ai toujours pu compter sur les conseils, les idées et l'aide du Pr. Garreau. Merci à toi Yves pour ton encadrement officieux, tu m'as appris énormément, tant sur les aspects expérimentaux que théoriques. Un grand merci aussi à Laurent, pour ton accueil à Lyon, et pour les expériences que nous avons réalisées ensemble. Grâce à toi, la catalyse est devenue un peu moins mystérieuse à mes yeux. Pour finir ces mentions spéciales, je tiens à remercier Roberto, sans qui les portes de SOLEIL n'auraient pas pu s'ouvrir à moi.

De nombreuses autres personnes ont contribué de près ou de loin à l'aboutissement de mes travaux de thèse, et je tiens à les remercier vivement. Un immense merci à toute l'équipe SixS de SOLEIL pour tous les moments passés avec vous. Merci Alina pour ton enthousiasme scientifique constant, ta vision de l'espace réciproque, pour ton aide précieuse et tes conseils avisés. Merci Andréa pour toutes les discussions techniques (scientifiques, pythonesques, photographiques et culinaires), et pour ton aide et tes conseils pendant les temps de faisceau. Merci Benjamin pour ta bonne humeur et ton bon humour, et pour ton aide technique irremplaçable. Merci Fred pour les discussions aussi bien musicales que scientifiques, et pour ton aide informatique. Merci Michèle pour toutes les discus-

sions scientifiques que nous avons pu avoir. Merci à Stefan et François pour leur aide avec les mesures AFM. Enfin, je tiens à remercier Sandrine et Véronique pour leur aide dans les moments compliqués de la fin de thèse.

Un grand merci aussi à l'équipe 203 de l'IJL pour son accueil, son aide et les discussions que nous avons pu avoir. Merci Julian pour tes conseils, tes idées, et ton aide précieuse avec les mesures STM. Merci Muriel et Vincent pour vos conseils, expertises et pour toutes les discussions scientifiques. Merci Marie-Cécile pour tes superbes échantillons, et pour ton initiation à la croissance Czochralski. Merci Florian pour ton aide avec les calculs DFT et avec VASP. Merci aussi à Christine pour ton aide administrative sans faille. Je tiens aussi à remercier tous les membres du réseaux du ECMetAC, en particulier Marc, pour sa participation et son aide lors de mes premiers temps de faisceau, et Peter, pour ses monocristaux.

Merci à tous les doctorants que j'ai pu côtoyer au cours des trois dernières années, pour leurs soutiens, la bonne ambiance, et l'entraide. Merci donc aux thésards de SOLEIL, Anthony, Julie, Benjamin, Antoine, Cynthia, Arthur, David; merci aux thésards de l'IJL, Kanika, Firas, Thibaud, Philippe, Alexandre, Sébastien, Aurélia, Dominique, Thiago, et mention toute spéciale pour mi Catalina (gracias por haberme recibido tantas veces!); et enfin un grand merci aux thésards du réseaux ECMetAC pour les très bons moments passés en conférence, merci Maïke, Ana, Kristian, et Monika.

Une thèse sans des amis proches autour de soi est sans doute quelque chose d'impossible à faire. Merci Agathe et Adrien, Béryl, Célien (merci pour le Airbnb maître Zacharie), Emmanuelle, Gael, Laurène, Maéva, Manu d'Houssay, Martin et Laureen, Samuel, Sara, Steve, et Vincent, pour votre soutien constant et votre aide dans les moments difficiles. Je n'oublie pas les canadiens, qui, malgré la distance, ont toujours su garder le contact, merci à Billy, Kartik, Thomas and the Mathieu family. Un immense merci aux musiciens de l'Orchestre Symphonique du Campus d'Orsay pour leur accueil, leur musique, et tout particulièrement à mon cher co-pupitre Gael pour tous les fous rires que nous avons pu avoir en répétition (ou en concert!).

Pour conclure, je souhaite remercier infiniment mes grands-parents, mes parents et mon frère, c'est grâce à vous que j'en suis arrivé jusque là. Votre soutien constant et indéfectible est le socle sur lequel j'ai eu la chance de construire ce que je suis devenu. Merci.

Résumé

Remplacer les catalyseurs à base de métaux nobles (Pd, Pt, Au) par des substituts peu coûteux, stables, sélectifs et actifs est un grand défi pour l'industrie chimique. Plusieurs intermétalliques complexes à base d'aluminium se sont révélés prometteurs pour les réactions d'hydrogénation d'alcynes et d'alcènes, importantes dans l'industrie des polymères. C'est le cas des approximants quasicristallins Al_5Co_2 , $\text{Al}_{13}\text{Co}_4$ et $\text{Al}_{13}\text{Fe}_4$. L'étude des propriétés catalytiques de ces derniers nécessite plusieurs approches, théoriques et expérimentales, afin de déterminer les structures de surface hors et sous conditions de réaction, première étape avant la détermination des propriétés d'adsorption et des mécanismes de réaction. La combinaison d'expériences de sciences de surface (microscopie à effet tunnel, diffraction de surface des rayons X) et de calculs de chimie théorique (énergies de surface, énergies d'adsorption, chemins de réaction) a permis d'établir des modèles de surface détaillés, leurs propriétés d'adsorption et de mieux comprendre les facteurs clés à l'origine des propriétés catalytiques prometteuses de ces matériaux.

Abstract

Replacing noble metal (Pd, Pt, Au) catalysts with inexpensive, environmentally harmless, active, selective, and stable substitutes is a big challenge for the chemical industry. Several aluminium-based complex intermetallic compounds have shown promises for alkynes and alkenes hydrogenation reactions, which are of interest in the chemical industry. It is the case for Al_5Co_2 , $\text{Al}_{13}\text{Co}_4$ and $\text{Al}_{13}\text{Fe}_4$ quasicrystalline approximants. The study of their catalytic properties demands different approaches – both theoretical and experimental – in order to determine first their surface structures under ultra-high vacuum or reaction conditions, then their catalytic properties. The combination of surface science experiments (scanning tunneling microscopy, surface X-ray diffraction) and theoretical chemistry calculations (surface energies, adsorption energies and reaction pathways) allows for a better understanding of the key parameters behind the promising catalytic properties of these materials.

Synthèse

La synthèse qui suit est un résumé étendu des travaux de recherche présentés dans ce manuscrit. Il s'agit d'une présentation générale des principaux résultats obtenus tout au long de la thèse.

Introduction

De nos jours, la catalyse – modification de la vitesse d'une réaction chimique sous l'influence d'une substance capable, par sa seule présence, de déclencher cette réaction sans subir elle-même d'altération finale – joue un rôle crucial dans l'industrie chimique. Il existe une demande forte de la part des industriels pour des catalyseurs actifs, sélectifs, stables, ayant un impact environnemental minimal, tout en restant peu coûteux (réduction de l'utilisation de métaux nobles).

L'hydrogénation sélective des alcynes et des alcènes est une classe de réaction importante de la pétrochimie. Le raffinage du pétrole par craquage induit la formation de résidus et impuretés hautement réactifs tels que l'acétylène ou le butadiène. Ces derniers doivent être hydrogénés de manière sélective avant d'être ultérieurement transformés (*e.g.* par polymérisation). Les catalyseurs industriels sont actuellement à base de palladium pour ce type de réaction. Bien qu'actifs et stables, leur sélectivité n'est pas optimale et peut être améliorée par l'ajout d'autres métaux comme l'or, l'argent ou le cuivre [1, 2, 3, 4]. Ces catalyseurs à base de métaux nobles peuvent néanmoins souffrir par exemple de modifications de leurs surfaces du fait de l'adsorption des réactifs, induisant une baisse de leur sélectivité [2, 5, 6] : les réactifs pouvant inhiber des sites actifs, des intermédiaires néfastes pour le catalyseur pouvant être produits, *etc.*

Au cours de la dernière décennie, de nouveaux catalyseurs ont été identifiés : les intermétalliques complexes à base d'aluminium. Ces derniers présentent de sérieux atouts vis-à-vis de la catalyse. Ils sont stables, sélectifs, bon marché, et ont un impact très limité sur l'environnement. Certains comme $\text{Al}_{13}\text{Fe}_4(010)$ et $\text{Al}_{13}\text{Co}_4(010)$ présentent une activité aussi bonne voire meilleure que celle du palladium pour les réactions d'hydrogénation du butadiène [7, 8] : $\text{C}_4\text{H}_6(\text{g}) + \text{H}_2(\text{g}) \longrightarrow \text{C}_4\text{H}_8(\text{g})$. Néanmoins, ils peuvent faire l'objet de potentielles désactivation du fait de contamination (par l'oxygène par exemple) [9]. Ils restent néanmoins de bons systèmes modèles.

L'objectif des travaux de recherches présentés dans ce manuscrit est de déterminer les structures de surfaces de certains de ces intermétalliques complexes, de comprendre les phénomènes d'adsorption intervenants à leurs surfaces et d'étudier leurs réactivités spé-

cifiques. Une approche transverse a été choisie afin de mener à bien cette étude, et combine des calculs *ab initio* de chimie quantique, des mesures de diffraction de surface des rayons X, de la microscopie à effet tunnel ainsi que des mesures de performances catalytiques sur des monocristaux. Trois composés de la famille des intermétalliques complexes à base d'aluminium ont été choisis : Al_5Co_2 [10, 11, 12, 13, 14, 15], $\text{Al}_{13}\text{Co}_4$ [16, 17, 18, 19] et $\text{Al}_{13}\text{Fe}_4$ [20, 21, 22].

Structure de surface et propriétés catalytiques de $\text{Al}_5\text{Co}_2(2\bar{1}0)$

La première étude présentée dans ce manuscrit s'intéresse à la structure de la surface ($2\bar{1}0$) du composé Al_5Co_2 (appartenant au groupe d'espace $P6_3/mmc$, No. 194, symbole de Pearson $hP28$ [10, 11, 12]). Il a été montré expérimentalement [23] que $\text{Al}_5\text{Co}_2(2\bar{1}0)$ est un catalyseur potentiel de la semi-hydrogénation du butadiène, ayant une grande sélectivité malgré une activité modérée. La structure de ce composé (Fig. 1.8) peut être vue comme une succession de plans atomiques de types ($2\bar{1}0$) plats (F, *flat*) et corrugués (P, *puckered*). Une étude préliminaire se basant sur des mesures LEED (diffraction d'électrons lents) et STM (microscopie à effet tunnel) suggère une reconstruction de surface (2×1). Plusieurs modèles de surface sont donc proposés. Les deux modèles les plus probables présentent une terminaison P (Fig. 1.9). Cette terminaison P peut être décrite comme une succession de motifs bipentagonaux d'aluminium avec en leurs centres des atomes de cobalt placés alternativement au dessus et en dessous du plan moyen desdits bipentagones. Des calculs DFT ainsi que des mesures STM suggèrent la présence d'un seul bipentagone (au dessus d'un atome de cobalt) sur deux, induisant de fait une reconstruction (2×1). La présence ou non des atomes de cobalt protubérants reste indéterminée. Le premier modèle de surface présente tous les atomes de cobalt protubérants (au nombre de 4) et se nomme P_B . Le second modèle quant à lui n'en présente aucun et se nomme $P_{B-4\text{Co}}$. Le nombre de cobalt présents en surface est facteur important puisqu'il peut influencer grandement les propriétés de catalyse.

Les atomes de cobalt protubérants n'étant pas cristallographiquement équivalents deux autres modèles de surface sont donc imaginés et se nomment $P_{B-2\text{Co},1}$ et $P_{B-2\text{Co},2}$ (Fig. 3.5). Des calculs *ab initio* d'énergies de surface montrent que les différents modèles peuvent être stables sur différents domaines de potentiel chimique (Fig. 3.6). Des simulations d'image STM ne permettent pas de discriminer les quatre modèles précédemment évoqués (Fig. 3.7).

Des mesures de diffraction de surface des rayons X (SXRD, Fig. 3.9) sont donc effectuées afin de permettre une discrimination entre les différents modèles de surface. Une analyse basée sur la mesure de 12 tiges de troncature et 10 tiges de reconstruction montre une prédominance du modèle $P_{B-2\text{Co},1}$ (présentant seulement deux atomes de cobalt protubérants par maille de surface). Une combinaison des modèles $P_{B-2\text{Co},1}$ et $P_{B-2\text{Co},2}$ dans un ratio 3:1 permet d'améliorer l'accord entre les mesures expérimentales et les simulations. Néanmoins, $P_{B-2\text{Co},1}$ est retenu comme étant le modèle principal pour la suite de l'étude.

Des calculs d'adsorption sont par la suite effectués afin de déterminer les différents

sites stables de l'hydrogène, du butadiène ainsi que du but-1-ène sur $P_{B-2Co,1}$. En tenant compte du site le plus favorable pour le butadiène (une double liaison adsorbée sur un cobalt protubérant, et l'autre sur un aluminium), il existe deux façons de l'hydrogéner pour obtenir du but-1-ène (Fig. 3.12). Ces deux voies mènent à deux modes d'adsorption différent du butène (Fig. 3.13), à savoir un mode chimisorbé (hydrogénation de la liaison liée à un aluminium) et un mode physisorbé (hydrogénation de la liaison adsorbée sur un cobalt). Grâce à la détermination des différents sites d'adsorption de l'hydrogène sur la surface, il est possible de calculer les énergies de coadsorption du butadiène/but-1-ène avec différents taux de couverture d'hydrogène. Les différents résultats sont intégrés dans un modèle thermodynamique qui calcule l'enthalpie de coadsorption en fonction de la température et des pressions partielles des réactifs. Ce modèle permet de déterminer la faisabilité thermodynamique de la réaction sur ce modèle de surface.

Aux conditions expérimentales ($p_{tot} = 5.5$ mbar et $T = 383$ K), le modèle thermodynamique prédit que les deux modes d'adsorption (chimisorption et physisorption) sont stables (Fig. 3.15). Néanmoins le mode physisorbé possède une énergie de coadsorption plus faible que le mode chimisorbé. D'après les mesures expérimentales, la surface est 100% sélective pour la semi-hydrogénation pour cette condition de pression et de température, et la conversion totale. Cela induit donc une adsorption très faible du but-1-ène, empêchant une hydrogénation complète en butane. Le modèle prédit une température de désorption de 440 K pour le mode physisorbé (57 K au dessus de la température expérimentale), et de 572 K pour le mode chimisorbé (189 K au dessus de la température expérimentale). Ce résultat permet donc d'entrevoir un possible mécanisme de réaction qui consisterait à hydrogéner en premier la double-liaison C=C adsorbée sur les cobalt protubérants. La présence de seulement deux atomes de cobalt par maille de surface affecterait donc les propriétés de catalyse de $Al_5Co_2(2\bar{1}0)$, le comportement étant bien différent lorsque l'on considère un modèle avec plus de cobalt (Fig. 3.17).

Des calculs supplémentaires permettant d'établir un chemin de réaction possible sont toutefois nécessaires pour déterminer le mécanisme de réaction et la réactivité de cette surface vis-à-vis de la semi-hydrogénation du butadiène.

Hydrogénation et nanostructuration de $Al_{13}Co_4(100)$

La deuxième étude présentée dans cette thèse porte sur la structure de la surface (100) du composé $Al_{13}Co_4$ (groupe d'espace No. 31 $Pmn2_1$, symbole de Pearson $oP102$). La structure de ce composé peut être décrite de deux manières différents : soit par une succession (le long de la direction [100]) de plans plats (F, *flat*) et corrugués (P, *puckered*), soit par une assemblage de clusters (blocs atomiques) identiques (Fig. 1.12). Deux modèles ont été proposés par le passé pour la surface (100) [24, 18] (Fig. 4.1). Un premier modèle suggère une surface corruguée et nanostructurée où les clusters sont préservés [24]. Ce modèle possède deux atomes de cobalt protubérants par maille de surface (modèle P_{14}). Il a été déterminé par des calculs *ab initio* par clivage de la structure bulk. Un deuxième modèle a été par la suite suggéré et est plus en accord avec les mesures expérimentales sous con-

dition ultra-vide (STM, LEED, SXRD). Il s'agit d'une terminaison présentant un plan dense P privé d'atomes de cobalt protubérants (modèle P₂₄) [18]. Il a été montré expérimentalement que cette surface était un potentiel catalyseur pour des réactions d'hydrogénation [8]. Des calculs DFT (adsorption, barrières de réaction) ont cependant montré que le modèle P₂₄ – observé expérimentalement – ne pouvait être une surface active en catalyse [15] contrairement au modèle P₁₄ (actif et sélectif) [24].

Des calculs d'énergies de surface montrent que les deux modèles P₁₄ et P₂₄ sont tous deux stables sur des domaines de potentiel chimique (Fig. 4.2). Des calculs d'adsorption d'hydrogène, de butadiène et de butène permettent de déterminer les différents sites favorables des différents adsorbats sur les deux surfaces (Figs. 4.3, 4.4, 4.5, 4.6 et 4.7). Il est possible alors de modifier le modèle thermodynamique évoqué précédemment pour corriger l'énergie de surface en fonction des taux de couvertures des adsorbats (adsorption/coadsorption). Ce nouveau modèle permet de prédire l'énergie de surface en fonction de la pression, de la température et du potentiel chimique de l'aluminium. Aux conditions expérimentales ($p_{\text{tot}} = 5.5$ mbar et $T = 383$ K), l'adsorption de butadiène inhibe l'adsorption d'hydrogène sur P₂₄ (Fig. 4.10 et 4.11). Cette surface est donc inactive vis-à-vis de l'hydrogénation du butadiène. P₁₄ a un comportement inverse : la coadsorption de butadiène et de six hydrogènes stabilise la surface. Puisque P₂₄ a été observé expérimentalement sous condition ultra-vide, et que seule la surface P₁₄ semble favorable sous les conditions de réaction (d'un point de vue thermodynamique), les résultats prédisent donc une transition d'une surface plate vers une surface corruguée présentant des atomes de cobalts protubérants.

De manière similaire à la première étude précédemment évoquée, une fois le butadiène adsorbé, il existe deux façons de l'hydrogéner en butène. Ces deux voies mènent à deux modes d'adsorption différent du butène, à savoir un mode chimisorbé (hydrogénation de la liaison liée à un aluminium) et un mode physisorbé (hydrogénation de la liaison adsorbée sur un cobalt). Dans le cas du butène chimisorbé (Fig. 4.12b) et aux conditions expérimentales ($p_{\text{tot}} = 5.5$ mbar), la température calculée de désorption est de 502 K (119 K au dessus de la température expérimentale). Dans le cas du butène physisorbé (Fig. 4.12c), la température calculée de désorption est de 420 K (37 K au dessus de la température expérimentale). Puisque les mesures expérimentales montrent une sélectivité de 100% et une conversion totale, le butène ne peut rester adsorbé et s'hydrogéner de nouveau en butane. Ce résultat donne des pistes de réflexion quant à un potentiel mécanisme de réaction, qui consisterait une fois de plus à hydrogéner en premier la double-liaison C=C adsorbée sur les cobalts protubérants.

Ces résultats restant théoriques, il est nécessaire d'établir une vérification expérimentale de la nanostructuration de Al₁₃Co₄(100) sous des conditions d'hydrogénation. Des mesures *operando* de diffraction de surface des rayons X permettraient d'apporter la réponse à cette question.

Stabilisation et activation de $\text{Al}_{13}\text{Co}_4(010)$ par facettage

La troisième étude présentée dans ce document s'intéresse à la structure de la surface (010) de l'intermétallique complexe $o\text{-Al}_{13}\text{Co}_4$ et sur ses propriétés d'adsorption de l'hydrogène. Une étude récente [8] a montré que cette surface était active et sélective vis-à-vis de la semi-hydrogénation du butadiène (Fig. 1.26). La structure de sa surface ainsi que les mécanismes liés à sa réactivité sont donc des sujets d'intérêts.

L'analyse des clichés LEED (Fig. 5.3) met principalement en évidence une structure de surface (1×1) coexistant avec des reconstructions de types (2×1) et (3×1) . Ces clichés montrent aussi la présence de facettes le long de la direction $[100]$. Une intensité continue entre les pics de diffraction le long de la direction $[001]$ suggère de plus la présence de défauts planaires. Des mesures AFM et STM (Fig. 5.4) confirment la présence de facettes et montrent une structure en colonne le long de la direction $[100]$. Les images STM confirment aussi la coexistence de surfaces (1×1) , (2×1) et (3×1) . Au total, 17 modèles de surfaces sont proposés (Fig. 5.11). Un modèle se distingue – modèle dénommé O_0 – en possédant la plus faible énergie de surface (1.66 J/m^2) sur tout le domaine de potentiel chimique autorisé (Fig. 5.9). La simulation des images STM de ce modèle pour un bias positif est en accord avec les données expérimentales (Fig. 5.13). Des mesures de diffraction de surface permettent de confirmer ce modèle de surface comme étant la structure la plus pertinente (Fig. 5.14). Ces mesures montrent aussi la présence de facettes à la surface de l'échantillon et permettent d'entrevoir leurs structures. Elles montrent que ces dernières n'ont pas la même structure que le volume : il s'agit de la phase monoclinique $\text{Al}_{13}\text{Co}_4$ et plus précisément de la surface $m\text{-Al}_{13}\text{Co}_4(\bar{2}01)$. De nouveau, 17 modèles de surface sont proposés (Fig. 5.16) et deux modèles se distinguent (modèles $M_{0,9}$ et $M_{3,15}$, plans denses) par leurs faibles énergies de surface ($1.2\text{--}1.3 \text{ J/m}^2$, Fig. 5.17).

Des calculs d'adsorption d'hydrogène atomique permettent de dresser une cartographie des énergies d'adsorption des terrasses orthorhombiques et des facettes monocliniques (Fig. 5.21). Les sites les plus favorables sur les terrasses orthorhombiques sont les atomes d'aluminium protubérants placés au dessus d'atomes de cobalt ($E_{\text{ads}} = -0.59 \text{ eV}$, un seul site par maille de surface). Sur les facettes, les sites les plus favorables sont les atomes de cobalt protubérants ($E_{\text{ads}} = -0.53 \text{ eV}$, 4 sites par maille de surface). L'adsorption d'hydrogène est forte sur les deux surfaces (mais reste moins forte que sur Pd(111) ou Pd(100), qui est de l'ordre de -1 eV [25]). Cela suggère que la dissociation de l'hydrogène moléculaire est très probable. D'autres sites d'adsorption légèrement moins favorables se retrouvent en nombre sur les deux surfaces et sont probablement favorable pour la diffusion de l'hydrogène pendant les réactions d'hydrogénation.

Ces résultats offrent des pistes intéressantes pour comprendre en détails les propriétés catalytiques de $\text{Al}_{13}\text{Co}_4(010)$. Des mesures *operando* sous conditions catalytiques et des calculs complémentaires sont nécessaires pour déterminer le mécanisme de réaction et la réactivité de cette surface.

Structure de surface et réactivité de $\text{Al}_{13}\text{Fe}_4(010)$

La dernière étude présentée dans ce manuscrit porte sur la détermination de la structure de la surface (010) de $\text{Al}_{13}\text{Fe}_4$ et de sa réactivité vis-à-vis de la réaction d'hydrogénation du butadiène. Le composé $\text{Al}_{13}\text{Fe}_4$ appartient au groupe d'espace $C2/m$ (No. 12, symbole de Pearson $mC102$). Le long de cette direction [010], la structure de $\text{Al}_{13}\text{Fe}_4$ peut être décrite par une succession de plan plats (F, *flat*) et corrugués (P, *puckered*) ou bien par un assemblage de clusters atomiques (similaires à ceux de $\text{Al}_{13}\text{Co}_4$, Fig. 1.15). Des mesures LEED (Fig. 6.1) et STM (Fig. 6.2), ainsi que des simulations DFT, suggèrent un modèle de surface corruguée présentant une terminaison de type P et préservant la structure en clusters. La présence d'atomes d'aluminiums entre ces clusters (atomes dits "glue") n'est pas entièrement déterminée et dépendrait des conditions de préparation de l'échantillon (température de recuit, paramètres de bombardement ionique) [26]. Il a été montré que cette surface était un catalyseur actif et relativement sélectif vis-à-vis de la semi-hydrogénation du butadiène [7].

Afin de déterminer la structure de surface de $\text{Al}_{13}\text{Fe}_4(010)$, cinq modèles de surface sont proposés (Fig. 6.3) et leurs énergies de surface sont calculées (Fig. 6.4). Deux modèles se distinguent par leurs faibles énergies de surface sur deux domaines distincts de potentiel chimique : le modèle P, plan P complet ($1.67\text{--}1.68\text{ J/m}^2$), et le modèle P_2^{inc} , plan P incomplet et corrugué ($1.68\text{--}1.73\text{ J/m}^2$), préservant les clusters en surface et présentant deux atomes d'aluminium "glue" par maille de surface. Les trois autres modèles envisagés présentent de même des terminaisons par des plans P incomplets, seul le nombre d'atomes d'aluminium "glue" varie. La mesure des tiges de troncatures par diffraction de surface des rayons X suggère que seulement un atome Al "glue" est présent par maille de surface (Fig. 6.13). Néanmoins la présence de deux atomes d'aluminium "glues" reste probable, et ce modèle de surface est retenu comme étant le meilleur pour $\text{Al}_{13}\text{Fe}_4(010)$.

Dans le but de déterminer la réactivité de cette surface, une première étape consiste à déterminer les sites d'adsorption favorables de l'hydrogène atomique, du butadiène et du butène (Figs. 6.14 et 6.15). Au total, 14 sites d'adsorption de l'hydrogène sont stables ($E_{\text{ads}} > -0.61\text{ eV}$). Le butadiène s'adsorbe quant à lui préférentiellement sur un atome de fer protubérant et sur un atome d'aluminium du pentagone environnant ($E_{\text{ads}} = -1.90\text{ eV}$). Les deux voies d'hydrogénation du butadiène permettent d'obtenir deux modes d'adsorption différents du butène. Cependant ces deux modes présentent des énergies similaires. Le modèle montre que la réaction est faisable d'un point de vue thermodynamique aux conditions expérimentales ($p_{\text{tot}} = 5.5\text{ mbar}$ et $T = 297\text{ K}$, Fig. 6.16). Néanmoins, contrairement aux études précédentes, il n'est pas possible d'envisager un quelconque mécanisme de réaction en se basant simplement sur des résultats thermodynamiques. Des calculs de barrières énergétiques sont donc nécessaires.

Des calculs NEB (*Nudged Elastic Band*) permettent de déterminer les énergies d'activation des différentes étapes du mécanisme de réaction envisagé. La dissociation de l'hydrogène sur un atome de fer protubérant possède une énergie d'activation relativement faible

($E_a = 0.06$ eV) comparé à $\text{Al}_{13}\text{Co}_4(100)$ ($E_a = 0.18$ eV, [24]). Les barrières d'activation les plus grandes sont calculées pour des étapes intermédiaires de diffusion de l'hydrogène sur la surface pour la réaction de semi-hydrogénation et sont de l'ordre de 0.75 eV. L'étape limitante de l'hydrogénation totale est quant à elle la troisième hydrogénation (C_4H_8 en C_4H_9) avec une énergie d'activation de l'ordre de 0.86 eV. La détermination d'un potentiel chemin de réaction (Fig. 6.19) permet l'estimation des constantes de réaction (facteurs pré-exponentiels et énergies d'activation) pour chaque étape intermédiaire.

Connaissant toutes les constantes de réaction, il est possible de construire un modèle microcinétique de réaction d'hydrogénation du butadiène sur $\text{Al}_{13}\text{Fe}_4(010)$. Ce modèle prédit les taux de couvertures et de productions au cours du temps des différentes molécules mises en jeu dans la réaction chimique considérée (Fig. 6.20). Il est ainsi possible d'étudier la réaction pour différentes conditions de pression et de température et de prédire les taux de production de butène et de butane pour un couple (p,T). Ainsi, pour une pression totale de 5.5 mbar (5 mbar d'hydrogène, 0.5 mbar de butadiène), la température optimale calculée est de 423 K. À ces conditions, la production de butène atteint 353 molécules par seconde et par maille de surface (Fig. 6.21). La production calculée de butane est négligeable (de l'ordre de 10^{-6} molécule par seconde et par maille de surface), ce qui confirme la grande sélectivité vis-à-vis de la semi-hydrogénation du butadiène.

Ces résultats doivent encore être confrontés à des mesures expérimentales plus complètes telles que des mesures de performances catalytiques à différentes pressions et températures, ainsi que des mesures *operando* de diffraction de surface sous conditions de réaction.

Conclusions et perspectives

Les travaux de recherches effectués au cours de cette thèse ont permis d'apporter de nouvelles connaissances sur les structures de surface et les propriétés d'adsorption et de catalyse de certains intermétalliques à base d'aluminium (Al_5Co_2 , $\text{Al}_{13}\text{Co}_4$, $\text{Al}_{13}\text{Fe}_4$). Le couplage théorique/expérimental de la DFT et de la diffraction de surface des rayons a été la combinaison idéale à utiliser. À l'avenir, une utilisation plus poussée de ces outils (diffraction de surface *in situ* et/ou *operando*, couplés à des calculs de chemins réactionnels) est nécessaire afin de comprendre encore plus en détail les mécanismes à l'origine de la réactivité spécifique de ces intermétalliques complexes.

D'un point vue plus théorique, les prédictions des énergies et les modèles thermodynamiques/microcinétiques pourraient être améliorés en augmentant la précision des calculs (discrétisation de l'espace réciproque) et en changeant la fonctionnelle utilisée. Une analyse plus systématique en fonction des fonctionnelles pourraient s'avérer très pertinente. Enfin, une utilisation de *machine learning* pour le calcul de barrières de réaction et d'algorithmes génétiques pour la prédiction de nouvelles structures – assistés par des calculs *ab initio* – pourrait être un pas de plus en avant pour trouver d'autres matériaux capables de répondre aux demandes du monde de la catalyse [27, 28].

D'autres intermétalliques complexes à base d'aluminium, comme Al_5Fe_2 pourraient s'avérer être de bons candidats pour la catalyse et mériteraient une étude approfondie de leurs propriétés. Cependant, du fait de la présence d'aluminium, ces intermétalliques sont sujet à une désactivation par oxydation [9], ce qui rend leur utilisation difficile à une échelle industrielle. D'autres matériaux moins sensibles à une contamination par l'oxygène pourraient aussi être un axe à développer. Le gallium pourrait être un bon substitut à l'aluminium et permettrait de contourner de potentielles désactivations du fait d'une contamination des surfaces. Ces matériaux pourraient aussi se présenter sous d'autres formes telles que des couches minces [29] ou des nanoparticules. Auquel cas, une approche théorique pourraient être couplées avec d'autres méthodes expérimentales, telle que l'imagerie par diffraction cohérente des rayons X (*coherent x-ray diffraction imaging*) [30].

Contents

Résumé	v
Abstract	vii
Synthèse	ix
Index	xxv
Introduction	1

Chapter 1

Catalysis and Al-based intermetallics

1.1	Heterogeneous Catalysis	5
1.1.1	Definition and historical background	5
1.1.2	Key parameters and theory of adsorbate-surface interactions	7
1.1.3	Alkynes and alkenes partial hydrogenation	8
1.2	Materials	10
1.2.1	Quasicrystals	10
1.2.2	Intermetallic compounds	11
1.2.3	Complex intermetallic compounds	11
1.3	Al-based complex intermetallics	13
1.3.1	Al_5Co_2	13
1.3.2	Al_5Fe_2	15
1.3.3	$\text{Al}_{13}\text{Co}_4$	16
1.3.4	$\text{Al}_{13}\text{Fe}_4$	21
1.3.5	Defects in complex intermetallics : twins and metadislocations	22
1.3.6	The need for single-crystalline materials	26
1.3.7	Crystal growth using Czochralski process	27

1.4	Catalytic preliminary results	29
1.4.1	Al ₁₃ TM ₄	29
1.4.2	Al ₅ Co ₂	34

<p>Chapter 2</p> <p>Theoretical and Experimental Methodologies</p>
--

2.1	Principles of Density Functional Theory	36
2.1.1	Schrödinger equation	36
2.1.2	The Hohenberg and Kohn theorems	37
2.1.2.1	Existence theorem	38
2.1.2.2	Variational principle	38
2.1.3	The Kohn-Sham method and the Exchange-Correlation energy	38
2.1.3.1	Local density approximation (LDA)	39
2.1.3.2	Generalized gradient approximation (GGA)	40
2.1.4	The PBE and DFT-D3 functionals	40
2.1.5	Numerical implementation	41
2.1.5.1	VASP code	41
2.1.5.2	Reciprocal space discretization	41
2.1.5.3	Plane waves basis definition	43
2.1.5.4	Pseudo-potentials and Projector-Augmented Wave method	44
2.2	DFT applications to Al-based intermetallics	44
2.2.1	Bulk and surfaces simulations	44
2.2.2	Electronic structure	44
2.2.2.1	Density of states	44
2.2.2.2	STM images simulations	46
2.2.3	Thermodynamic simulations	46
2.2.3.1	Surface energy calculations	47
2.2.3.2	Adsorption of molecules	48
2.2.3.3	Thermodynamic modelling	49
2.2.4	Kinetic calculations	50
2.2.4.1	Nudged elastic band method	50
2.2.4.2	Butadiene hydrogenation elementary steps	52
2.2.4.3	Microkinetic modelling	53
2.3	Surface X-ray Diffraction (SXRD)	55
2.3.1	Basics of x-ray diffraction	55

2.3.2	Crystal truncation rods	56
2.3.3	Reciprocal space exploration	57
2.3.4	Data collection and analysis	58
2.3.5	Experimental end-stations at SixS beamline	59
2.4	Conventional surface investigation techniques	61
2.4.1	Surface preparation	61
2.4.2	Auger electron spectroscopy (AES)	61
2.4.3	Low energy electron diffraction (LEED)	61
2.4.4	Scanning tunneling microscopy (STM)	62
2.4.5	Atomic force microscopy (AFM)	62
2.4.6	Catalysis experiments	62

Chapter 3

From the surface structure to the catalytic properties of $\text{Al}_5\text{Co}_2(2\bar{1}0)$

3.1	Introduction	66
3.2	Preliminary experimental results	66
3.2.1	Sample preparation	66
3.2.2	STM	66
3.2.3	Catalytic measurements	68
3.3	DFT results – Surface structure	69
3.3.1	Surface models	69
3.3.2	Surface energy calculations	70
3.3.3	STM image simulations	71
3.4	SXRD analysis	72
3.4.1	In-plane measurements	72
3.4.2	CTRs and SSRs extraction	72
3.5	Adsorption calculations	75
3.5.1	Hydrogen adsorption	76
3.5.2	Butadiene adsorption	76
3.5.3	But-1-ene adsorption	78
3.5.4	Coadsorption of hydrogen and butadiene/but-1-ene	79
3.5.5	Competition between chemisorption and physisorption	80
3.5.6	Influence of Co surface density	82
3.6	Conclusion	84

Chapter 4

Nanostructuring of $\sigma\text{-Al}_{13}\text{Co}_4(100)$ under reaction conditions

4.1	Introduction	88
4.2	Surface energy calculations	89
4.3	Hydrogen adsorption	90
4.3.1	On corrugated $\sigma\text{-Al}_{13}\text{Co}_4(100)$	90
4.3.2	On flat $\sigma\text{-Al}_{13}\text{Co}_4(100)$	91
4.4	Butadiene and but-1-ene adsorptions	92
4.4.1	C_4H_6 on corrugated $\sigma\text{-Al}_{13}\text{Co}_4(100)$	92
4.4.2	C_4H_6 on flat $\sigma\text{-Al}_{13}\text{Co}_4(100)$	93
4.4.3	Adsorption of C_4H_8	94
4.5	Nanostructuring under reaction conditions	94
4.5.1	Thermodynamic modelling and modification of the surface energy	95
4.5.2	Hydrogen optimum coverages	96
4.5.3	Coadsorption of hydrogen and butadiene	98
4.6	Catalytic activation and hydrogenation reaction	99
4.6.1	Catalytic activation	99
4.6.2	Coadsorption of hydrogen and but-1-ene	99
4.7	Conclusion	101

Chapter 5

Stabilization and activation of $\sigma\text{-Al}_{13}\text{Co}_4(010)$ through faceting

5.1	Introduction	104
5.2	Preliminary catalytic results	104
5.3	Surface experiment results	106
5.3.1	LEED analysis	106
5.3.2	AFM and STM measurements	107
5.3.3	SXRD analysis	109
5.3.3.1	In-plane and out-of-plane measurements	109
5.3.3.2	Diffuse scattering	109
5.3.4	Simulation of the reciprocal space	112
5.3.5	Experimental conclusion	114
5.4	DFT results : surface structures	115
5.4.1	$\sigma\text{-Al}_{13}\text{Co}_4(010)$ – Flat terraces	115

5.4.2	$m\text{-Al}_{13}\text{Co}_4(\bar{2}01)$ – Facets	121
5.5	Relative stability of $\text{Al}_{13}\text{Co}_4(010)$ and $\text{Al}_{13}\text{Co}_4(100)$	123
5.5.1	Surface energies	123
5.5.2	DOS	125
5.6	Hydrogen adsorption on $\text{Al}_{13}\text{Co}_4$	126
5.7	Conclusions and perspective	128

Chapter 6

Surface structure and reactivity of $m\text{-Al}_{13}\text{Fe}_4(010)$

6.1	Introduction	132
6.2	Preliminary experimental and theoretical results	132
6.2.1	LEED measurements	132
6.2.2	STM images	133
6.2.3	Surface energy calculations	134
6.2.4	STM image simulation	135
6.2.5	Catalytic measurements	136
6.3	SXRD analysis	137
6.3.1	In-plane measurements	137
6.3.2	CTRs extraction	143
6.4	Adsorption calculations	145
6.4.1	Hydrogen adsorption	145
6.4.2	Butadiene and but-1-ene adsorptions	146
6.4.3	Coadsorption of hydrogen and butadiene/but-1-ene	147
6.5	Hydrogenation of butadiene : reaction pathways and kinetics	148
6.5.1	NEB calculations	148
6.5.1.1	H_2 dissociation	148
6.5.1.2	Partial hydrogenation	149
6.5.1.3	Complete hydrogenation	150
6.5.1.4	Rate constants calculations	150
6.5.1.5	Summary of the reaction path	151
6.5.2	Microkinetic modelling	152
6.6	Conclusion	155

Conclusions and Future Works

157

Appendices	163
Appendix A Publications	163
Appendix B Crystallographic data	165
B.1 Al_5Co_2	166
B.2 Al_5Fe_2	166
B.3 $o\text{-Al}_{13}\text{Co}_4$	167
B.4 $m\text{-Al}_{13}\text{Co}_4$	168
B.5 $m\text{-Al}_{13}\text{Fe}_4$	169
Appendix C Python scripts	171
C.1 Thermodynamic modelling	171
C.2 Pre-exponential factors	172
C.3 Microkinetic modelling	187
C.4 Reciprocal space simulation	191
Appendix D Diffraction data	195
D.1 SXRD data of $\text{Al}_{13}\text{Co}_4(010)$	195
D.2 Fourier transform of $\text{Al}_{13}\text{Co}_4$	195
D.3 SXRD data of $\text{Al}_{13}\text{Fe}_4(010)$	195
Bibliography	203

Glossary

2D : 2-dimensional
3D : 3-dimensional
AES : Auger Electron Spectroscopy
AFM : Atomic Force Microscopy
CIC : Complex Intermetallic Compound
CTR : Crystal Truncation Rod
DFT : Density Functional Theory
DOS : Density of States
FT : Fourier Transform
GC : Gas Chromatography
GGA : Generalized Gradient Approximation
HRTEM : High-Resolution Transmission Electron Microscopy
LEED : Low Energy Electron Diffraction
LDA : Local Density Approximation
MS : Mass Spectrometry
QC : Quasicrystal
SSR : Super-Structure Rod
STEM : Scanning Transmission Electron Microscopy
STM : Scanning Tunneling Microscopy
SXRD : Surface X-ray Diffraction
TOF : Turn-Over Frequency
TM : Transition Metal
UHV : Ultra-High Vacuum

Index

A	Surface area (m^2)
A_0	Preexponential factor (s^{-1})
ε	Eigenvalue of a wavefunction
$f(\mathbf{q})$	Atomic form factor
$F(\mathbf{q})$	Structure factor
G	Free enthalpy (eV)
γ	Surface energy (J/m^2)
h	Planck constant
c	Speed of light
ΔH_f	Formation enthalpy (eV)
\hat{H}	Hamiltonian operator
I_{hkl}	Scattered intensity
I_t	Tunneling current (A)
k	Wave vector
k_f	Forward rate constant (s^{-1})
k_r	Reverse rate constant (s^{-1})
k_B	Boltzmann constant
m	Mass (kg)
μ	Chemical potential (eV)
ν	Vibration frequency (THz)
p	Pressure (bar or Pa)
φ	Multi-electronic wave function
Ψ	Eigenvector of \hat{H}
ψ	Wave function
q	Momentum transfer
R	Ideal gas constant
ρ	Electron density
σ	Symmetry number
T	Temperature (K or $^\circ\text{C}$)
ϑ	Coverage
ϑ_{rot}	Rotational temperature (K)
Z	Partition function

Introduction

Catalysis plays a large role in today's chemical industry and there is a constant demand for better and cheaper catalysts. In this regard, the selective hydrogenation of alkynes and dienes from streams containing alkenes are important class of reactions in the petrochemical industry. Steam cracking, catalytic cracking and coking lead to traces of alkynes (*e.g.* acetylene) and/or dienes (*e.g.* butadiene), which have to be selectively hydrogenated into olefinic compounds before alkenes can be further processed by polymerization (*e.g.* the polyethylene production is 80 megatons per year in 2008 [22]) or selective oxidation (*e.g.* the ethylene oxidation into oxirane, around 20 megatons per year in 2018). In this context, the development of catalysts with a high activity, stability and selectivity is crucial.

Typical catalysts for the alkynes and dienes hydrogenations are Pd-based materials. The reaction selectivities to partially hydrogenated products can be improved by the addition of other metal such as Ag [1]. First-principles calculations suggested Ni–Zn alloys as low-cost substitutes to reference Pd–Ag [31] for acetylene partial hydrogenation. However, these alloys may suffer from adsorption-induced surface segregation under reaction conditions, which usually leads to a decrease in selectivity [5, 2, 6]. Searching for stable, selective, low-cost and environmentally benign catalysts for acetylene and butadiene semi-hydrogenations led to the recent identification of transition-metal (TM) Al-based complex intermetallics such as $\text{Al}_{13}\text{Fe}_4$, $\text{Al}_{13}\text{Co}_4$, and $\text{Al}_{13}\text{Ru}_4$ as efficient catalysts [22, 21, 7, 26, 9, 32, 19, 8]. A great asset of these compounds is related to their covalent-like chemical bonding network, that may prevent any surface segregation process, ensuring the structural stability of the catalyst [33, 34]. The activity towards the gas-phase butadiene hydrogenation was shown to increase in the order $o\text{-Al}_{13}\text{Co}_4(100) \ll m\text{-Al}_{13}\text{Ru}_4(010) < m\text{-Al}_{13}\text{Fe}_4(010)$ (at room temperature), when comparing the same types of pseudo 10-fold surfaces [8]. Above room temperature, another surface orientation of $\text{Al}_{13}\text{Co}_4$ (the pseudo 2-fold surface $o\text{-Al}_{13}\text{Co}_4(010)$) was determined as the most active one while remaining 100% selective towards butenes, unlike $\text{Al}_{13}\text{Fe}_4(010)$.

The promising catalytic performances of another Al-based complex intermetallic surface – $\text{Al}_5\text{Co}_2(2\bar{1}0)$ – were suggested by a recent theoretical investigation [15]. This study highlighted the influence of the topmost surface Co atoms on the adsorption properties and catalytic activity, in the case of the semi-hydrogenation of acetylene.

Several factors may influence the catalytic performances of intermetallic compounds [35]. Isolating active transition metal atoms into single-sites through alloying generally increases the selectivity [36, 37]. In the case of pure metals, the adsorption properties of the

reactants and therefore the reaction barriers can be rationalized by their electronic structure (d-band position and width) [38, 39]. Correlations between electronic structure and selectivity also exist in the case of intermetallic compounds [40, 41]. Last, surface corrugation plays a role, *i.e.* mono-atomic steps may offer completely new reaction pathways with highly reduced energy barriers compared to flat surfaces [42].

The objective of this project is to determine the surface structures (under ultra-high vacuum and reaction conditions), the adsorption and catalytic properties of these complex intermetallics. To do so, an approach combining surface science experiments and theoretical chemistry calculations (surface energies, adsorption energies and reaction paths calculations) is adopted. Because of the complexity of industrial processes (complex catalytic systems made of nanoparticles, faceted structures, promoters, *etc*), this work focuses on ideal surface models and single-crystalline materials with unique surface orientation. The overall strategy is the following. First, single crystals of Al-based intermetallics are grown and used to determine experimentally their surface structures (scanning tunneling microscopy – STM, surface X-ray diffraction – SXRD) as well as their catalytic performances. Then model catalysts are theoretically investigated through the means of *ab initio* calculations (density functional theory) in order to estimate their surface energies, adsorption properties, and reaction pathways. Finally and based on both experimental and theoretical analyses, the reaction thermodynamic feasibility and kinetic are determined to provide macroscale insights regarding their specific reactivity.

The present manuscript is divided into six main parts, detailed as follow. A fundamental and concise review regarding catalysis and intermetallics is presented in Chapter 1. The reader will find all the relevant definitions that are useful for the reading of the manuscript, as well as some preliminary results of different Al-based complex intermetallics catalytic performances.

Chapter 2 of this thesis focuses on the different methodologies that are used throughout this entire work. The two principal techniques – DFT and SXRD – are treated in detail. Different numerical tools used to determine the thermodynamic feasibility and reaction kinetic are also presented.

Chapter 3 deals with the question of the surface structure of $\text{Al}_5\text{Co}_2(2\bar{1}0)$ using a combination of SXRD and *ab initio* calculations. Since it has been experimentally shown that this surface catalyzes the reaction of butadiene partial hydrogenation, its catalytic properties are studied through the means of a thermodynamic modelling. The influence of surface Co atoms on the butadiene adsorption is also investigated.

Chapter 4 is focused on the pseudo 10-fold surface of $\text{Al}_{13}\text{Co}_4$ that has been shown to present fair catalytic performances while being theoretically poorly active. This chapter thus tackles the question of a possible surface restructuring of $o\text{-Al}_{13}\text{Co}_4(100)$ under hydrogenation conditions – using *ab initio* calculations and thermodynamic modelling – that might explain the experimental observations.

Chapter 5 investigates the surface structure of $o\text{-Al}_{13}\text{Co}_4(010)$ that has been experimentally shown to be a good (active and selective) catalyst for the partial hydrogenation of butadiene. Here again a combination of SXRD and DFT calculations is used to study the surface structure. Hydrogen adsorption is also investigated using first-principle calculations to provide insights regarding the good catalytic properties of this surface.

Finally, Chapter 6 presents the surface structure SXRD study of $m\text{-Al}_{13}\text{Fe}_4(010)$. Butadiene adsorption as well as reaction pathway calculations are performed in order to provide a possible reaction mechanism. Kinetic modelling results are then compared to experimental measurements.

Last but not least, a final part provides the general conclusions and some future perspectives that might be of interest in the future development of this topic in light of the conclusion of the present work.

Chapter 1

Catalysis and Al-based intermetallics

Contents

1.1 Heterogeneous Catalysis	5
1.1.1 Definition and historical background	5
1.1.2 Key parameters and theory of adsorbate-surface interactions	7
1.1.3 Alkynes and alkenes partial hydrogenation	8
1.2 Materials	10
1.2.1 Quasicrystals	10
1.2.2 Intermetallic compounds	11
1.2.3 Complex intermetallic compounds	11
1.3 Al-based complex intermetallics	13
1.3.1 Al_5Co_2	13
1.3.2 Al_5Fe_2	15
1.3.3 $\text{Al}_{13}\text{Co}_4$	16
1.3.4 $\text{Al}_{13}\text{Fe}_4$	21
1.3.5 Defects in complex intermetallics : twins and metadislocations	22
1.3.6 The need for single-crystalline materials	26
1.3.7 Crystal growth using Czochralski process	27
1.4 Catalytic preliminary results	29
1.4.1 $\text{Al}_{13}\text{TM}_4$	29
1.4.2 Al_5Co_2	34

1.1 Heterogeneous Catalysis

1.1.1 Definition and historical background

According to the *International Union of Pure and Applied Chemistry* (IUPAC), a catalyst is "a substance that increases the rate of a reaction without modifying the overall standard

Gibbs energy change in the reaction; the process is called catalysis" [43]. From the greek καταλυσις – meaning to loosen – catalysis has played and still plays a tremendous role in societal and technological advances : photocatalysis, biocatalysis (*e.g.* ethanol fermentation, dairy production), energy conversion (*e.g.* catalytic cracking), nanocatalysis, *etc.* Fundamentally, catalysts aim to speed up a chemical process.

There are two main types of catalysis : homogeneous and heterogeneous catalysis. While the catalyst acts in the same phase as the reactants in homogeneous catalysis, it works in a different phase in heterogeneous catalysis (*e.g.* a solid catalyst in a mixture of gases). The latter will be of particular interest in many processes such as catalytic cracking. The main advantage lies in the fairly easy separation of the products and the catalyst. In heterogeneous catalysis, two mechanisms are generally considered : the Langmuir–Hinshelwood mechanism [44, 45, 46] and the Eley–Rideal mechanism [47]. In the first mechanism both reactants are adsorbed at the surface of the catalyst, react at the surface and then happen the desorption of the product. In Eley–Rideal mechanism, only one of the reactant is adsorbed while the other one reacts with it directly from the gas phase. The first mechanism (Langmuir–Hinshelwood) appears to be generally preferred [48] (Fig. 1.1).

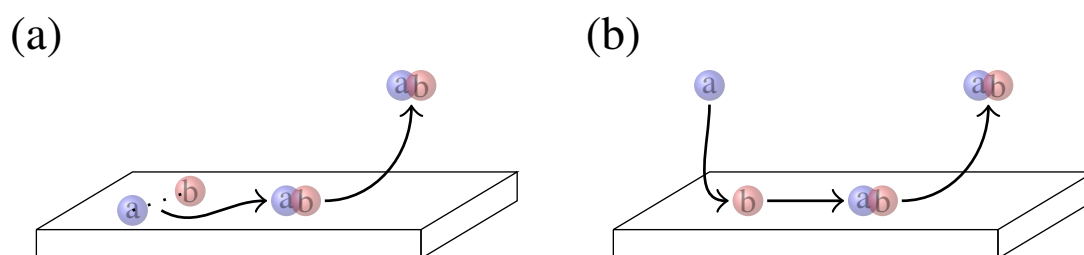


Figure 1.1: (a) Langmuir–Hinshelwood versus (b) Eley–Rideal mechanism.

The overall heterogeneous catalytic reaction generally consists of a series of elementary steps : adsorption of the reactants, diffusion on the surface, breaking of reactants bonds, creation of new bonds to form products and finally desorption of these new chemicals. Catalysts are usually complex systems in powder form (presenting different surface orientation, *i.e.* facets) coupled with promoters (chemicals that improve the catalytic activity). It is therefore difficult to provide a molecular-level understanding of such processes. Model catalysts can therefore be used to simplify the investigation. A well-built theory has been proposed by Hammer and Nørskov [49] and lays down the basic rules behind catalysis. Some key parameters are used to rationalize and describe a catalytic process and catalysts performances. More recent approaches involving the use of machine learning can help predict the key descriptors for catalysis [50, 51]. Hammer and Nørskov theory is more of a model theoretical approach that could be experimentally questioned by model catalysts.

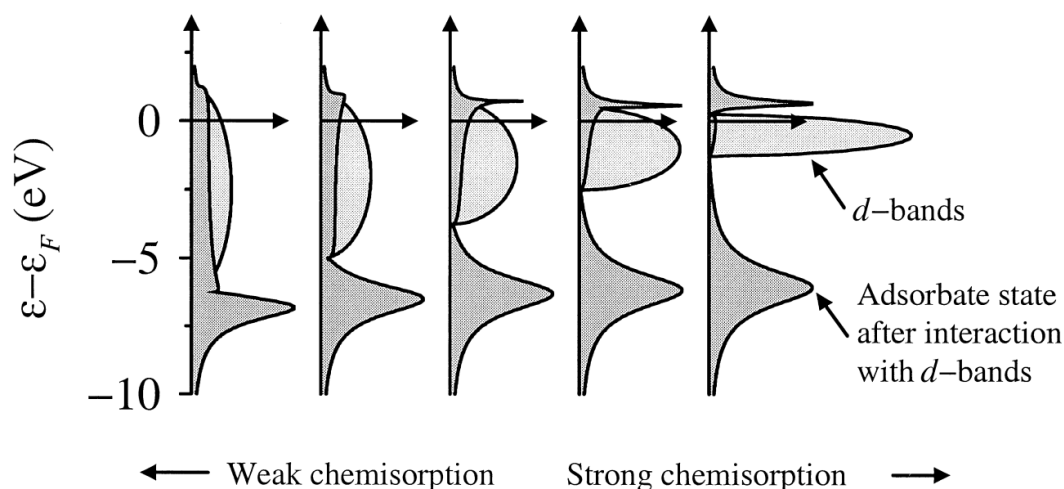


Figure 1.2: Newns–Anderson model of adsorbate–surface interactions [49, 52] : the local density of states projected onto an adsorbate state interacting with the d -bands at a surface. The strength of the adsorbate–surface coupling is kept fixed as the center of the d bands ϵ_d is shifted up toward the Fermi energy ($\epsilon_F = 0$).

1.1.2 Key parameters and theory of adsorbate-surface interactions

Catalysis is described by key parameters such as the stability (the propensity of the catalyst to stay unchanged after the reaction), the activity and the turn-over frequency (TOF, number of mole of reactant that can be converted per mole of catalyst over time), the selectivity (for example targetting the production of one particular isomer), the propensity to deactivation of the catalyst (for instance due to its oxidation). Depending on the chemical reaction, one wishes to have an active catalyst that is very stable and very selective towards a unique product, and doing so for a long time. However, it is difficult to meet all the requirements at once. A high activity is unfortunately often linked to a poor selectivity.

Hammer and Nørskov [49] have compiled and provided a well-built theory of adsorbates-surface interactions for simple transition metals. As shown in Fig. 1.2, the model predicts that as the d -band of the metal shifts up towards the Fermi level (the filling of the band is kept fixed so that as the center of the d -band is shifted up, the band width decreases), the electron density of states of the adsorbate is modified and antibonding states appear above the Fermi level. Therefore they are empty and the bonds become stronger as the number of empty antibonding states increases. In short, the closer to the Fermi level and the narrower the d -band, the stronger the bonding *i.e.* the chemisorption.

This model seems to work fine for simple transition metals (3d, 4d and 5d) [38, 39] for chemisorption (*e.g.* oxygen adsorption [49]) and also for molecular dissociation (*e.g.* CO

dissociation [53], NO dissociation on Ru(0001) [42]). A clear linear correlation between adsorption energies and d-band position is determined both experimentally and theoretically. This is similar to the Brønsted-Evans-Polanyi linear relation between the activation and reaction energies. In the case of a monolayer of a transition metal over a substrate, a similar behavior is observed and the model still works fine (*e.g.* 5d metals on Pt(111) [54]).

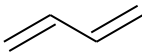
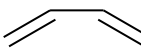
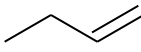
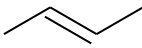
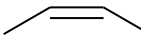
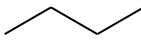
Looking at more complex structures – such as alloys or intermetallics – the rules become much more complicated. This is due to the rather more complex electronic structures of such materials (compared to simple metals). This is also due to the binding interactions between the adsorbates and the surface that are different than on simple metals. Nevertheless, correlations between electronic structure and selectivity can exist for intermetallic compounds [40, 41]. In the case of Al-based intermetallics, transition metal (TM, *e.g.* Fe or Co) atoms are 'diluted' inside an Al matrix. TM atoms can therefore be considered as isolated sites. This concept of site isolation was shown to be relevant in catalysis. Unique catalytic properties are achieved thanks to the site isolation of active species on surfaces [55]. Single atom catalysis is the extreme limit of that concept and has become over the last few years a hot topic in catalysis [37, 56]. However, when the TM atoms get isolated at the surface (*e.g.* single atom on an oxide, or at the surface of an intermetallic compound), this previously detailed model (Newns–Anderson) is not valid anymore [54, 37]. The rational design of TM-based catalysts is therefore much complicated than expected. This will be later on of interest when considering Al-based intermetallics as potential catalysts for the partial hydrogenation of alkynes and alkenes.

1.1.3 Alkynes and alkenes partial hydrogenation

Nowadays catalysis plays a great role in the chemical industry and there is a constant demand for better and cheaper catalysts. In this regard, the selective hydrogenation of alkynes (C_nH_{2n-2}) and dienes (alkenes with two C=C bonds) from streams containing alkenes are important class of reactions in the petrochemical industry (over 80 millions of tons of acetylene *per annum* [57]). Steam cracking, catalytic cracking and coking lead to traces of alkynes and/or dienes, which have to be selectively hydrogenated into olefinic compounds before alkenes can be further processed by polymerization or selective oxidation. In this context, the development of catalysts with a high activity, stability and selectivity is crucial.

The main reaction that will be studied in the present work is the semi-hydrogenation of 1,3-butadiene (C_4H_6), the simplest conjugated diene. The reaction can be reduced to the following one: $C_4H_6(g) + H_2(g) \rightarrow C_4H_8(g)$. Nevertheless, different chemicals are involved in the reaction. They are presented in Table 1.1. The whole reaction scheme is presented

Table 1.1: Molecules that are involved in the butadiene hydrogenation.

trans-1,3-butadiene	cis-1,3-butadiene	but-1-ene
		
trans-2-butene	cis-2-butene	butane
		

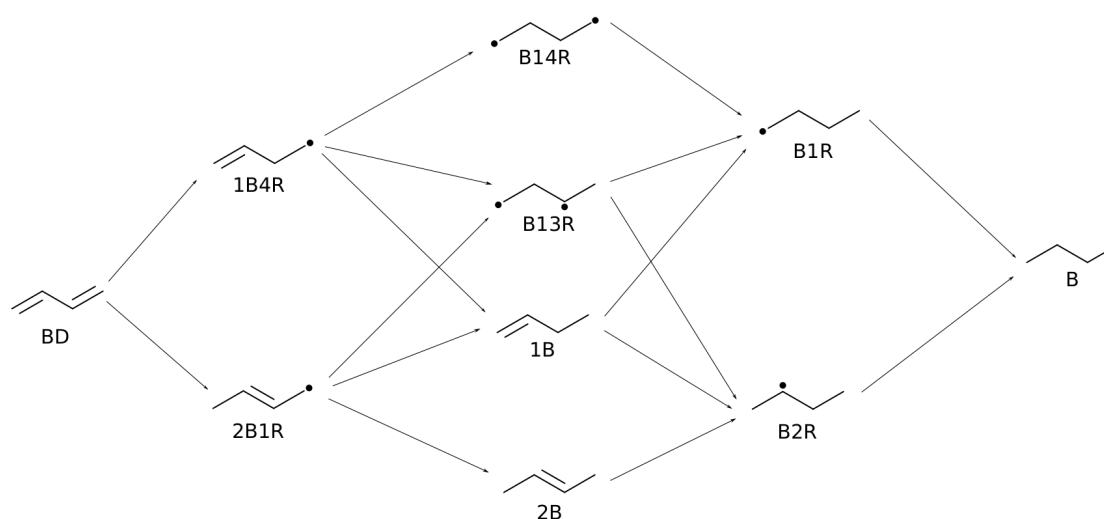


Figure 1.3: Horiuti–Polanyi reaction scheme of the hydrogenation of butadiene where BD stands for butadiene, 1B and 2B for but-1-ene and 2-butene, respectively, B for butane and R for radical [58].

in Fig. 1.3.

Noble metal Pd-based catalysts are typical ones for the alkynes and dienes hydrogenations, *i.e.* expensive, non-environmental friendly, poorly selective catalysts. The reaction selectivities to partially hydrogenated products can be improved by the addition of an inactive coinage metal such as Ag, Au or Cu [1, 2, 3, 4]. First-principles calculations suggested Ni–Zn alloys as low-cost substitutes to reference Pd–Ag [31] for acetylene partial hydrogenation. These substitutional alloys may nevertheless suffer from adsorption-induced surface segregation under reaction conditions, which usually leads to a decrease in selectivity [5, 2, 6].

Searching for stable, selective, low-cost and environmentally benign catalysts for acetylene and butadiene semi-hydrogenations led to the recent identification of transition-metal

(TM) Al-based quasicrystalline approximants such as $\text{Al}_{13}\text{Fe}_4$, $\text{Al}_{13}\text{Co}_4$, and $\text{Al}_{13}\text{Ru}_4$ [22, 21, 7, 26, 32, 19, 8].

1.2 Materials

As stated previously, a new class of materials has recently been studied as potential catalysts : the Al-based complex intermetallic compounds. They are crystalline compounds made of metals, alloyed with metalloids. They exhibit large unit cells, containing up to thousands of atoms [59]. Some of them appear to have local symmetries similar to the one of quasicrystals such as 10-fold symmetry.

1.2.1 Quasicrystals

Quasicrystals are ordered crystals without any translational symmetry. They were first discovered by Dan Schechtman in 1982. He was awarded the Nobel Prize in Chemistry in 2011 for this discovery. Since then many quasicrystalline phases have been found (*e.g.* the decagonal phase *d*-AlNiCo [60] or the icosahedral *i*-AuAlYb [61]).

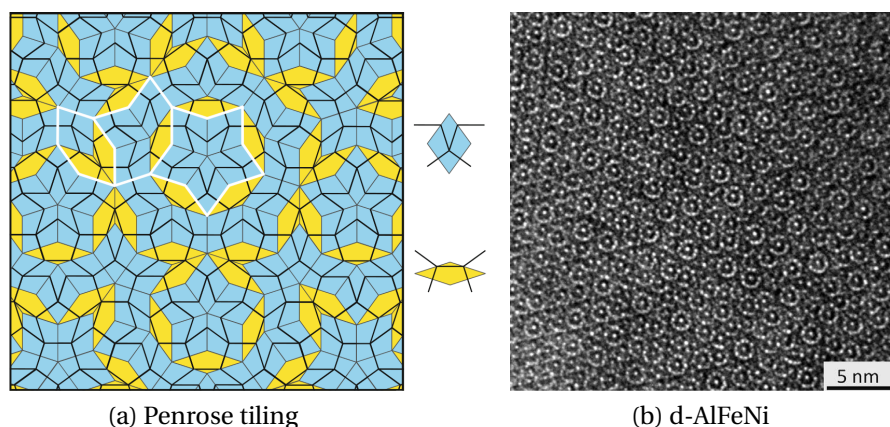


Figure 1.4: (a) Penrose tiling, involved in quasicrystalline model structures, made of rhomb prototiles (blue and yellow) [62]; (b) HRTEM image of *d*-AlFeNi [63].

A 2D quasiperiodic structure can be modelled for example by the famous Penrose tiling (Fig. 1.4a). This tiling is made of two rhomb prototiles and 5-fold symmetries can be locally observed. This kind of tiling can be observed in real crystals such as the decagonal phase *d*-AlFeNi [63]. High-resolution microscopy can reveal this particular structure (Fig 1.4b).

Although these compounds show no periodicity in their structures, diffraction measurements clearly provide information regarding their overall symmetries (5-fold, 10-fold,

Fig. 1.5a–b) – because of their long-range order structure – that used to be commonly accepted as forbidden symmetries in conventional crystallography. This kind of material – although promising in the field of catalysis [64, 65] – is however out of the scope of the present work. The interest will be focused on simpler structures such as complex intermetallics compounds. This perfect symmetry (5-fold or 10-fold) is not observed in the systems that are studied in this work (Al-based complex intermetallics). Only resembling symmetries are observed (defined as pseudo- n -fold), hence the term 'approximant' of quasicrystals.

1.2.2 Intermetallic compounds

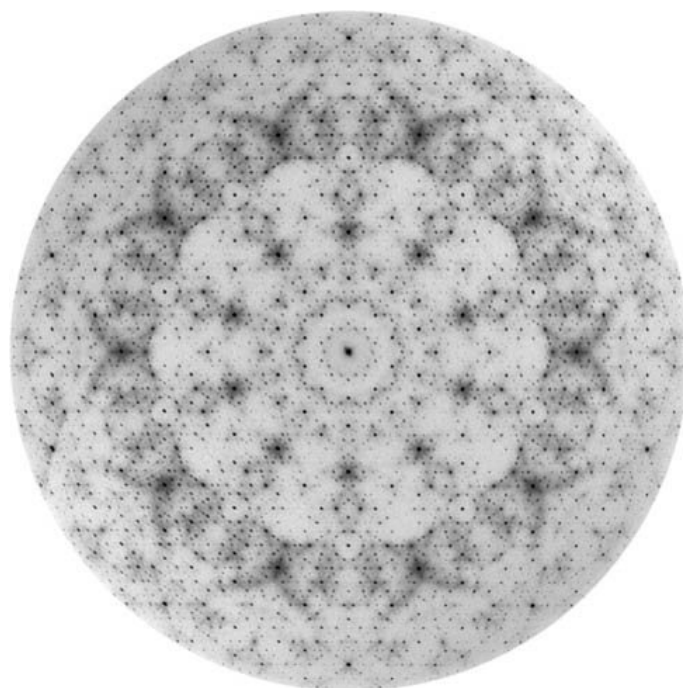
Before describing what are complex intermetallics, one shall define more precisely what is an intermetallic compound. For example, when two metals are mixed, the product is typically called a bimetallic alloy. Depending on the nature of the interaction between the two elements and the composition of the mix, they can be classified into two categories : solid-solution alloys – either substitutional (if the two elements are of similar size) or interstitial (if one of the elements is small enough to fit in the lattice of the bigger one) – and intermetallic compounds (Fig. 1.6 [35]).

Intermetallic compounds are thus well-ordered structures with precise compositions. They can present particular physical and chemical properties (electronic [67], mechanical [68], thermal [69] and/or even catalytic properties [22]).

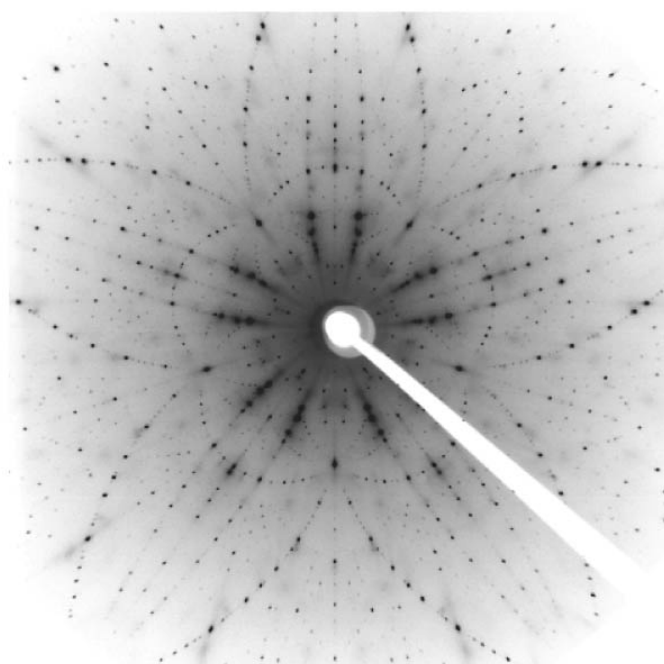
1.2.3 Complex intermetallic compounds

As explained previously, complex intermetallic compounds (CIC) are large unit cell intermetallic compounds that can have from 20 atoms (Al_5Co_2 and Al_9Co_2 , arbitrary low limit) up to few thousand of atoms (*e.g.* W-AlNiCo [60], or AlCuTa [70, 71, 72], with more than 20000 atoms) in their unit cell. The extreme scenario is a quasicrystal which could be defined as a crystal having an infinite number of atoms in its unit cell.

Among the complex intermetallic compounds, some of them are very close to their quasicrystal counterparts and are therefore called quasicrystalline 'approximants'. They are different from the 'true' quasicrystal approximants, which arise from the projection of a hyper crystal along rational directions (while QC arise from irrational directions of the same hyper crystal). They are periodic crystals that derive from quasicrystalline phases : similar local arrangements, high-symmetry clustered structures (*e.g.* 10-fold), similar physical and chemical properties.



(a) d-AlCoNi



(b) i-AlPdPn

Figure 1.5: (a) Diffraction pattern of *d*-AlCoNi quasicrystal (10-fold symmetry) and (b) Laue diffraction pattern of *i*-AlPdPn (5-fold symmetry) [66].

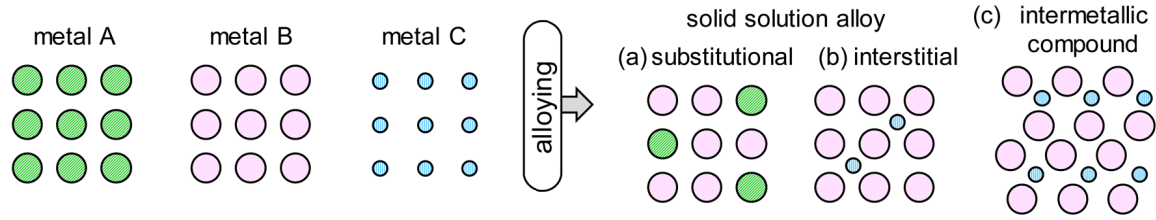


Figure 1.6: Comparison of different bimetallic alloys : (a) substitutional solid-solution alloy, (b) interstitial solid-solution alloy and (c) intermetallic compound [35].

These compounds appear to exist thanks to an electronic stabilization due to small discrepancies between electronegativities and atomic radii of the different alloying elements. This is called the Hume-Rothery mechanism, linked to the particular interaction between the Fermi surface (which is depending on the ratio of the number of valence electrons and the number of atoms, $\frac{e}{a}$) and the first Brillouin zone [73, 74, 75, 76]. This mechanism seems valid for Al-TM systems [77] such as the ones that will be later focused on in this work. Other electronic effects such as sp-d hybridization could also explain/enhance this stabilization.

Another stabilization phenomenon has to be mentioned : the $18 - n$ rule [78, 79]. For example, in a Al-TM system, each TM atom in the intermetallic phase will need $18 - n$ electrons to achieve a closed-shell 18-electron configuration, where n is the number of electron pairs it shares with neighboring TM atoms. For instance, $B2\text{-AlCo}$ and Al_5Co_2 – both are intermetallics in the Al-Co system – appear to follow this $18 - n$ rule [78].

1.3 Al-based complex intermetallics

Over the course of this work, four Al-based complex intermetallics are focused on : Al_5Co_2 , Al_5Fe_2 , $\text{Al}_{13}\text{Co}_4$, and $\text{Al}_{13}\text{Fe}_4$. All the structural models that are presented in this work are plotted using the VESTA software [80].

1.3.1 Al_5Co_2

The Al_5Co_2 bulk structure belongs to the $P6_3/mmc$ (No. 194, Pearson symbol $hP28$) space group [10, 11, 12, 81]. The hexagonal cell contains 28 atoms (20 Al and 8 Co) and the lattice parameters are detailed in Tab. 1.2. The bulk structure can be described by a stacking of two different clusters [81] : a 2D cluster made of 3 Al and 3 Co atoms (bounded atoms in Fig. 1.7) and a 3D cluster made of 6 Al and 1 Co atoms (yellow cluster in Fig. 1.7).

A second description based on a stacking of two types of atomic ($2\bar{1}0$) planes that alternate (Fig. 1.8) is also possible. More precisely, it involves a flat (F-type) and a puckered

Table 1.2: Al_5Co_2 crystallographic parameters.

Phase	Space group	a (Å)	b (Å)	c (Å)	Ref.
Al_5Co_2	$P6_3/mmc$	7.67(2)	7.67(2)	7.60(5)	[12]

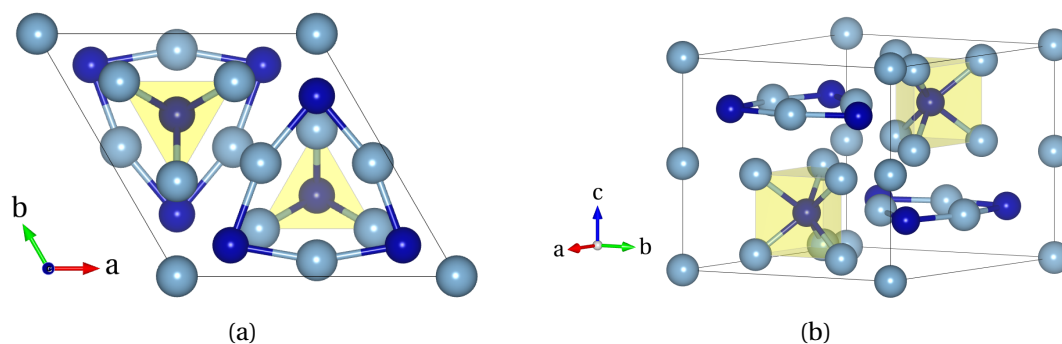


Figure 1.7: Bulk structure of Al_5Co_2 (a) along the $[001]$ direction and (b) perspective projection. Al and Co atoms are drawn in light blue and dark blue, respectively. 2D (bounded atoms) and 3D (yellow) clusters are drawn.

(P-type) plane containing 12 (4 Co and 8 Al) and 16 (4 Co and 12 Al) atoms in the surface unit cell, respectively.

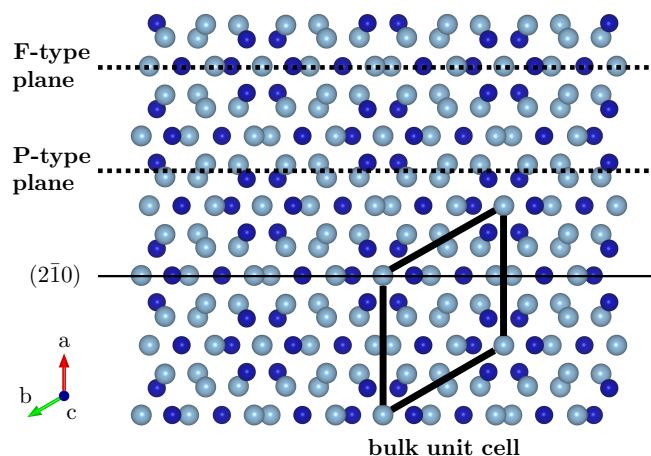


Figure 1.8: Bulk structure of Al_5Co_2 . Flat (F) and puckered (P) planes are indicated using dashed lines.

Different low-index surface orientations have been previously investigated – both experimentally (LEED, STM) and theoretically (DFT) – such as the (001) [13], (100) and $(2\bar{1}0)$ surfaces [14]. The latter might present Co protruding atoms at the surface and could be thus considered as a good candidate for catalytic reactions. The $(2\bar{1}0)$ surface structure results from a bulk truncation and selection of the P-type (puckered) planes termination,

with every four bipentagonal motifs missing, thus forming a (2×1) reconstruction. It means that the surface structure consists of nano-structured bands of 1.2 nm wide separated by gaps of 0.7 nm wide. Several surface models were built, based on the knowledge gained by the experimental observations. Two of them (Fig. 1.9) – named P_B and P_{B-4Co} – fit equally well (for two different ranges of the allowed chemical potential) both STM and LEED measurements, and present low surface energies. However, the detailed surface composition, especially the presence/absence of these topmost surface Co atoms, could not be deduced from surface energy calculations, even combined with the comparison of simulated and experimental STM images.

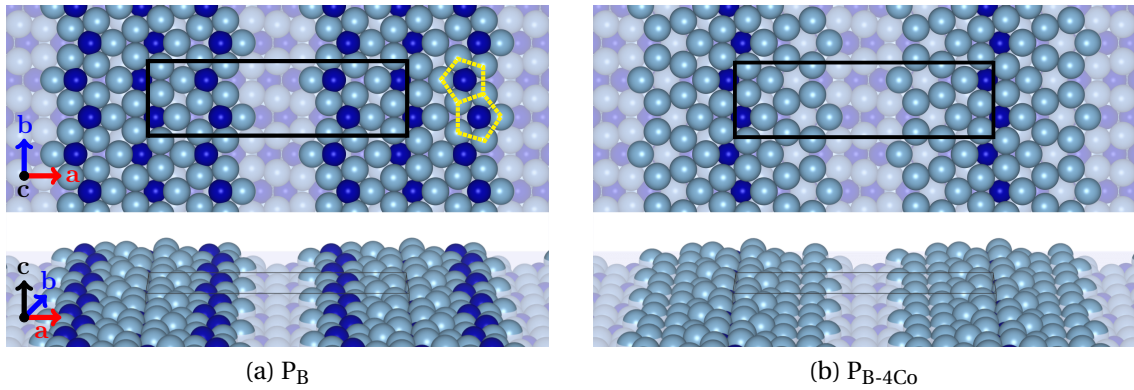


Figure 1.9: Top and perspective views of (a) P_B surface model and (b) P_{B-4Co} surface model of $Al_5Co_2(2\bar{1}0)$. Al and Co atoms are drawn in light blue and dark blue, respectively. The unit cells and bipentagonal Al arrangements are drawn in black lines and yellow dashed lines, respectively.

1.3.2 Al_5Fe_2

The Al_5Fe_2 bulk structure belongs to the $Cmcm$ (No. 63) space group [82] and is constituted of 20 Al atoms and 4 Fe atoms. The lattice parameters are detailed in Tab. 1.3. The atomic structure is described by a rigid framework of pentagonal antiprisms (polyhedron composed of two parallel copies of pentagons) extending along the $[001]$ direction and connected by side edges as shown in Fig. 1.10a. These channels are formed by fully occupied Fe (Wyckoff site 4c) and Al1 (8g) sites. Additional partially occupied Al sites form a disordered chain confined within the channels (Fig. 1.10b). It was proposed [82] to describe the Al chains by Al2 (4a) and Al3 (8f) sites with site occupations of 0.36 and 0.23, respectively. Unexpected (inconsistent with the $Cmcm$ symmetry) split satellite reflections were observed in electron diffraction patterns and were attributed to the partially disordered Al chains

in the channels along the [001] direction [83], which would correspond to a doubling of the lattice parameter c .

Table 1.3: o -Al₅Fe₂ crystallographic parameters.

Phase	Space group	a (Å)	b (Å)	c (Å)	Ref.
Al ₅ Fe ₂	$Cmcm$	7.65(6)	6.41(5)	4.21(9)	[82]

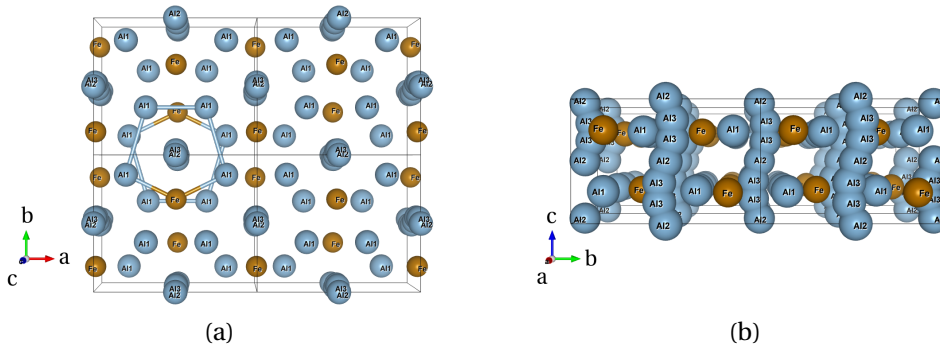


Figure 1.10: Bulk structure of Al₅Fe₂ (perspective views) : (a) along [001] (the pentagonal structures made of Al1 and Fe are highlighted), (b) along [100]. The unit cell, Al and Fe atoms are drawn in black, light blue and orange, respectively.

No surface studies have yet been conducted. Different surface orientations (dense atomic layers) could be investigated such as the (100), the (001) or even the (02 $\bar{1}$) orientations.

1.3.3 Al₁₃Co₄

Many varieties of Al₁₃Co₄ can be found in the Al–Co phase diagram : o -Al₁₃Co₄, m -Al₁₃Co₄, o' -Al₁₃Co₄, Z -Al₁₃Co₄, Y_1 -Al₁₃Co₄ and Y_2 -Al₁₃Co₄ [84]. The two latter structures are metastable. Like Al₅Co₂, all of them can be described by a stacking of flat (F) and puckered (P) atomic planes as well as 3D clusters. The first flat atomic planes of the different Al₁₃Co₄ phases are presented in Fig. 1.11.

In this work, only o -Al₁₃Co₄ and m -Al₁₃Co₄ will be focused on. o -Al₁₃Co₄ crystallizes in the $Pmn2_1$ (No. 31, Pearson symbol $oP102$) space group while m -Al₁₃Co₄ crystallizes in the $C2/m$ (No. 12, Pearson symbol $mC102$) space group. The crystallographic information of o -Al₁₃Co₄ and m -Al₁₃Co₄ are presented in Table 1.4. Both structures present a pseudo 10-fold symmetry axes (along the [100] _{o} and [010] _{m}) as one can see in Fig. 1.12a and 1.13a (pentagonal and bipentagonal arrangements).

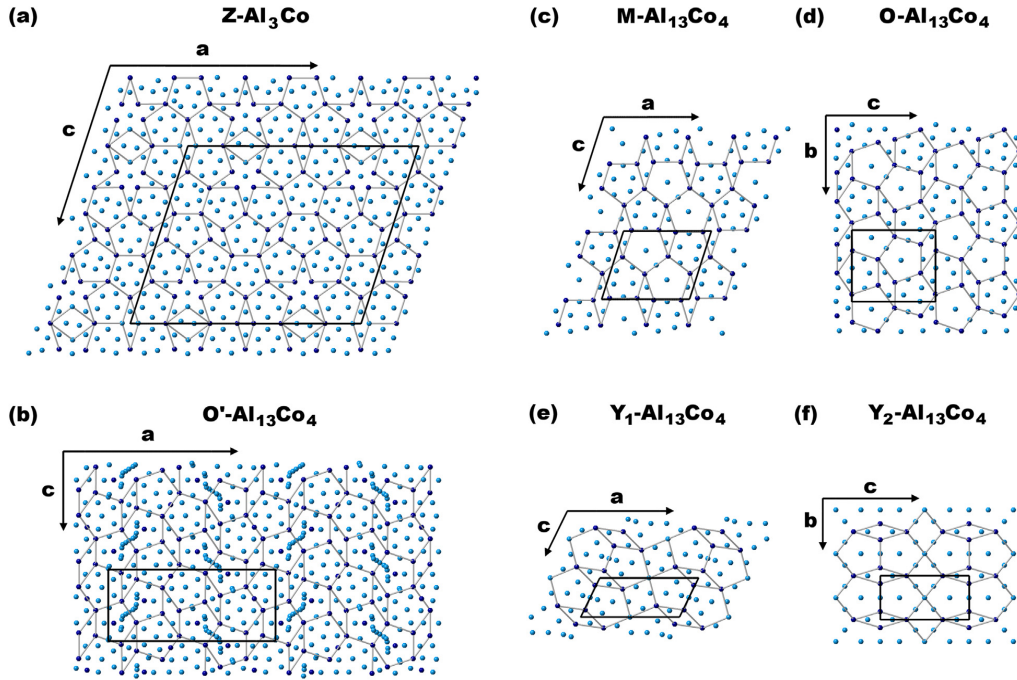


Figure 1.11: Flat atomic planes in $\text{Al}_{13}\text{Co}_4$: (a) $Z\text{-Al}_{13}\text{Co}_4$, (b) $o'\text{-Al}_{13}\text{Co}_4$, (c) $m\text{-Al}_{13}\text{Co}_4$, (d) $o\text{-Al}_{13}\text{Co}_4$, (e) $Y_1\text{-Al}_{13}\text{Co}_4$ and (f) $Y_2\text{-Al}_{13}\text{Co}_4$ [84]. Al and Co atoms are drawn in light blue and dark blue, respectively. Pentagonal and quasicrystal-like atomic arrangements are clearly visible.

Table 1.4: o - and $m\text{-Al}_{13}\text{Co}_4$ crystallographic parameters.

Phase	Space group	a (Å)	b (Å)	c (Å)	β (°)	Ref.
$o\text{-Al}_{13}\text{Co}_4$	$Pmn2_1$	8.158	12.342	14.452	–	[20]
$m\text{-Al}_{13}\text{Co}_4$	$C2/m$	15.173	8.109	12.349	107.84	[16]

As said previously, the structure can be seen as a stacking of flat (F) and puckered (P) layers (Figs. 1.12b-c and 1.13b-c) as well as a stacking of QC-like clusters (*e.g.* Henley-type [85], as detailed in Fig. 1.12d and 1.13d) where the F-type planes intercept the cluster in the middle. In $o\text{-Al}_{13}\text{Co}_4$ the clusters are not crystallographically equivalent (two clusters, red and blue, are needed to describe the structure). The Al atoms at their centers do not have the same Wyckoff position. In $m\text{-Al}_{13}\text{Co}_4$ all the clusters (in blue) are crystallographically equivalent. The Al atoms at their centers have the same Wyckoff position. The linear structure Co–Al–Co that is present in the cluster is calculated to be quite strong and of a covalent-like bond [34]. Other cluster types exist to describe this kind of structure [86]. Nevertheless, the Henley-type is chosen here to describe the $\text{Al}_{13}\text{TM}_4$ structures.

The local structures are similar between the orthorhombic and the monoclinic phases. The only difference lies in the relative cluster arrangements. A bigger structure made of 6

Henley-type clusters – thus forming an irregular hexagon – may also be a fair description of the bulk structure. In the monoclinic phase, all the hexagonal clusters point towards the same direction whereas they change orientation every other cluster in the orthorhombic phase (Figs. 1.12a and 1.13a). One can see lone Al atoms in the middle of these hexagonal clusters : these Al atoms are not part of any clusters but connect them together and are thus referred as "glue" atoms.

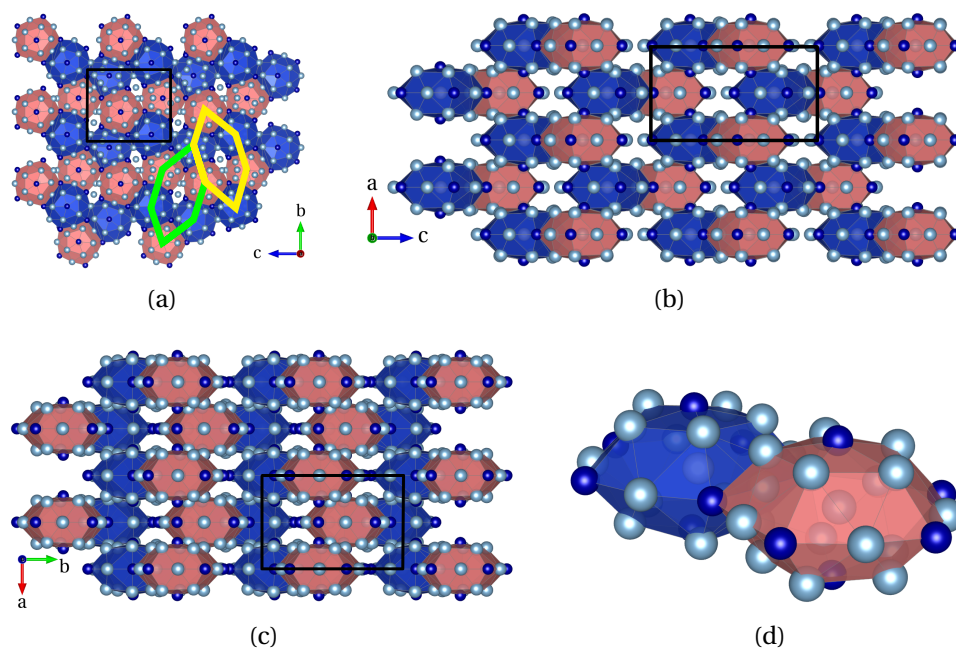


Figure 1.12: Bulk structure of o -Al₁₃Co₄: (a) along [100] (the hexagonal structures are drawn in green and yellow), (b) along [010], (c) [001] and (d) two Al–Co Henley-type clusters. The unit cell, Al and Co atoms are drawn in black, light blue and dark blue, respectively.

So far, the structure of one surface orientation – o -Al₁₃Co₄(100) (pseudo 10-fold crystallographic direction) – has been both theoretically and experimentally investigated. Three different studies had been conducted since 2011 and proposed three possible surface models.

In 2009, Addou et al. [87] showed, thanks to STM measurements and DFT calculations, that there is a coexistence of two terminations at the surface : a rather flat one (a F-type layer) and a corrugated one (an incomplete P-type layer) consisting of 12 atoms (10 Al and 2 Co atoms) – named P₁₂, Fig. 1.14c – per surface unit cell (only the bottom of two Henley-type clusters at the surface). This latter surface model could be seen as Co atoms embedded in Al bipentagonal motifs. The surface terminations and their relative abundance appeared to be quite affected by surface preparation conditions (annealing temperature, sputtering).

In 2011, Shin et al. [88] conducted further investigations (LEED-I(V) and STM measure-

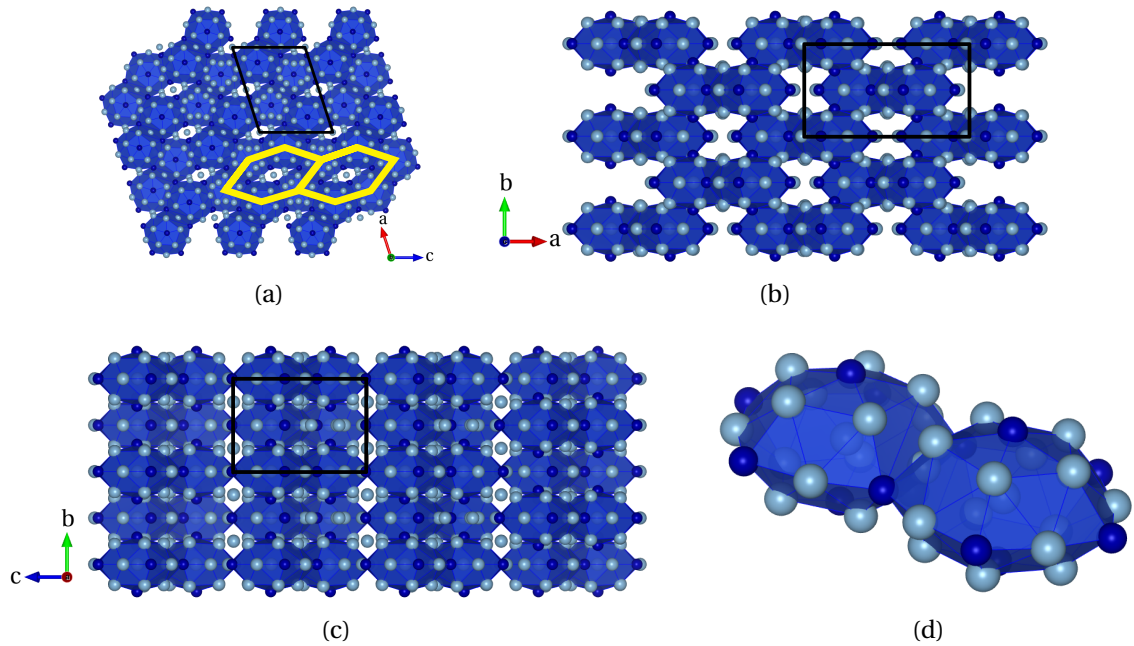


Figure 1.13: Bulk structure of $m\text{-Al}_{13}\text{Co}_4$: (a) along [010] (the hexagonal structures are drawn in yellow), (b) along [001], (c) [100] and (d) two Al–Co Henley-type clusters. The unit cell, Al and Co atoms are drawn in black, light blue and dark blue, respectively.

ments coupled with DFT calculations) that suggested two other surface models that both fits LEED-I(V), STM images simulations and present low surface energies : a complete P layer with 22 Al and only 2 low Co atoms – named P_{24} , Fig. 1.14a – and a complete P layer (22 Al atoms) with no Co atom – named P_{22} , Fig. 1.14b.

In the meantime, Krajci et al. [89] did a simulated cleavage experiment – using DFT calculations – and determined theoretically that the clusters are preserved at the surface because of strong Co–Al–Co bonds inside. Hence, according to their study they suggested another surface model (P_{14} , Fig. 1.14d), an incomplete P layer consisting of Al bipentagonal motifs with Co protruding atoms (top part of the clusters as seen in Fig. 1.12d).

Finally in 2016, Gaudry et al. [90] conducted surface X-ray diffraction (SXRD) experiments coupled with *ab initio* calculations to determine the actual surface structure under UHV conditions. The X-ray diffraction and DFT analyses suggested one particular surface model: a complete P layer without Co protruding atoms (P_{24}). This model presents a rather low energy ($1.09 \text{ J}\cdot\text{m}^{-2}$).

The other low-index surfaces – such as (010) and (001) – have not yet been structurally investigated. We will see later in this chapter that one of the latter might be a good candidate from a catalytic point of view.

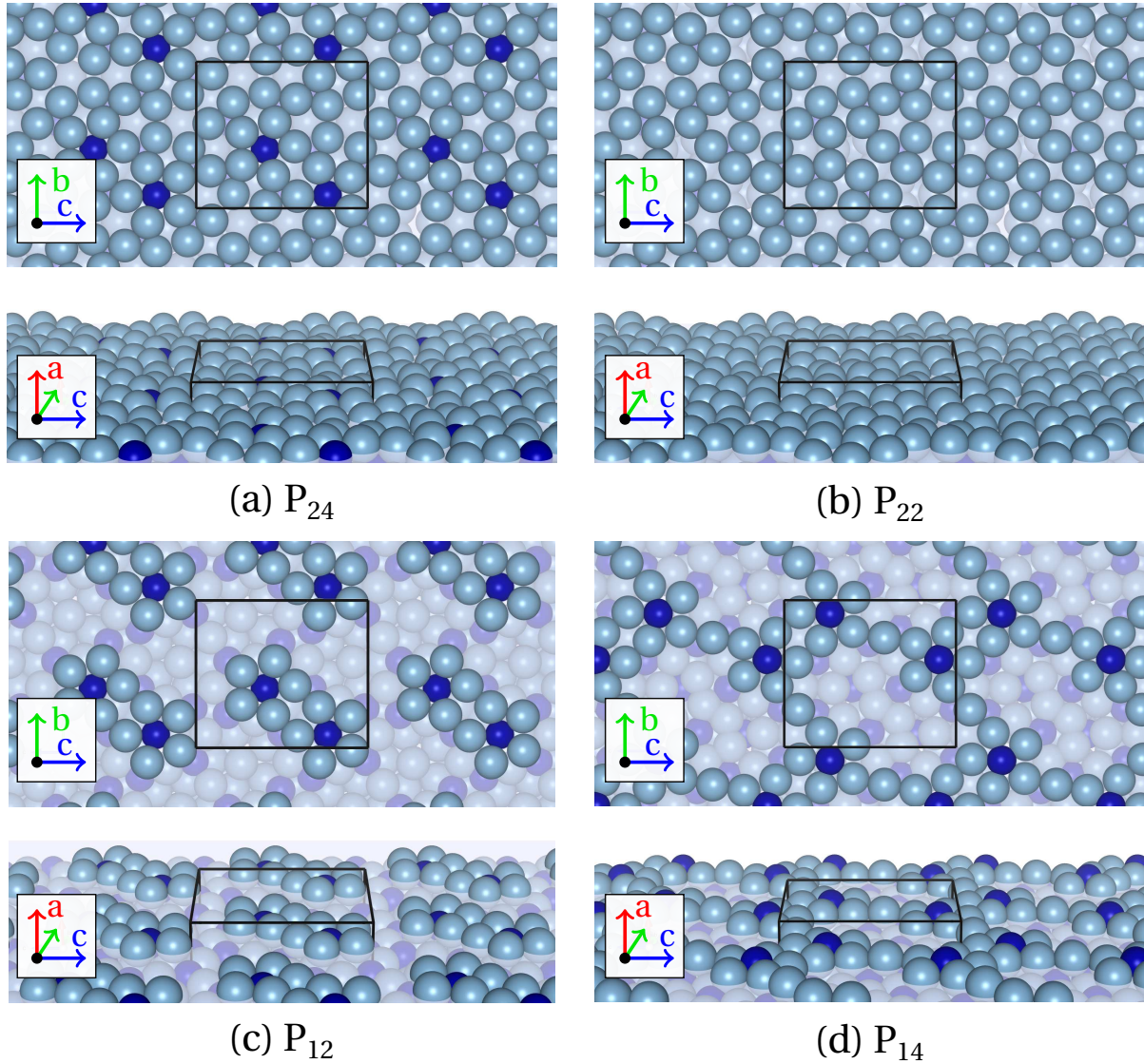


Figure 1.14: Surface models of $o\text{-Al}_{13}\text{Co}_4(100)$ (top and perspective views) : (a) P_{24} model (22 Al atoms and 2 Co atoms), (b) P_{22} model (22 Al atoms), (c) P_{12} model (10 Al atoms and 2 Co atoms) and (d) P_{14} model (12 Al atoms and 2 Co atoms). The unit cell, Al and Co atoms are drawn in black, light blue and dark blue, respectively.

1.3.4 $\text{Al}_{13}\text{Fe}_4$

Focusing on the Al–Fe system, a few intermetallics can be found. Among them one can find $m\text{-Al}_{13}\text{Fe}_4$ (monoclinic phase). It crystallizes in the $C2/m$ (No. 12, Pearson symbol $mC102$) space group. Table 1.5 presents the crystallographic information of $m\text{-Al}_{13}\text{Fe}_4$.

Table 1.5: $m\text{-Al}_{13}\text{Fe}_4$ crystallographic parameters.

Phase	Space group	a (Å)	b (Å)	c (Å)	β (°)	Ref.
$m\text{-Al}_{13}\text{Fe}_4$	$C2/m$	15.492	8.078	12.471	107.69	[91]

The bulk structure of $m\text{-Al}_{13}\text{Fe}_4$ is very similar to the one of $m\text{-Al}_{13}\text{Co}_4$. It can be described the same way as either a stacking of P-type and F-type layers – along the $[010]$ direction – or a stacking of pentagonal bipyramidal clusters (Fig. 1.15a–d) – also along the $[010]$ direction – together connected by Al glue atoms. Similarly to $\text{Al}_{13}\text{Co}_4$, a strong covalent-like Fe–Al–Fe arrangement is present in the clusters [34].

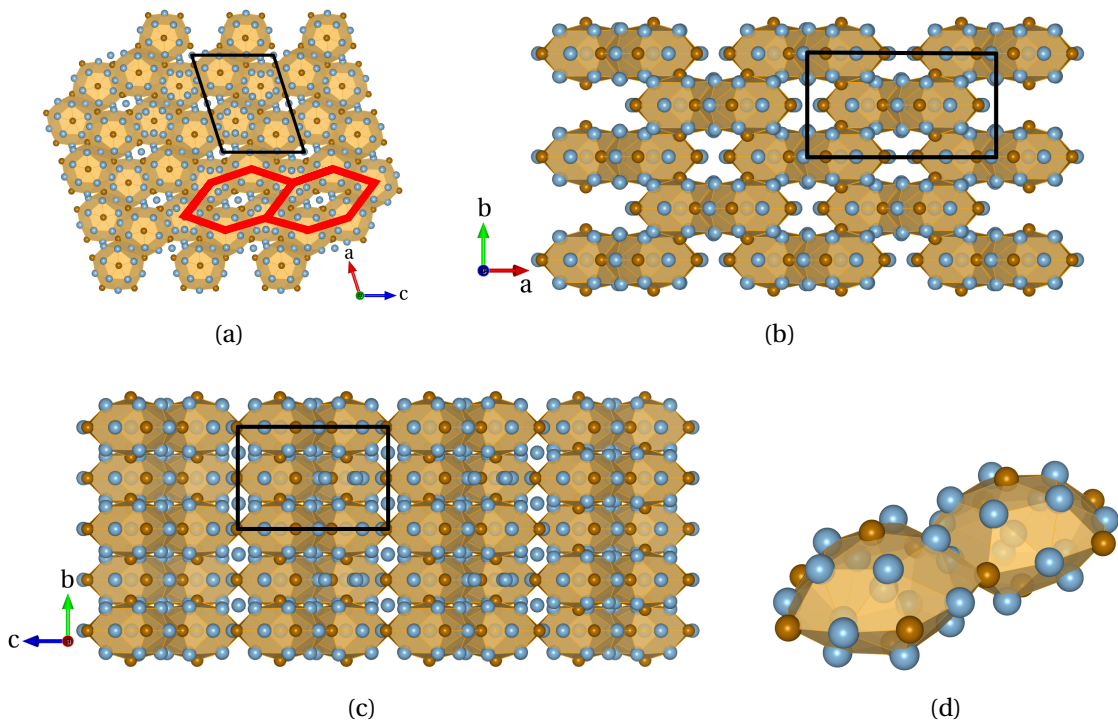


Figure 1.15: Bulk structure of $m\text{-Al}_{13}\text{Fe}_4$: (a) along $[010]$ (the hexagonal clusters are drawn in red), (b) along $[001]$, (c) $[100]$ and (d) two Al–Fe Henley-type clusters. Al and Fe atoms are drawn in light blue and dark orange, respectively.

Up to now, only one surface orientation has been studied : $m\text{-Al}_{13}\text{Fe}_4(010)$. Both STM [26] (Fig. 1.16(a–b)) and LEED-I(V) [92] analyses suggest a P-type surface termination with

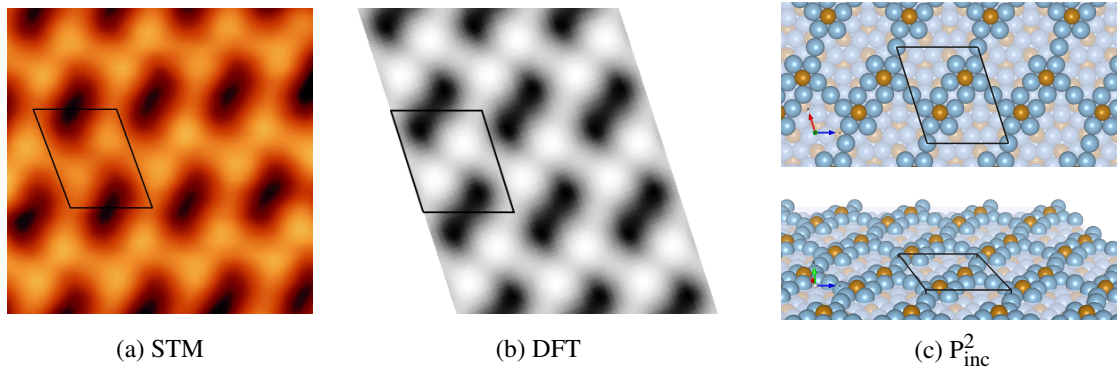


Figure 1.16: Surface model of $m\text{-Al}_{13}\text{Fe}_4(010)$: (a) STM image ($5 \times 5 \text{ nm}^2$, $V_b = -1\text{V}$) of $m\text{-Al}_{13}\text{Fe}_4(010)$ prepared at 600°C [26], (b) STM image simulation ($V_b = -1\text{V}$) [26] and (c) surface structure model of $m\text{-Al}_{13}\text{Fe}_4(010)$. The unit cell, Al and Fe atoms are drawn in black, light blue and dark orange, respectively.

only one bipentagonal Al motifs with protruding Fe atoms embedded in each Al pentagons. The presence of Al glue atoms in between the bipentagonal motifs seems to depend on the annealing temperature : at 600°C both Al glue atoms could be observed while at 720°C both of them might be gone. The surface thus preserves the cluster structure as well as the Fe–Al–Fe bonding. We will see later on that this surface structure could explain some particular catalytic properties of $\text{Al}_{13}\text{Fe}_4$.

1.3.5 Defects in complex intermetallics : twins and metadislocations

Having such complex materials and peculiar structures gives naturally rise to defects. Defects in alloys and intermetallics are common and can be of different type. Point defects (0D) occur at a single lattice point : vacancy defects (vacant sites), interstitial defects (extra occupied sites) or even antisite defects (exchanged sites). In the case of $\text{Al}_{13}\text{Co}_4$ it was shown that vacancy hopping stabilizes the crystal structure [93]. Line defects (1D) are mainly occurring through dislocations (around which the atoms of the crystal lattice are misaligned). Planar defects (2D) are usually grain boundaries (abrupt change of the direction of the lattice) and twin boundaries (mirror plane in the crystal structure). Other defects can occur in quasicrystalline structure such as phason defects. This can be seen as a local rearrangement of the quasicrystalline tile structure. This kind of defect was shown to stabilize quasicrystals [94]. The two main defects that are observed in complex intermetallic compounds and especially in $\text{Al}_{13}\text{TM}_4$ (where TM is a transition metal) are twins and a particular type of dislocations called metadislocations.

When two crystals are twins they share some crystal lattice point from a symmetrical

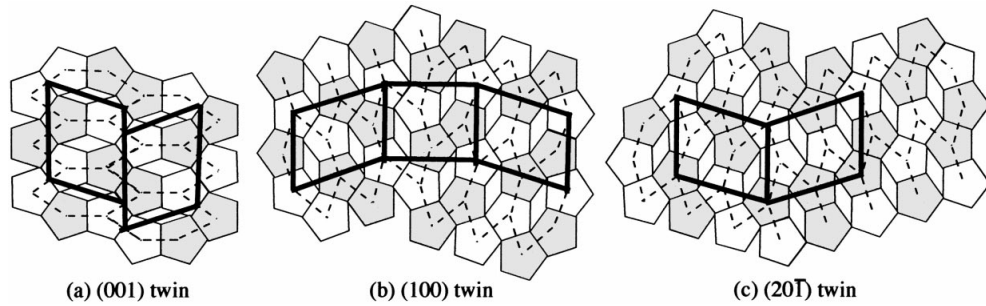


Figure 1.17: Twin models in $\text{Al}_{13}\text{TM}_4$: (a) (001) twin (b) (100) twin and (c) $(20\bar{1})$ twin [95].

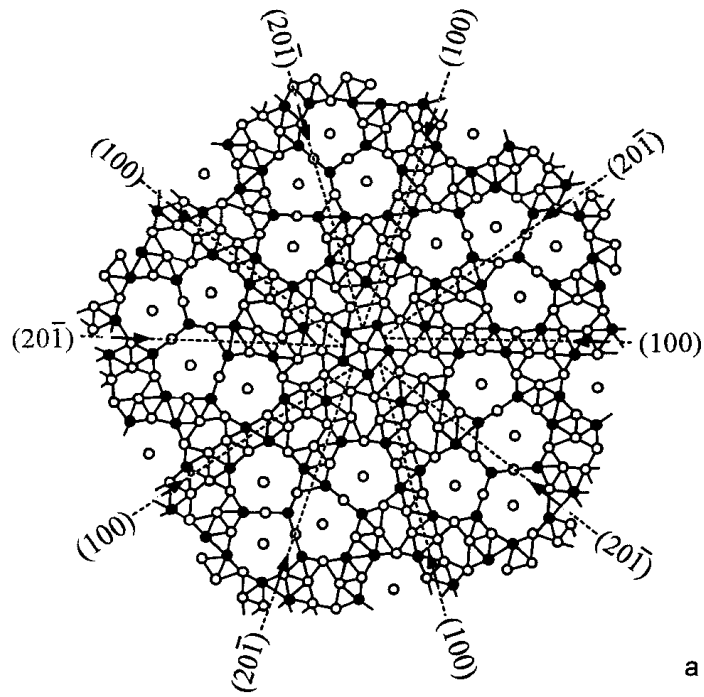
operation. The shared surface is called the twin plane. In the $\text{Al}_{13}\text{TM}_4$ case, three main twin planes are reported [95]: (001), (100) and $(20\bar{1})$ planes (Fig. 1.17). In the case of the (001) and (100) planes, it is not rigorously correct to call them twin planes, since (a) there are a mirror plane and a translation operation, and (b) a change in the crystal structure (orthorhombic cell in between monoclinic ones). This is due to the relative orientation of the clusters at the interface between the monoclinic cells. Nevertheless, these defects are referred to twin defects in the following discussion.

Due to the pseudo 10-fold axis and the local 5-fold symmetry of the clusters, twinning can occur quite easily in such materials. As shown in Fig. 1.18, both (100) and $(20\bar{1})$ twins are based on glide-reflection mechanisms. This structure model has actually been seen in crystals at a macroscale level and are formed during crystal growth. They are not introduced by deformation. The formation energy of such structure is therefore low.

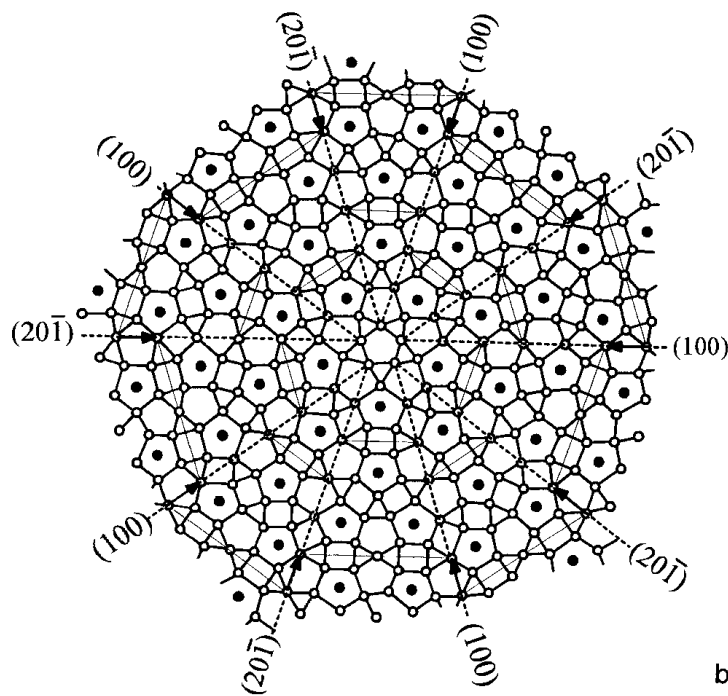
Experimentally, it is possible to observe those features thanks to high resolution TEM [95]. In $\text{Al}_{13}\text{Fe}_4$, (001) twins are observed in the bulk material. Fig. 1.19(a) shows that twinning is quite frequent in $\text{Al}_{13}\text{Fe}_4$. It suggests that the interfacial energy is low and the feature favorable. In $\text{Al}_{13}\text{Co}_4$, (100) and $(20\bar{1})$ twins are observed (due to the coexistence of orthorhombic and monoclinic phases). From a geometrical point of view it is possible to explain these twinning effects with the tiling rules requirements for pentagonal motifs arrangements (Fig. 1.18).

A second type of defect can also be observed in complex intermetallic compounds and are related to dislocations. They are called metadislocations and could appear due to plastic deformations [97, 98, 99]: they are line defects with a Burger vector corresponding to a τ^{-n} -fraction of a lattice constant, with τ the golden ratio defined by $\tau = \frac{1+\sqrt{5}}{2}$ and $n \in \mathbb{N}^*$. The golden ratio is known to be a key parameter in quasicrystalline structure and appears to be also present in quasicrystalline approximants. In short, metadislocations are highly complex defects mediating plasticity in complex intermetallic compounds.

Metadislocations are always associated with a region of transformed phase, by which

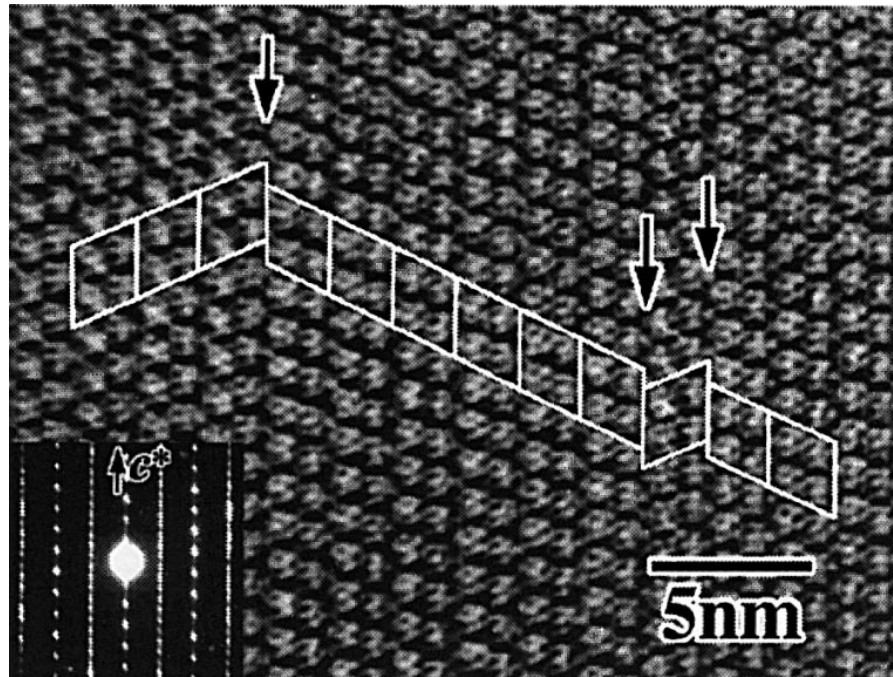


(a) F-type plane

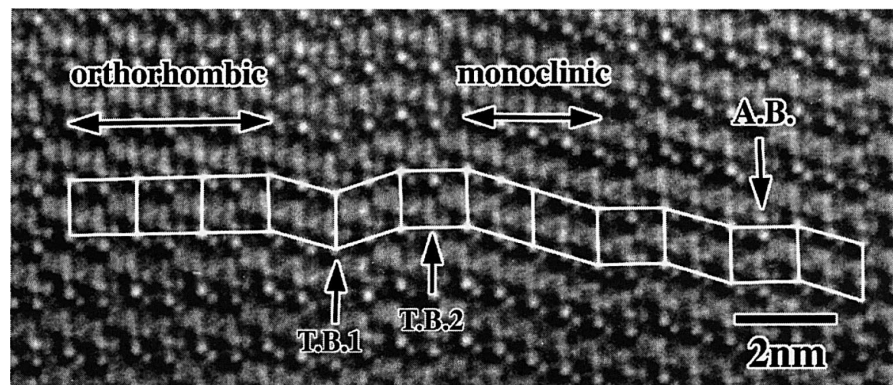


(b) P-type plane

Figure 1.18: Structural models of (100) and $(20\bar{1})$ twins in $m\text{-Al}_{13}\text{Fe}_4$ (F-type and P-type planes) [96]. Al and Fe atoms are drawn in white and black, respectively.



(a) $\text{Al}_{13}\text{Fe}_4$



(b) $\text{Al}_{13}\text{Co}_4$

Figure 1.19: HRTEM observations of twins in (a) $\text{Al}_{13}\text{Fe}_4$ ((001) twin) and (b) $\text{Al}_{13}\text{Co}_4$ ((100) and $(20\bar{1})$ twins) [95]. TB and AB stand for twin boundary and anti-phase boundary, respectively.

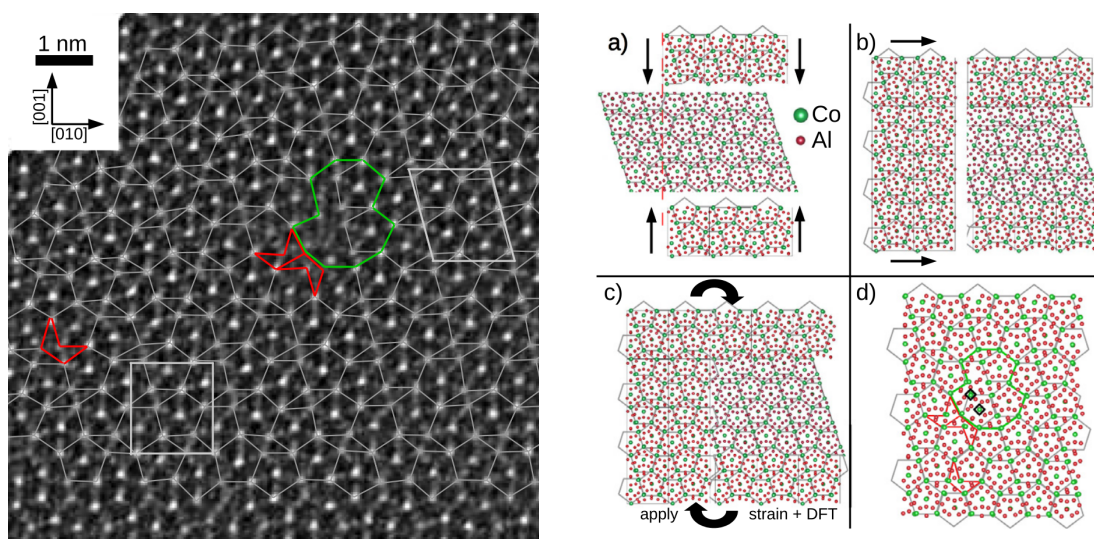


Figure 1.20: Metadislocation in $\text{Al}_{13}\text{Co}_4$: HRTEM image and structural model (building of the model a–d) [100].

the irrational Burgers vector is accommodated in the crystal lattice [100]. The transformed region is therefore affected by other defects, called phason defects (same kind of defects that are encountered in quasicrystals). Unlike metadislocations that are linear defects, phasons could also form planar defects called phason planes. The phason structures affect the dislocation motions and are thus of importance to understand mechanical properties of such complex phases.

Metadislocations and phasons defects are observed in $\text{Al}_{13}\text{Co}_4$ [100]. Fig. 1.20 shows a STEM micrograph of a metadislocation in $\sigma\text{-Al}_{13}\text{Co}_4$. The metadislocation core is drawn in green while the "crown-shaped" phasons are marked in red. Both orthorhombic and monoclinic phases are observed around this dislocation. A slab of a model metadislocation was built by Heidelmann et al. [100] using monoclinic cells (Fig. 1.20a) surrounded by orthorhombic cells (Fig. 1.20b–c). The authors did a geometric optimization of this first-order model using DFT calculations and obtain a good agreement with the experimental measurements (Fig. 1.20d). All of these defects (vacancies, twins, metadislocations, phasons) occur because they stabilize the complex intermetallic compounds.

1.3.6 The need for single-crystalline materials

In today's industrial processes, the catalysts are rather complex systems (powders, nanoparticles, faceted structures, *etc*) coupled with promoters. The systems that are investigated in this work – Al-based complex intermetallics – are also quite complicated. In order to rationalize the investigation, one has to simplify the approach using ideal surface models

and single-crystal materials with unique surface orientation. This is the best strategy to investigate the catalytic properties of such systems under controlled reaction conditions. Nevertheless, one has to keep in mind that the so-called "material gap" (real catalyst are not single crystals) and "pressure gap" (ultra-high vacuum studies are too ideal compared to the real conditions that sees the surface) are major issues in the field of catalysis.

Two main processes exist in order to make single crystalline materials : the Czochralski method [101] and the Bridgman technique [102]. In the latter, a polycrystalline material is heated above its melting point and slowly cooled down from one end of the container (at the bottom of which a single crystal seed is placed). This technique allows for the formation of a single crystalline material with the same orientation as the aforementioned seed. In the Czochralski method, a seed is placed at the tip of a rod and dipped into a melt of the desired composition that is close to thermodynamic equilibrium with the growing solid. The rod is then slowly pulled out (few millimeters per hour) while rotating. This allows for the growth of a single crystal with the same orientation as the crystal seed.

1.3.7 Crystal growth using Czochralski process

The melting points (at the atmospheric pressure) of Al_5Co_2 , $\text{Al}_{13}\text{Co}_4$, and $\text{Al}_{13}\text{Fe}_4$ are 1182°C , 1092°C and 1160°C [103], respectively. The three previously mentioned phases are incongruently melting intermetallic compounds as shown in the Al-Co and Al-Fe phase diagrams in Fig. 1.21 and can be grown by Czochralski growth from Al-rich solution [103, 104, 13].

The initial compositions have to be richer in Al than the targeted intermetallic phases since all of them come from a peritectic phase transition. Therefore the growth temperature has to be lower than the melting temperature of the desired structures. During the growth, the temperature has to be progressively lowered since the melt pool become less and less rich in Co or Fe (following the liquidus equilibrium line). Unlike the previously mentioned phase, Al_5Fe_2 forms congruently at 1169°C .

In the case of $\text{Al}_{13}\text{Co}_4$, it is only possible to obtain an orthorhombic phase from a Czochralski growth. The monoclinic phase could then be obtained through a peritectoid transformation at 1090°C [84].

The previous sections detailed how the Al-based complex intermetallic compounds are formed, what are their crystallographic structures and what kind of defects they could bear. The following section focuses on their catalytic properties and how they could be related to their electronic and surface structures.

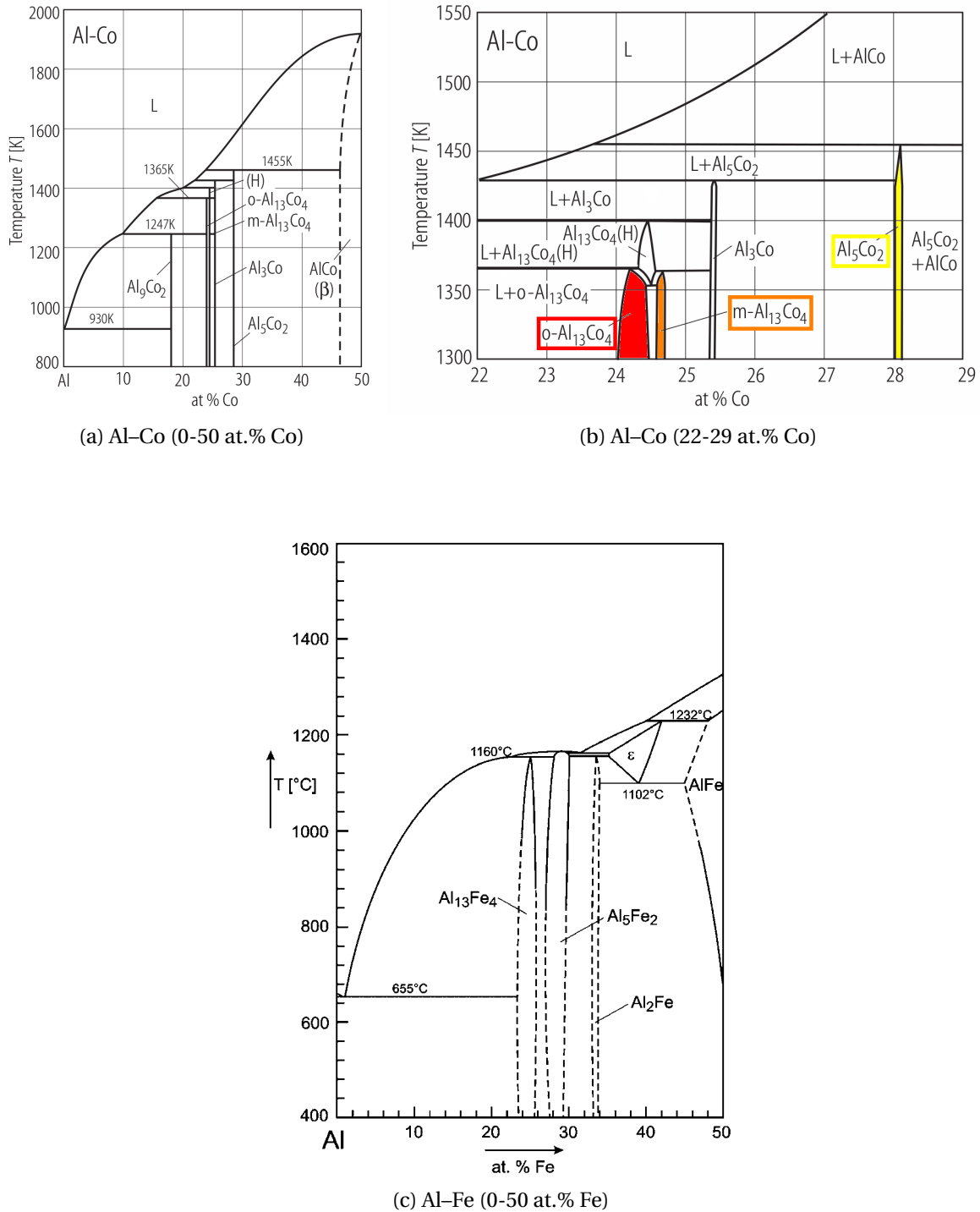


Figure 1.21: (a–b) Al–Co [104, 105] and (c) Al–Fe [103] phase diagrams.



Figure 1.22: (a) Al_5Co_2 single crystal grown from an Al-rich solution of initial composition $\text{Al}_{76}\text{Co}_{24}$ [13, 106], (b) $o\text{-Al}_{13}\text{Co}_4$ single crystal grown from an Al-rich solution of initial composition $\text{Al}_{86.5}\text{Co}_{13.5}$ and (c) $m\text{-Al}_{13}\text{Fe}_4$ single crystal grown from an Al-rich solution of initial composition $\text{Al}_{89.5}\text{Fe}_{10.5}$ [103].

1.4 Catalytic preliminary results

1.4.1 $\text{Al}_{13}\text{TM}_4$

In 2012, Armbrüster et al. showed that $m\text{-Al}_{13}\text{Fe}_4(010)$ (and $o\text{-Al}_{13}\text{Co}_4(100)$) was a low-cost alternative for palladium in heterogeneous hydrogenation and more particularly for the partial hydrogenation of acetylene in ethylene [22, 21]. As shown in Fig. 1.23, $\text{Al}_{13}\text{Fe}_4$ is a highly active and selective catalyst towards the ethylene production from an industry-like ethylene feed. Hydrogen treatment does not influence the catalytic properties of the sample unlike oxygen treatment. The catalyst takes a few hours to recover some of its previous activity and selectivity. Lower values suggest detrimental and irreversible changes of the surface (oxidation). The authors link the good catalytic properties to the so-called site-isolation concept because of a low count of well separated Fe atoms in the bulk lattice.

In 2013, L. Piccolo showed that $m\text{-Al}_{13}\text{Fe}_4(010)$ was also a good alternative for the partial hydrogenation of butadiene into butene at room temperature [7] using a dedicated static catalytic reactor coupled with a UHV preparation chamber, mass spectrometer and gas chromatographer [107]. As shown in Fig. 1.24 butadiene is fully converted into butene within 50 min on $m\text{-Al}_{13}\text{Fe}_4(010)$. This is exactly the time needed for the same conversion on clean $\text{Pd}(100)$. The non-precious metallic compound is highly active, both for butadiene and butene hydrogenation, and highly selective to butene during butadiene hydrogenation, even at room temperature. However, $\text{Al}_{13}\text{Fe}_4$ is subject to deactivation [9] (oxidation) unlike Pd.

Gas chromatography allowed for the determination of the different ratio of butene iso-

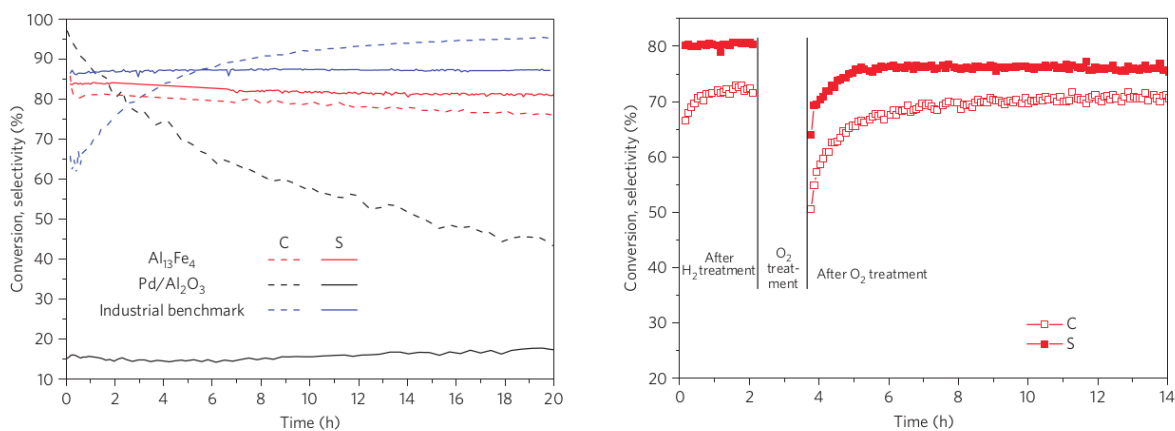


Figure 1.23: Catalytic properties of Al₁₃Fe₄: (left) Conversion (C) and selectivity (S) to ethylene of unsupported Al₁₃Fe₄, 5 wt% Pd/Al₂O₃ and an industrial benchmark catalyst in the semi-hydrogenation of acetylene over 20 h time on stream (reaction conditions: 0.5% C₂H₂, 5% H₂, 50% C₂H₄ in He, 30 ml.min⁻¹ total flow, 200°C). (right) Catalytic properties of Al₁₃Fe₄ after treatment in hydrogen and oxygen.

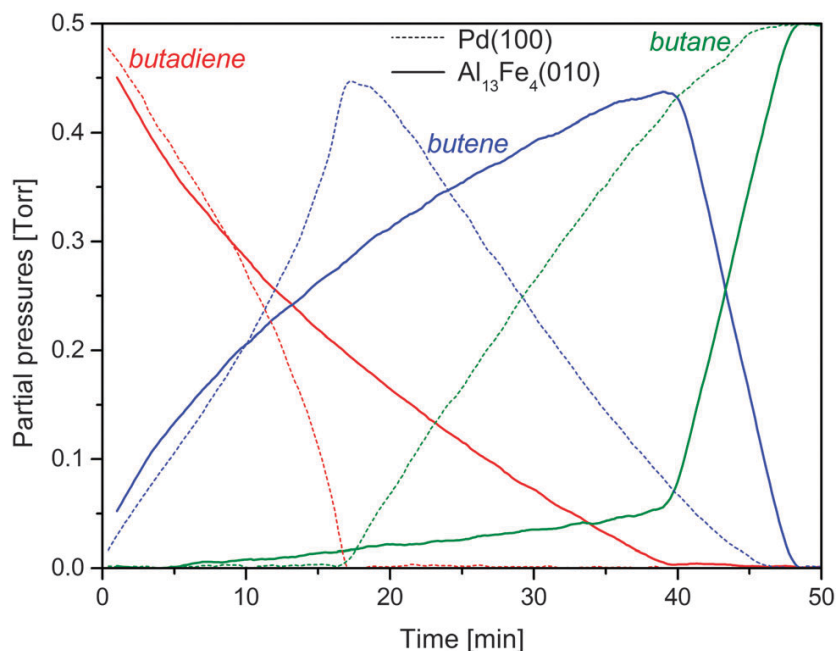


Figure 1.24: Catalytic properties of Al₁₃Fe₄ regarding the partial hydrogenation of butadiene : Hydrocarbon partial pressures during butadiene hydrogenation on a single crystal of Al₁₃Fe₄(010) (straight lines) and Pd(100) (dashed lines) at 24°C [7].

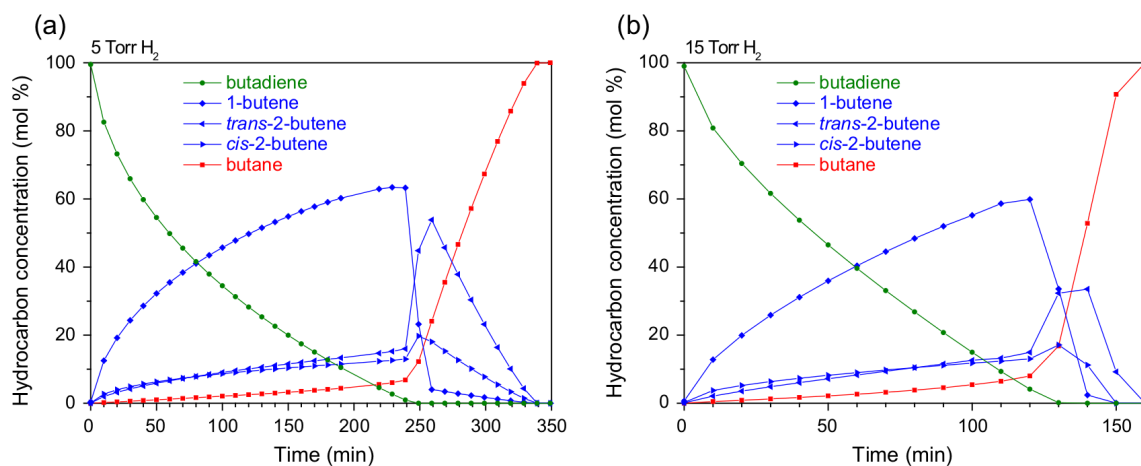


Figure 1.25: Hydrogenation of butadiene on $\text{Al}_{13}\text{Fe}_4(010)$ at room temperature for initial hydrogen pressures of (a) 5 Torr (≈ 6.7 mbar) and (b) 15 Torr (≈ 20 mbar) [9].

mers that are produced during butadiene hydrogenation [9]. As shown in Fig. 1.25 1-butene is the major product during the first hydrogenation reaction with a selectivity close to 70% for two hydrogen concentration (6.7 and 20 mbar) at room temperature.

Regarding $\text{Al}_{13}\text{Co}_4$, Kandaskalov et al. performed in 2014 and 2017 theoretical investigations of the catalytic properties of $\text{Al}_{13}\text{Co}_4(100)$ [32, 19]. Their results suggested an easier hydrogen dissociation on this intermetallic compound than on simple Al surfaces. They also provided a possible mechanism for the hydrogenation of acetylene highlighting a high selectivity but low activity towards the formation of ethylene. The activation energy was calculated to be of 0.86 eV for ethylene and 1.15 eV for ethane.

Finally, in 2019 Piccolo et al. studied the influence of the transition metal and the surface orientation on butadiene hydrogenation in $\text{Al}_{13}\text{TM}_4$ [8]. Pseudo 10-fold surfaces of $\text{Al}_{13}\text{Fe}_4$, $\text{Al}_{13}\text{Ru}_4$ and $\text{Al}_{13}\text{Co}_4$ and the pseudo 2-fold surface of $\text{Al}_{13}\text{Co}_4$ were compared: $\text{Al}_{13}\text{Fe}_4(010)$ appears to be the most active model catalyst at room temperature whereas $\text{Al}_{13}\text{Co}_4(010)$ (pseudo 2-fold) is revealed to be the most active at 110°C while remaining 100% selective to butenes (unlike $\text{Al}_{13}\text{Fe}_4(010)$). Fig. 1.26 presents the comparison of the different activities. It has to be noted that no surface model for $\text{Al}_{13}\text{Co}_4(010)$ has yet been proposed since no investigation has been carried on.

Adsorption as well as electronic (density of states, DOS) calculations were also performed in order to determine if those compounds tend to follow the Newns–Anderson model [49]. First, the results suggest that the higher adsorption energy of C_4H_x the higher the activity towards butadiene hydrogenation (Tab. 1.6). Then, it is noticeable that site-isolation induces a narrowing of the d-band (Fig. 1.27) compared to the one of relative

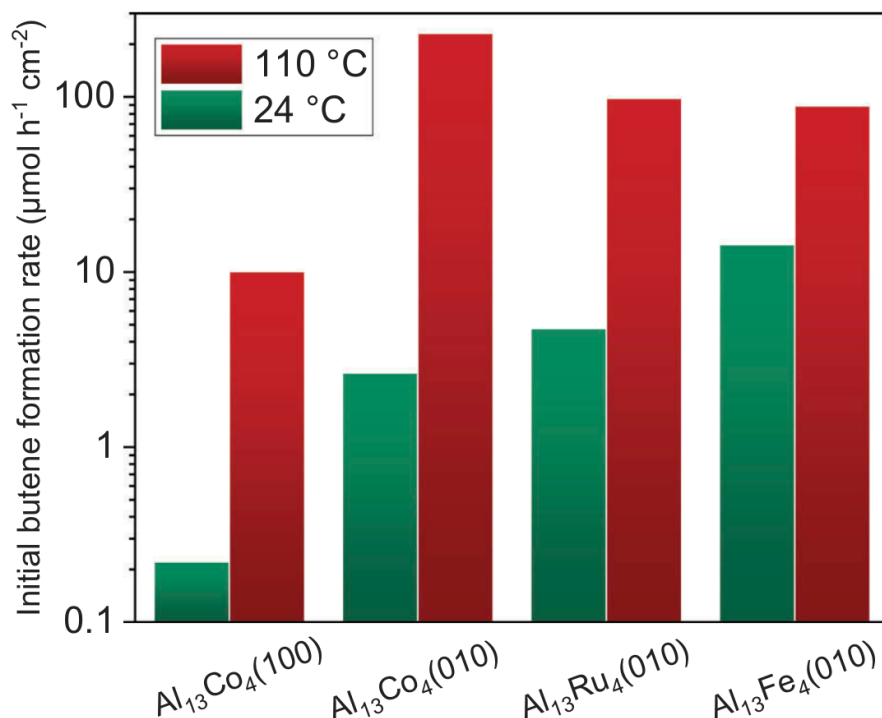


Figure 1.26: Comparison of initial butene formation rates of Al₁₃TM₄ surfaces at room temperature and 110°C [8].

Table 1.6: Adsorption, catalytic and electronic properties of Al₁₃TM₄ (TM = Co, Ru, Fe) [8].

Phase	$E_{\text{ads}}^{\text{C}_4\text{H}_6}$ (eV)	$E_{\text{ads}}^{\text{C}_4\text{H}_8}$ (eV)	Activity ($\mu\text{mol}/\text{h}/\text{cm}^2$)	d-band center (eV)
<i>o</i> -Al ₁₃ Co ₄	1.06	0.62	0.2	-1.97
<i>m</i> -Al ₁₃ Ru ₄	1.15	0.70	4.5	-2.48
<i>m</i> -Al ₁₃ Fe ₄	1.30	0.91	13	-1.41

simple metal (bcc Fe, hcp Co and Ru). Therefore a stronger chemisorption (than on simple metals) and a narrowing of the d-band are observed, enhancing the hydrogenation activity. Focusing on Al₁₃Fe₄ and Al₁₃Co₄, there is a correlation between the position of the d-band (last column of Tab. 1.6) and the adsorption properties. As long as one stay on one line of the periodic table (3d TM, Fe and Co), the Al₁₃TM₄ compounds seem to follow the Newns–Anderson model. It is more difficult to rationalize the correlation between the position of the d-band and the adsorption properties when one adds the 4d TM (Al₁₃Ru₄) into the equation.

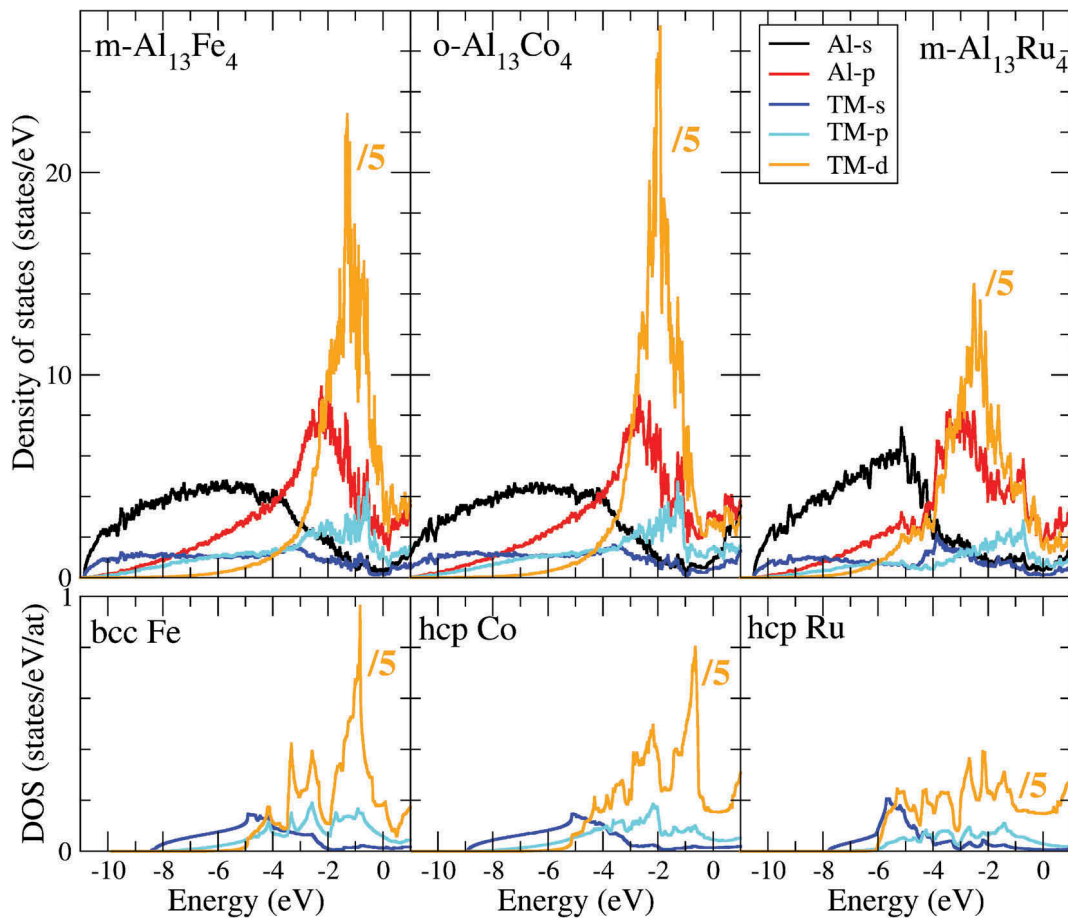


Figure 1.27: Contributions of s-, p-, and d-states to the density of states (DOS) for bulk $\text{Al}_{13}\text{TM}_4$ and TM. The Fermi energy corresponds to 0 eV [8].

1.4.2 Al_5Co_2

Concerning Al_5Co_2 , in 2017 Meier et al. used theoretical calculations to investigate the catalytic properties of $\text{Al}_5\text{Co}_2(2\bar{1}0)$, $\text{Al}_5\text{Co}_2(100)$ and $\text{Al}_5\text{Co}_2(001)$ towards the partial hydrogenation of acetylene (C_2H_2) [15]. On $\text{Al}_5\text{Co}_2(2\bar{1}0)$, the activation energy was calculated to be around 60 kJ/mol while the one towards total hydrogenation (into ethane) was estimated to be around 106 kJ/mol. These results suggested a selective catalyst.

Recently, it was shown that $\text{Al}_5\text{Co}_2(2\bar{1}0)$ was a selective yet not highly active catalyst towards the partial hydrogenation of butadiene into butene at 110°C [23]. As shown in Fig. 1.28(a) the sample is quite selective towards the formation of butene (butane is formed only after the full conversion of butadiene). The main butene isomer that is produced is here again 1-butene (determined by gas chromatography, Fig. 1.28b).

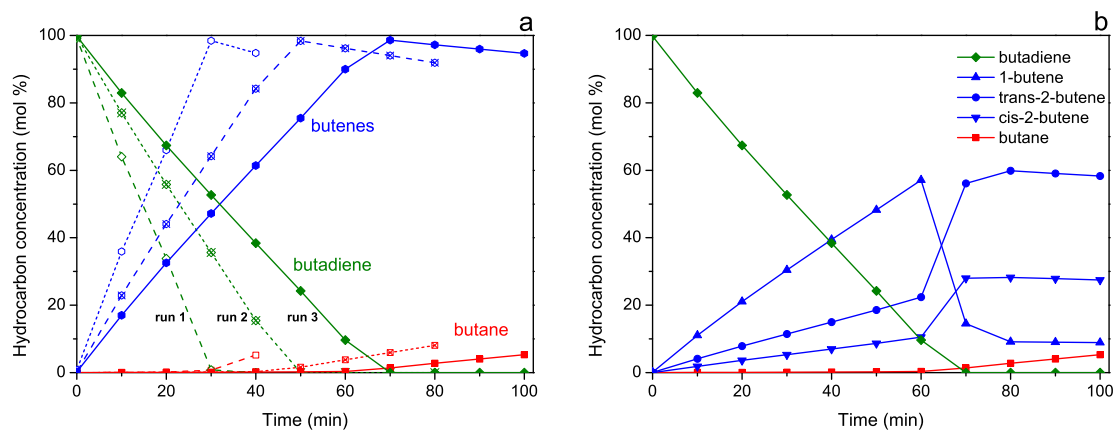


Figure 1.28: (a) Catalytic performances of $\text{Al}_5\text{Co}_2(2\bar{1}0)$ at $T = 110^\circ\text{C}$, with initial pressures $p_{\text{H}_2} = 5$ mbar and $p_{\text{C}_4\text{H}_6} = 0.5$ mbar (first, second and third runs are respectively drawn in dashed, dotted and full lines). (b) Detailed catalytic performances of $\text{Al}_5\text{Co}_2(2\bar{1}0)$ for the third run showing the concentrations of the different butene isomers [23].

Chapter 2

Theoretical and Experimental Methodologies

Contents

2.1 Principles of Density Functional Theory	36
2.1.1 Schrödinger equation	36
2.1.2 The Hohenberg and Kohn theorems	37
2.1.3 The Kohn-Sham method and the Exchange-Correlation energy . . .	38
2.1.4 The PBE and DFT-D3 functionals	40
2.1.5 Numerical implementation	41
2.2 DFT applications to Al-based intermetallics	44
2.2.1 Bulk and surfaces simulations	44
2.2.2 Electronic structure	44
2.2.3 Thermodynamic simulations	46
2.2.4 Kinetic calculations	50
2.3 Surface X-ray Diffraction (SXRD)	55
2.3.1 Basics of x-ray diffraction	55
2.3.2 Crystal truncation rods	56
2.3.3 Reciprocal space exploration	57
2.3.4 Data collection and analysis	58
2.3.5 Experimental end-stations at SixS beamline	59
2.4 Conventional surface investigation techniques	61
2.4.1 Surface preparation	61
2.4.2 Auger electron spectroscopy (AES)	61
2.4.3 Low energy electron diffraction (LEED)	61

2.4.4	Scanning tunneling microscopy (STM)	62
2.4.5	Atomic force microscopy (AFM)	62
2.4.6	Catalysis experiments	62

2.1 Principles of Density Functional Theory

This first section focuses on the well-established Density Functional Theory, its fundamental equations, limitations and approximations. The numerical implementation using the code VASP is also detailed. In the following bold letters will refer to vectors.

2.1.1 Schrödinger equation

A crystalline structure can be seen as a system of n electrons and N nuclei and therefore as a $3n + 3N$ many-body quantum problem. The interactions between those particles are governed by the law of quantum mechanics. The time-independent Schrödinger equation describes such system and is expressed by the following equation :

$$\hat{H}\Psi(\mathbf{r}_1, \mathbf{r}_2, \dots, \mathbf{R}_1, \mathbf{R}_2, \dots) = E\Psi(\mathbf{r}_1, \mathbf{r}_2, \dots, \mathbf{R}_1, \mathbf{R}_2, \dots) \quad (2.1)$$

where \hat{H} is the Hamiltonian operator, E one eigenvalue of the system, \mathbf{r}_i and \mathbf{R}_i the positions of electrons and nuclei, respectively, and Ψ its associated eigenvector also known as the many-body wave function of the system. In the following, all the equations will be written in atomic units. The Hamiltonian operator can be expressed as follows.

$$\hat{H} = T_{el} + T_{nuc} + U_{el-el} + V_{el-nuc} + V_{nuc-nuc}$$

where T_{el} and T_{nuc} are respectively the kinetic energies of the electrons and the nuclei, U_{el-el} the interaction potential of the electrons, V_{el-nuc} the Coulomb attraction of the electrons and the nuclei, and finally $V_{nuc-nuc}$ the interaction potential of the nuclei. The developed form of the Hamiltonian is presented by Eq. 2.2.

$$\hat{H} = \underbrace{-\frac{1}{2} \sum_i^n \nabla_i^2}_{T_{el}} - \underbrace{\frac{1}{2} \sum_k^N \frac{\nabla_k^2}{M_k}}_{T_{nuc}} - \underbrace{\sum_i^n \sum_{j \neq i}^n \frac{1}{|\mathbf{r}_i - \mathbf{r}_j|}}_{U_{el-el}} - \underbrace{\sum_i^n \sum_k^N \frac{Z_k}{|\mathbf{r}_i - \mathbf{R}_k|}}_{V_{el-nuc}} - \underbrace{\sum_k^N \sum_{l \neq k}^N \frac{Z_k Z_l}{|\mathbf{R}_k - \mathbf{R}_l|}}_{V_{nuc-nuc} = \text{constant}} \quad (2.2)$$

where ∇^2 is the Laplacian operator, M_k the mass of nucleus k , $|\mathbf{r}_i - \mathbf{r}_j|$ the distance between electrons i and j , $|\mathbf{r}_i - \mathbf{R}_k|$ the distance between electron i and nucleus k , $|\mathbf{R}_k - \mathbf{R}_l|$ the distance

between nuclei k and l , and Z_k the atomic number of nucleus k . The analytical solution of this equation is unreachable (many-body problem). Numerical solutions are possible within some approximations.

The first one is the Born-Oppenheimer approximation. Since the nuclei are much heavier than the electrons (mass ratio $1:2000 \rightarrow T_{\text{nuc}} \ll T_{\text{el}}$), we only solve the electronic structure for frozen configurations of the nuclei. In this scenario, $V_{\text{nuc-nuc}}$ is assumed to be constant. The relevant Hamiltonian is thus $\hat{H}_{\text{el}} = T_{\text{el}} + U_{\text{el-el}} + V_{\text{el-nuc}}$. Therefore our problem is simplified to a $3n$ many-body problem describe by Eq. 2.3.

$$\hat{H}_{\text{el}} \varphi(\mathbf{r}_1, \mathbf{r}_2, \dots) = E_{\text{el}} \varphi(\mathbf{r}_1, \mathbf{r}_2, \dots) \quad (2.3)$$

where φ is the multi-electronic wave function. The total electronic energy E_{el} depends only parametrically on the position \mathbf{R}_k of the nuclei. Nevertheless we still have a $3n$ many-body quantum problem. Two main types of methods were developed in order to solve this kind of problems : the Hartree-Fock methods [108, 109] and the Density Functional Theory [110, 111].

The first one approximates the multi-electronic wave function φ as a Slater determinant [112]. It is a mathematical way to approach the wave function of a system as it respects the antisymmetry principle of such function for the fermions.

$$\varphi = \begin{vmatrix} \varphi_1(\mathbf{r}_1) & \cdots & \varphi_n(\mathbf{r}_1) \\ \vdots & \ddots & \vdots \\ \varphi_1(\mathbf{r}_n) & \cdots & \varphi_n(\mathbf{r}_n) \end{vmatrix}$$

Density Functional Theory is a post-Hartree-Fock method that uses the total electronic density as the main variable instead of the multi-electronic wave function. This method comes from the 1927 Thomas-Fermi model [113, 114]. In this model the kinetic energy of a non-interacting electrons cloud depends only on its electron density. This electron density is expressed by the following equation (Eq. 2.4).

$$\rho(\mathbf{r}) = \int_{\mathbf{r}_2} \cdots \int_{\mathbf{r}_n} |\varphi(\mathbf{r}, \mathbf{r}_2, \dots, \mathbf{r}_n)|^2 d\mathbf{r}_2 \dots d\mathbf{r}_n \quad (2.4)$$

2.1.2 The Hohenberg and Kohn theorems

The Density Functional Theory lies on two main theorems that were established by Hohenberg and Kohn in 1964 [110].

2.1.2.1 Existence theorem

All observable quantities of a quantum system are uniquely determined by its density, and all properties can be calculated as an explicit or implicit functional of density. A functional is a function of a function : it refers to a linear mapping from a vector space V into its field of scalars. Therefore the energy of a system can be written as Eq. 2.5 (from Eq. 2.2).

$$E_{\text{el}}[\rho(\mathbf{r})] = T_{\text{el}}[\rho(\mathbf{r})] + U_{\text{el-el}}[\rho(\mathbf{r})] + V_{\text{el-nuc}}[\rho(\mathbf{r})] \quad (2.5)$$

$V_{\text{el-nuc}}$ can be seen as an external potential and the previous equation can be generalized by Eq. 2.6 where F_{HK} is the universal functional that does not depend on any external potential to the system but only on the kinetic energies and interaction potentials of the electrons of the system.

$$E_{\text{el}}[\rho(\mathbf{r})] = F_{\text{HK}}[\rho(\mathbf{r})] + \int V_{\text{ext}}(\mathbf{r})\rho(\mathbf{r})d\mathbf{r} \quad (2.6)$$

2.1.2.2 Variational principle

Derived from the variational principle of quantum mechanics, this theorem implies that the calculated energy of a system is higher than the exact energy determined by the exact electronic density (Eq. 2.7). Thanks to this principle, it is possible to choose an electronic density the closest to the real one in order to minimize the total energy of the system.

$$E_{\text{el}}[\rho(\mathbf{r})] \geq E_{\text{true}}[\rho_{\text{true}}(\mathbf{r})] \quad (2.7)$$

However, these theorems do not allow the determination of the density $\rho(\mathbf{r})$ since the interaction potential $U_{\text{el-el}}$ is still unknown.

2.1.3 The Kohn-Sham method and the Exchange-Correlation energy

In 1965 Kohn and Sham developed a method – called the Kohn-Sham method – to determine the energy and the electronic density of a system in its fundamental state (stationary solution with the lowest eigenvalue) [111]. In this method, the many-body problem of n interacting electrons (density $\rho(\mathbf{r})$) is seen as a system of n non-interacting electrons having the same density $\rho(\mathbf{r})$. The many-body problem is thus transformed into a system of n

uncoupled single-body equations. Therefore Eqs. 2.3 and 2.4 could be written as follows :

$$\hat{H}_{\text{KS}} \psi_i(\mathbf{r}) = \varepsilon_i \psi_i(\mathbf{r}) \quad \text{and} \quad \rho(\mathbf{r}) = \sum_{i=1}^n |\psi_i(\mathbf{r})|^2 \quad \text{with } i \in 1, \dots, n \quad (2.8)$$

where \hat{H}_{KS} is the Kohn-Sham Hamiltonian, $\psi_i(\mathbf{r})$ the Kohn-Sham wave functions, and ε_i the eigenvalues of their associated energies. The Kohn-Sham Hamiltonian is expressed as follows :

$$\hat{H}_{\text{KS}} = \underbrace{-\frac{1}{2}\nabla_i^2}_{\text{kinetic}} - \underbrace{\sum_{i=1}^N \frac{Z_i}{|\mathbf{r}-\mathbf{R}_i|}}_{e^-/\text{nuclei}} + \underbrace{\int_{\mathcal{V}} \frac{\rho(\tilde{\mathbf{r}})}{|\mathbf{r}-\tilde{\mathbf{r}}|} d^3\tilde{\mathbf{r}}}_{e^-/e^-} + \underbrace{\frac{\delta E_{\text{xc}}[\rho]}{\delta \rho}}_{V_{\text{xc}}} \quad (2.9)$$

It could be seen as if each electron does not see the others, but only a external potential and a electronic density equals to the one of all the electrons ρ . Here, the only approximation lies inside the functional $E_{\text{xc}}[\rho]$ called the exchange-correlation energy that contains both the exchanges between electrons, their correlations and the corrections on the kinetic energies due to the Kohn-Sham method. Using the Hohenberg-Kohn theorems, it is possible to determine an expression of the groundstate energy of the system E_{el}° (Eq. 2.10).

$$E_{\text{el}}^{\circ} = F[\rho(\mathbf{r})] = \sum_i \varepsilon_i + E_{\text{xc}}[\rho] - \int_{\mathcal{V}} V_{\text{xc}}(\mathbf{r})\rho(\mathbf{r})d^3\mathbf{r} - \frac{1}{2} \int_{\mathcal{V}} \int_{\tilde{\mathcal{V}}} \frac{\rho(\mathbf{r})\rho(\tilde{\mathbf{r}})}{|\mathbf{r}-\tilde{\mathbf{r}}|} d^3\tilde{\mathbf{r}} d^3\mathbf{r} \quad (2.10)$$

where F is the universal functional of the electronic density, and $V_{\text{xc}}(\mathbf{r}) = \frac{\delta E_{\text{xc}}[\rho]}{\delta \rho}(\mathbf{r})$ the exchange-correlation potential. If the exact form of $E_{\text{xc}}[\rho]$ is known, one could get the exact value of E_{el}° . But it is not possible to obtain this exact form.

It is therefore necessary to approximate the exchange-correlation energy, in order to compute it numerically. There are a few ways to estimate this energy and the simplest one if called the Local Density Approximation.

2.1.3.1 Local density approximation (LDA)

In this approximation proposed by Kohn and Sham [111], the density is considered to be locally homogeneous and barely varying. The exchange-correlation energy is linearly decomposed into the sum of an exchange term and a correlation term, and is defined by :

$$E_{\text{xc}}^{\text{LDA}}[\rho] = \int_{\mathcal{V}} \rho(\mathbf{r})\varepsilon_{\text{xc}}(\rho)d\mathbf{r}$$

where ε_{xc} is the exchange-correlation energy per particle of a homogeneous electron gas

of electronic density ρ that can be computed with high accuracy (local calculation).

2.1.3.2 Generalized gradient approximation (GGA)

This approximation is an improvement of the LDA where ϵ_{xc} also depends on the gradient (first derivative) of the electronic density [115] and is defined by :

$$E_{xc}^{GGA}[\rho] = \int_{\mathcal{V}} \rho(\mathbf{r}) \epsilon_{xc}(\rho, \nabla\rho) d\mathbf{r}$$

Other functionals exist such as the Hybrid-GGA (that uses the Hartree-Fock method), the Meta-GGA (that uses the gradient and the Laplacian of the density), or even the Hybrid-Meta-GGA that combines both functionals. In the case of Al-based intermetallics, it is better to use GGA functionals because of the relatively different electronic structures of Al and Co/Fe. A locally homogeneous electronic density hypothesis is not correct. In this work, the functionals that we use are therefore based on the GGA functional : the Perdew-Burke-Ernzerhof (PBE) and the DFT-D3 (dispersive) functionals.

2.1.4 The PBE and DFT-D3 functionals

The PBE functional [115, 116, 117] could be referred to as the "classical" GGA functional used in common DFT calculations. It is an improvement upon the first GGA functionals (such as PW91) and corrects some features of LDA [116]. Atomization energies of molecules are for instance better predicted using PBE functional. GGA-PBE is well-designed for the study of intermetallics (bulk and surfaces) as well as adsorption properties [106].

Nevertheless, by studying the adsorption of molecules onto a metallic surface, one has to consider van der Waals interactions. GGA-PBE functionals do not describe correctly this kind of interaction resulting from dynamical correlations between fluctuating charge distributions. An easy way to bear this issue is to add a dispersive term to the Kohn-Sham energy :

$$E_{DFT-D} = E_{KS} + E_{disp}$$

In 2010, Grimme et al. developed the DFT-D3 corrections [118, 119, 120] in which the dispersion coefficient are geometry-dependent as they are adjusted on the basis of local geometry (coordination number) around the considered atoms. This functional presents numerous advantages : it is robust, numerically stable, fast, purely *ab initio* (no empirical coefficients, depending on input parameters only), and is applicable to all elements, molecules, and solids. Van der Waals forces are also present at metallic surfaces, and they

non negligibly affect the surface energies [121]. It is therefore interesting to use this approximation when it comes to molecular adsorption on metallic surfaces.

2.1.5 Numerical implementation

The computational way to solve the aforementioned equations is to use self-consistent loops (as presented in Fig. 2.1) with convergence criteria as stop conditions. In practice, different methods exist to tackle the resolution of a DFT calculation. For example one can use gaussian orbitals (code Gaussian), or plane waves inside periodic boundary conditions (code VASP). The fundamental difference between them is the basis set used to represent Kohn-Sham orbitals. The code VASP will be the one used all over the present work.

High power computing (HPC) ressources are needed to perform such calculations. Three HPC clusters were mainly used in this work : *Occigen* at CINES (Centre Informatique National de l'Enseignement Supérieur, Montpellier, France), *Explor* at IJL (Université de Lorraine, Institut Jean Lamour, Nancy, France) and *Cobalt* at TGCC (Très Grand Centre de calcul du CEA, Saclay, France).

2.1.5.1 VASP code

The Vienna *Ab initio* Simulation Package (VASP) is developped by Kresse et al. since the 1990's and is based on the use of plane waves to represent the electrons, combined either with pseudopotentials or the projector augmented wave (PAW) method [122, 123, 124, 125, 126].

2.1.5.2 Reciprocal space discretization

When looking at crystal structures (bulk materials and surfaces), VASP tackles the problem using periodic boundary conditions in order to avoid dealing with $\sim 10^{23}$ electrons ! If we recall the Kohn-Sham main equation ($\hat{H}_{KS} \psi_i(\mathbf{r}) = \varepsilon_i \psi_i(\mathbf{r})$), one has to describe the wave functions inside those periodic boundary conditions. Thanks to the translational invariant principle and the Bloch theorem [127], the wave functions could be written as follows :

$$\psi_{n\mathbf{k}}(\mathbf{r}) = u_{n\mathbf{k}}(\mathbf{r}) e^{i\mathbf{k}\cdot\mathbf{r}} \quad \text{with} \quad u_{n\mathbf{k}}(\mathbf{r} + \mathbf{R}) = u_{n\mathbf{k}}(\mathbf{r}) \quad \text{and} \quad \psi_{n\mathbf{k}}(\mathbf{r} + \mathbf{R}) = \psi_{n\mathbf{k}}(\mathbf{r}) e^{i\mathbf{k}\cdot\mathbf{R}}$$

where \mathbf{R} is a translation vector that leaves \hat{H} unchanged, \mathbf{k} is the Bloch wavevector (constrained to lie within the first Brillouin zone of the reciprocal space lattice), n is the band index, and $u_{n\mathbf{k}}(\mathbf{r})$ is the periodic part due to the lattice and its periodicity. The electronic

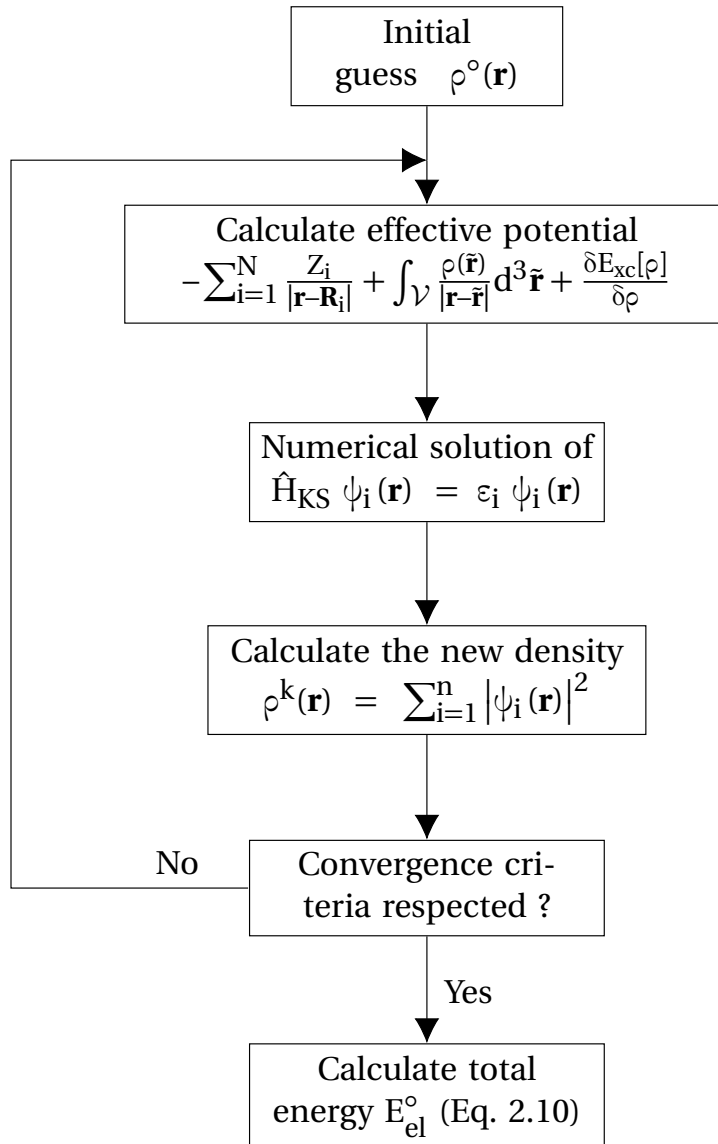


Figure 2.1: Self-consistent loop used in Density Functional Theory

density is obtained by integration over the first Brillouin zone (BZ) and is given by:

$$\rho(\mathbf{r}) = \frac{1}{\Omega_{\text{BZ}}} \sum_n \int_{\text{BZ}} f_{n\mathbf{k}} |\psi_{n\mathbf{k}}(\mathbf{r})|^2 d\mathbf{k}$$

where Ω_{BZ} is the volume of the first Brillouin zone and $f_{n\mathbf{k}}$ are the occupation numbers (*i.e.* the number of electrons in the state $n\mathbf{k}$). The integration is transformed for numerical purposes into a discrete weighted (for normalization purposes) sum over a discrete set of \mathbf{k} -points :

$$\rho(\mathbf{r}) = \frac{1}{\Omega_{\text{BZ}}} \sum_n \sum_{\mathbf{k}} w_{\mathbf{k}} f_{n\mathbf{k}} |\psi_{n\mathbf{k}}(\mathbf{r})|^2 d\mathbf{k} \quad \text{with} \quad \sum_{\mathbf{k}} w_{\mathbf{k}} = 1$$

Ideally, one would like to have an equally spaced mesh of the Brillouin zone that provides a good calculation precision while being fast enough in order to have reasonable computing costs. In practice, the following rule of thumb is applied for a $(N_1 \times N_2 \times N_3)$ \mathbf{k} -points grid and its N_i ratio :

$$N_1 : N_2 : N_3 \simeq \frac{1}{|\mathbf{a}_1|} : \frac{1}{|\mathbf{a}_2|} : \frac{1}{|\mathbf{a}_3|}$$

where \mathbf{a}_i are the Bravais lattice vectors of the considered crystal. This grid will be a VASP input parameter. In the case of bulk Al_5Co_2 , a $(8 \times 8 \times 8)$ grid is enough to ensure a precision below 1 meV (as presented later on in Fig. 2.3). For a bulk $\text{Al}_{13}\text{Co}_4$, a $(13 \times 9 \times 7)$ grid is enough to have a similar precision.

2.1.5.3 Plane waves basis definition

As seen previously, the wave functions are defined using a periodic part due to the lattice and its periodicity ($u_{n\mathbf{k}}(\mathbf{r})$). In order to numerically calculate them, it is possible to express this periodic part as Fourier series, transforming the previous wave functions into sums of plane waves :

$$u_{n\mathbf{k}}(\mathbf{r}) = \sum_{\mathbf{G}} C_{\mathbf{G}n\mathbf{k}} \cdot e^{i\mathbf{G}\cdot\mathbf{r}} \rightarrow \psi_{n\mathbf{k}}(\mathbf{r}) = \sum_{\mathbf{G}} C_{\mathbf{G}n\mathbf{k}} \cdot e^{i(\mathbf{G}+\mathbf{k})\cdot\mathbf{r}} \quad (2.11)$$

where \mathbf{G} covers all the reciprocal space vectors and $C_{\mathbf{G}n\mathbf{k}}$ are the coefficient of the plane waves. In practice, not all the reciprocal space vectors are probed. We introduce then the cut-off energy $E_{\text{cut-off}}$ that represents the maximum kinetic energy of the considered plane waves. This energy will be a VASP input parameter.

$$\frac{1}{2} |\mathbf{G} + \mathbf{k}|^2 \leq E_{\text{cut-off}}$$

2.1.5.4 Pseudo-potentials and Projector-Augmented Wave method

Finally, in order to solve the Kohn-Sham equations one has to know the electronic structures of the atoms. In our case, VASP uses the frozen core approximation where only the valence electrons are considered since the core electrons barely affect the electronic properties. Their potentials are therefore approximated and pseudo-potentials – that are equal to the real potential far from the atom core – are used. The Projector-Augmented Wave (PAW) method is a generalization of the pseudo-potential method and allows for DFT calculations to be performed with greater computational efficiency [126, 128].

2.2 DFT applications to Al-based intermetallics

DFT will be a powerful tool used all along this work. From bulk electronic structures to surfaces reactivity all kind of relevant properties may be predicted : bulk and slabs total energies, bulk and surface density of states, partial surface charge density, surface energies, adsorption energies, reaction paths and barriers, etc.

2.2.1 Bulk and surfaces simulations

Before doing more complex calculations, it is necessary to tune the VASP input parameters for the considered systems in order to have reasonable computing time while reaching convergence within a good precision. It is for example crucial to determine the right k-points mesh and cut-off energy. Concerning surfaces calculations, slabs must be built : a sufficiently thick vacuum has to be put along the surface direction to have no interaction between the periodic slabs as shown in Fig. 2.2.

Fig. 2.3 presents the different convergence tests regarding (a) the k-points mesh, (b) the cut-off energy and (c) the thickness of the vacuum between two slabs. For bulk Al_5Co_2 and $\text{Al}_5\text{Co}_2(2\bar{1}0)$, a $(8 \times 8 \times 8)$ k-points grid ($(8 \times 8 \times 1)$ for the surface), a cut-off energy of 450 eV and a vacuum thickness (for the surface) of 16 Å are enough to reach a precision below 1 meV while remaining fast enough (using the PBE functional).

2.2.2 Electronic structure

2.2.2.1 Density of states

The density of states (DOS) is the number of states that are to be occupied by the system at each level of energy. High DOS at a specific energy level means that many states are

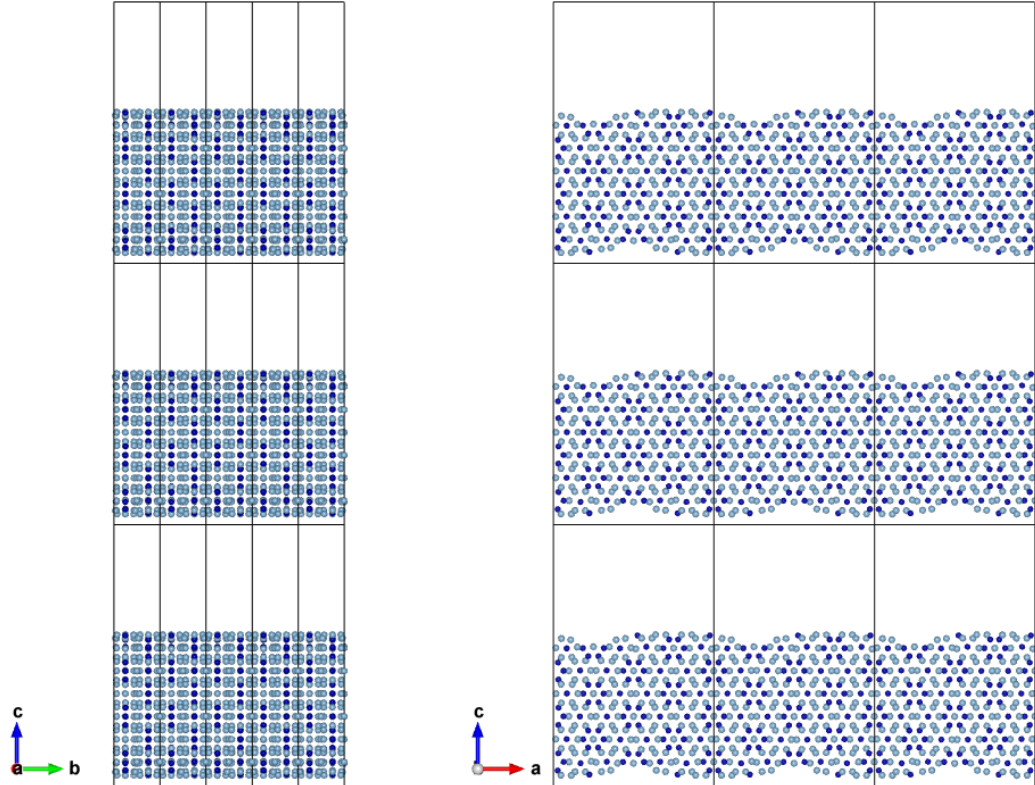


Figure 2.2: Slab construction of $\text{Al}_5\text{Co}_2(2\bar{1}0)$. Al and Co atoms are drawn in light blue and blue, respectively.

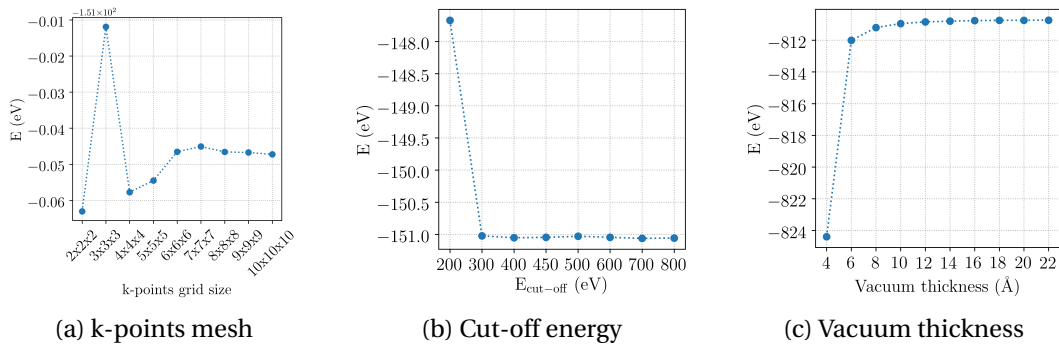


Figure 2.3: Convergence tests for (a–b) bulk Al_5Co_2 and (c) surface $\text{Al}_5\text{Co}_2(2\bar{1}0)$

available for occupation. In metals, the DOS is continuous while it is discrete in atoms and molecules. Numerically, the calculated DOS \bar{n} is determined as the difference of the integrated DOS between two energies :

$$\bar{n} = \frac{N(\varepsilon_i) - N(\varepsilon_{i-1})}{\Delta\varepsilon} \quad \text{with} \quad \Delta\varepsilon = \varepsilon_i - \varepsilon_{i-1} \quad \text{and} \quad N(\varepsilon_i) = \int_{-\infty}^{\varepsilon_i} n(\varepsilon) d\varepsilon$$

where $N(\varepsilon_i)$ is the integrated DOS and $\Delta\varepsilon$ the energy discretization. This numerical method conserves exactly the total number of electrons. The calculation of the DOS allows to verify if there is a gap or a pseudo-gap at the Fermi level that could be correlated to some particular properties.

2.2.2.2 STM images simulations

The experimental description of scanning tunneling microscopy (STM) will be further developed in section 2.4.4. Simulations of STM images are done using the Tersoff-Hamann approximations [129, 130]. The tunneling current I_t is calculated and assumed to be proportional to the local DOS of the surface at the position of the tip of the microscope.

The surface and the tip are considered to be independant systems having little interactions. The tunneling current is therefore calculated by first-order perturbation theory [129]. The tip is considered to be punctual : only the surface electronic density below the tip is thus relevant. Finally, we consider that the tip has a spherical local potential with s-type wave functions. All these approximations give the following equation for the calculated tunnelling current :

$$I_t(\mathbf{r}_o) \approx \frac{4\pi^2 e}{h} \rho_{\text{tip}}(\varepsilon_F) \int_{\varepsilon_F}^{\varepsilon_F + V_b} \rho_{\text{surf}}(\mathbf{r}_o, \varepsilon) d\varepsilon$$

where \mathbf{r}_o is the position of the tip, ρ_{tip} its electronic density, $\rho_{\text{surf}}(\mathbf{r}_o, \varepsilon)$ the one of the surface at \mathbf{r}_o (local density), ε_F the Fermi level and V_b the applied bias between the tip and the surface (here the bias is positive).

2.2.3 Thermodynamic simulations

DFT calculations allow for the determination of the total energy of a system as well as the adsorption energies of different elements of molecules to the surface of a material. Thanks to those results, one can calculate surface energies or even extrapolate pressure and temperature stability conditions of an adsorbed gas.

2.2.3.1 Surface energy calculations

Let's assume a symmetrical slab of $\text{Al}_{13}\text{Co}_4$, the surface energies γ of the surface models are defined by the following equations 2.12 and 2.13 [106].

$$2A\gamma = E^{\text{slab}} - \sum_i \mu_i N_i^{\text{slab}} \quad \text{with } i \in (\text{Al}, \text{Co}) \quad \text{and} \quad \mu_i = \left. \frac{\partial G}{\partial N_i} \right|_{p,T,N_j} \quad (2.12)$$

$$\gamma = \frac{1}{2A} \left(E^{\text{slab}} - \mu_{\text{Al}} N_{\text{Al}}^{\text{slab}} - \mu_{\text{Co}} N_{\text{Co}}^{\text{slab}} \right) \quad (2.13)$$

where A is the surface area, E^{slab} is the total energy of the slab (determined through DFT calculations), μ_X is the chemical potential of X in $\text{Al}_{13}\text{Co}_4$, G the free enthalpy of the system and N_X^{slab} the number of X atom in the slab ($X = \text{Al}, \text{Co}$). In the bulk material the $\text{Al}_{13}\text{Co}_4$ atomic chemical potential – also known as the cohesive energy – is defined by (Gibb's rule):

$$E_{\text{cohesive}}^{\text{Al}_{13}\text{Co}_4} = \mu_{\text{Al}_{13}\text{Co}_4}^{\text{bulk}} = 13\mu_{\text{Al}} + 4\mu_{\text{Co}} \quad (2.14)$$

The Al and Co cohesive energies are defined by the following equation :

$$E_{\text{cohesive}}^X = \mu_X^{\text{bulk}} = \frac{E_X^{\text{bulk}} - N_X^{\text{bulk}} E_X^{\text{alone}}}{N_X^{\text{bulk}}} \quad \text{with } X \in (\text{Al}, \text{Co})$$

where E_X^{bulk} is the energy of a pure X bulk, N_X^{bulk} the number of atoms in the unit cell and E_X^{alone} the energy of an isolated X atom ($X = \text{Al}, \text{Co}$). The cohesive energy of $\text{Al}_{13}\text{Co}_4$ can also be defined using its formation enthalpy :

$$E_{\text{cohesive}}^{\text{Al}_{13}\text{Co}_4} = \mu_{\text{Al}_{13}\text{Co}_4}^{\text{bulk}} = 13\mu_{\text{Al}}^{\text{bulk}} + 4\mu_{\text{Co}}^{\text{bulk}} + 17\Delta H_f^{\text{Al}_{13}\text{Co}_4} \quad (2.15)$$

where $\Delta H_f^{\text{Al}_{13}\text{Co}_4}$ is the atomic formation enthalpy of $\text{Al}_{13}\text{Co}_4$. Using all the previous definition, it is possible to express the surface energy as a function of $\mu_{\text{Al}} - \mu_{\text{Al}}^{\text{bulk}}$, where μ_{Al} – the potential of Al in $\text{Al}_{13}\text{Co}_4$ – is the only unknown variable :

$$\gamma = \frac{1}{2A} \left[E^{\text{slab}} - \frac{\mu_{\text{Al}_{13}\text{Co}_4}^{\text{bulk}} N_{\text{Co}}^{\text{slab}}}{4} - \mu_{\text{Al}}^{\text{bulk}} \left(N_{\text{Al}}^{\text{slab}} - \frac{13 N_{\text{Co}}^{\text{slab}}}{4} \right) - (\mu_{\text{Al}} - \mu_{\text{Al}}^{\text{bulk}}) \left(N_{\text{Al}}^{\text{slab}} - \frac{13 N_{\text{Co}}^{\text{slab}}}{4} \right) \right] \quad (2.16)$$

Assuming the surface is in equilibrium with the bulk (no segregation is occurring), the following inequalities must be respected : $\mu_{\text{Al}} \leq \mu_{\text{Al}}^{\text{bulk}}$ and $\mu_{\text{Co}} \leq \mu_{\text{Co}}^{\text{bulk}}$. In other words the system is bounded between pure bulk Al and pure Co bulk. Finally, the range of chemical

potential for $\mu_{\text{Al}} - \mu_{\text{Al}}^{\text{bulk}}$ is bounded by these two limits (Eq. 2.17, detailed in footnote¹). The surface energy could then be plotted as a function of $\mu_{\text{Al}} - \mu_{\text{Al}}^{\text{bulk}}$ in between $\frac{17}{13}\Delta H_f^{\text{Al}_{13}\text{Co}_4}$ and 0.

$$\left. \begin{array}{l} \mu_{\text{Al}} \leq \mu_{\text{Al}}^{\text{bulk}} \rightarrow \mu_{\text{Al}} - \mu_{\text{Al}}^{\text{bulk}} \leq 0 \\ \mu_{\text{Co}} \leq \mu_{\text{Co}}^{\text{bulk}} \rightarrow \frac{17}{13}\Delta H_f^{\text{Al}_{13}\text{Co}_4} \leq \mu_{\text{Al}} - \mu_{\text{Al}}^{\text{bulk}} \end{array} \right\} \Rightarrow \frac{17}{13}\Delta H_f^{\text{Al}_{13}\text{Co}_4} \leq \mu_{\text{Al}} - \mu_{\text{Al}}^{\text{bulk}} \leq 0 \quad (2.17)$$

The vacuum thickness – between the periodic images of the slab – barely affects the results. The key for comparison between the surface energies of different converged surface models (having the same surface reconstruction type) is to keep constant the calculations parameters (k-points grids, cut-off energy, vacuum thickness, etc) [131].

Tab. 2.1 presents some calculated energies (in this work) that are relevant for the determination of the surface energies. The DFT-D3 functional was used for these calculations.

Table 2.1: Total and cohesive energies of Al, Co and $\text{Al}_{13}\text{Co}_4$ and formation enthalpy of $\text{Al}_{13}\text{Co}_4$.

System	Value	Litterature
$E_{\text{Al}}^{\text{bulk}}$	- 3.91 eV/at	-
$E_{\text{Co}}^{\text{bulk}}$	- 7.38 eV/at	-
$E_{\text{Al}}^{\text{alone}}$	- 0.24 eV/at	-
$E_{\text{Co}}^{\text{alone}}$	- 1.88 eV/at	-
$E_{\text{Al}_{13}\text{Co}_4}^{\text{bulk}}$	- 524.32 eV	-
$E_{\text{cohesive}}^{\text{Al}}$	- 3.67 eV/at	3.39 eV/at [132]
$E_{\text{cohesive}}^{\text{Co}}$	- 5.50 eV/at	4.39 eV/at [132]
$E_{\text{cohesive}}^{\text{Al}_{13}\text{Co}_4}$	- 76.68 eV/motif	-
$\Delta H_f^{\text{Al}_{13}\text{Co}_4}$	- 0.41(2) eV/at	- 0.41 eV/at [133]

2.2.3.2 Adsorption of molecules

Let's focus now on the reaction of interest in this work : the hydrogenation of butadiene. On the clean surface, the most stable sites for the adsorption of C_4H_x molecules ($x = 6$ for butadiene and $x = 8$ for butene) and hydrogen atoms are deduced from the calculation of

¹ $\mu_{\text{Co}} \leq \mu_{\text{Co}}^{\text{bulk}} \xrightarrow{\times 4} 4\mu_{\text{Co}} \leq 4\mu_{\text{Co}}^{\text{bulk}} \xrightarrow{+13\mu_{\text{Al}}^{\text{bulk}}} 4\mu_{\text{Co}} + 13\mu_{\text{Al}}^{\text{bulk}} \leq 4\mu_{\text{Co}}^{\text{bulk}} + 13\mu_{\text{Al}}^{\text{bulk}} \rightarrow 4\mu_{\text{Co}} + 13\mu_{\text{Al}}^{\text{bulk}} \leq 4\mu_{\text{Co}} + 13\mu_{\text{Al}} - 17\Delta H_f^{\text{Al}_{13}\text{Co}_4}$ (using Eqs. 2.14 and 2.15)
 $4\mu_{\text{Co}} + 13\mu_{\text{Al}}^{\text{bulk}} \leq 4\mu_{\text{Co}} + 13\mu_{\text{Al}} - 17\Delta H_f^{\text{Al}_{13}\text{Co}_4} \rightarrow 13\mu_{\text{Al}}^{\text{bulk}} \leq 13\mu_{\text{Al}} - 17\Delta H_f^{\text{Al}_{13}\text{Co}_4} \rightarrow 17\Delta H_f^{\text{Al}_{13}\text{Co}_4} \leq 13\mu_{\text{Al}} - 13\mu_{\text{Al}}^{\text{bulk}} \xrightarrow{\div 13} \frac{17}{13}\Delta H_f^{\text{Al}_{13}\text{Co}_4} \leq \mu_{\text{Al}} - \mu_{\text{Al}}^{\text{bulk}}$

adsorption energies (E_{ads}^X with $X = \text{C}_4\text{H}_x$ or $X = \text{H}$):

$$E_{\text{ads}}^{\text{C}_4\text{H}_x} = E_{\text{tot}} - E_{\text{slab}} - E_{\text{C}_4\text{H}_x}$$

$$E_{\text{ads}}^{\text{nH}} = E_{\text{tot}} - E_{\text{slab}} - \frac{n}{2}E_{\text{H}_2}$$

where E_{slab} , E_X and E_{tot} are respectively the energies of the clean slab, the X molecule in the gas phase, and the slab when X is adsorbed. The interaction between the adsorbed molecule and the surface can be analyzed in terms of the deformation energy costs $-E_{\text{def,mol}}^{\text{C}_4\text{H}_x}$ and $E_{\text{def,surf}}^{\text{C}_4\text{H}_x}$ – for relaxing the surface and the molecule upon forming the adsorbate complex from their respective isolated forms: $E_{\text{ads}}^{\text{C}_4\text{H}_x} = E_{\text{def,mol}}^{\text{C}_4\text{H}_x} + E_{\text{def,surf}}^{\text{C}_4\text{H}_x} + E_{\text{int}}^{\text{C}_4\text{H}_x}$, where $E_{\text{int}}^{\text{C}_4\text{H}_x}$ is the "true" interaction energy between the molecule and the surface.

Co-adsorption energies were also considered as inputs for the thermodynamic model described in the following section. They are referred either to the clean surface (Eq. 2.18) or to the hydrogenated slab (Eq. 2.19), using:

$$E_{\text{clean-surf}}^{\text{C}_4\text{H}_x+\text{nH}_2\text{H}_2} = E_{\text{tot}} - E_{\text{slab}} - E_{\text{C}_4\text{H}_x} - \frac{n}{2}E_{\text{H}_2} \quad (2.18)$$

$$E_{\text{H-surf}}^{\text{C}_4\text{H}_x+\text{nH}_2\text{H}_2} = E_{\text{tot}} - E_{\text{slab}}^{\text{nH}_2\text{H}_2} - E_{\text{C}_4\text{H}_x} \quad (2.19)$$

In the previous equations, $E_{\text{slab}}^{\text{nH}_2\text{H}_2}$ and $n = 2n_{\text{H}_2}$ are the total energy of the hydrogenated slab and the number of hydrogen atoms adsorbed, respectively.

2.2.3.3 Thermodynamic modelling

The thermodynamic feasibility of the hydrogenation is deduced from the comparison of the Gibbs free adsorption energy of butadiene and butene ($G_{\text{ads}}^{\text{C}_4\text{H}_x}$) [134]. These energies are computed as a function of the pressure ($p = p^{\text{H}_2} + p^{\text{C}_4\text{H}_x}$) and the temperature (T):

$$G_{\text{ads}}^{\text{C}_4\text{H}_x}(T, p) = E_{\text{clean-surf}}^{\text{C}_4\text{H}_x+\text{nH}_2\text{H}_2} + k_{\text{B}}T \sum_{i \in \mathcal{X}} \ln(z_{\text{trans}}^i \cdot z_{\text{rot}}^i)^{n_i} - k_{\text{B}}T \sum_{i \in \mathcal{X}} n_i \ln\left(\frac{p^i}{k_{\text{B}}T}\right) \quad (2.20)$$

with $\mathcal{X} = (\text{nH}_2\text{H}_2, \text{C}_4\text{H}_x)$. The quantities z_{trans} and z_{rot} are the translational and rotational partition functions. They are calculated with

$$z_{\text{trans}}^i = \left(\frac{4\pi m_i k_{\text{B}}T}{h^2}\right)^{\frac{3}{2}}$$

$$z_{\text{rot}}^{\text{C}_4\text{H}_x} = \frac{\pi^{1/2}}{\sigma} \left(\frac{8\pi^2 k_B T}{h^2} \right)^{3/2} \cdot I_a I_b I_c \quad \text{and} \quad z_{\text{rot}}^{\text{H}_2} = \frac{1}{\sigma} \left(\frac{8\pi^2 k_B T}{h^2} \right) \cdot I_{\text{H}_2}$$

where m_i are the masses of the molecules, k_B the Boltzmann constant and h the Planck constant. The inertia constants (I_i) are taken from Craig et al. [135] for butadiene ($I_a = 2.01 \cdot 10^{-46} \text{ kg.m}^2$, $I_b = 1.89 \cdot 10^{-45} \text{ kg.m}^2$, $I_c = 2.09 \cdot 10^{-45} \text{ kg.m}^2$), from Bouchy et al. [136] for but-1-ene ($I_a = 5.54 \cdot 10^{-46} \text{ kg.m}^2$, $I_b = 1.54 \cdot 10^{-45} \text{ kg.m}^2$, $I_c = 1.99 \cdot 10^{-45} \text{ kg.m}^2$). For hydrogen molecules, the inertia constant is equal to $I_{\text{H}_2} = 4.57 \cdot 10^{-48} \text{ kg.m}^2$. The symmetry parameter σ is equal to 2 for hydrogen and butadiene and 1 for but-1-ene.

This kind of calculations has already been performed for butadiene and butene on simple metals (such as Pd(111) and Pd(100) [25], and Pt(111) [137]) or surface alloys (Pt₂Sn(111) [137]) but has yet to be done on Al-based complex intermetallics.

2.2.4 Kinetic calculations

Thermodynamic calculations allow for the determination of the feasibility of a reaction. Further simulations are therefore necessary to provide the kinetic properties such as the selectivity and activity of a material. First we have to estimate the activation energy (or energy barrier) for each step of a chemical mechanism, then we have to model it through the means of microkinetic approaches.

2.2.4.1 Nudged elastic band method

The nudged elastic band (NEB) [138, 139] is a method for finding saddle points and minimum energy paths (MEP) between known reactants and products. The method works by optimizing a number of intermediate images along the reaction path. Each image finds the lowest energy possible while maintaining equal spacing to neighboring images. This constrained optimization is done by adding spring forces along the band between images and by projecting out the component of the force due to the potential perpendicular to the band [140].

Fig. 2.4 [141] shows an example of a 2D potential map with an initial point (the reactant), a final point (the product), and two paths between them: the initial NEB path, and the final MEP with its maximum being the saddle point (transition state). The climbing image method (CI-NEB) is a small modification to the NEB method in which the highest energy image is driven up to the saddle point.

The MEP saddle point is equivalent to the activation energy E_a of the reaction and therefore allows for the calculation of the reaction rate constant through the Arrhenius equation

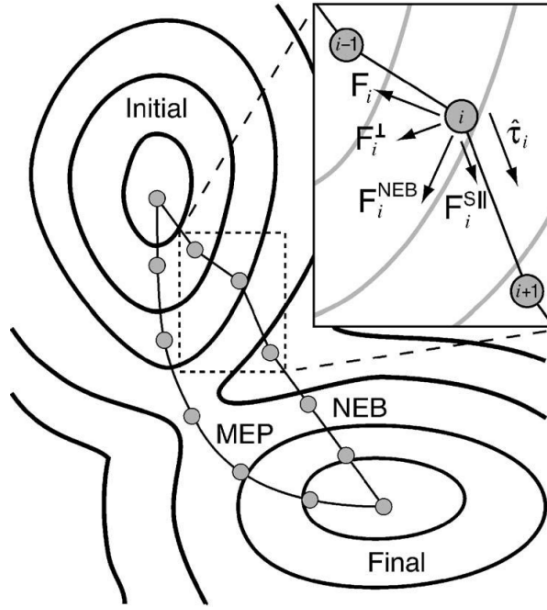


Figure 2.4: Nudged Elastic Band (NEB) and Minimum Energy Path (MEP) [141].

[142, 143] :

$$k = A e^{\frac{-E_a}{RT}}$$

where k is the rate constant (frequency of collisions resulting in a reaction), T is the absolute temperature (in K), A is the pre-exponential factor (constant for each chemical reaction), and R is the universal gas constant. The pre-exponential factor can be estimated using the transitional state theory (first introduced by Eyring, Evans and Polanyi in 1935 [144, 145]) :

$$A = \frac{k_b T}{h} \frac{Z^{TS}}{Z^{react}} \quad \text{with} \quad Z^i = z_{trans}^i \cdot z_{rot}^i \cdot z_{vib}^i$$

where k_B and h are the Boltzmann and Planck constants, respectively; Z^{TS} and Z^{react} are the partition functions of the transition state and the reactant, respectively; z_{trans} , z_{rot} , z_{vib} are the translational, rotational and vibrational partition functions. The translational and rotational partition functions are previously defined in section 2.2.3.3.

In order to determine the vibration frequencies of the transition state and the local minimum state (initial or final), vibrational calculations have to be performed using VASP. For each configuration, only the molecules were let free. In these type of calculation, each atom (total of \mathcal{N} atoms) of the molecules is displaced in each direction (x , y and z) by a small positive and negative displacement (here 0.1 \AA). The system will have a total of $3\mathcal{N} - 6$ vibration frequencies for non-linear molecules ($3\mathcal{N} - 5$ for linear molecules such as H_2). If the system is in a transition state, one of these frequencies will be an imaginary one and will thus

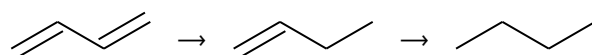
not be considered in the calculation of the partition function (total of $3N - 7$ modes). This only imaginary value implies a negative force constant applied to the system, which means that in only one direction the energy presents a maximum. Once all the frequencies ν_i are calculated, the vibrational partition function z_{vib} as a function of the temperature T can be determined using the following equation :

$$z_{\text{vib}}(T) = \prod_i \left[\frac{1}{1 - e^{-\frac{h\nu_i}{k_B T}}} \right]$$

This kind of calculations can be done for each intermediate reaction of a more complex mechanism, such as the hydrogenation of butadiene. The vibration frequencies of the different states as well as a script that calculates all the partition functions are available in the Appendices of the present manuscript.

2.2.4.2 Butadiene hydrogenation elementary steps

Let's consider the following reactions transforming buta-1,3-diene into but-1-ene (partial hydrogenation) then into butane (complete hydrogenation) :



The full mechanism can be divided into elementary steps. The following reactions will therefore occur. The star symbol represents either an unoccupied site (\star) or an adsorbed molecule (X^\star). First the molecules are adsorbed :



Then hydrogen molecules get dissociated at the surface :



Hydrogenation of the first double C=C bond occurs, and butene is produced :



After once again r_1 and r_3 , hydrogenation of the second double C=C bond occurs, and bu-

tane is finally produced :



Knowing all the elementary steps, their related energy barriers and pre-exponential factors, it is possible to build a microkinetic model that determines the relevant kinetic informations such as the turn-over frequencies (production rates) and the adsorbate coverages over time, as a function of temperature.

2.2.4.3 Microkinetic modelling

In order to determine the kinetic predictions, we introduce a microkinetic modelling that takes as input parameters the previously presented elementary steps, as well as the DFT results (activation energies and pre-exponential factors).

The different reaction rates r_i (per surface unit cell) can be expressed as follow, where k_{f_i} and k_{r_i} are the forward and reverse rate constants (determined through the means of NEB and vibrational calculations), k_i^{ads} and k_i^{des} are the adsorption and desorption rate constants, and ϑ_i the surface coverages :

$$\left\{ \begin{array}{l} r_1 = k_{\text{H}_2}^{\text{ads}} \cdot \vartheta_\star - k_{\text{H}_2}^{\text{des}} \cdot \vartheta_{\text{H}_2} \\ r_2 = k_{\text{C}_4\text{H}_6}^{\text{ads}} \cdot \vartheta_\star - k_{\text{C}_4\text{H}_6}^{\text{des}} \cdot \vartheta_{\text{C}_4\text{H}_6} \\ r_3 = k_{f_3} \cdot \vartheta_{\text{H}_2} \cdot \vartheta_\star - k_{r_3} \cdot \vartheta_{\text{H}}^2 \\ r_4 = k_{f_4} \cdot \vartheta_{\text{C}_4\text{H}_6} \cdot \vartheta_{\text{H}} - k_{r_4} \cdot \vartheta_{\text{C}_4\text{H}_7} \cdot \vartheta_\star \\ r_5 = k_{f_5} \cdot \vartheta_{\text{C}_4\text{H}_7} \cdot \vartheta_{\text{H}} - k_{r_5} \cdot \vartheta_{\text{C}_4\text{H}_8} \cdot \vartheta_\star \\ r_6 = k_{\text{C}_4\text{H}_8}^{\text{des}} \cdot \vartheta_{\text{C}_4\text{H}_8} - k_{\text{C}_4\text{H}_8}^{\text{ads}} \cdot \vartheta_\star \\ r_7 = k_{f_7} \cdot \vartheta_{\text{C}_4\text{H}_8} \cdot \vartheta_{\text{H}} - k_{r_7} \cdot \vartheta_{\text{C}_4\text{H}_9} \cdot \vartheta_\star \\ r_8 = k_{f_8} \cdot \vartheta_{\text{C}_4\text{H}_9} \cdot \vartheta_{\text{H}} - k_{r_8} \cdot \vartheta_{\text{C}_4\text{H}_{10}} \cdot \vartheta_\star \\ r_9 = k_{\text{C}_4\text{H}_{10}}^{\text{des}} \cdot \vartheta_{\text{C}_4\text{H}_{10}} - k_{\text{C}_4\text{H}_{10}}^{\text{ads}} \cdot \vartheta_\star \end{array} \right. \quad (2.21)$$

The adsorption (k_i^{ads}) and desorption (k_i^{des}) rate constants are defined as follow [146, 147]:

$$k_i^{\text{ads}} = \frac{p_i \cdot A_i}{\sqrt{2\pi \cdot m_i \cdot k_B T}} \quad \text{and} \quad k_i^{\text{des}} = \frac{k_B^2 T^3}{h^3} \frac{A_i \cdot 2\pi \cdot m_i}{\sigma_i \cdot \vartheta_{\text{rot},i}} e^{-\frac{E_{\text{des},i}}{k_B T}} \quad (2.22)$$

where p_i is the partial pressure of molecule i , A_i is the area of the surface site on which i is adsorbed, m_i is the mass of i , σ_i is the symmetry number of i , $\vartheta_{\text{rot},i}$ is the rotational

temperature of i (defined by $\vartheta_{\text{rot},i} = \frac{h^2}{8\pi^2 k_B I}$ [148]) and $E_{\text{des},i}$ is the desorption energy of i . T , h and k_B are the temperature, the Planck and the Boltzmann constants, respectively.

The variation over time of the different coverages is governed by the following ordinary differential equations (ODE) system ($\dot{\vartheta}_i = \frac{d\vartheta_i}{dt}$) using the previously defined reaction rates r_i :

$$\left\{ \begin{array}{l} \dot{\vartheta}_* = -2r_1 - r_2 - 2r_3 + r_4 + r_6 + r_7 + r_8 + r_9 \\ \dot{\vartheta}_H = 4r_3 - r_4 - r_5 - r_7 - r_8 \\ \dot{\vartheta}_{H_2} = 2(r_1 - r_3) \\ \dot{\vartheta}_{C_4H_6} = r_2 - r_4 \\ \dot{\vartheta}_{C_4H_7} = r_4 - r_5 \\ \dot{\vartheta}_{C_4H_8} = r_5 - r_6 - r_7 \\ \dot{\vartheta}_{C_4H_9} = r_7 - r_8 \\ \dot{\vartheta}_{C_4H_{10}} = r_8 - r_9 \end{array} \right. \quad (2.23)$$

This ODE system can not be solved analytically (because of coupled equations). Numerical methods have therefore to be used to integrate numerically the system over time. Based on the work of Filot [147], it was chosen to use the ODE solver of the SciPy library [149]. After reaching convergence, it is possible to retrieve the steady-state production rate of but-1-ene and butane as a function of temperature (r_6 and r_9 in 2.21). These values can then be compared to experimental measurements. The numerical implementation is presented in detail in the Appendices of the present manuscript.

A few hypotheses are made in order to build this model. First of all, no diffusion processes are considered (such as atom migrations) since it would involve a space-time coupling of differential equations (Fick's laws of diffusion). This would result in a partial differential equations (PDE) system that is more complicated to solve. A second hypothesis is made on the initial conditions : the initial coverage is assumed to be $\vartheta_* = 0$, while all other coverage is equal to 0. Moreover, this model tries to simulate a flow reactor : the pressures of the reactants do not vary over time and are constant to the initial pressure. The pressure of the products is therefore considered to be zero. This tends to simulate industrial processes.

To sum up, giving initial partial pressures of the reactants as well as a reaction temperature, energy barriers and pre-exponential factors, the model is able to provide the formation rates and coverages of the different intermediates for a steady-state reaction occurring in a flow reactor.

2.3 Surface X-ray Diffraction (SXR)

All of the surface X-ray diffraction experiments were performed at the *Surfaces and interfaces x-ray Scattering* (SixS) beamline at SOLEIL Synchrotron [150]. Before presenting the beamline and the SXR technique, let's focus on the x-ray diffraction theory. In the following, bold letters will refer to vectors.

2.3.1 Basics of x-ray diffraction

This section is a brief reminder of the basic equations of diffraction theory and is adapted from Robinson [151], and Als-Nielsen & McMorrow [152]. Let's consider an incoming plane wave (wavelength λ) – wave vector \mathbf{k}_i – and a wave scattered by an electron – wave vector \mathbf{k}_f – giving a momentum transfer $\mathbf{q} = \mathbf{k}_f - \mathbf{k}_i$. The norm of the wave vectors is $|\mathbf{k}| = |\mathbf{k}_i| = |\mathbf{k}_f| = \frac{2\pi}{\lambda}$. X-rays are chosen because their wavelength is of the same order of magnitude than the interatomic distance in a crystal lattice.

Considering A_i the amplitude of the incoming wave and A_f the amplitude of the wave scattered by an electron, one has the following relationship, where \mathbf{r} is the position of a scattering electron, e and m the charge and mass of the electron, and R the position of the observer :

$$A_f = A_i \cdot \frac{e^2}{mc^2} \frac{1}{R} e^{i\mathbf{q} \cdot \mathbf{r}} \quad (2.24)$$

When considering an atom with a particular electronic structure, one has to represent the electrons by the electron density. Then the amplitude of the scattered wave becomes :

$$A_{f,at_j^n} = A_i \cdot \frac{e^2}{mc^2} \frac{1}{R} \cdot f(\mathbf{q}) \cdot e^{i\mathbf{q} \cdot (\mathbf{R}_n + \mathbf{r}_j)} \quad \text{with } f(\mathbf{q}) = \iiint_{-\infty}^{+\infty} \rho(\mathbf{r}) \cdot e^{i\mathbf{q} \cdot \mathbf{r}} d^3\mathbf{r} \quad (2.25)$$

where $f(\mathbf{q})$ is the atomic form factor, \mathbf{R}_n the position of the n^{th} unit cell (lattice vectors \mathbf{a}_1 , $\mathbf{R}_n = n_1\mathbf{a}_1 + n_2\mathbf{a}_2 + n_3\mathbf{a}_3$), and \mathbf{r}_j the position of the j^{th} atom in this unit cell. The atomic form factor is the Fourier transform of the electron density $\rho(\mathbf{r})$ of a considered atom. If one considers a complete unit cell having N_c atoms, the scattered amplitude is then defined as follows :

$$A_{f,cell} = A_i \cdot \frac{e^2}{mc^2} \frac{1}{R} \cdot F(\mathbf{q}) \cdot e^{i\mathbf{q} \cdot \mathbf{R}_n} \quad \text{with } F(\mathbf{q}) = \sum_{j=1}^{N_c} f_j(\mathbf{q}) \cdot e^{i\mathbf{q} \cdot \mathbf{r}_j} \quad (2.26)$$

where $F(\mathbf{q})$ is the structure factor, *i.e.* the Fourier transform of the electron density of one unit cell.

Finally, when all the cells are summed up to build a whole crystal, the scattered ampli-

tude is defined by the following equation (under the kinematical approximation) :

$$A_{f,\text{crys}} = A_i \cdot \frac{e^2}{mc^2} \frac{1}{R} \cdot F(\mathbf{q}) \sum_{n_1=-\infty}^{+\infty} e^{in_1 \mathbf{q} \cdot \mathbf{a}_1} \sum_{n_2=-\infty}^{+\infty} e^{in_2 \mathbf{q} \cdot \mathbf{a}_2} \sum_{n_3=-\infty}^{+\infty} e^{in_3 \mathbf{q} \cdot \mathbf{a}_3} \quad (2.27)$$

It is then possible to define the reciprocal space coordinates (h, k, l) and the basis vectors \mathbf{b}_i of the crystal reciprocal lattice as follows :

$$\begin{cases} \mathbf{q} \cdot \mathbf{a}_1 = 2\pi \cdot h \\ \mathbf{q} \cdot \mathbf{a}_2 = 2\pi \cdot k \\ \mathbf{q} \cdot \mathbf{a}_3 = 2\pi \cdot l \end{cases} \quad \text{and} \quad \mathbf{q} = h\mathbf{b}_1 + k\mathbf{b}_2 + l\mathbf{b}_3 \quad \begin{cases} \mathbf{b}_1 = 2\pi \frac{\mathbf{a}_2 \times \mathbf{a}_3}{\mathbf{a}_1 \cdot (\mathbf{a}_2 \times \mathbf{a}_3)} \\ \mathbf{b}_2 = 2\pi \frac{\mathbf{a}_3 \times \mathbf{a}_1}{\mathbf{a}_1 \cdot (\mathbf{a}_2 \times \mathbf{a}_3)} \\ \mathbf{b}_3 = 2\pi \frac{\mathbf{a}_1 \times \mathbf{a}_2}{\mathbf{a}_1 \cdot (\mathbf{a}_2 \times \mathbf{a}_3)} \end{cases} \quad (2.28)$$

Eq. 2.27 can then be rewritten using the (h, k, l) coordinates of the reciprocal space, where the structure factor $F(\mathbf{q}) = F(h\mathbf{b}_1 + k\mathbf{b}_2 + l\mathbf{b}_3) = F_{hkl}$:

$$A_{f,\text{crys}} = A_i \cdot \frac{e^2}{mc^2} \frac{1}{R} \cdot F_{hkl} \sum_{n_1=-\infty}^{+\infty} e^{in_1 \cdot 2\pi h} \sum_{n_2=-\infty}^{+\infty} e^{in_2 \cdot 2\pi k} \sum_{n_3=-\infty}^{+\infty} e^{in_3 \cdot 2\pi l} \quad (2.29)$$

The intensity I_{hkl} of the scattered wave is then defined as follows using the Dirac function (δ) and the Dirac comb definition $\left(\sum_{n_1=-\infty}^{+\infty} e^{in_1 \cdot 2\pi h} = \sum_{n_1=-\infty}^{+\infty} \delta_{n_1}(h) \right)$:

$$I_{hkl} = |A_{f,\text{crys}}|^2 = \left| A_i \cdot \frac{e^2}{mc^2} \frac{1}{R} \cdot F_{hkl} \right|^2 \sum_{n_1=-\infty}^{+\infty} \delta_{n_1}(h) \sum_{n_2=-\infty}^{+\infty} \delta_{n_2}(k) \sum_{n_3=-\infty}^{+\infty} \delta_{n_3}(l) \quad (2.30)$$

For integer values of (h, k, l) – *i.e.* \mathbf{q} satisfying the Laue conditions – the intensity of the scattered wave reaches a maximum : this is the definition of the Bragg conditions.

2.3.2 Crystal truncation rods

The previous detailed mathematical development concerns the diffraction from a 3D crystal, where the scattered intensity is discrete and localized at the Bragg peaks in the reciprocal space. It is true for 3D infinite crystals. If one studies a surface, the crystal is considered to be infinite over two directions only. It is therefore referred to as a truncated crystal, and this has consequences on the scattered intensities [151]. The crystal can be seen as the product of an infinite crystal and a step function as presented in Fig. 2.5 [153] : one does not have Bragg peaks anymore but a convolution of an ideal diffraction pattern (Bragg) and

the Fourier transform of a step function. From a mathematical point of view, it consists in considering a semi-infinite sum along the third axis:

$$A_{f,\text{crys}} = A_i \cdot \frac{e^2}{mc^2} \frac{1}{R} \cdot F_{hkl} \sum_{n_1=-\infty}^{+\infty} e^{in_1 \cdot 2\pi h} \sum_{n_2=-\infty}^{+\infty} e^{in_2 \cdot 2\pi k} \sum_{n_3=-\infty}^0 e^{in_3 \cdot 2\pi l} e^{\eta n_3} \quad (2.31)$$

where η represents the attenuation due to the x-ray absorption of the material (typically of the order of magnitude of 10^{-6} [152]). Away from Bragg peaks – therefore far from integer values of l – it is possible to neglect this damping term (which is only a minor correction) and the third Fourier series can be simplified as follows :

$$\left| \sum_{n_3=-\infty}^0 e^{in_3 \cdot 2\pi l} e^{\eta n_3} \right|^2 = \left| \frac{1}{1 - e^{-(2i\pi l + \eta)}} \right|^2 \underset{\eta \rightarrow 0}{\approx} \frac{1}{4 \sin^2 \pi l} \quad \text{for } l \in \mathbb{R} \setminus \mathbb{Z}$$

The following equation (Eq. 2.32) is then obtained, where the intensities are not discrete anymore, but rather continuous and modulated in the direction normal to the surface. This feature is called a crystal truncation rod (CTR).

$$I_{\text{CTR}} = \left| A_i \cdot \frac{e^2}{mc^2} \frac{1}{R} \cdot F_{hkl} \right|^2 \cdot \left[\sum_{n_1=-\infty}^{+\infty} \delta_{n_1}(h) \sum_{n_2=-\infty}^{+\infty} \delta_{n_2}(k) \right] \cdot \frac{1}{4 \sin^2 \pi l} \quad \text{for } l \in \mathbb{R} \setminus \mathbb{Z} \quad (2.32)$$

If the surface exhibits a reconstruction, additional rods are measured in the direction normal to the surface for non-integer values of h and/or k and are called super-structure rods (SSR) as shown in Fig. 2.5 [153].

2.3.3 Reciprocal space exploration

The measurement of the reciprocal space can provide different information regarding the structure of the material. In-plane maps of the reciprocal space brings information regarding the atomic in-plane arrangement of the crystal (symmetry, reconstruction, etc). Out-of-plane measurements can be crucial in the analysis of potential facets that grow at the surface of a sample. Intensities along CTRs and SSRs can be collected in order to refine the crystal structure of the surface as well as to determine its roughness. Under catalytic conditions, CTRs and SSRs measurements could also bring information regarding the adsorption properties of the surface and its structural evolution during the reaction.

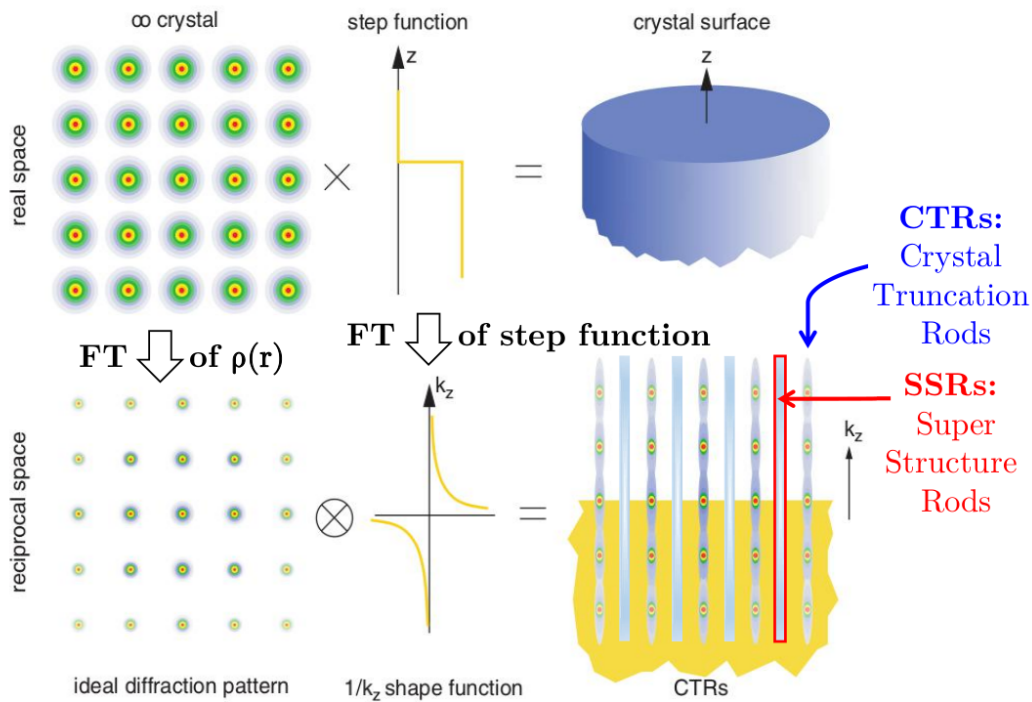


Figure 2.5: Truncation of a crystal and consequence on the diffraction pattern [153].

2.3.4 Data collection and analysis

During a SXRD experiment, different strategies can be undertaken. The conventional strategy is to align the sample surface and index different Bragg peaks in order to retrieve the sample orientation matrix. Then, it is possible to 'navigate' in the reciprocal space of the sample, to collect particular regions such as CTRs or larger portions.

Thanks to a 2D x-ray detector, it is possible to increase the data collection and therefore to scan faster the reciprocal space : this is the strategy that was chosen many times during this work. In this method, a very large volume of the reciprocal can be measured faster because no orientation matrix is determined. Afterwards, it is easy to calculate the orientation matrix and to extract all the relevant data of the reciprocal space (CTRs, SSRs, diffuse scattering, etc).

On a more technical side, the collected intensities are processed using the *BINoculars* software [154] (data reduction). The measurements are then integrated using the program *fitaid* from *BINoculars* package in order to retrieve the structure factors. Finally *AVE* and *ROD* softwares (from the *ANAROD* suite [155, 156, 157]) are used to analyze the processed data generated by *BINoculars*. Structure factors of CTRs and SSRs were simulated from DFT-relaxed surface models. The adequacy of the simulated CTRs and SSRs intensities

with the experimental data is quantified by the χ^2 factor or the R-factor:

$$\chi^2 = \frac{1}{N_{\text{data}} - N_p} \sum \left| \frac{F_{\text{exp}} - F_{\text{th}}}{\sigma} \right|^2 \quad \text{R-factor} = \frac{\sum |F_{\text{exp}} - F_{\text{th}}|}{\sum F_{\text{exp}}}$$

where N_{data} is the number of data points, F_{exp} (respectively F_{th}) the experimental structure factors (respectively simulated structure factors), N_p the number of refined parameters and σ the estimated error bar.

2.3.5 Experimental end-stations at SixS beamline

SOLEIL Synchrotron stands for *Source Optimisée d'Énergie Intermédiaire du LURE (Laboratoire pour l'Utilisation du Rayonnement Électromagnétique)* and is a third generation synchrotron source facility (energy of 2.75 GeV). The *Surfaces interfaces x-ray Scattering* beamline is one of SOLEIL's diffraction beamlines specialized in surfaces and interfaces studies using x-rays. A synchrotron radiation is produced thanks to a U20 undulator before SixS' front-end.

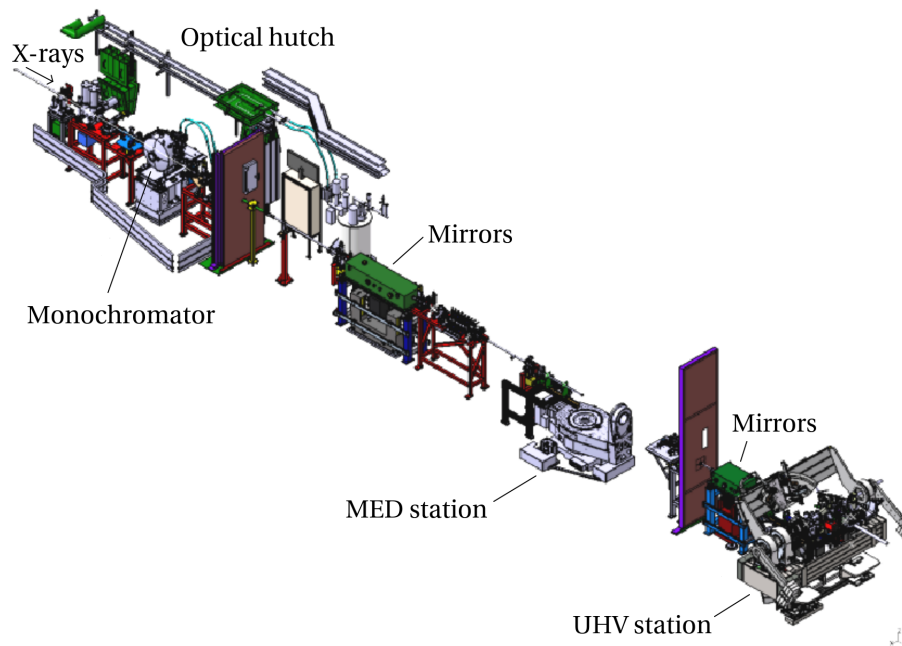


Figure 2.6: Schematic view of SixS : the optical hutch with the monochromator, the first hutch with the first focusing mirrors, the filters and the MED station, and the second hutch with a mirror and the UHV station

SixS is divided into three hatches : one optical hatch and two experimental hatches as presented in Fig. 2.6. In the optical hatch one can find the monochromator that pro-

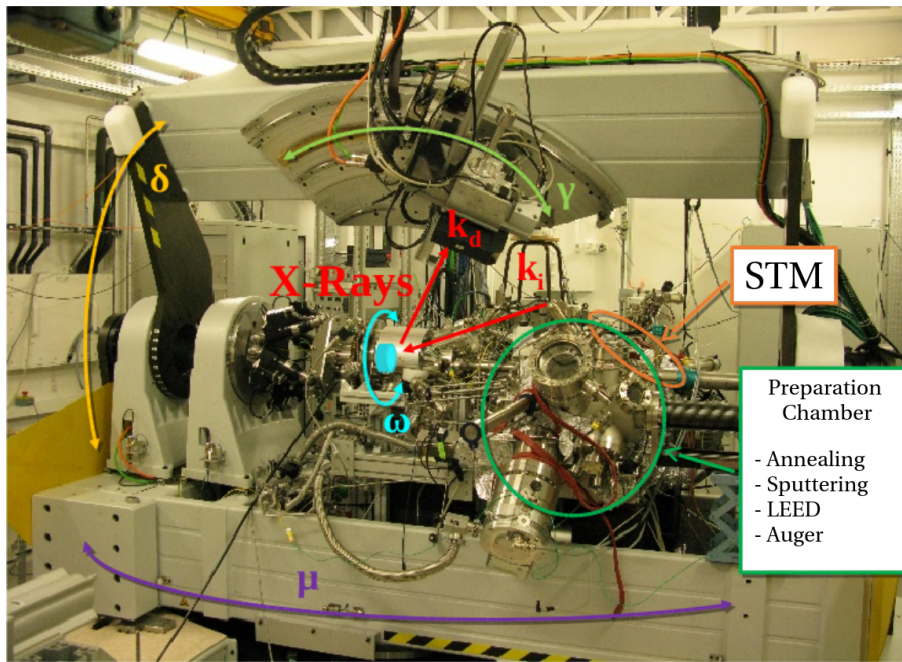


Figure 2.7: Photograph of SixS' UHV station : diffraction, carrousel, STM, and preparation chambers [158].

vides the desired photon energy (18.41 keV in our case). In the first experimental hutch, one can find the focusing mirrors as well as the automatic attenuators that attenuate the direct beam (if needed). The Multi-Environment Diffractometer station (MED) is also present in this first hutch. The last hutch also has a focusing mirror as well as the Ultra-High Vacuum station (UHV).

The UHV station is a Z-axis diffractometer on which are mounted three coupled UHV chambers : a diffraction chamber, a carrousel (connected to a scanning tunneling microscope), and a preparation chamber. Fig. 2.7 presents a view of the UHV setup (diffractometer's angles, equipments). The preparation chamber has everything a surface scientist needs for surface preparation : ion sputtering, evaporators, a low-energy electron diffractometer and an Auger electron spectrometer. During SXRD measurements, the sample is placed in the diffraction chamber (the sample is drawn in cyan in Fig. 2.7). Thanks to a hexapod, the sample is aligned with the incoming beam (\mathbf{k}_i). Four angles allow for the control of the reciprocal space scanning : ω represents the azimuthal rotation axis of the sample, μ represents the incidence angle of the x-ray beam; δ and γ are the in-plane and out-of-plane angles on which is mounted the x-ray detector. A $(\omega, \delta, \gamma, \mu)$ position in real space corresponds to a particular (Q_x, Q_y, Q_z) position in the reciprocal space.

Finally, a XPAD S140 detector is used to collect the scattered x-rays (\mathbf{k}_d) and is coupled to the automatic attenuators present in the first hutch [159]. This setup protects the detector

when the reciprocal space is scanned : when approaching intense Bragg peaks, the detector sends a signal to the automatic attenuators to attenuate the direct beam thus decreasing the measured intensity and maintain the detector in its linear range.

2.4 Conventional surface investigation techniques

Apart from surface x-ray diffraction, other conventional experimental and surface investigation techniques were used in this work. First the Czochralski method is used to grow single crystals of Al_5Co_2 , $\text{Al}_{13}\text{Co}_4$ and $\text{Al}_{13}\text{Fe}_4$. This technique is developed in Chapter 1. Our crystals were grown at *Institut Jean Lamour* (IJL) in Nancy and at *Ludwig-Maximilians-Universität* (LMU) in München, Germany.

2.4.1 Surface preparation

The newly grown single crystal is oriented using the back-scattered X-ray Laue technique, polished down to $0.25\ \mu\text{m}$ using a diamond paste, and mounted on a Ta plate. The sample surface is then prepared by cycles of Ar^+ sputtering (usually for 30 min at an energy of 1.5 keV, using an ion gun) followed by annealing (for 30 min to 1 h, between 873 K and 1073 K, depending on the crystal and on the surface orientation) in UHV. This kind of surface preparation was done at both IJL before STM analysis and SixS before SXRD experiments.

2.4.2 Auger electron spectroscopy (AES)

Auger electron spectroscopy is a technique used to determine the surface composition of a sample [160]. In this work, AES is performed to ascertain the cleanliness of a crystal under ultra-high vacuum conditions. All of the materials that will be studied in this work are Al-based compounds and are therefore quite sensitive to oxygen as well as carbon contaminations. This technique is used only qualitatively in the present work.

AES was performed at SOLEIL at SixS beamline during every beamtime to make sure the surface preparation was correct and the surface ready for diffraction measurements.

2.4.3 Low energy electron diffraction (LEED)

Low energy electron diffraction allows for the determination of the periodicity and symmetries of surface structure of crystalline materials [161]. The incoming beam of electron (monochromatic with an energy ranging from 20 to 200 eV) is diffracted by the very first atomic layers of the surface. In this work it was used to check the sample periodicity, the

presence of twins, the possible reconstructions, the crystallographic quality of the surfaces after sputtering and annealing process, the presence of facets.

LEED measurements were performed at both IJL before STM analysis and SixS before SXRD experiments to assess the quality of the surface structure.

2.4.4 Scanning tunneling microscopy (STM)

This technique is based on the concept of quantum tunneling effect. Scanning tunneling microscopy is performed to analyze the surface structure at an atomic scale. The local electron density of state is probed using a tip that ideally made of one atom. A voltage bias is applied between the surface and the tip. A constant current is maintained between the surface and the tip and is called the tunnelling current. This is a non-destructive method since no contact is done with the surface. An exchange of electrons is done with the surface thanks to the tunnelling effect. It is a technique that allows to measure not only the topography of surfaces, but their electronic structure as well.

STM measurements were done primarily at IJL using the ASURE setup, but also at SOLEIL at the SixS beamline.

2.4.5 Atomic force microscopy (AFM)

Atomic Force Microscopy consists in probing a surface using a cantilever having a sharp tip at its end [162]. When the tip approaches the surface, forces between the tip and the sample lead to a deflection of the cantilever. AFM analyses were achieved at room conditions (pressure and temperature) with a Nano-I AFM from Pacific Nanotechnology Inc. used in close contact mode with a Si tip. In contact mode, the tip is "dragged" across the surface of the sample and the contours of the surface are measured either using the deflection of the cantilever directly or, more commonly, using the feedback signal required to keep the cantilever at a constant position.

AFM measurements were performed at SOLEIL Synchrotron at the *Laboratoire de Surfaces*.

2.4.6 Catalysis experiments

The butadiene hydrogenation reaction was performed in a dedicated static catalytic reactor coupled with UHV preparation and analysis chambers (LEED and AES) [107]. The sample was heated from the back by an infrared laser beam. The surface temperature was controlled using an infrared pyrometer (surface emissivity set to 0.3). A mixture of

ultrapure gases (5 mbar hydrogen, 0.5 mbar butadiene, and 0.5 mbar Ar for internal calibration) was prepared in a separate chamber before injecting into the reactor. The reaction kinetics is followed by mass spectrometry and gas chromatography. This kind of catalysis experiments was performed at IRCELyon (Institut de Recherche sur la Catalyse et l'Environnement de Lyon).

Catalysis measurements were also done during surface x-ray diffraction experiments thanks to a UHV/high-pressure flow reactor especially made for grazing incidence small angle x-ray scattering studies. The XCAT setup [163] was used at SixS beamline on the MED station.

Chapter 3

From the surface structure to the catalytic properties of $\text{Al}_5\text{Co}_2(2\bar{1}0)$

Contents

3.1 Introduction	66
3.2 Preliminary experimental results	66
3.2.1 Sample preparation	66
3.2.2 STM	66
3.2.3 Catalytic measurements	68
3.3 DFT results – Surface structure	69
3.3.1 Surface models	69
3.3.2 Surface energy calculations	70
3.3.3 STM image simulations	71
3.4 SXRD analysis	72
3.4.1 In-plane measurements	72
3.4.2 CTRs and SSRs extraction	72
3.5 Adsorption calculations	75
3.5.1 Hydrogen adsorption	76
3.5.2 Butadiene adsorption	76
3.5.3 But-1-ene adsorption	78
3.5.4 Coadsorption of hydrogen and butadiene/but-1-ene	79
3.5.5 Competition between chemisorption and physisorption	80
3.5.6 Influence of Co surface density	82
3.6 Conclusion	84

3.1 Introduction

In this chapter, the catalytic performances of $\text{Al}_5\text{Co}_2(2\bar{1}0)$ for butadiene hydrogenation is investigated. The surface structure and chemical composition, especially the surface Co atom density, are determined in details by a combination of experimental measurements (SXR, STM) and *ab initio* surface calculations. A simple thermodynamic model, used to account for experimental reaction conditions, further addresses the influence of the surface structure on the adsorption properties towards butadiene and butene molecules, as well as on the thermodynamic feasibility of the reaction.

3.2 Preliminary experimental results

3.2.1 Sample preparation

The experiments were performed using Al_5Co_2 single crystal cut parallel to the $(2\bar{1}0)$ planes. The sample was extracted from an ingot, grown from an Al-rich solution by the Czochralski method (see 1.3.7 in Chapter 1 for more details concerning the growth process) and oriented using back-scattered x-ray Laue technique, polished down to $0.25\ \mu\text{m}$ using a diamond paste and mounted on a Ta plate.

The sample was prepared by cycles of 30 min $1.5\ \text{keV}\ \text{Ar}^+$ sputtering followed by 1 hour annealing at $973\ \text{K}$ in UHV. A (2×1) surface reconstruction was observed by LEED (Fig. 3.1). Neither oxygen, nor carbon surface contaminations were observed by AES (Fig. 3.2).

3.2.2 STM

STM analysis [14] shows the presence of terraces (Fig. 3.3a) separated by a unique step height of $3.8 \pm 0.2\ \text{\AA}$ corresponding to half the cell parameter in this direction ($\frac{a}{2}$) meaning that only a F or P termination is present at the surface (see Chapter 1 for more details concerning the bulk structure, Fig.1.8). Higher resolution (Fig. 3.3b) images show the presence of $26.3\ \text{\AA}$ wide rows along the $[001]$ direction with a $7.4\ \text{\AA}$ periodicity (corresponding to the c lattice parameter). This is consistent with a (2×1) reconstruction that was previously observed by LEED measurements.

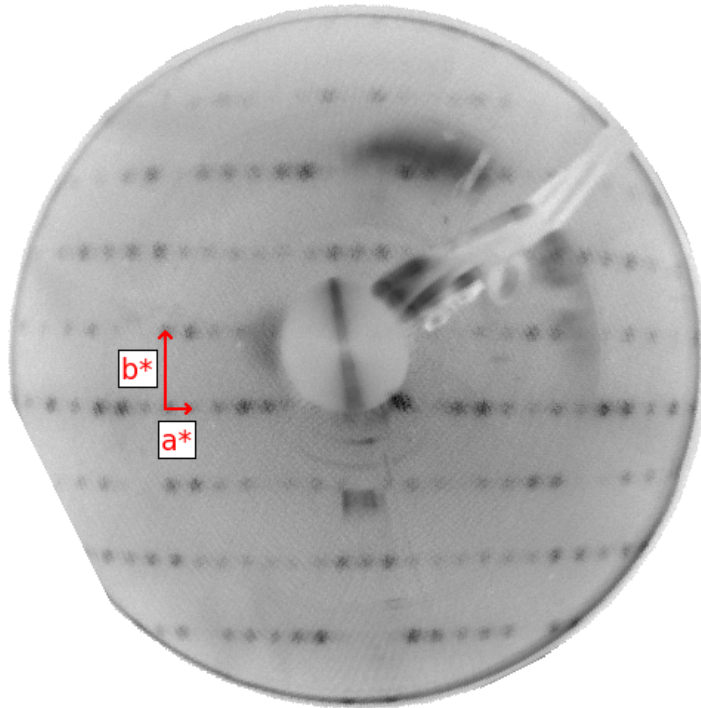


Figure 3.1: LEED pattern measured in the SixS UHV preparation chamber at 80 eV showing the (2×1) surface reconstruction ($\mathbf{a}^* = [120]$ and $\mathbf{b}^* = [001]$, in the surface lattice reference). The periodicity is doubled in the $[120]$ direction. Cell parameters are $a = 26.78 \text{ \AA}$ and $b = 7.63 \text{ \AA}$.

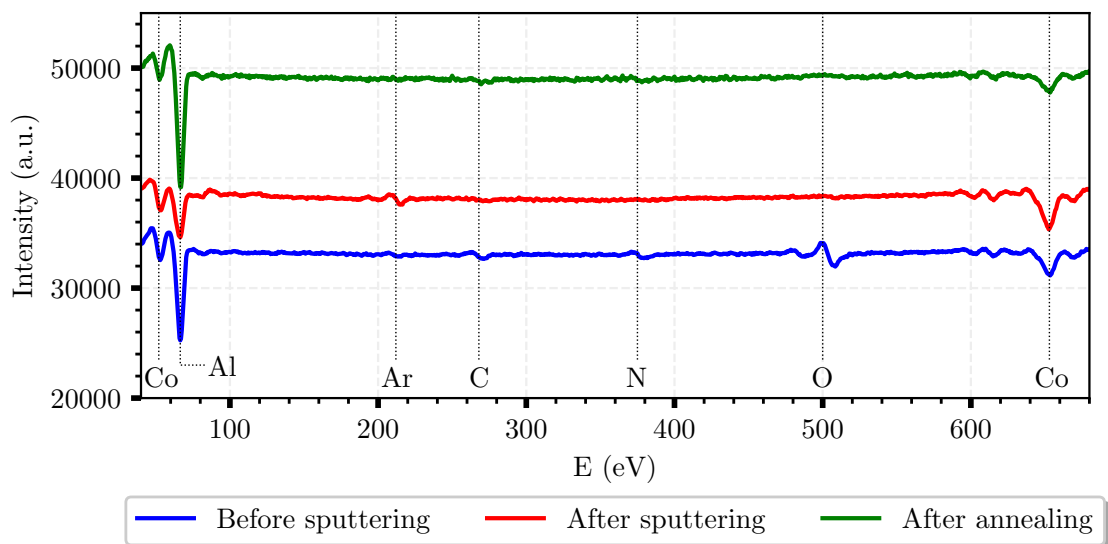


Figure 3.2: Auger Electron Spectra before and after Ar^+ sputtering (for 30 min at 1.5 keV) measured in the SixS UHV preparation chamber.

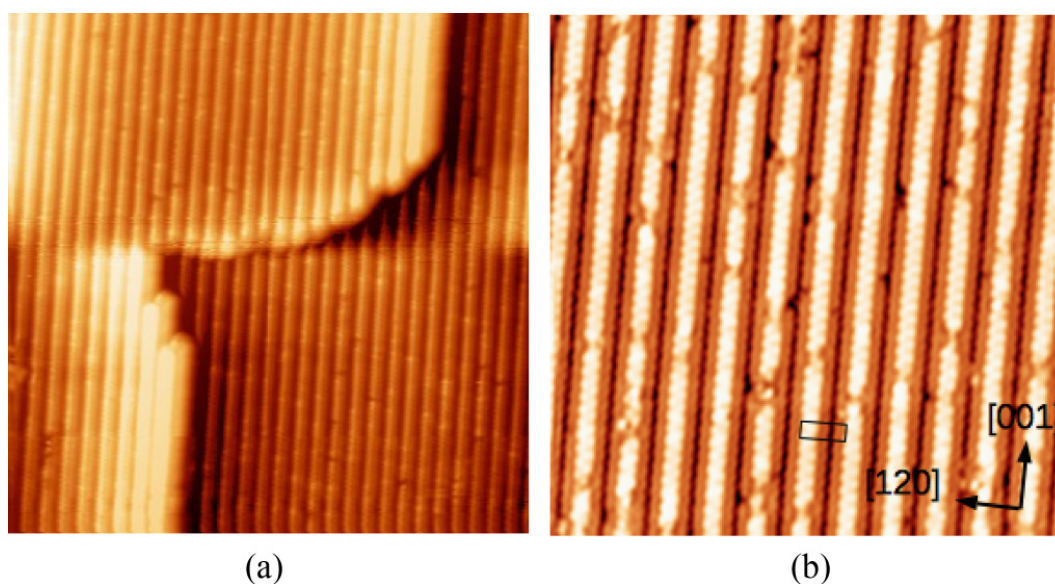


Figure 3.3: (a) $75 \times 75 \text{ nm}^2$ STM image of the $\text{Al}_5\text{Co}_2(2\bar{1}0)$ surface prepared at 973 K ($V_b = -2$ V and $I_t = 0.1$ nA) and (b) $20 \times 20 \text{ nm}^2$, $V_b = -1$ V and $I_t = 0.2$ nA). The unit cell of the (2×1) reconstruction is also shown. Images from [14].

3.2.3 Catalytic measurements

The reaction was performed in a dedicated static catalytic reactor coupled with UHV preparation and analysis chambers (LEED and AES). The sample was heated from the back by an infrared laser beam. The surface temperature was controlled using an infrared pyrometer (surface emissivity set to 0.3). A mixture of ultra pure gases (5 mbar hydrogen, 0.5 mbar butadiene and 0.5 mbar Ar for internal calibration) was prepared in a separate chamber before injection into the reactor. The reactants and products were monitored by mass spectroscopy and gas chromatography.

The catalytic performances of $\text{Al}_5\text{Co}_2(2\bar{1}0)$ for butadiene hydrogenation were evaluated at 383 K, with initial hydrogen and butadiene partial pressures of 5 and 0.5 mbar, respectively. Fig. 3.4 a displays three successive reaction runs. On the clean annealed surface (run 1), butadiene is fully converted after 30 min, with 100% selectivity to butenes throughout the conversion. Butane is formed – at a slower rate – only after complete conversion of butadiene into butenes. The butadiene hydrogenation activity of $\text{Al}_5\text{Co}_2(2\bar{1}0)$ is similar to that of $\text{Al}_{13}\text{Co}_4(100)$ [8].

The model catalyst gradually deactivated from one run to the next. This is due to surface contamination with oxygen-containing impurities (mostly water) inherently present in gases, as previously shown by post-reaction Auger electron spectroscopy for other transition metal aluminides [9, 8].

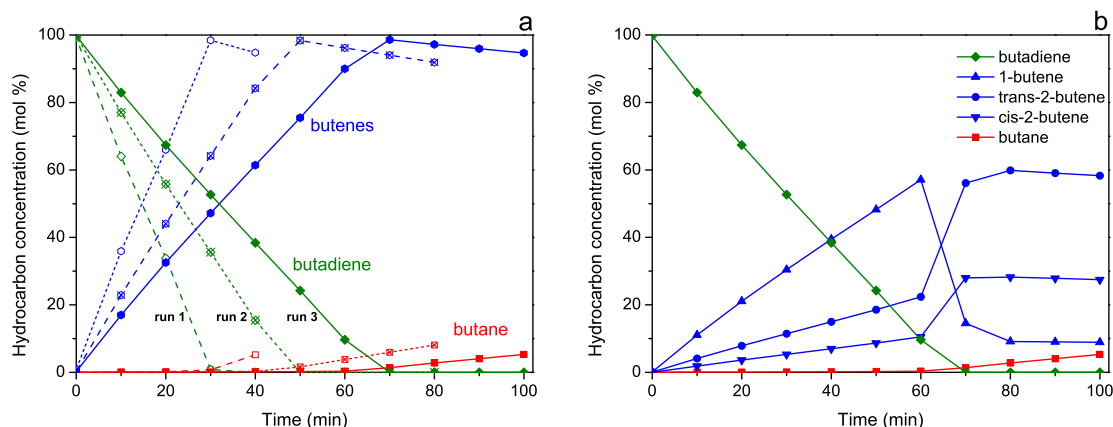


Figure 3.4: (a) Catalytic performances of $\text{Al}_5\text{Co}_2(2\bar{1}0)$ at $T = 383$ K, with initial pressures $p_{\text{H}_2} = 5$ mbar and $p_{\text{C}_4\text{H}_6} = 0.5$ mbar (first, second and third runs are respectively drawn in dashed, dotted and full lines). (b) Detailed catalytic performances of $\text{Al}_5\text{Co}_2(2\bar{1}0)$ for the third run showing the concentrations of the different butene isomers.

In Fig. 3.4b, the butenes distribution is shown in the case of the third reaction run. From $t = 10$ min to $t = 60$ min, it is about 65:24:11% for but-1-ene:trans-2-butene:cis-2-butene, which is similar to the results for $\text{Al}_{13}\text{Co}_4$ surfaces [8]. After complete conversion of butadiene, the butenes inter-convert through isomerization till thermodynamic equilibrium, with a final distribution of 9:62:29%.

3.3 DFT results – Surface structure

3.3.1 Surface models

According to a previous study [14], the $(2\bar{1}0)$ surface structure results from a bulk truncation and selection of the P-type (puckered) planes termination, with every four bipentagonal motifs missing, thus forming a (2×1) reconstruction. It means that the surface structure consists of nano-structured bands of 1.2 nm wide separated by gaps of 0.7 nm wide. Several surface models were built, based on the knowledge gained by the experimental observations. Two of them fit equally well (for two different ranges of the allowed chemical potential) both STM and LEED measurements, and present low surface energies. However, the detailed surface composition, especially the presence/absence of these topmost surface Co atoms, could not be deduced from surface energy calculations, even combined with the comparison of simulated and experimental STM images.

Fig. 3.5 shows the four considered surface models, presenting different Co surface com-

positions. They include the P_B and P_{B-4Co} models investigated previously, with four and zero protruding Co atoms per surface cell, respectively, as well as two additional models: $P_{B-2Co,1}$ and $P_{B-2Co,2}$, both containing 2 protruding Co atoms per surface cell, and differing by the position of the surface Co vacancy.

These models conform to the planar group of the surface, whose symmetry elements include a two-fold symmetry axis at the center of the surface unit cell perpendicular to the surface, and two mirror planes (**a**, **c**), positioned at $y = 0.25$ and $y = 0.75$. These symmetries highlight that the four protruding Co atoms at the surface are not equivalent, but only two-by-two equivalent.

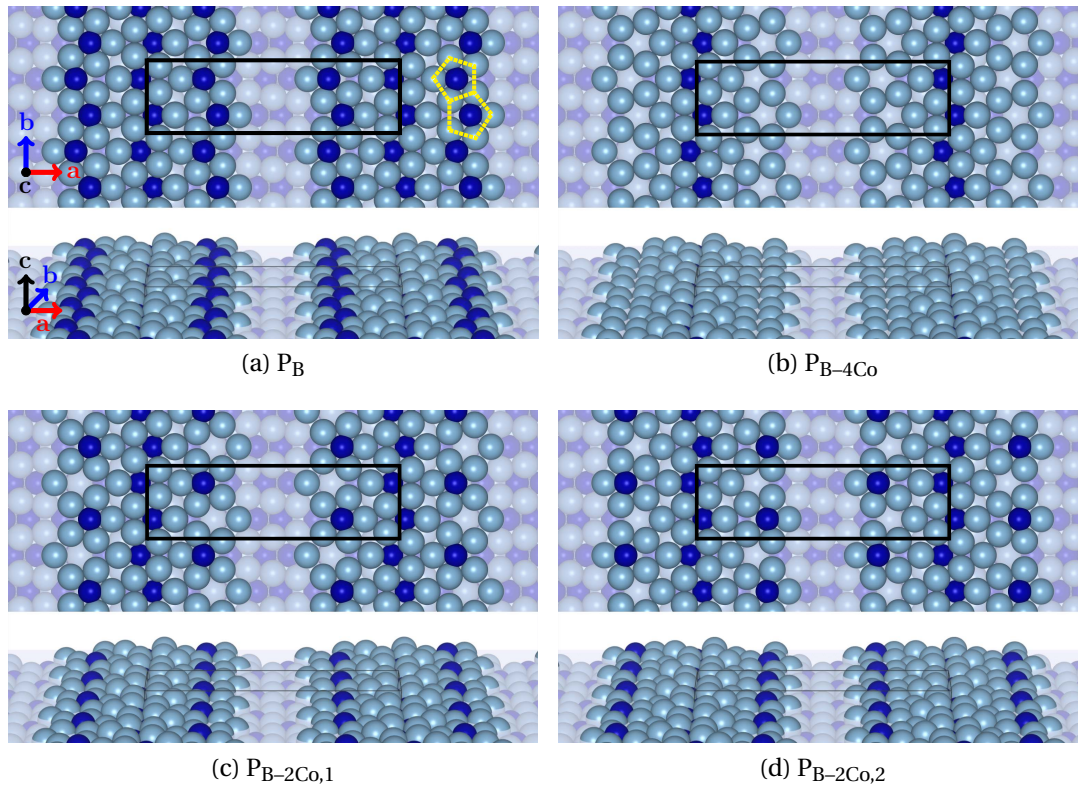


Figure 3.5: Top and perspective views of the surface models considered in this study. Al atoms and Co atoms are respectively drawn in light blue and dark blue. The surface cells are highlighted with black lines (top views). The Al bipentagonal motif is highlighted in yellow for model P_B .

3.3.2 Surface energy calculations

The surface energies of the four surface models described previously are shown in Fig. 3.6. The P_B surface model is the most stable in the Co-rich limit ($\mu_{Al} - \mu_{Al}^{bulk} \leq -0.5$ eV/at), while it

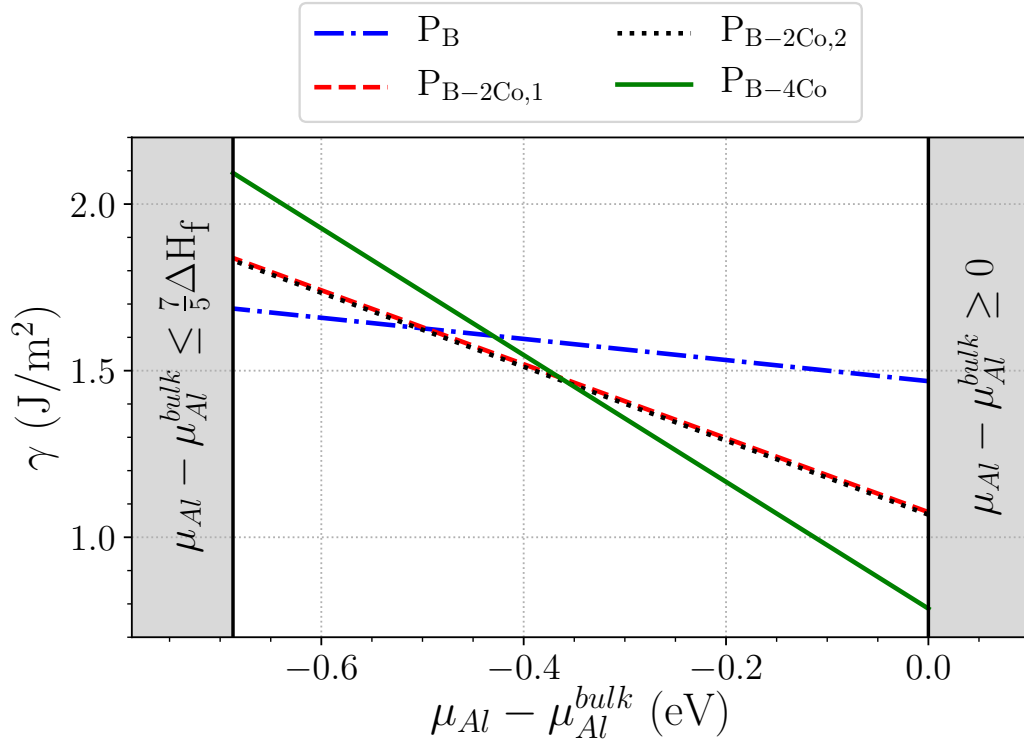


Figure 3.6: Calculated surface energies of $\text{Al}_5\text{Co}_2(2\bar{1}0)$ as a function of the Al chemical potential.

is the $\text{P}_{\text{B}-4\text{Co}}$ one in the Al-rich limit ($-0.36 \text{ eV/at} \leq \mu_{\text{Al}} - \mu_{\text{Al}}^{\text{bulk}}$), with a particularly low surface energy (0.79 J/m^2 at $\mu_{\text{Al}} = \mu_{\text{Al}}^{\text{bulk}}$) similar to the one of Al(111) (0.80 J/m^2 [164]). The two additional models ($\text{P}_{\text{B}-2\text{Co},1}$ and $\text{P}_{\text{B}-2\text{Co},2}$) present similar surface energies. They are the most stable ones for intermediate values of the chemical potentials, no significant energy difference being calculated between these two models. Although these results assess the stability of the considered surface models, they do not provide any accurate information about the surface composition of the sample used for the catalytic measurements, since the chemical potentials depend on the exact composition of the single crystalline ingot used for the experiments (amount of vacancies, anti-sites, etc) [165, 166].

3.3.3 STM image simulations

The comparison of the experimental and STM images simulated using the four considered models is shown in Fig. 3.7. The simulations are in good agreement with the experimental data. Nevertheless, they are very similar for all models and therefore do not allow for any discrimination between them.

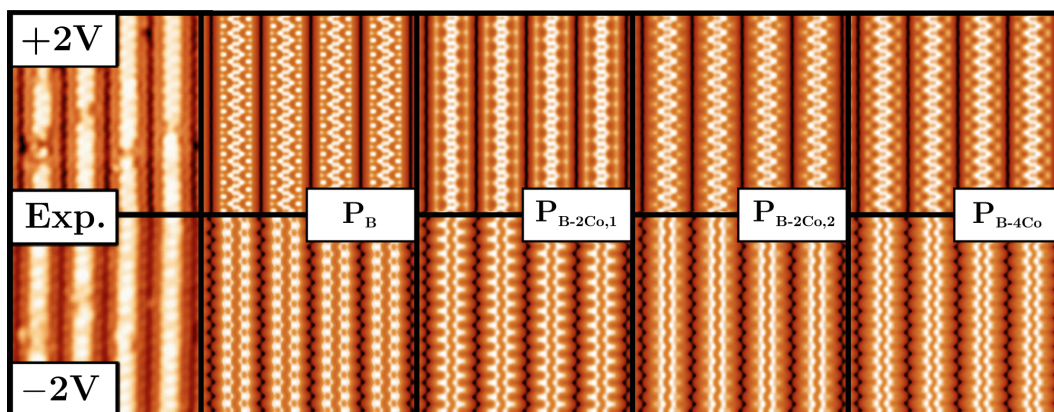


Figure 3.7: Experimental STM images (from Meier et al.), P_B , $P_{B-2Co,1}$, $P_{B-2Co,2}$ and P_{B-4Co} simulated STM images ($V_b = \pm 2V$).

3.4 SXR analysis

3.4.1 In-plane measurements

The surface structure and composition were further investigated using SXR. Fig. 3.8 shows the in-plane measurement of the reciprocal space highlighting (circled in blue) a pseudo 10-fold symmetry, i.e. nonequivalent in-plane reflections forming an irregular decagon. This is in agreement with the surface bi-pentagonal atomic arrangements (see Fig. 3.5a) which induce a modulation of the in-plane structure factors, thus allowing this particular symmetry to emerge on a rectangular lattice. The in-plane reciprocal space measurements also confirm the (2×1) surface reconstruction. Measured lattice parameters ($a_{\text{exp}} = 26.7(8) \text{ \AA}$ and $b_{\text{exp}} = 7.6(3) \text{ \AA}$) are in good agreement with the literature [12] ($a_{\text{lit}} = 26.58 \text{ \AA}$ and $b_{\text{lit}} = 7.61 \text{ \AA}$). Out-of-plane measurements were also done and 49 diffraction rods were collected. The complete dataset consists of 12 non-equivalent Crystal Truncation Rods (CTRs) and 10 non-equivalent Super Structure Rods (SSRs). Each rod was measured for $0 \leq L \leq 5$. Another set of diffraction spots is also observed (highlighted in green in Fig. 3.8). The measured lattice parameters ($b_{\text{exp}} = 2.87(1) \text{ \AA}$ and $a_{\text{exp}} = c_{\text{exp}} = 4.06 \text{ \AA}$) are consistent with the one of the B2-AlCo (110) surface ($a_{\text{lit}} = 2.862 \text{ \AA}$ [167]). This might be due to the presence of B2-AlCo precipitates – either in the bulk material and/or at the surface.

3.4.2 CTRs and SSRs extraction

The simulations of the CTRs and SSRs were performed based on the four considered surface models, whose structures were relaxed using DFT calculations (Fig. 3.9). The only

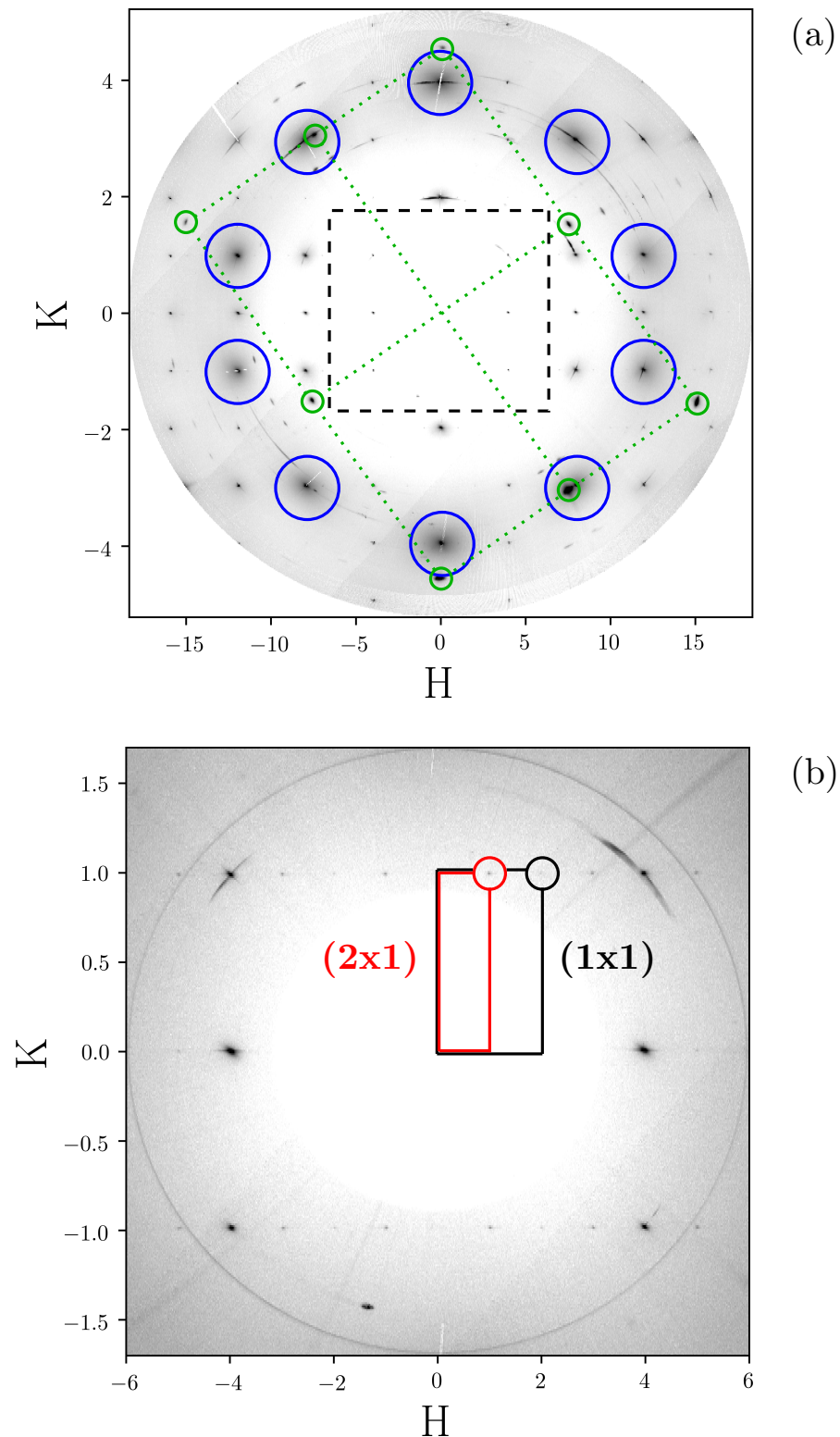


Figure 3.8: In-plane reciprocal space maps of $\text{Al}_5\text{Co}_2(2\bar{1}0)$: (a) full map highlighting the pseudo 10-fold symmetry in blue circles and the B2-AlCo (110) diffraction spots in green circles, (b) inner map (dashed region in (a)) showing the (2×1) surface reconstruction cell.

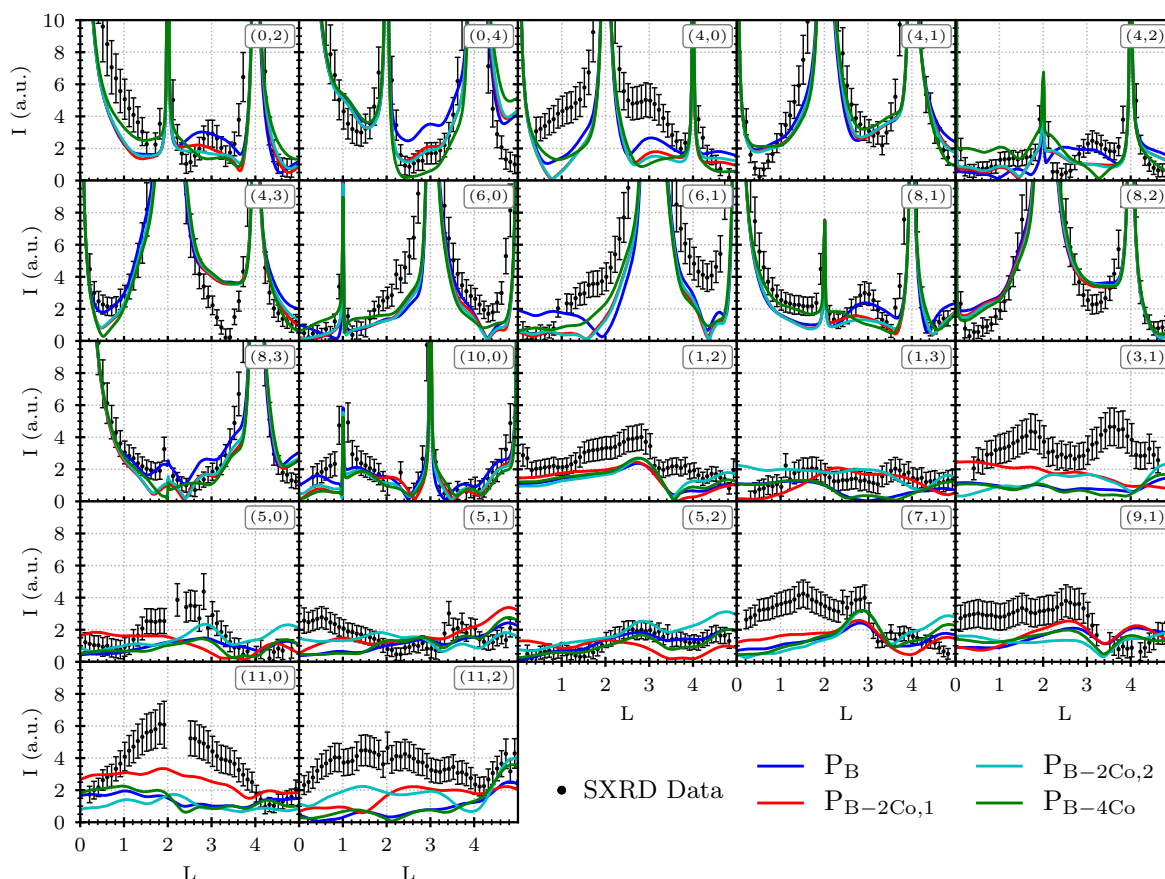


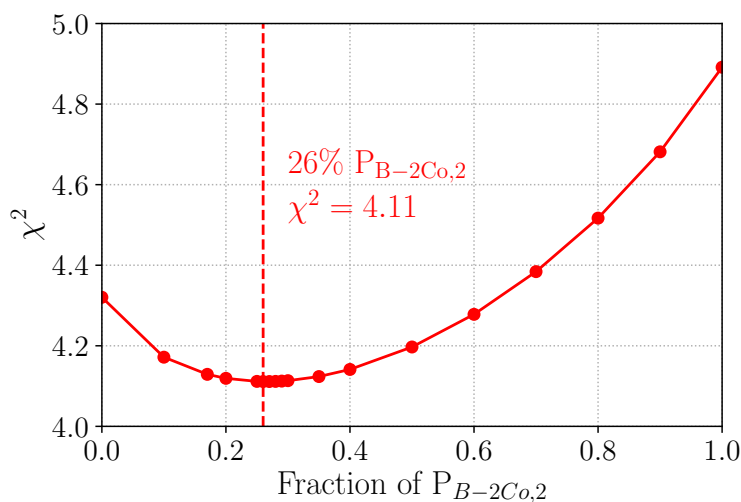
Figure 3.9: Measured crystal truncation rods (CTRs, even value of H) and super structure rods (SSRs, odd value of H) of $\text{Al}_5\text{Co}_2(2\bar{1}0)$ and the related DFT-based simulations of the four surface models.

needed free parameter for the simulations was the scaling factor (ca. 0.040 and ca. 0.037 for the CTR and SSR calculations, respectively). All simulations reproduce quite well several CTRs and SSRs features such as surface-related anti Bragg positions (e.g. CTRs (0,2) or (8,1)). CTR χ^2 calculations show that models which present protruding Co atoms are more suitable. However, SSR χ^2 calculations are required to discriminate between the four models (SSRs are only due to the surface reconstruction). The $\text{P}_{\text{B}-2\text{Co},1}$ χ^2 is indeed lower than the others ($\chi_{\text{SSR}}^2 = 3.33$ and $\chi_{\text{CTR}}^2 = 5.13$, see Tab. 3.1). The improvement of χ^2 is of almost 10% from the P_{B} model to the new model proposed for this surface ($\text{P}_{\text{B}-2\text{Co},1}$). It reaches 25% when considering only the SSRs. However, one cannot exclude a combination of several models.

Fits based on a linear combination of the $\text{P}_{\text{B}-2\text{Co},1}$ and $\text{P}_{\text{B}-2\text{Co},2}$ models lead to an optimum ratio of 74:26 with a χ^2 of 4.11 (Fig. 3.10). Other fitting processes (atom positions and occupancies refinements) have been tried out but none allowed for better results.

Table 3.1: Comparison between the four DFT-based surface structures and SXRD measurements : χ^2 calculations

Model	SSRs χ^2	CTRs χ^2	Global χ^2
P _B	4.19	5.19	4.74
P_{B-2Co,1}	3.33	5.13	4.32
P _{B-2Co,2}	4.54	5.18	4.89
P _{B-4Co}	4.44	5.32	4.93

Figure 3.10: χ^2 calculations for a linear combination of P_{B-2Co,1} and P_{B-2Co,2}. The minimum of χ^2 is obtained for a 74:26 ratio.

Nevertheless, the combination of experimental approaches allows the identification of the P_{B-2Co,1} model to describe the surface structure the best. In the following, this model is used to perform the investigation of the surface adsorption properties.

3.5 Adsorption calculations

The determination of adsorption properties for butadiene and butene on Al₅Co₂(2 $\bar{1}$ 0) is a prerequisite to feed the thermodynamic model used in the following to analyze the catalytic properties of Al₅Co₂(2 $\bar{1}$ 0). The complex energy landscape of this surface may however lead to a huge number of adsorption sites, including several molecular configurations for the adsorbates. Rather than performing a systematic, blindfolded and computationally expensive search, it is preferred to rely on the knowledge gained from the previous study,

which identified favorable adsorption sites for atomic hydrogen, acetylene and ethylene, using the P_B and P_{B-4C_0} models [15].

3.5.1 Hydrogen adsorption

According to Ref. [15], the Co-rich surface model (P_B) presents a large number of exothermic adsorption sites for atomic hydrogen. The labels were chosen to be consistent with the previous study. Most atomic hydrogen adsorption sites are found close to a protruding surface Co atom ($\#i$, $i \in \{1,2,4,5,7,8,10,11\}$) with adsorption energies in the range $[-0.39 \text{ eV}, -0.14 \text{ eV}]$, or on top of the Co atoms belonging to the subsurface atomic plane ($\#6$, $E_{\text{ads}} = -0.31 \text{ eV}$), as well as on top of a specific Al surface atom ($\#3$, $E_{\text{ads}} = -0.36 \text{ eV}$). The number of favorable adsorption sites is reduced when protruding atoms are missing at the surface (Al-rich P_{B-4C_0} surface model). Only a few sites are favorable: $\#i'$ with $i \in \{3,4,6,7,10,11\}$ with adsorption energies in the range $[-0.37 \text{ eV}, -0.09 \text{ eV}]$. Figure 3.11 shows the 12 sites that were considered in this study ($\#i$, $i \in \{1,3,4,5,6,10,11\}$). Other favorable sites were not considered because of the adsorption of butadiene/butene.

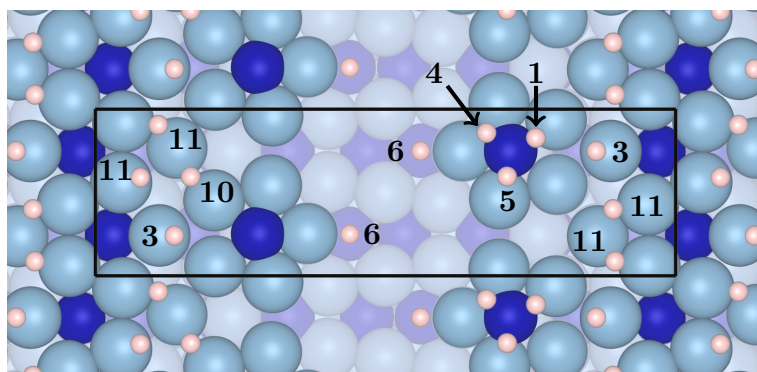


Figure 3.11: Co-adsorption of 12 hydrogen atoms (labelled i , $i \in \{1,3,4,5,6,10,11\}$) on $P_{B-2C_0,1}$. The surface unit cell is drawn in black. The color code is the same as Fig. 3.5.

3.5.2 Butadiene adsorption

According to previous studies [24, 8, 168, 169] stable sites for the adsorption of unsaturated molecules with carbon-carbon double bonds, like ethylene and butadiene, on complex polar intermetallic surfaces, generally occur through a π -bonding to a surface protruding transition metal atom. On $Al_5Co_2(2\bar{1}0)$, the di- σ configuration ($\sigma_{Al}\sigma_{Al}$), was identified [15] as a stable site as well. In the following, only four configurations for butadiene is considered on $Al_5Co_2(2\bar{1}0)$ shown in Fig. 3.12 : three starting configurations (A, B and C) involve

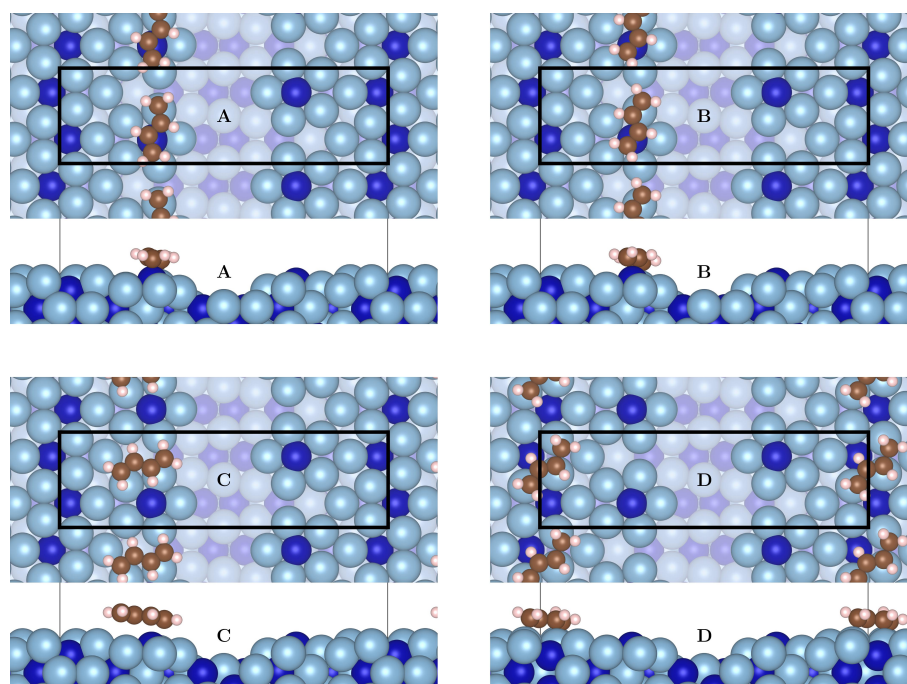


Figure 3.12: Adsorption sites and geometries for trans-1,3-butadiene on $P_{B-2Co_0.1}$. The surface unit cell is drawn in black. Al and Co atoms are drawn in light blue and dark blue, while C and H atoms are drawn in brown and white, respectively.

a C=C bond on top of a surface protruding/vacancy Co atom and one configuration (D) involves the $\sigma_{Al}\sigma_{Al}$ configuration.

The most stable site (labelled A in Fig. 3.12 and also Fig. 3.14a) is a $\pi_{Co}(\text{allyl})\sigma_{Al}(C)$ site ($E_{\text{ads}}^{\text{C}_4\text{H}_6} = -1.92$ eV). The molecule is slightly deformed ($E_{\text{def,mol}}^{\text{C}_4\text{H}_6} = 1.10$ eV), with a C-C bond length of the allyl radical similar to the one of the free radical (1.43 Å [170]). Other favorable adsorption configurations include di- π bonds ($\pi_{Al}(CC)\pi_{Co}(CC)$, $E_{\text{ads}}^{\text{C}_4\text{H}_6} = -1.74$ eV) or tri- σ bonds ($\text{tri}\sigma_{Al}(C)$, $E_{\text{ads}}^{\text{C}_4\text{H}_6} = -1.72$ eV). Physisorbed butadiene is less bounded on the surface ($E_{\text{ads}}^{\text{C}_4\text{H}_6} = -0.53$ eV).

As expected, a stronger butadiene/ $Al_5Co_2(2\bar{1}0)$ interaction was identified on the Co-rich surface model (P_B model), with butadiene adsorbed in between the two closest protruding Co atoms ($\pi_{Co}(\text{allyl})\sigma_{Al}(C)$, $E_{\text{ads}}^{\text{C}_4\text{H}_6} = -2.26$ eV). More interesting, such a strong adsorption energy is calculated on the Al-rich surface model as well (P_{B-4Co} model, $E_{\text{ads}}^{\text{C}_4\text{H}_6} = -2.27$ eV). Butadiene is adsorbed with a 1,4-di σ -2,3 π configuration, in a site involving Al atoms, neighboring of the surface Co vacancies. The molecule here is strongly distorted ($E_{\text{def,mol}}^{\text{C}_4\text{H}_6} = 1.90$ eV), but the 'true' interaction energy is large ($E_{\text{int}}^{\text{C}_4\text{H}_6} = -4.35$ eV). This shows that the presence of a protruding Co-site at the surface is not required to strongly adsorb the butadiene molecule.

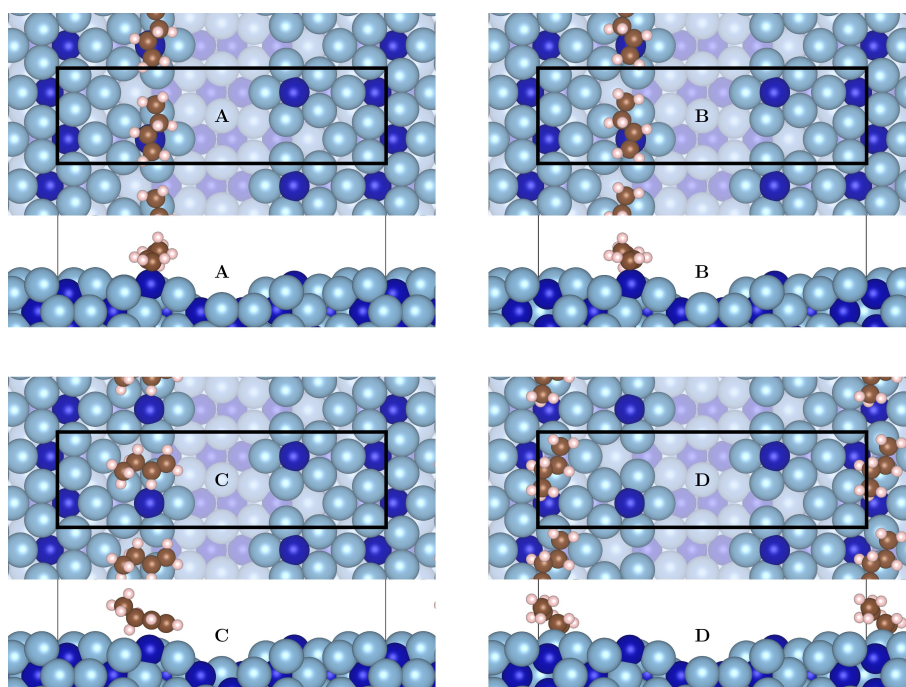


Figure 3.13: Adsorption sites and geometries for but-1-ene on $P_{B-2Co,1}$. The surface unit cell is drawn in black. Al and Co atoms are respectively drawn in light blue and dark blue, while C and H atoms are drawn in brown and white, respectively.

3.5.3 But-1-ene adsorption

There are two possible ways to obtain but-1-ene from adsorbed butadiene : either through the hydrogenation of the free C=C bond or the hydrogenation of the one that is bonded to a Co (or Al) atom. In the latter scenario but-1-ene is physisorbed while in the first case it is chemisorbed.

Chemisorbed butene on $P_{B-2Co,1}$ site A leads to a π_{Co} configuration with an adsorption energy equal to -1.52 eV (Fig. 3.13, Tab. 3.2 and Fig. 3.14b). Fig. 3.14e presents the charge density deformation around the chemisorbed butene molecule. A di- σ configuration involving one Al-Al pair is also identified with a lower adsorption energy ($E_{ads}^{C_4H_8} = -1.25$ eV).

Physisorption – showed in Fig. 3.14c – leads to a smaller adsorption energy ($E_{ads}^{C_4H_8} = -0.61$ eV for site A). Fig. 3.14f presents the charge density deformation around the butene molecule, confirming the physisorbed mode. Other sites appear to be more stable for physisorbed butene (-0.63 eV for site B and -0.82 eV for site D). Nevertheless site A is the one considered for consistency since it was the most stable adsorption site for butadiene.

Here, since the strongest butene adsorption occurs through a π bonding involving only one surface protruding Co atom, it is not surprising to obtain similar strongest adsorption

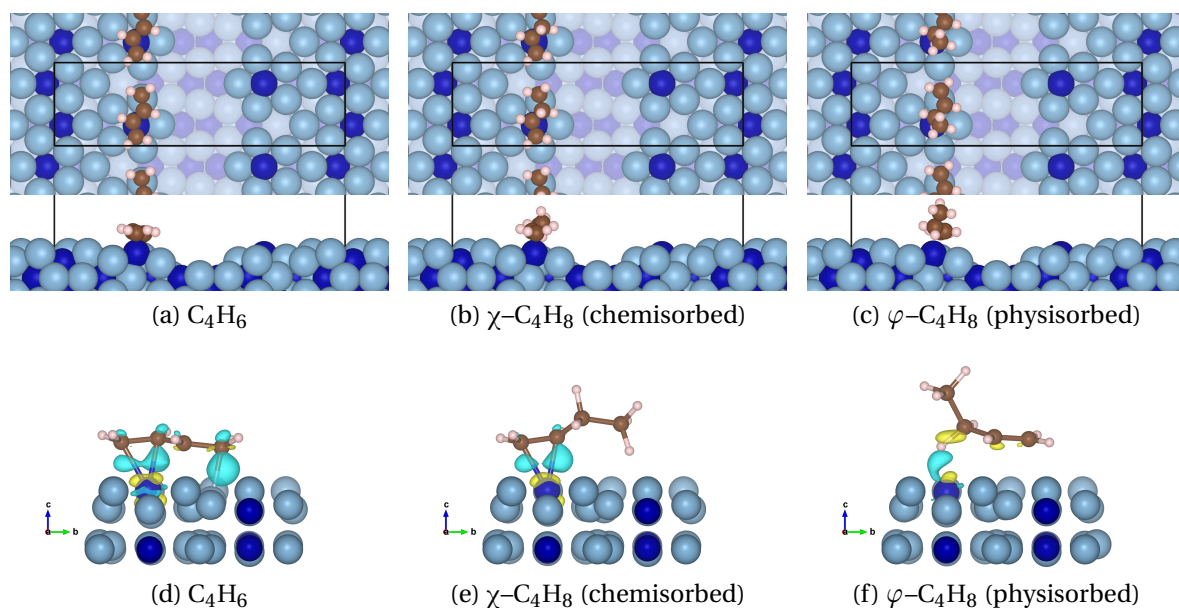


Figure 3.14: Adsorption configurations on $P_{B-2Co,1}$ (site A) for (a) C_4H_6 , (b) $\chi-C_4H_8$ (chemisorbed through a double $C=C$ bond on a protruding Co atom) and (c) $\varphi-C_4H_8$ (physisorbed through a H atom on a Co atom). Isosurface of charge density differences for (d) C_4H_6 ($0.01 e^-/\text{\AA}$), (e) $\chi-C_4H_8$ ($0.01 e^-/\text{\AA}$) and (f) $\varphi-C_4H_8$ ($0.006 e^-/\text{\AA}$). Negative (resp. positive) isosurfaces are plotted in light blue (resp. yellow).

energies on the $P_{B-2Co,2}$ and P_B models ($E_{ads}^{C_4H_8} \in [-1.48 \text{ eV}; -1.54 \text{ eV}]$). Again, the presence of a protruding surface Co atom is not mandatory for the adsorption properties, since σ_{Al} and $\sigma_{Al}\sigma_{Co}$ configurations also lead to large adsorption energies (e.g. $E_{ads}^{C_4H_8} = -1.37 \text{ eV}$ on P_{B-4Co} model).

3.5.4 Coadsorption of hydrogen and butadiene/but-1-ene

Atomic hydrogen and C_4H_6 need to be simultaneously adsorbed on the surface for the hydrogenation reaction to occur according to the Langmuir–Hinshelwood mechanism. Here, we determine how the previous adsorption energies are impacted by co-adsorption with hydrogen under realistic conditions (pressure, temperature).

The determination of the realistic hydrogen coverage, with the constrain of one alkene molecule adsorbed per surface cell, would require the determination of the complete surface stability diagram for hydrogen, which is beyond the scope of the present investigation. Here, 7 hydrogen coverages are considered ($\vartheta_H = 0, 2, 4, 6, 8, 10$ or 12). This means that for each (p,T) condition the optimum coverage ϑ_H is determined. The hydrogen adsorption sites are selected amongst the one presented in Fig. 3.11 following their relative adsorption

Table 3.2: Trans-1,3-butadiene (C_4H_6) and but-1-ene (C_4H_8) adsorption energies on $P_{B-2Co,1}$

$P_{B-2Co,1}$	E_{ads} (eV) for different sites			
	A	B	C	D
C_4H_6	-1.92	-1.74	-0.53 φ	-1.72
$\chi-C_4H_8$	-1.52	-1.54	-0.51 φ	-1.25
$\varphi-C_4H_8$	-0.61	-0.63	-0.36 φ	-0.82

χ : chemisorbed, φ : physisorbed

energies, i.e. for $\vartheta_H = 2$, $i \in (1, 3)$; for $\vartheta_H = 4$, $i \in (1, 3, 4)$; for $\vartheta_H = 6$, $i \in (1, 3, 4, 5, 6)$; for $\vartheta_H = 8$, $i \in (1, 3, 4, 5, 6)$; for $\vartheta_H = 10$, $i \in (1, 3, 4, 5, 6, 10, 11)$ and for $\vartheta_H = 12$, $i \in (1, 3, 4, 5, 6, 10, 11)$.

The next step in the analysis is the prediction of the stability of these adsorbates under operating conditions using a thermodynamic model (developped in Chapter 2, section 2.2.3.3). The thermodynamic diagrams related to the Gibbs free adsorption energies of hydrogen, butadiene and butene (chemi- and physisorbed) are plotted in Figs. 3.15a–c for the $P_{B-2Co,1}$ model, as a function of the temperature and the total pressure (a 1:10 ratio was considered for the partial pressures of C_4H_6 and H_2 , in agreement with the experimental conditions).

Figs. 3.15d–f show the respective hydrogen coverages ϑ_H as a function of p and T . They show that the alkene molecules are adsorbed under usual hydrogenation conditions. At the experimental (p, T) conditions, the optimum hydrogen coverage appears to be $\vartheta_H = 6$ (resp. $\vartheta_H = 8$) for C_4H_6 (resp. $\chi-C_4H_8$ and $\varphi-C_4H_8$) with a coadsorption enthalpy of -1.84 eV (resp. -1.49 eV and -0.49 eV).

3.5.5 Competition between chemisorption and physisorption

There are two possible ways to obtain but-1-ene from adsorbed butadiene (site A): through the hydrogenation of the C=C fragment bounded either to one surface Co or to one Al surface atom. In the latter scenario, but-1-ene is chemisorbed, while in the first case, it is physisorbed. Both products – chemisorbed or physisorbed butene – appear to be adsorbed at $p = 5.5$ mbar and $T = 383$ K (experimental conditions).

Chemisorbed butene on $P_{B-2Co,1}$ leads to a π_{Co} configuration with an adsorption energy equal to -1.52 eV (Tab. 3.2 and Fig. 3.14b). This rather large adsorption energy results from the strong molecule surface bonding, involving charge transfer (three lobes of charge

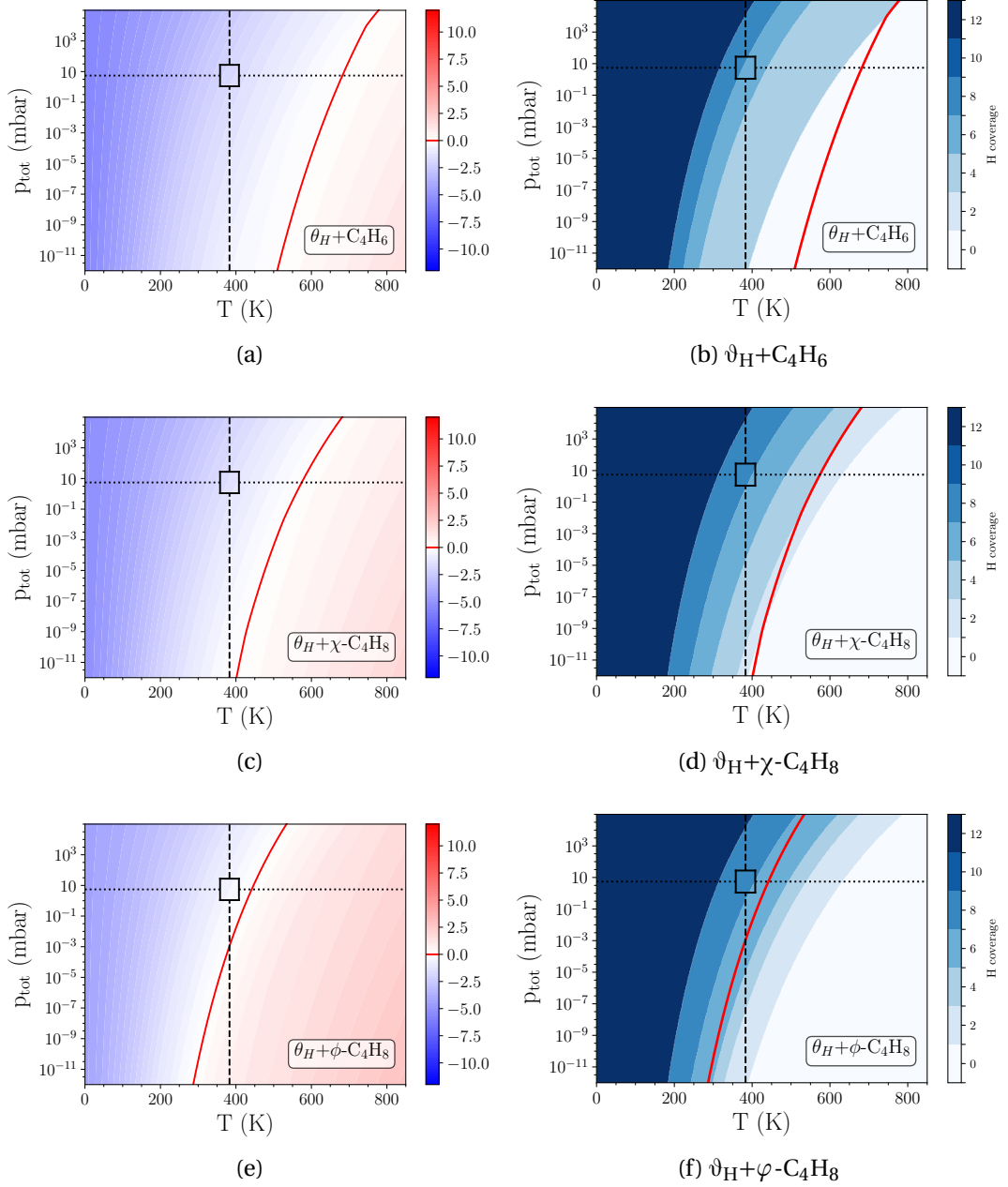


Figure 3.15: Co-adsorption enthalpy in eV (color scale) of (a) hydrogen atoms and C_4H_6 , (b) hydrogen atoms and $\varphi\text{-C}_4\text{H}_8$ and (c) hydrogen atoms and $\chi\text{-C}_4\text{H}_8$, as a function of p and T for $\text{P}_{\text{B-2Co,1}}$. Corresponding hydrogen coverage as a function of p and T plotted for (c) hydrogen atoms and C_4H_6 , (d) hydrogen atoms and $\chi\text{-C}_4\text{H}_8$ and (e) hydrogen atoms and $\varphi\text{-C}_4\text{H}_8$ for $\text{P}_{\text{B-2Co,1}}$ model. χ - and φ - describe chemisorbed and physisorbed modes, respectively. The red line represents $G_{\text{ads}} = 0$. The dotted and dashed lines represent $p = 5.5$ mbar and $T = 383$ K *i.e.* the experimental conditions, respectively.

accumulation between the molecule and the surface, Fig. 3.14e). Physisorbed butene leads to a smaller adsorption energy ($E_{\text{ads}}^{\text{C}_4\text{H}_8} = -0.51$ eV). Charge deformation (Fig. 3.14f) highlights a bonding through one hydrogen atom.

According to the experimental results obtained at $(p, T) = (5 \text{ mbar}, 393 \text{ K})$, butene has to be desorbed once produced because a 100% selectivity toward semihydrogenation as well as full conversion is observed. Our thermodynamic study predicts a desorption temperature of 440 K for $\varphi\text{-C}_4\text{H}_8$, which is only 57 K higher than the experimental temperature. Conversely, it is calculated that $\chi\text{-C}_4\text{H}_8$ would desorb at $T = 572$ K (189 K higher than T_{exp} , Fig. 3.16). Uncertainties are still present on the experimental temperature measurements and on the desorption temperature calculations. Nevertheless, the combination of experimental and theoretical results may indicate that the π_{Co} (allyl) bond is hydrogenated first. Such a conclusion should however be strengthened by the evaluation of a possible reaction path on the surface, which is out of the scope of this work.

3.5.6 Influence of Co surface density

Adsorption properties are found to be strongly influenced by the density of surface protruding Co atoms (Fig. 3.17). When comparing the P_{B} and $P_{\text{B-2Co,1}}$ models, one observes that molecules are more strongly adsorbed at the Co-rich surface model, as already noticed in our preliminary calculations without atmosphere. The previous observations have a consequence on the catalytic properties. Using the P_{B} model, with four protruding cobalt atoms, the most stable site involves two protruding surface Co atoms ($E_{\text{ads}} = -2.26$ eV, Table S1), leading to a rather high adsorption energy. Regardless of the double bond that is hydrogenated first, the hydrogenated molecule (but-1-ene) is strongly adsorbed as well, through one Co atom, which may prevent a good selectivity.

A strong molecule surface interaction was already calculated for acetylene on the P_{B} model. This was shown to alter the activity of the catalyst: in [15], the considered reaction path did not consider the most stable site because in this case the adsorption energies of the reactants are more stable than the products.

Using the $P_{\text{B-2Co,1}}$ model, only one protruding Co atom is involved in the bonding between the surface and butadiene. Protruding surface Co atoms are isolated, which may favor the selectivity. When the $\pi_{\text{Co-allyl}}$ bonding is hydrogenated first, this scenario is shown to lead to theoretical results in agreement with the catalytic observations.

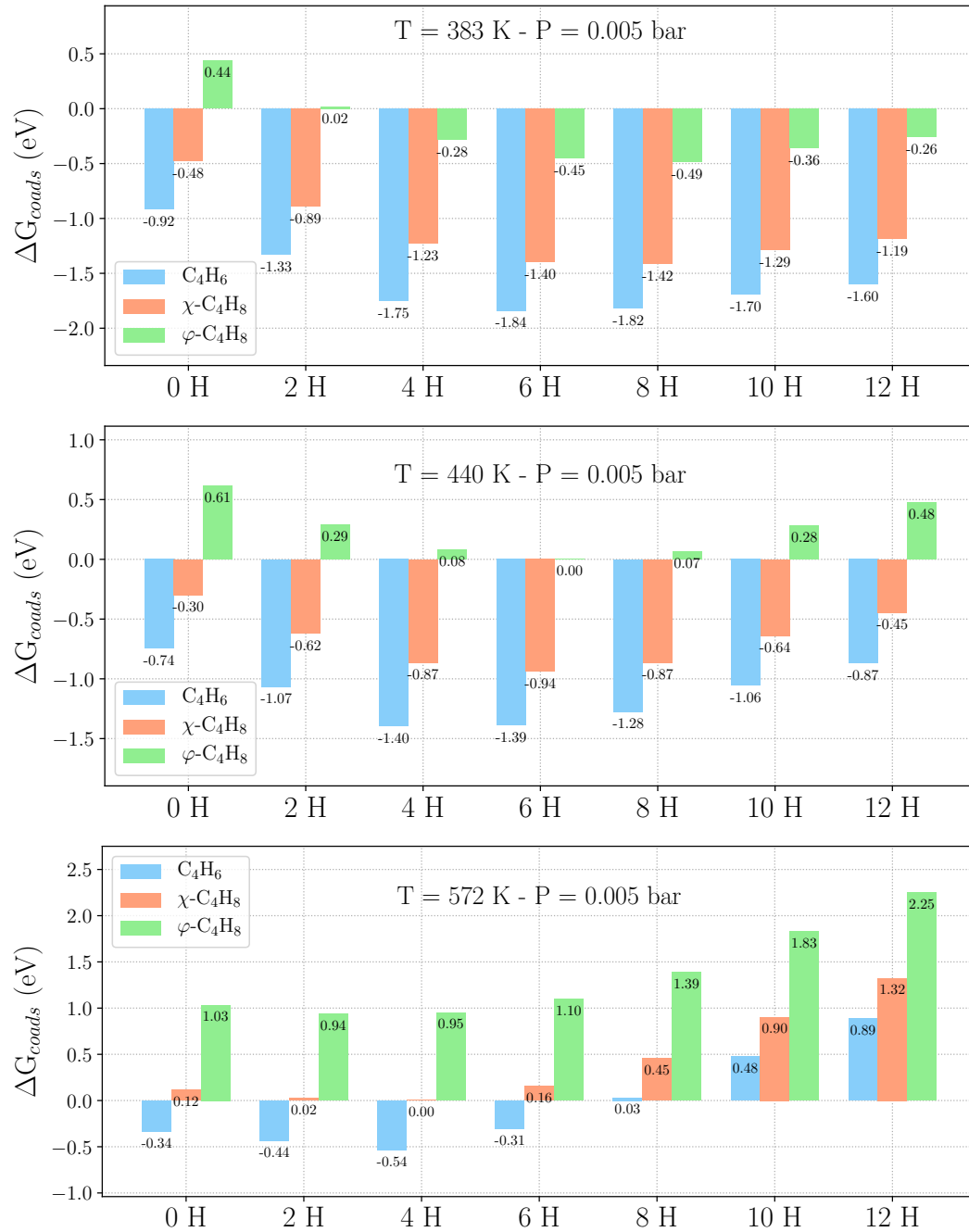


Figure 3.16: Co-adsorption enthalpies of hydrogen atoms, butadiene and butene plotted for $P_{B-2Co,1}$ model, under the following reaction conditions: $p = 5.5$ mbar, $T = 383$ K, 440 K or 572 K.

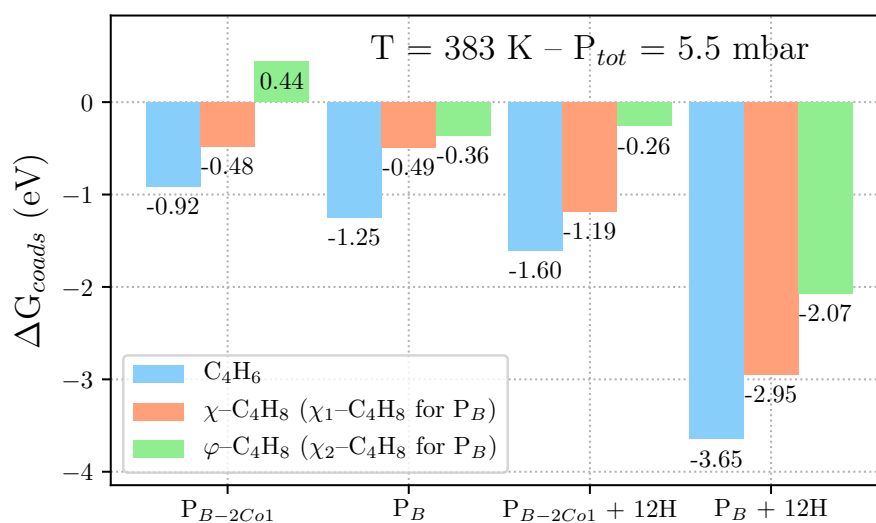


Figure 3.17: Coadsorption energies of hydrogen and C_4H_x as a function of the surface model.

3.6 Conclusion

This work identified the $Al_5Co_2(2\bar{1}0)$ surface as a highly selective catalyst though moderately active for the semi-hydrogenation of butadiene. The surface activity and selectivity strongly depends on the surface structure, which is determined by a combination of SXRD measurements and DFT calculations. Stable surface models differ only by the presence/absence of a few surface Co atoms, but their discrimination is shown to be possible, thanks to the SXRD/DFT approach. Our analysis leads to the conclusion that surface Co atoms are well isolated from each other at the surface, the distance between two closest Co atoms being 7.6 Å.

In addition, DFT calculations show that the density of surface Co atoms has a significant influence on the adsorption energies of butadiene and butene, which may impact the activity and selectivity of the catalyst. The consideration of atomic hydrogen and butadiene co-adsorption, in agreement with the Langmuir-Hinshelwood mechanism, as well as the influence of operating conditions (p,T), weaken the adsorption energies of butadiene and butene. Both chemisorbed and physisorbed butene molecules are adsorbed at reaction conditions, but less strongly than butadiene. The hydrogenation leading to physisorption of butene seems more realistic when comparing to experimental results. Chemisorbed butene does not naturally desorb after the hydrogenation of the first C=C bond. This would explain the hydrogenation of butene experimentally observed once butadiene is fully converted.

Our study clearly show that although $\text{Al}_{13}\text{Fe}_4(010)$ and $\text{Al}_5\text{Co}_2(2\bar{1}0)$ present similar surface structures under ultra-high vacuum, with the presence of well isolated transition metal atoms protruding at the surface, and show analogous adsorption properties, their catalytic performances are rather different. This may come from kinetic factors, or from the emergence of a different surface structure under reaction conditions. Further theoretical and experimental investigations, including the determination of the surface structure under reaction condition, and of a possible reaction path, have to be conducted to fully get the catalytic properties of $\text{Al}_5\text{Co}_2(2\bar{1}0)$.

Chapter 4

Nanostructuring of $o\text{-Al}_{13}\text{Co}_4(100)$ under reaction conditions

Contents

4.1 Introduction	88
4.2 Surface energy calculations	89
4.3 Hydrogen adsorption	90
4.3.1 On corrugated $o\text{-Al}_{13}\text{Co}_4(100)$	90
4.3.2 On flat $o\text{-Al}_{13}\text{Co}_4(100)$	91
4.4 Butadiene and but-1-ene adsorptions	92
4.4.1 C_4H_6 on corrugated $o\text{-Al}_{13}\text{Co}_4(100)$	92
4.4.2 C_4H_6 on flat $o\text{-Al}_{13}\text{Co}_4(100)$	93
4.4.3 Adsorption of C_4H_8	94
4.5 Nanostructuring under reaction conditions	94
4.5.1 Thermodynamic modelling and modification of the surface energy	95
4.5.2 Hydrogen optimum coverages	96
4.5.3 Coadsorption of hydrogen and butadiene	98
4.6 Catalytic activation and hydrogenation reaction	99
4.6.1 Catalytic activation	99
4.6.2 Coadsorption of hydrogen and but-1-ene	99
4.7 Conclusion	101

4.1 Introduction

In this chapter the (100) surface of $o\text{-Al}_{13}\text{Co}_4$ is theoretically investigated under reaction conditions through the means of DFT. This surface has already been both theoretically and experimentally studied under UHV and two surface models emerged. A first one is derived from a theoretical cleavage [24] (Fig. 4.1a, model P_{14}) and consists in an incomplete and nanostructured puckered layer built from the preservation of the cluster building blocks at the surface, in relation to strong covalent interactions present in this compound [34]. This first model appears to be inconsistent with the experimental observations of the surface prepared by sputtering–annealing under UHV conditions [88]. A second model was proposed, in agreement with the experimental observations (STM, SXRD), that consists in a dense puckered layer that lacks two protruding Co atoms (Fig. 4.1b, model P_{24}) [18].

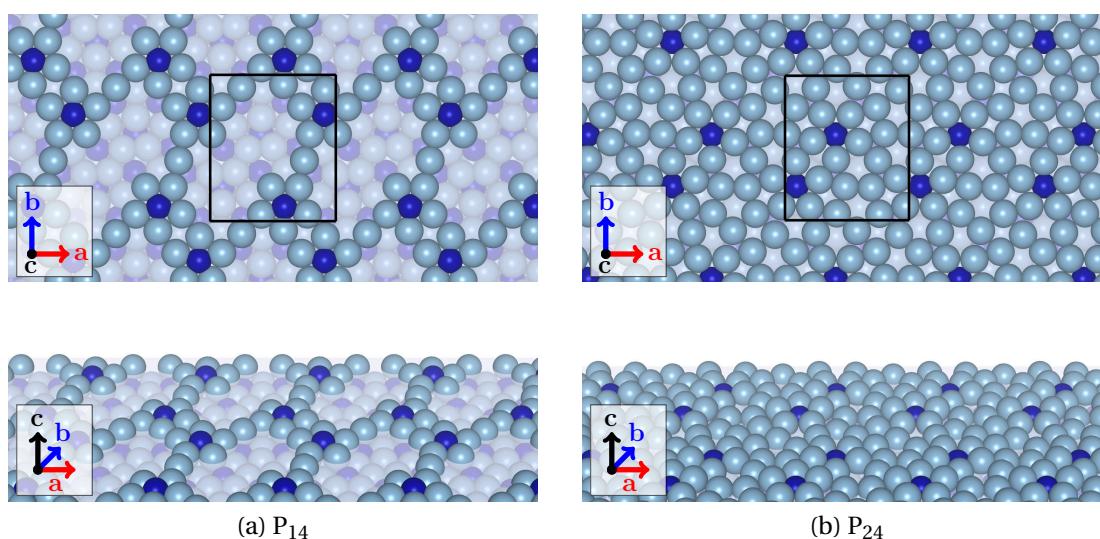


Figure 4.1: $\text{Al}_{13}\text{Co}_4(100)$ – (a) P_{14} and (b) P_{24} – surface models. Al and Co atoms are drawn in light blue and dark blue, respectively.

$\text{Al}_{13}\text{Co}_4$ has recently been shown to exhibit unexpected performances in the partial hydrogenation of alkynes [22, 21] and alkydienes [7, 9, 8]. A possible reaction path for the partial hydrogenation of acetylene was identified using first-principles calculations on $o\text{-Al}_{13}\text{Co}_4(100)$, with energy barriers similar to the ones calculated for conventional Pd and Pd–Ag catalysts [24]. However, the starting point of this investigation was the P_{14} surface model, which is inconsistent with the experimental observations performed under UHV, *i.e.* P_{24} surface model, on which rather large hydrogenation barriers have been calculated [19]. Thus the question of its surface structure under catalytic hydrogenation conditions re-

mains open. Investigations to probe possible adsorbate-induced restructuring of complex intermetallic surfaces under hydrogenation conditions, and its influence on their catalytic performances, have never been reported so far.

4.2 Surface energy calculations

Preliminary DFT calculations allow for the estimation of the surface energies of both models (see section 2.2.3.1 in Chapter 2 for more details). In the following, all calculations are done using the DFT-D3 functional (if not mentioned otherwise). The results are plotted in Fig. 4.2. In the chemical potential range $[-0.5 \text{ eV}; -0.15 \text{ eV}]$, P₁₄ is the most stable surface model with a surface energy ranging from 1.64 J/m^2 to 1.68 J/m^2 . In the chemical potential range $[-0.15 \text{ eV}; 0 \text{ eV}]$, P₂₄ is the most stable surface model with a surface energy ranging from 1.49 J/m^2 to 1.64 J/m^2 .

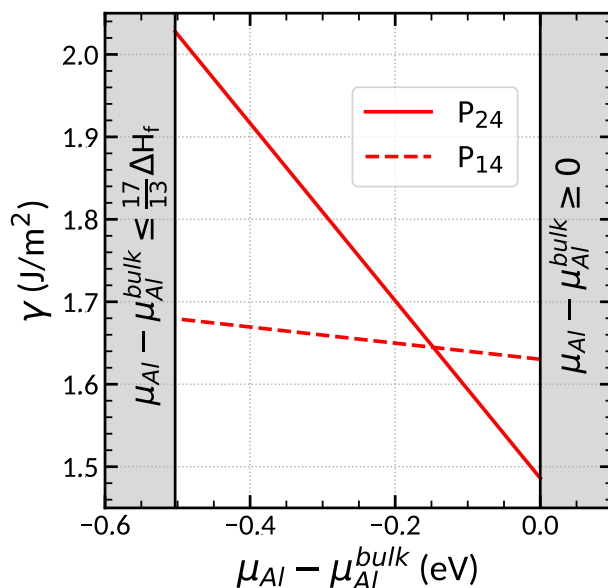


Figure 4.2: Surface energies of $o\text{-Al}_{13}\text{Co}_4(100)$ as a function of the Al chemical potential

Both models are therefore stable over a rather long range of chemical potential with similar surface energies in the range $[1.49 \text{ J/m}^2; 1.68 \text{ J/m}^2]$. It is thus of interest to determine how these surface energies are changed when molecules are adsorbed at the surfaces. To predict adsorption thermodynamics under reaction conditions, the first step consists in the determination of the energetically favorable adsorption structures and sites for H, C₄H₆ and C₄H₈.

4.3 Hydrogen adsorption

Weak hydrogen binding and easy H_2 dissociation are key descriptors in hydrogenation catalysis. These factors are related to the atomic hydrogen adsorption properties of the $o\text{-Al}_{13}\text{Co}_4$ surfaces, an overview of which is obtained through potential energy surfaces (Fig. 4.3 and Fig. 4.4). The adsorption has been computed on specific points of regular grids covering the surfaces, using point densities of $2.3 \text{ pts}/\text{\AA}^2$ (total of 400 adsorption positions for each surface).

4.3.1 On corrugated $o\text{-Al}_{13}\text{Co}_4(100)$

The adsorption energy landscape of P_{14} is presented in the right-hand map of Fig. 4.3. The left-hand map of the figure shows particular and stable adsorption sites (top, bridge and hollow local minima) for which the adsorption energies are displayed in Tab. 4.1.

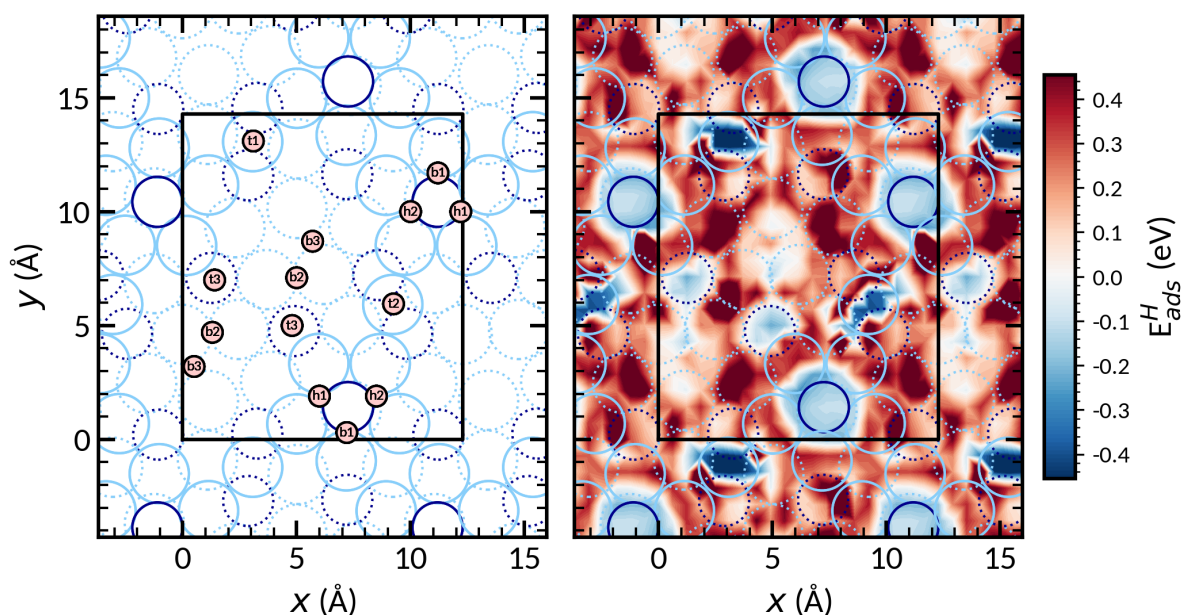


Figure 4.3: Hydrogen adsorption energy maps on P_{14} . Al and Co atoms are drawn in light blue and dark blue, respectively.

The most stable adsorption sites appear to be the Al "glue atoms" – that link the bipentagonal motifs – and one of the subsurface Co atom ($E_{\text{ads}}^{\text{H}} = [-0.51 \text{ eV}; -0.45 \text{ eV}]$). The second most stable sites are – as expected – the protruding Co atoms (top site, bridge site with one Al atom, and hollow site with two Al atoms). In total, 14 sites are considered to be stable sites (considering symmetry and steric hindrance) and are labelled $t1$ to $t3$ for top sites,

Table 4.1: Hydrogen adsorption energies on P₁₄

Adsorption energies (eV)					
	top	bridge		hollow	
t1	-0.51	b1	-0.24	h1	-0.22
t2	-0.45	b2	-0.21	h2	-0.18
t3	-0.25	b3	-0.17	-	-

b1 to *b3* for bridge sites and *h1/h2* for hollow sites.

4.3.2 On flat *o*-Al₁₃Co₄(100)

The adsorption energy landscape of P₂₄ is presented in Fig. 4.4. The left-hand map of the figure shows particular and stable adsorption sites (only bridge sites) for which the adsorption energies are displayed in Tab. 4.2.

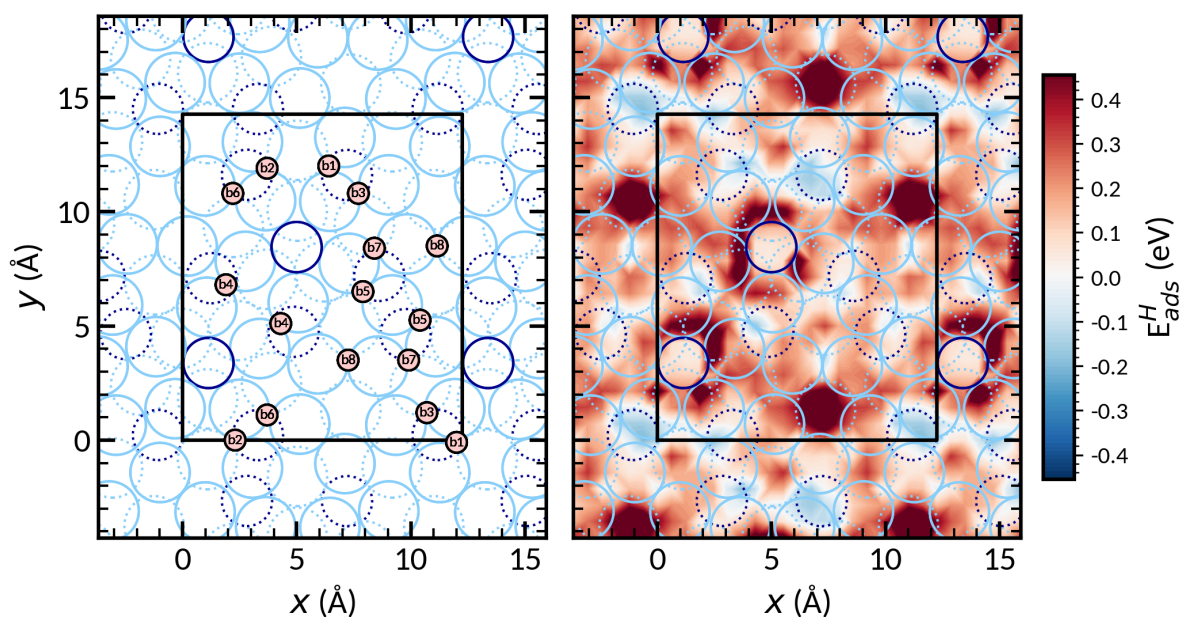


Figure 4.4: Hydrogen adsorption energy maps on P₂₄. Al and Co atoms are drawn in light blue and dark blue, respectively.

The most stable adsorption sites appear to be on bridges between two Al atoms above a subsurface Co atom : the favorable adsorption sites are stabilized by the electronic donor

Table 4.2: Hydrogen adsorption energies on P₂₄

Adsorption energies (eV)			
bridge		bridge	
b1	-0.23	b5	-0.16
b2	-0.22	b6	-0.06
b3	-0.20	b7	-0.03
b4	-0.18	b8	-0.11

character of Co atoms positioned in the subsurface layer [32]. In total, 16 sites are considered to be stable sites (considering symmetry and steric hindrance) and are labelled *b1* to *b8* for bridge sites.

Thanks to these results on both surface models, it will be possible to build hydrogenated surface models with hydrogen coverage ranging from 1 to 12 hydrogen atoms per surface cell (5.6×10^{-3} at/Å² to 6.7×10^{-2} at/Å²). A maximum of 12 hydrogen atoms will be adsorbed because of the coadsorption with a C₄H_x molecule which will take a few possible adsorption sites.

4.4 Butadiene and but-1-ene adsorptions

The next step is to find the stable adsorption sites of butadiene and but-1-ene on both surface models. Regardless of the surface model, the *trans* configuration of butadiene is always preferred. The molecule–surface interaction typically occurs through π -bonds, di- σ -bonds or a combination of both types.

4.4.1 C₄H₆ on corrugated *o*-Al₁₃Co₄(100)

For the P₁₄ model, all considered adsorption sites involve protruding surface Co atoms and neighboring Al atoms. No adsorption sites were found in between the surface clusters, on the exposed part of the F-type layer. The most stable sites are drawn in Fig. 4.5a–d and their related adsorption energies are presented in Tab. 4.3. For all configurations, butadiene is adsorbed with a $\pi_{\text{Co}}-\sigma_{\text{Al}}$ mode.

The butadiene adsorption energies range from –1.26 eV to –1.59 eV on P₁₄. For comparison, butadiene is more strongly adsorbed (–1.94 eV) on Al₁₃Fe₄(010) – which has the same

nanostructured surface – than on P_{14} [171]. This difference is attributed to a decreased filling of the adsorbate–metal antibonding states in agreement with DOS calculations [171].

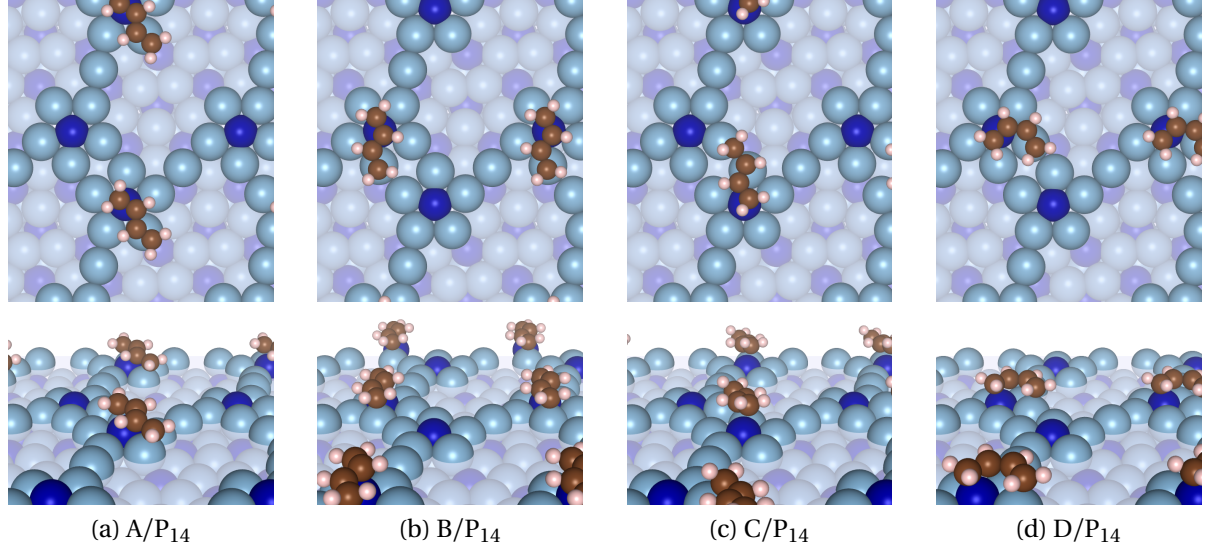


Figure 4.5: Adsorption sites of butadiene on P_{14} (top and perspective views). Al and Co atoms are drawn in light blue and dark blue, respectively.

4.4.2 C_4H_6 on flat $o-Al_{13}Co_4(100)$

Only surface Al atoms are involved in the case of the P_{24} model since no Co atoms are protruding unlike in the corrugated model. The most stable sites are drawn in Fig. 4.6a–d and their related adsorption energies are presented in Tab. 4.3. Butadiene is adsorbed with a $di\sigma-\pi$ mode (configuration E) or a $tri\sigma$ mode (configurations F, G and H). These sites appear to be stabilized thanks to subsurface Co atoms positioned right below. The butadiene adsorption energies range from -1.67 eV to -1.90 eV on P_{24} . It is therefore more strongly adsorbed on P_{24} than on P_{14} .

Table 4.3: Butadiene adsorption energies on P_{14} and P_{24}

P_{14}	A	B	C	D
E_{ads} (eV)	-1.59	-1.53	-1.26	-1.31
P_{24}	E	F	G	H
E_{ads} (eV)	-1.90	-1.75	-1.75	-1.67

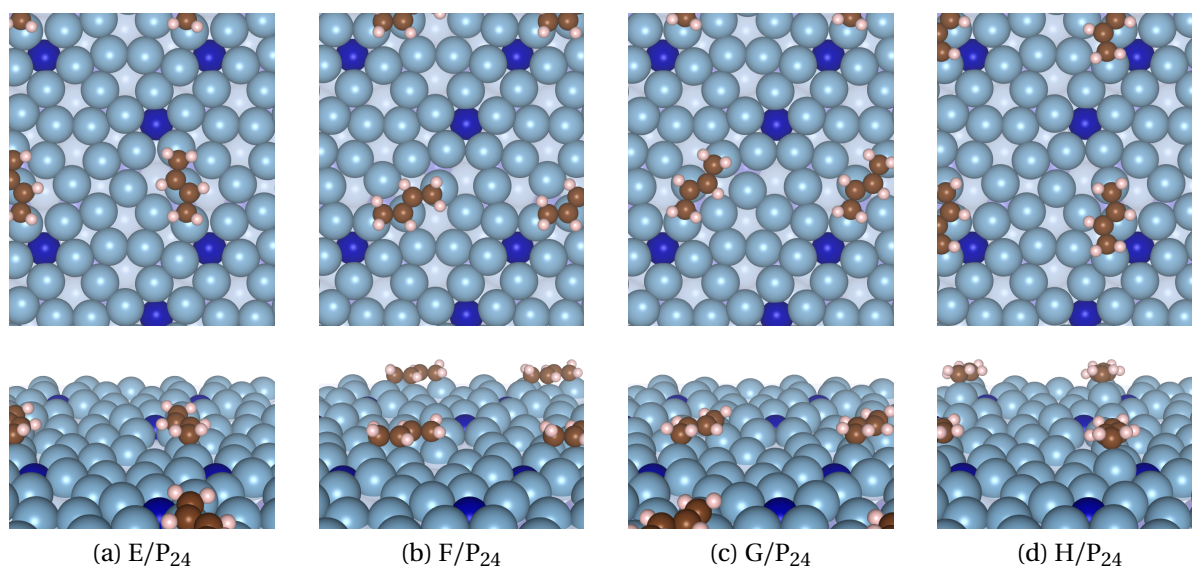


Figure 4.6: Adsorption sites of butadiene on P_{24} (top and perspective views). Al and Co atoms are drawn in light blue and dark blue, respectively.

4.4.3 Adsorption of C_4H_8

Only four butene configurations are presented in Fig. 4.7a–d : two on P_{14} (a–b) and two on P_{24} (c–d). The different adsorption energies are presented in Tab. 4.4. The first configuration is a butene molecule that is chemisorbed (χ) with a π_{Co} mode (-1.13 eV). This simulates the hydrogenation of the $\text{C}=\text{C}$ bond that was not adsorbed on the protruding Co atom.

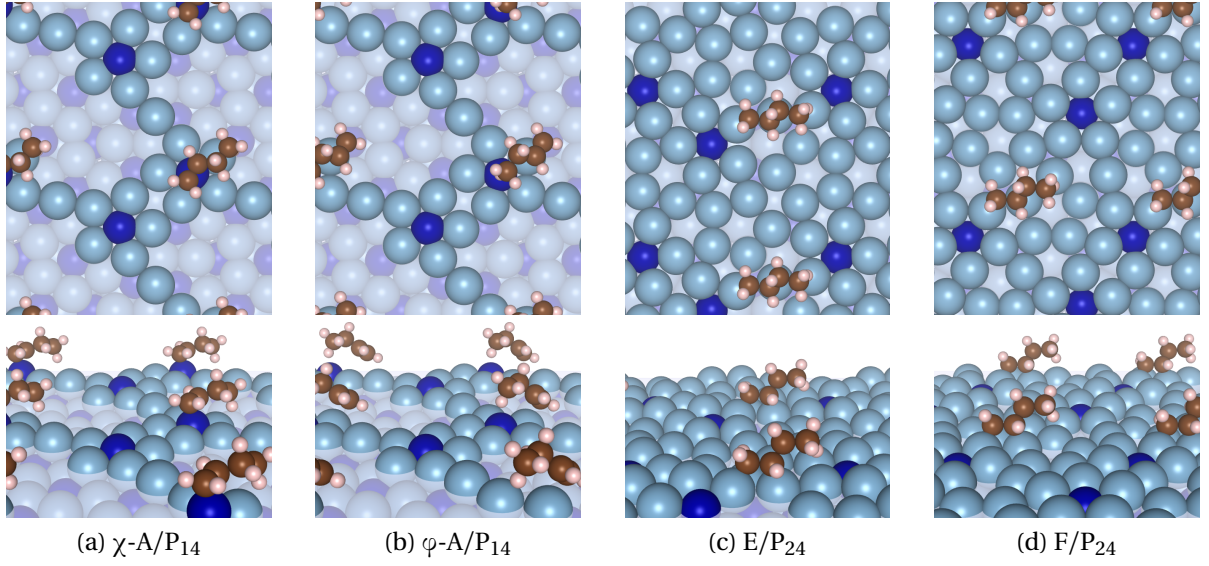
The second configuration on P_{14} is a butene molecule that is physisorbed (φ) with a $\sigma_{\text{Co}}(\text{H})$ mode (-0.73 eV). This simulates the hydrogenation of the $\text{C}=\text{C}$ bond that was adsorbed on the protruding Co atom. This configuration is less stable than the previous one.

On P_{24} the stable configurations are quite different. The two main configurations presented in Figs. 4.7c–d are butene molecules that are chemisorbed with a di- σ_{Al} mode having adsorption energies of -1.23 eV and -1.32 eV.

The di- σ_{Al} mode adsorption energies are rather similar to the one of the π_{Co} mode. In all cases, butene adsorption is found to be weaker than butadiene adsorption.

4.5 Nanostructuring under reaction conditions

The butadiene hydrogenation reaction is known to follow a Horiuti–Polanyi-type mechanism [172], which requires the presence of coadsorbed butadiene and hydrogen species.

Figure 4.7: Adsorption sites of but-1-ene on P₁₄ and P₂₄Table 4.4: Butene adsorption energies on P₁₄ and P₂₄

Site	χ-A/P ₁₄	φ-A/P ₁₄	E/P ₂₄	F/P ₂₄
E _{ads} (eV)	-1.13	-0.73	-1.23	-1.32

These adsorbates may induce modifications of the surface structure. This is questioned here in the case of Al₁₃Co₄(100), using the previous surface models and adsorption energies as inputs for the thermodynamic model introduced before in Chapter 2 (section 2.2.3.3).

4.5.1 Thermodynamic modelling and modification of the surface energy

As detailed in Chapter 2 section 2.2.3.1, the surface energy of a clean slab can be expressed as follow :

$$\gamma_{\text{clean}} = \frac{1}{2A} \left[E^{\text{slab}} - \frac{\mu_{\text{Al}_3\text{Co}_4}^{\text{bulk}} N_{\text{Co}}^{\text{slab}}}{4} - \mu_{\text{Al}}^{\text{bulk}} \left(N_{\text{Al}}^{\text{slab}} - \frac{13 N_{\text{Co}}^{\text{slab}}}{4} \right) - (\mu_{\text{Al}} - \mu_{\text{Al}}^{\text{bulk}}) \left(N_{\text{Al}}^{\text{slab}} - \frac{13 N_{\text{Co}}^{\text{slab}}}{4} \right) \right]$$

where E^{slab} is the total energy of the slab (determined through DFT calculations), μ_X is the chemical potential of X in Al₁₃Co₄, G the free enthalpy of the system and N_X^{slab} the number of X atom in the slab ($X = \text{Al}, \text{Co}$).

Possible modifications of the surface structure under operating conditions (pressure p

and temperature T) can be investigated by calculating the surface energies modified by adsorption γ_{cov} [173, 174, 175] defined as follow :

$$\gamma_{\text{cov}}(\mathbf{p}, T, \mu_{\text{Al}} - \mu_{\text{Al}}^{\text{bulk}}) = \gamma_{\text{clean}}(\mu_{\text{Al}} - \mu_{\text{Al}}^{\text{bulk}}) + \gamma_{\text{ads}}(\mathbf{p}, T) \quad (4.1)$$

where the part due to the adsorption is defined by :

$$\gamma_{\text{ads}}(\mathbf{p}, T) = \frac{1}{A} \left[E_{\text{coads}}^{\text{C}_4\text{H}_x + n_{\text{H}_2}\text{H}_2} + k_{\text{B}}T \sum_{i \in \mathcal{X}} \ln(z_{\text{trans}}^{*,i} \cdot z_{\text{rot}}^i)^{n_i} - k_{\text{B}}T \sum_{i \in \mathcal{X}} n_i \ln\left(\frac{p^i}{k_{\text{B}}T}\right) \right] \quad (4.2)$$

with $\mathcal{X} = (n_{\text{H}_2}\text{H}_2, \text{C}_4\text{H}_x)$. The quantities z_{trans}^* and z_{rot} are the translational and rotational partition functions (see section 2.2.3.3 of Chapter 2 for more information).

4.5.2 Hydrogen optimum coverages

It is possible then to calculate the surface energy of each model as a function of $(\mathbf{p}, T, \mu_{\text{Al}})$ and, consequently, to compare between the two structures, which one is the most stable at a given $(\mathbf{p}, T, \mu_{\text{Al}})$ condition. To do so, the surface energies of a slab with i adsorbed H atoms ($\forall i \in \llbracket 1, \dots, 12 \rrbracket$) are calculated for each surface model. The surface coverages are progressively increased with less and less stable adsorption sites (*e.g.* starting for P_{14} with $t1$, then $t2$, *etc.*). Finally, the $(\gamma_{\text{cov}}^{\text{P}_{14}} - \gamma_{\text{cov}}^{\text{P}_{24}})$ difference is calculated for every $(\mathbf{p}, T, \mu_{\text{Al}})$ condition : if the value is negative (respectively positive) then P_{14} (respectively P_{24}) is the most stable one at this condition.

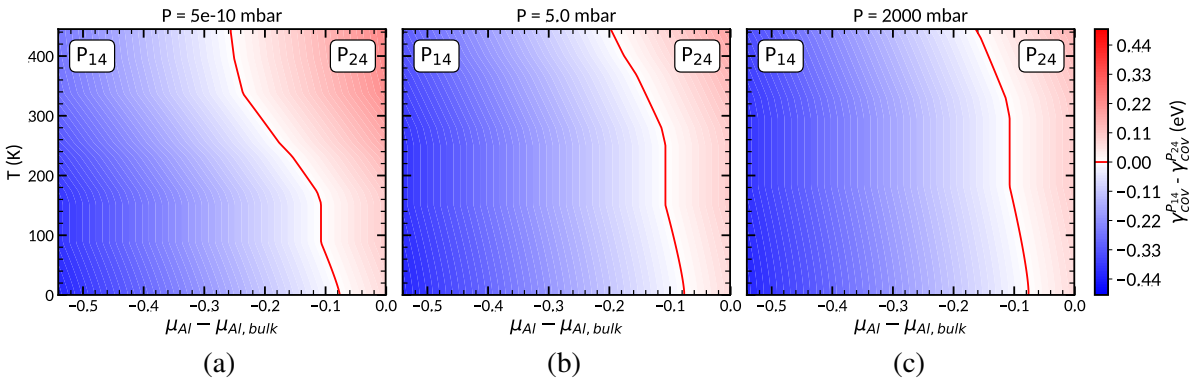


Figure 4.8: Hydrogen adsorption : surface energy differences $(\gamma_{\text{cov}}^{\text{P}_{14}} - \gamma_{\text{cov}}^{\text{P}_{24}})$ for (a) $P = 5 \times 10^{-10}$ mbar, (b) $p = 5$ mbar and (c) $p = 2$ bar. The red line corresponds to $\gamma_{\text{cov}}^{\text{P}_{14}} = \gamma_{\text{cov}}^{\text{P}_{24}}$.

The surface energy differences diagrams of hydrogenated surfaces are drawn in Fig. 4.8a–c for three different pressures, simulating UHV conditions (5×10^{-10} mbar), the reaction

conditions of ref. [8] and the industrial catalysis (2 bar) [176]. The surface energy is clearly affected by the (p,T) conditions and the hydrogen coverage.

For each domain, it is possible to know which hydrogen coverage is the optimum one. The stability phase diagrams of hydrogenated surfaces are thus drawn in Fig. 4.9a–c for the same three different pressures as before. At 300 K and under UHV conditions, the corrugated surface model appears to have an optimum coverage of 6 hydrogen atoms per surface cell. This increases up to 8 hydrogen atoms when increasing the pressure even up to 2 bar. Overall, the higher the pressure and the lower the temperature, the higher the coverage.

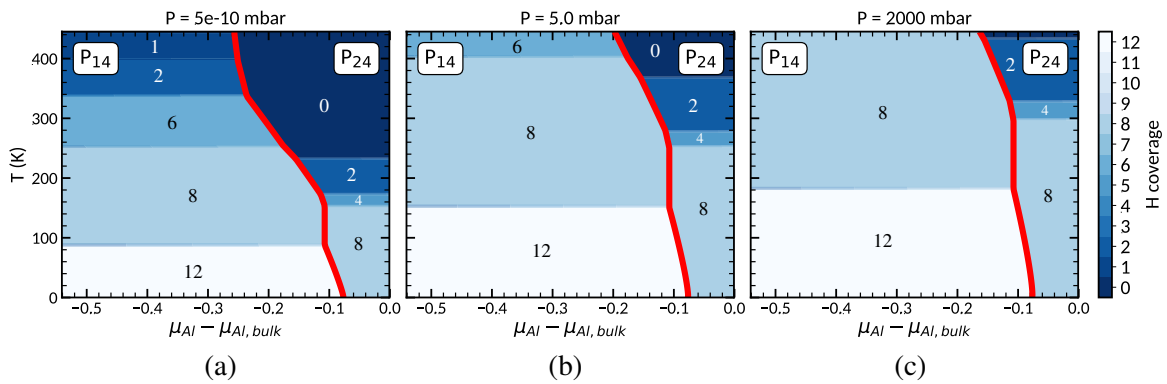


Figure 4.9: Hydrogen coverages for (a) $P = 5 \times 10^{-10}$ mbar, (b) $P = 5$ mbar and (c) $p = 2$ bar. The red line corresponds to $\gamma_{cov}^{P_{14}} = \gamma_{cov}^{P_{24}}$.

The flat surface model behaves similarly. However, the optimum coverages are overall lower. Under UHV conditions and at 300 K, no hydrogen atom can get adsorbed. For $p = 5$ mbar, only 2 atoms can be adsorbed. This increases up to 6 hydrogen atoms atom for $p = 2$ bar.

In all cases, the corrugated surface model (P_{14}) is the most stable one in the Co-rich limit while the flat surface model (P_{24}) is the most stable one in the Al-rich limit. This is similar to what was found using standard DFT ($T = 0$, $p = 0$), and is in agreement with experimental observations [88, 18]. However, the reaction conditions significantly affect the region where the P_{24} model is more stable than the P_{14} ($\gamma_{cov}^{P_{14}} \geq \gamma_{cov}^{P_{24}}$). Indeed, since atomic hydrogen adsorption is calculated to be more favorable for the P_{14} model, and since exothermic adsorption on solid surfaces contributes to reduce their surface energy, a narrowing of this region occurs, at a given T as the pressure increases, and at a given p as the temperature decreases.

4.5.3 Coadsorption of hydrogen and butadiene

Atomic hydrogen and C_4H_6 need to be simultaneously adsorbed on the surface for the hydrogenation reaction to occur according to the Langmuir–Hinshelwood mechanism [172]. Coadsorption with one butadiene molecule adsorbed per surface unit cell is considered as well as a variable surface coverage of adsorbed hydrogen atoms. The most stable isolated adsorption structure is considered for butadiene and the gas phase contains H_2 and C_4H_x ($x \in \{6, 8\}$) in the ratio 10:1 as in ref. [8]. The same type of calculations as before were performed in order to draw the surface energy differences maps presented in Fig. 4.10a–c for the same three different pressures. The surface energy is clearly affected by the (p,T) conditions and the coadsorption of hydrogen and butadiene.

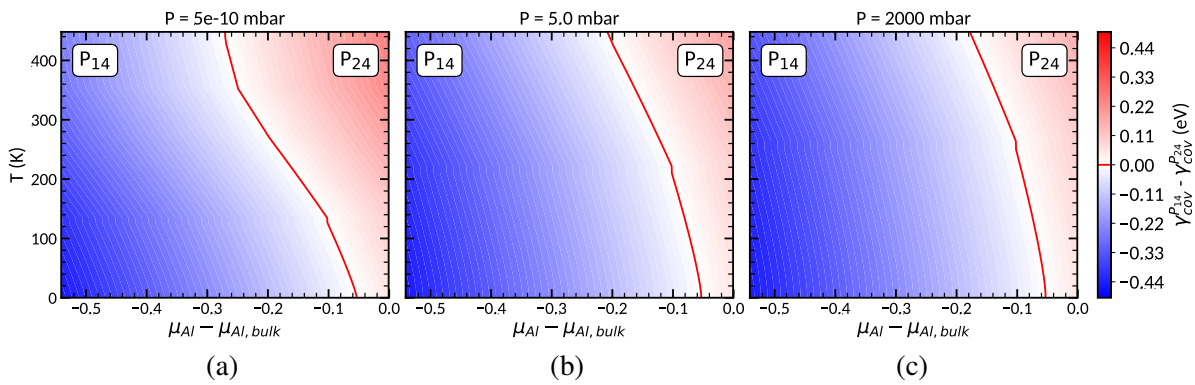


Figure 4.10: Coadsorption of hydrogen and butadiene : surface energy differences ($\gamma_{\text{cov}}^{\text{P14}} - \gamma_{\text{cov}}^{\text{P24}}$) for (a) $p = 5 \times 10^{-10}$ mbar, (b) $p = 5$ mbar and (c) $p = 2$ bar. The red line corresponds to $\gamma_{\text{cov}}^{\text{P14}} = \gamma_{\text{cov}}^{\text{P24}}$.

For each domain, it is again possible to know which hydrogen coverage is the optimum one. The stability phase diagrams of hydrogenated surfaces coadsorbed with butadiene are thus drawn in Fig. 4.11a–c for the same three different pressures as before. At 300 K and under UHV conditions, the corrugated surface model appears to have an optimum coverage of 5 hydrogen atoms per surface cell. This increases up to 6 hydrogen atoms when increasing the pressure up to 5 mbar. Overall, the trends already observed for the hydrogenated surfaces are reproduced in the coadsorption phase diagrams. The optimal hydrogen coverage is however found to be lower, due to the steric hindrance caused by the presence of the adsorbed butadiene molecule.

At this temperature ($T = 300$ K), no hydrogen atom are adsorbed on the flat surface model for a pressure below 2 bar. The temperature has to be lowered in order to start adsorbing H atoms. This suggests that this surface model is not active for the (p, T) conditions

of ref. [8].

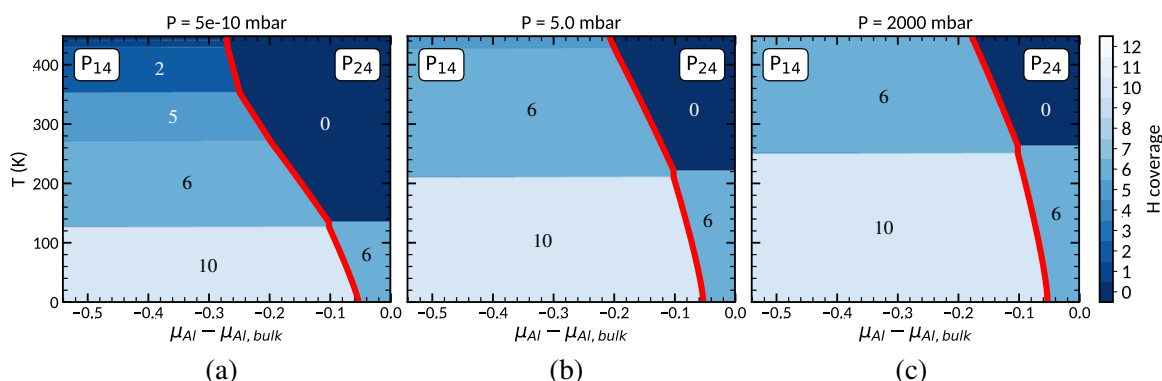


Figure 4.11: Coadsorption of hydrogen and butadiene : hydrogen coverages for (a) $p = 5 \times 10^{-10}$ mbar, (b) $p = 5$ mbar and (c) $p = 2$ bar. The red line corresponds to $\gamma_{\text{cov}}^{\text{P}_{14}} = \gamma_{\text{cov}}^{\text{P}_{24}}$.

4.6 Catalytic activation and hydrogenation reaction

4.6.1 Catalytic activation

The previous results suggest the nanostructuring of the surface under hydrogenation conditions. They indeed confirm that, in order to have adsorption of hydrogen atoms at ($T = 300$ K, $p = 5$ mbar), *i.e.* the necessary reaction condition, only the P_{14} could be considered. On top of that this surface model is the most stable one – at these pressure and temperature – on a larger range of Al chemical potential. So the clusters already present in the bulk substructure are predicted to emerge at the surface under hydrogenation conditions.

Since the P_{24} surface model was identified under UHV conditions [88, 18], and since $\text{Al}_{13}\text{Co}_4(100)$ was experimentally proved to be active and selective [8], the results predict the activation of $\text{Al}_{13}\text{Co}_4(100)$ under reaction conditions through the transition P_{24} to P_{14} .

4.6.2 Coadsorption of hydrogen and but-1-ene

The next step is the comparison of the adsorption energies of butadiene and butene, under operating conditions. We focus here on the P_{14} model only. Indeed, the P_{24} model has been found unreactive in the case of $\text{Al}_{13}\text{Co}_4(100)$, no hydrogen atom being coadsorbed with butadiene under reaction conditions.

An optimal H coverage of 6 atoms per surface cell is chosen based on the previous calculations. Site A is chosen for the butadiene configuration as it is the most stable one. The

coadsorption (six hydrogen atoms and one butadiene molecule) free enthalpy as a function of pressure and temperature is plotted in Fig. 4.12a. C_4H_6 appears to be well adsorbed ($G_{\text{coads}} < 0$) on the surface for the reaction condition ($T = 383 \text{ K}$, $p = 5 \text{ mbar}$).

Similarly to the adsorption configuration of butadiene on $\text{Al}_5\text{Co}_2(2\bar{1}0)$ (see Chapter 3 for more details), there are two ways to hydrogenate C_4H_6 that leads to two different adsorption modes of but-1-ene: chemisorption or physisorption. The coadsorption (six hydrogen atoms and one but-1-ene molecule) free enthalpy as a function of pressure and temperature are plotted in Fig. 4.12b (chemisorbed butene) and Fig. 4.12c (physisorbed butene).

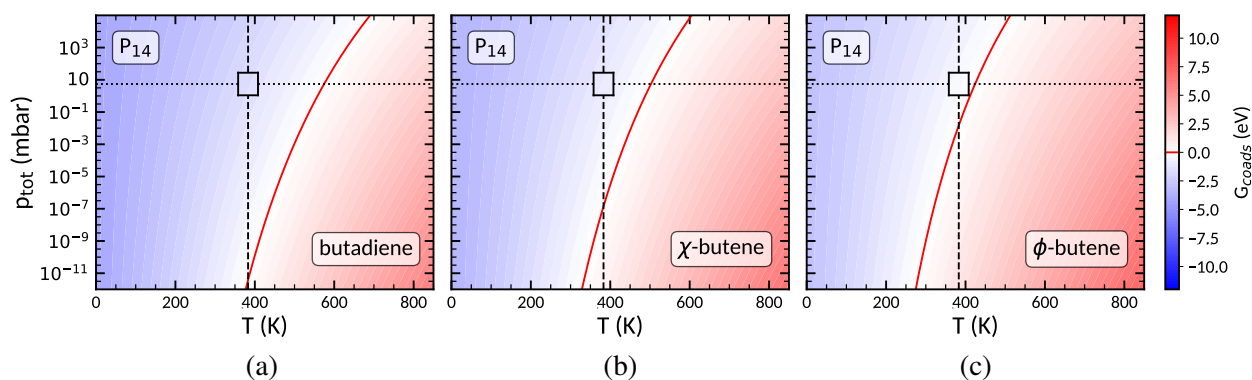


Figure 4.12: Adsorption free enthalpies (G_{coads} in eV) as a function of pressure and temperature for butadiene and butene (chemi- and physisorbed) on P_{14} for a H coverage of 6 atoms per surface cell.

In the case of chemisorbed butene, the spontaneous desorption is predicted for $T \simeq 502 \text{ K}$, which is 119 K above the experimental temperature. This behavior, obtained with chemisorbed butene resulting from the hydrogenation of the $\text{C}=\text{C}$ bond not bounded to the protruding surface Co atoms, is not consistent with the experimental observations showing 100% butene selectivity [8]. In contrast, the hydrogenation of the $\text{C}=\text{C}$ fragment bounded to the protruding surface Co atoms leads to physisorbed butene, weakly coadsorbed on the surface. Here, the spontaneous desorption is predicted for $T \simeq 420 \text{ K}$, *i.e.* only 37 K above the experimental temperature. Hence, these results favor the hypothesis of protruding Co atoms as active hydrogenation sites.

To summarize, the hydrogenation reaction is calculated to be thermodynamically possible with a high selectivity of Co centers thanks to the possible physisorption of but-1-ene.

4.7 Conclusion

In this study, the catalytic behavior of the $\text{Al}_{13}\text{Co}_4(100)$ surface towards butadiene partial hydrogenation is rationalized. On the basis of surface phase diagrams determined through DFT calculations, it is shown that the (p, T, μ_{Al}) conditions where the $\text{Al}_{13}\text{Co}_4(100)$ dense Al-rich flat termination is the most stable narrow as the pressure increases and the temperature decreases. Moreover, the dense Al-rich flat termination of $\text{Al}_{13}\text{Co}_4(100)$ is unlikely under hydrogenation conditions, and the adsorption of butadiene inhibits any further adsorption of hydrogen at the surface, which prevents butadiene hydrogenation. According to atomistic thermodynamics, the reaction conditions promote a nanostructured surface termination, in the form of highly cohesive clusters emerging from the bulk lattice.

The comparison of butadiene and butene adsorption modes and energies under thermodynamic conditions give insights of the catalytic behavior of $\text{Al}_{13}\text{Co}_4(100)$. According to the calculations, butene may not desorb when chemisorbed through a π bonding involving a Co atom protruding at the surface. A better agreement with the experimental observation is obtained with the hydrogenation of the butadiene C=C fragment adsorbed on the protruding Co atom. Our calculations thus suggest the attack of the π -bonded C=C fragment on the protruding Co atom first. Reaction conditions are also expected to influence the kinetics, for which further investigation is required. Experimental verification of the predicted nanostructuring requires in situ characterization (*e.g.* surface X-ray diffraction) to identify the actual working surface under gas pressure conditions.

Chapter 5

Stabilization and activation of $o\text{-Al}_{13}\text{Co}_4(010)$ through facetting

Contents

5.1	Introduction	104
5.2	Preliminary catalytic results	104
5.3	Surface experiment results	106
5.3.1	LEED analysis	106
5.3.2	AFM and STM measurements	107
5.3.3	SXRD analysis	109
5.3.4	Simulation of the reciprocal space	112
5.3.5	Experimental conclusion	114
5.4	DFT results : surface structures	115
5.4.1	$o\text{-Al}_{13}\text{Co}_4(010)$ – Flat terraces	115
5.4.2	$m\text{-Al}_{13}\text{Co}_4(\bar{2}01)$ – Facets	121
5.5	Relative stability of $\text{Al}_{13}\text{Co}_4(010)$ and $\text{Al}_{13}\text{Co}_4(100)$	123
5.5.1	Surface energies	123
5.5.2	DOS	125
5.6	Hydrogen adsorption on $\text{Al}_{13}\text{Co}_4$	126
5.7	Conclusions and perspective	128

5.1 Introduction

The surface structure as well as the adsorption properties of *o*-Al₁₃Co₄(010) is experimentally and theoretically investigated in this fifth chapter. This pseudo-twofold (Al₁₃Co₄ being an approximant of *d*-AlNiCo quasicrystal) surface exhibits efficient catalytic properties towards the semi-hydrogenation of butadiene [8]. Its activity was found much larger than the one of the pseudo-tenfold orientation, and a 100% selectivity to butene was achieved [8]. While the pseudo-tenfold surface has been extensively studied these last years [87, 88, 177, 18, 171], very few is known about the *o*-Al₁₃Co₄(010) pseudo-twofold surface structure and properties. A combination of surface science techniques, including SXRD and STM, combined with DFT calculations, is used in this study.

Fig. 5.1 presents the bulk structure of Al₁₃Co₄ (more details can be found in Chapter 1). Here an orthorhombic crystal of Al₁₃Co₄ is used, whose structure belong to the *Pmn*2₁ space group (No. 31, Pearson symbol *oP*102) and whose crystal cell is defined with the following lattice parameters: $a_o = 8.158 \text{ \AA}$, $b_o = 12.342 \text{ \AA}$, and $c_o = 14.452 \text{ \AA}$ (102 atoms per cell, Fig. 5.1a/c) [20, 12]. The *o*-Al₁₃Co₄ compound is known to be unstable at low temperatures, but stabilized at higher temperatures by the entropy of Al vacancy hopping and low frequency vibrational modes [93]. Monoclinic *m*-Al₁₃Co₄ crystallizes in the *C2/m* space group (No. 12, Pearson symbol *mC*102, Fig. 5.1b/d) with the lattice parameters: $a_m = 15.173 \text{ \AA}$, $b_m = 8.109 \text{ \AA}$, $c_m = 12.349 \text{ \AA}$ and $\beta = 107.84^\circ$ [16]. Because of the relatively close structures of orthorhombic and monoclinic Al₁₃Co₄, their coexistence is possible and can give rise to defects. Metadislocations, due to plastic deformations [97, 98, 99, 100], as well as twins [95], are frequent in complex intermetallic phases. Twins in Al₁₃Co₄ are generally related to orthorhombic/monoclinic interfaces. In the following, ideal structures with full atomic occupations are considered.

5.2 Preliminary catalytic results

The clean annealed surface of Al₁₃Co₄(010) is exposed to a mixture of hydrogen (5 mbar) and butadiene (0.5 mbar) under batch conditions at 24°C (RT) and 110°C. Fig. 5.2 shows the results of the experiment (see also Fig. 1.26 in Chapter 1). The reaction kinetics is slow at RT, *i.e.* only a small fraction of butadiene was converted after ca. 30 min, so that the tests at 110°C are generally performed during the same reaction run. Fig. 5.2a shows that the selectivity of Al₁₃Co₄(010) to butenes is 100%, both at RT and 110°C, butane being formed only after complete butadiene conversion. Butene hydrogenation to butane is always slow both at 110°C.

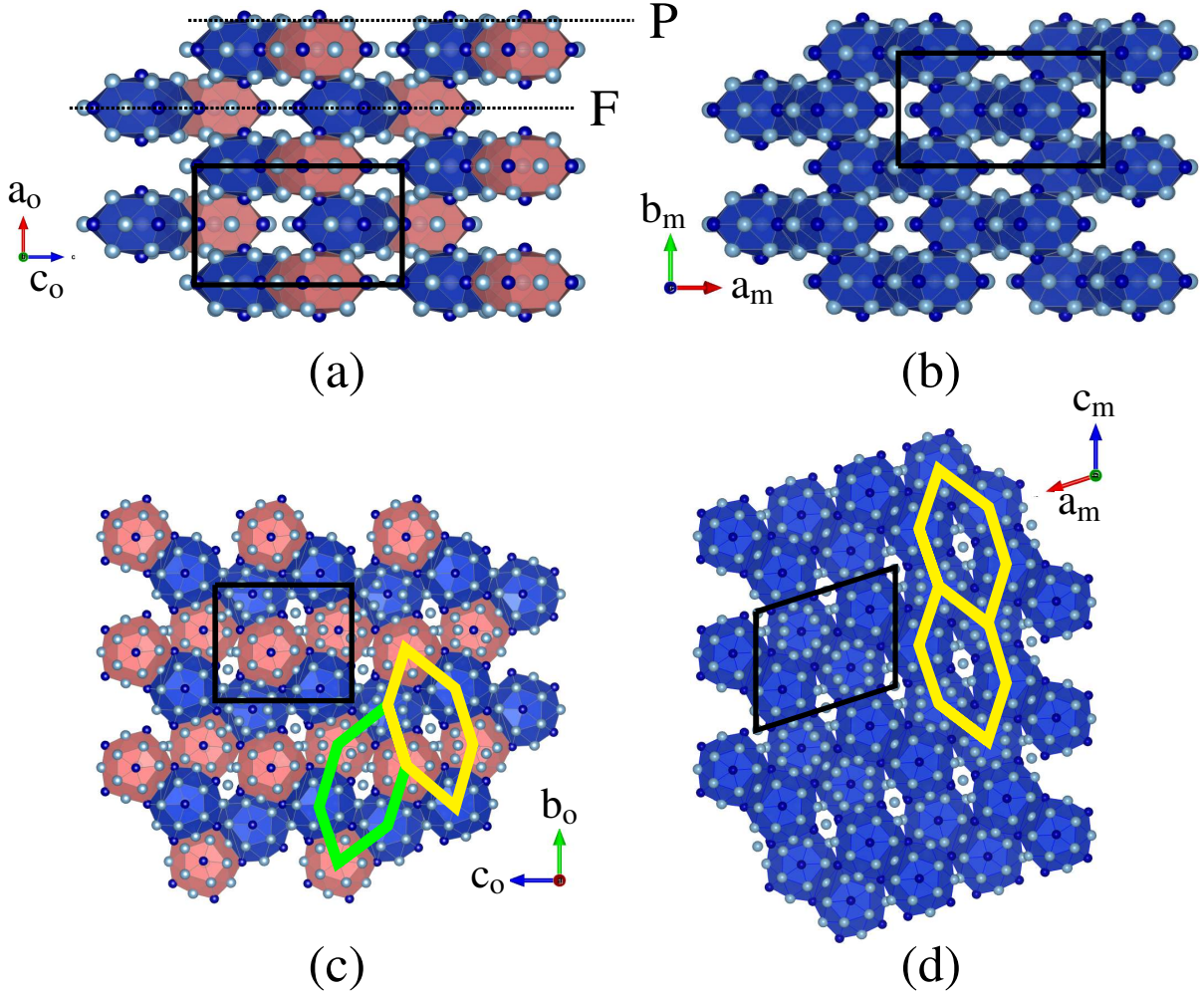


Figure 5.1: Bulk structure of (a) $o\text{-Al}_{13}\text{Co}_4$ along the $o\text{-}[010]$ direction showing the Henley-type clustering (in red and blue, both clusters are not crystallographically equivalent, the Al atoms in the center of the clusters do not have the same Wyckoff position, as detailed in the Appendices) as well as the stacking structure of F-type and P-type atomic planes, (b) $m\text{-Al}_{13}\text{Co}_4$ along the $m\text{-}[001]$ direction showing the Henley-type clustering (in blue, all the clusters are crystallographically equivalent, the Al atoms in the center of the clusters have the same Wyckoff position, as detailed in the Appendices), (c) $o\text{-Al}_{13}\text{Co}_4$ along the pseudo-tensfold axis (the squashed-hexagonal tile, obtained by connecting together all Co atoms of the P-type plane, is highlighted in yellow and green) and (d) $m\text{-Al}_{13}\text{Co}_4$ structure along the pseudo-tensfold axis. Unlike $o\text{-Al}_{13}\text{Co}_4$ all hexagons of the hexagonal tile in the P-type plane have the same orientation in $m\text{-Al}_{13}\text{Co}_4$. The unit cells, Al and Co atoms are drawn in black, light blue and dark blue, respectively.

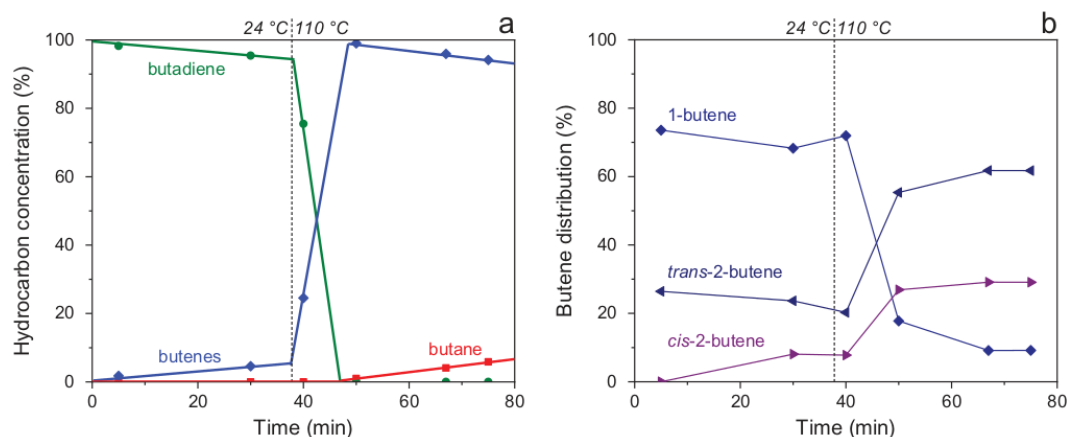


Figure 5.2: Hydrocarbon concentrations (a) and butene distribution (b) during butadiene hydrogenation over $\text{Al}_{13}\text{Co}_4(010)$ at 24°C, then 110°C [8]. The data points were obtained from GC analysis in (b), whereas it was obtained from MS in (a).

In terms of initial butene distribution at 24°C (but-1-ene:trans-2-butene:cis-2-butene = 74:26:0%, Fig. 5.2b), cis-2-butene is not a primary product and its fraction remains lower than 10% throughout the reaction, as long as butadiene is present in the reactor, at both investigated temperatures. After butadiene conversion, the butenes distribution evolves towards a near-equilibrium value, 9:62:29%, through isomerization.

$\text{Al}_{13}\text{Co}_4(010)$ is much more active than $\text{Al}_{13}\text{Co}_4(100)$ both at 24°C and 110°C [8]. Whereas in terms of activity at 24°C $\text{Al}_{13}\text{Fe}_4(010)$ has no rival, $\text{Al}_{13}\text{Co}_4(010)$ appears as the most active system at 110°C while keeping a butene selectivity of 100% at any temperature [8]. The structure of $\text{Al}_{13}\text{Co}_4(010)$ under UHV, if retained under reaction conditions, may play an important role in its good catalytic performance. Nevertheless $\text{Al}_{13}\text{Co}_4(010)$ contains, after reaction, not only oxygen but also traces of carbon (determined through Auger electron spectroscopy).

5.3 Surface experiment results

5.3.1 LEED analysis

According to LEED measurements, a (1×1) surface structure is mainly observed (Fig. 5.3). Diffuse scattering resembling a (2×1) and a (3×1) surface reconstructions is also visible beside the (1×1) surface structure (Fig. 5.4a). When scanning the energy range 5–300 eV, secondary peaks appear and move away from the center in between the main diffraction spots. They are attributed to the presence of facets at the surface : the facets diffused rods, tilted

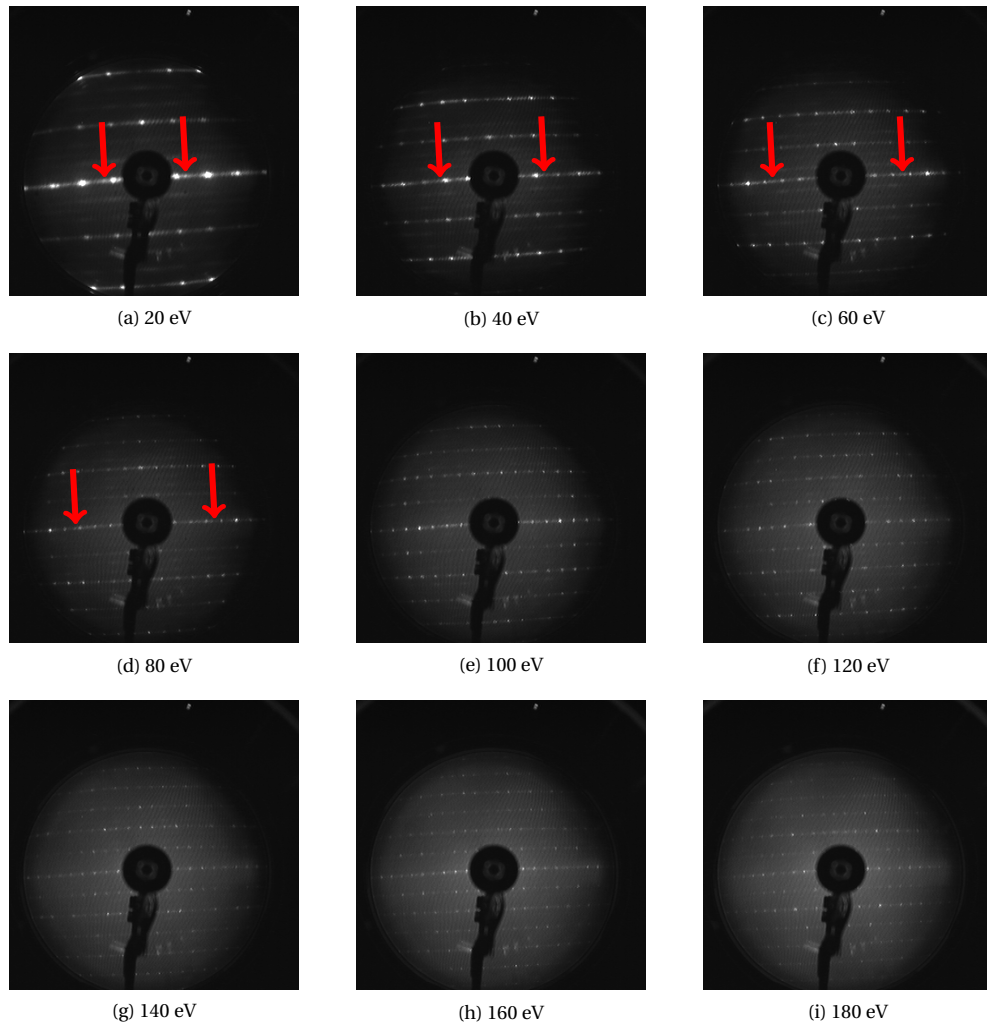
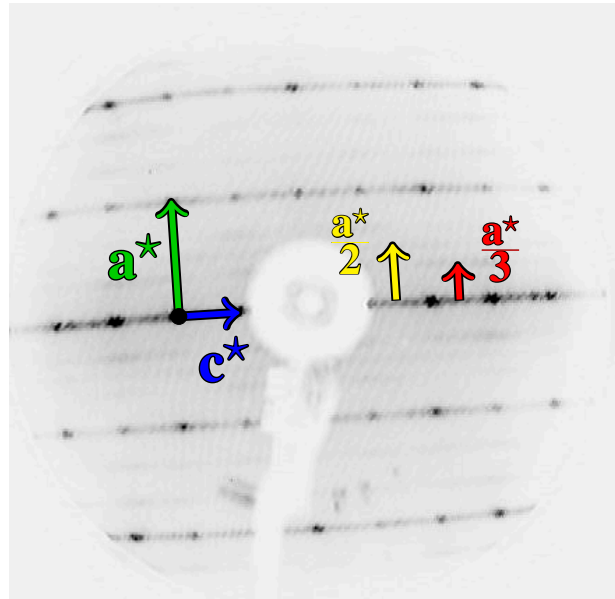


Figure 5.3: LEED patterns measured at (a) 20 eV, (b) 40 eV, (c) 60 eV, (d) 80 eV, (e) 100 eV, (f) 120 eV, (g) 140 eV, (h) 160 eV and (i) 180 eV. The facets spots are indicated using red arrows for (a), (b), (c) and (d).

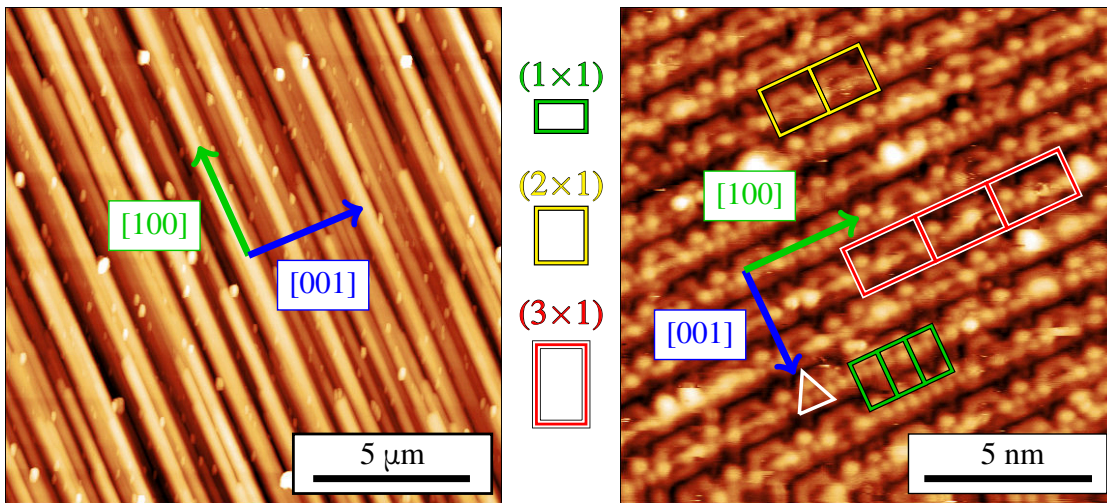
with respect to the average surface CTRs, intercept the Ewald sphere at different points when increasing/decreasing the energy, giving rise to points that "move" between the (1×1) structure points. Continuous intensity can also be seen in between the main diffraction spots. This signal could be linked to line or planar defects such as metadislocations or interfaces close to the surface.

5.3.2 AFM and STM measurements

According to AFM, a columnar structure appears along the o -[100] direction as shown in Fig. 5.4(b). This feature is similar to that observed at the (12110) and (10000) two-fold d -Al-Ni-Co quasicrystalline surfaces [178], revealing faceting at the o -Al₁₃Co₄(010) surface. Ac-



(a) LEED pattern



(b) AFM image

(c) STM image

Figure 5.4: (a) LEED pattern measured at 30 eV. Diffuse scattering resembling a (2×1) and a (3×1) surface reconstructions are shown in yellow and red arrows, respectively. (b) AFM image of $o\text{-Al}_{13}\text{Co}_4(010)$ ($15\times 15\ \mu\text{m}^2$) showing a columnar and faceted structure. (c) STM image of a flat terrace at the $o\text{-Al}_{13}\text{Co}_4(010)$ surface ($15\times 15\ \text{nm}^2$) at $V_b = 0.6\ \text{V}$. The (1×1) , (2×1) and (3×1) cells are drawn in green, yellow and red, respectively. A triangular motif is highlighted in white.

According to STM, terraces extend over a few hundreds of nanometers, separated by a single-step height equal to $6.1 \pm 0.2 \text{ \AA}$, *i.e.* corresponding to half of the lattice parameter ($b_o/2 = 6.17 \text{ \AA}$). High-resolution images (Fig. 5.4c) show a mixture of three different surface reconstruction motifs, in agreement with the LEED pattern, randomly distributed on the sample surface: (1×1) , (2×1) and (3×1) . These reconstructions may be due to local vacancies stabilization. For the (1×1) surface structure, a triangular motif is observed (white triangle in Fig. 5.4(c)).

5.3.3 SXR D analysis

5.3.3.1 In-plane and out-of-plane measurements

A large part of the reciprocal space was completely measured during the SXR D experiment: $|H_{\max}| = 9.5$, $|K_{\max}| = 5.5$ and $L_{\max} = 4.8$. The o -(010) surface orientation is confirmed by the in-plane reciprocal space map of o - $\text{Al}_{13}\text{Co}_4$ (Fig. 5.5). A total of 34 inequivalent CTRs were extracted from the measured reciprocal space region and further compared to DFT-based simulations using different surface structure models (see section page 118). Fig. 5.6 presents two out-of-plane (H,L) reciprocal space maps of o - $\text{Al}_{13}\text{Co}_4$ (010) at $K = 2$ and $K = 3$ (more data can be found in the Appendices Figs. D.1 and D.2). The facets' signal is clearly visible in the map at $K = 2$: the facets' rods make an angle of 54.2° with the direction normal to the surface (indicated with green and red arrows in Fig. 5.6). The facet's rods do not intercept each other at the Bragg peaks of the orthorhombic structure (labeled with black circles), meaning that the facets do not present the o - $\text{Al}_{13}\text{Co}_4$ structure. Facets are therefore related to the m - $\text{Al}_{13}\text{Co}_4$ structure. Two types of twin domains are considered, the positions of their respective diffraction peaks are plotted in red and green circles (Fig. 5.6). The facets' rods intercept the m - $(\bar{2}21)$ diffraction peaks. The facets are therefore consistent with a m - $(\bar{2}01)$ orientation. Their signal is less clearly visible on the maps at an odd value of K but is still present. These conclusions are consistent with the fairly continuous intensity measured in between Bragg peaks along the H direction for integer values of K and L (similar observation as in LEED measurements, Figs. 5.4, 5.5 and 5.6). This kind of signal can be produced by planar defects such as interfaces between two phases. It is reasonable to assume these planar defects to be monoclinic/orthorhombic interfaces.

5.3.3.2 Diffuse scattering

Additional information can be extracted from SXR D. Intensity is observed in between integer values of K (indicated by a yellow rectangle in Fig. 5.5 for $K = 3.5$). Complementary

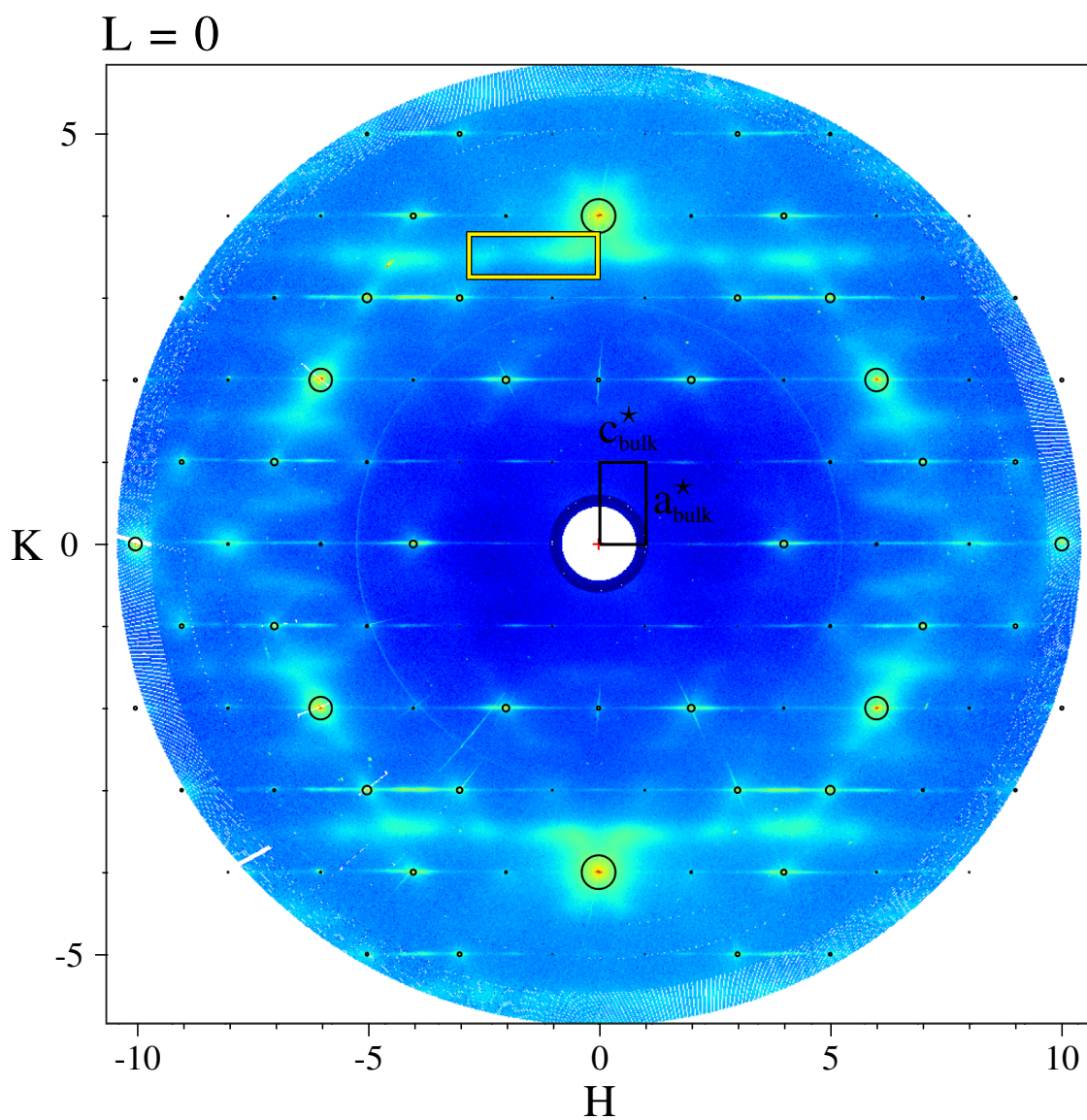


Figure 5.5: In-plane (H,K) reciprocal space map of $o\text{-Al}_{13}\text{Co}_4$. The diffraction spots of the orthorhombic phase are indexed with black circles. The region presented in Fig. 5.7 is highlighted in yellow.

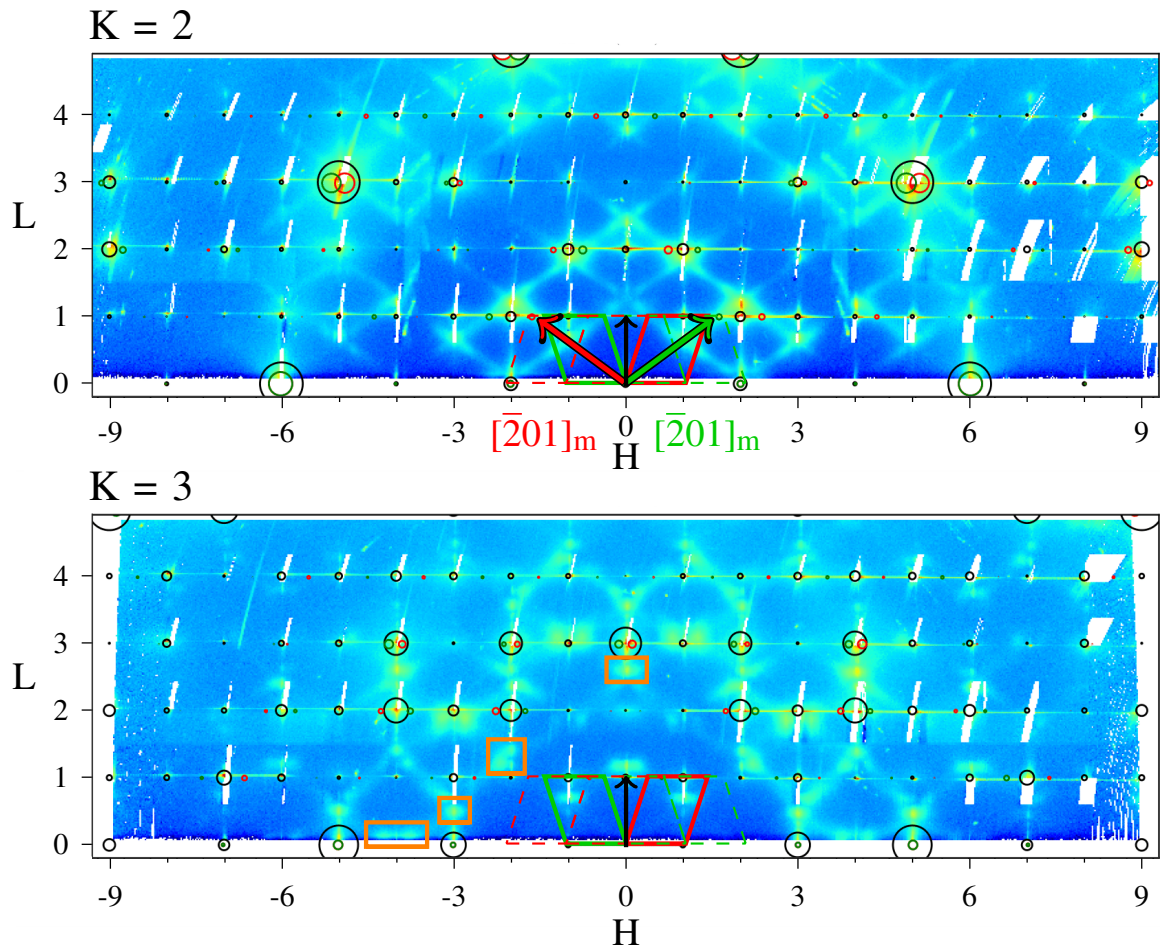


Figure 5.6: Out-of-plane (H,L) – for $K = 2$ and $K = 3$ respectively – reciprocal space maps of $o\text{-Al}_{13}\text{Co}_4$. The position of the monoclinic diffraction spots are represented in green and red circles (two different domains). Facets appear to present the $m\text{-}\bar{2}01$ orientation (red and green arrows). The monoclinic cells are drawn in red and green depending on the domain. Additional monoclinic cells are displayed using dashed lines for a better understanding of the $m\text{-}\bar{2}21$ directions. Blank regions are areas where the signal was too intense to be collected (too close to Bragg peaks).

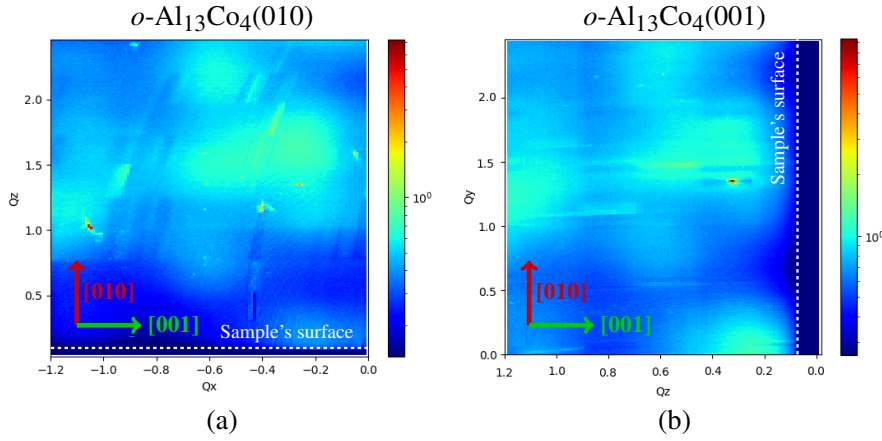


Figure 5.7: Portion of out-of-plane reciprocal space map along $[100]$ at $Q = 2.7 \text{ \AA}^{-1}$ for (a) $o\text{-Al}_{13}\text{Co}_4(010)$ and (b) for $o\text{-Al}_{13}\text{Co}_4(001)$. These two area of the reciprocal space are the same for $o\text{-Al}_{13}\text{Co}_4(010)$ and $o\text{-Al}_{13}\text{Co}_4(001)$.

SXRD analysis on another surface orientation – $o\text{-Al}_{13}\text{Co}_4(001)$, using a single crystal also grown by the Czochralski process, shows a similar diffuse scattering in between integer values of K . Fig. 5.7 displays the same reciprocal space area (yellow rectangle in Fig. 5.5) for (a) $o\text{-Al}_{13}\text{Co}_4(010)$ and (b) $o\text{-Al}_{13}\text{Co}_4(001)$. This section is a plane along the $[100]$ direction at $Q = 2.7 \text{ \AA}^{-1}$. The fact that the diffuse scattering is almost identical in both cases suggests that this signal mainly comes from the bulk material and not from the surface.

5.3.4 Simulation of the reciprocal space

Other distinct features can be seen in the (H,L) map for $K = 2$ and a few examples of them are framed in orange in Fig. 5.6. They are neither part of the orthorhombic nor of the monoclinic (facets) lattices. The following hypothesis is made : these features are due to the defects induced by monoclinic/orthorhombic interfaces.

First of all, it is of interest to mention that the formation of monoclinic/orthorhombic interfaces is calculated to be exothermic ($E_{\text{int}}^{\text{m/o}} = -4 \text{ mJ/m}^2$). Thus, they stabilize the structure, which may explain why they are naturally and profusely present in the bulk compound. For comparison purposes, the formation energy of monoclinic/monoclinic interfaces is endothermic ($E_{\text{int}}^{\text{m/m}} = 50 \text{ mJ/m}^2$). The calculations are done using slabs of 2 unit cells : either 2 monoclinic cells forming a $(20\bar{1})$ twin (Fig. 1.17 in Chapter 1), or one orthorhombic cell and one monoclinic cell thus forming an interface.

It was shown that the coexistence of monoclinic and orthorhombic structures can lead to the formation of metadislocations (see Chapter 1 for more details). Heidelmann *et al.* [100] have build and relaxed a system that fits well the experimental measurements of a metadis-

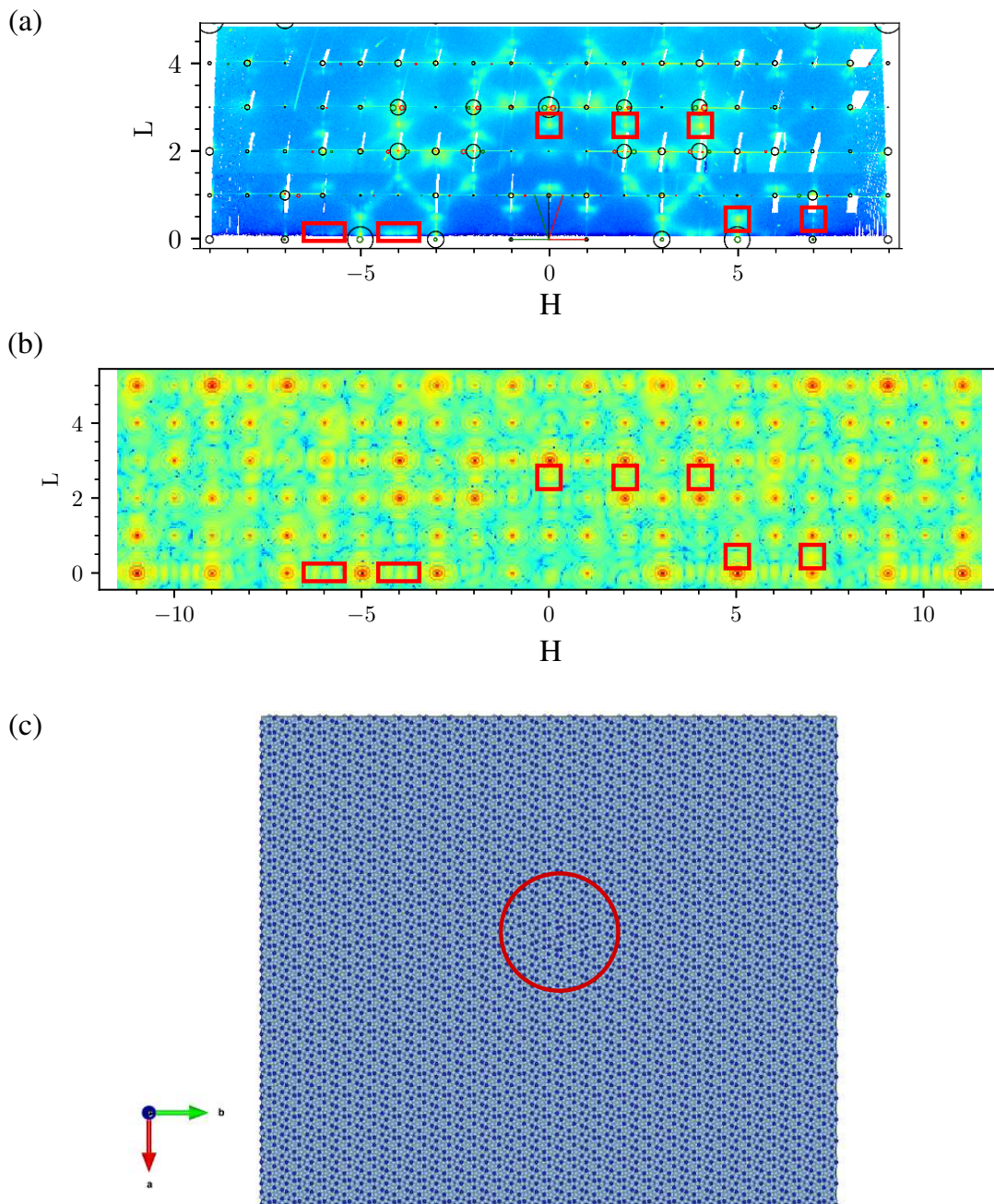


Figure 5.8: (a) (H,L) out-of-plane reciprocal space maps for $K = 3$ of $o\text{-Al}_{13}\text{Co}_4(010)$. (b) Simulated out-of-plane maps for $K = 3$: FT simulation of a $23 \times 23 \times 1$ orthorhombic cell with a core dislocation in the center of the cell. Features that do not come from the orthorhombic structure are highlighted in red for both figures (a) and (b). Similarities between the measurements and the simulation are observed. (c) Atomic structure of the FT $23 \times 23 \times 1$ simulation box: Al and Co atoms are drawn in light blue and dark blue, respectively; the metadislocation core is circled in red.

location in $\text{Al}_{13}\text{Co}_4$. A similar atomic structure – based on the dislocation model of Heidelbergmann *et al.* [100] – is displayed in Fig. 5.8c (see Fig. 1.20 in Chapter 1 for more details on the construction of the defect) and is used to simulate the reciprocal space of a metadislocation. A simulation of the Fourier transform of a $\text{Al}_{13}\text{Co}_4$ metadislocation is therefore done and shown in Fig. 5.8b. The script of the simulation and more simulation results can be found in the Appendices (Figs. D.3 and D.4). The comparison with the experimental diffraction measurements (Fig. 5.8a) shows there are similarities between the simulation and the SXRD data (highlighted in red). This results proves that the features displayed in orange in Fig. 5.6 may therefore be generated by defects such as metadislocations. This kind of diffraction peaks and diffuse scattering might also be generated by periodically stacked phason planes (related to metadislocations) but the simulation was not performed in this work.

5.3.5 Experimental conclusion

To summarize, the SXRD analysis led to a macroscopic surface structure model for $o\text{-Al}_{13}\text{Co}_4(010)$. It consists in a coexistence of orthorhombic (flat terraces) and monoclinic (facets) structures at the surface separated by monoclinic/orthorhombic interfaces, as well as the possible presence of metadislocations close to the surface (Fig. 5.9).

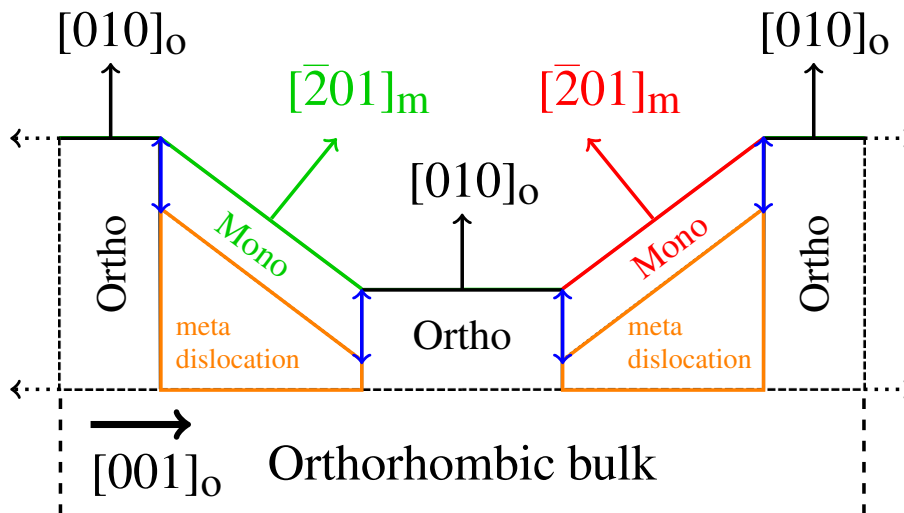


Figure 5.9: Schematic of the suggested surface model based on the experimental observations. Orthorhombic flat terraces and monoclinic facets coexist in this model and are drawn in black and red/green (two different twin domains), respectively. Monoclinic/orthorhombic interfaces are represented in blue. Metadislocations are displayed in orange.

5.4 DFT results : surface structures

5.4.1 $o\text{-Al}_{13}\text{Co}_4(010)$ – Flat terraces

Bulk $o\text{-Al}_{13}\text{Co}_4$ cannot be described as a stacking of well-separated atomic layers along the o -[010] direction. The strategy to build surface models was then the following. First, eight bulk truncated models – almost regularly spaced along [010] – were considered (labeled O_0 to $O_{5.7}$ in Fig. 5.10, depending on the distance in Å to the center of the cell, *e.g.* 0.6 Å). Variations of models $O_{0.6}$ and $O_{1.2}$ (named $O_{0.6}^i$ and $O_{1.2}^i$) were then considered, based on the refinement of the most stable models identified in the first step. Thus, a total of 17 models were investigated. Their surface atomic structures are drawn in Fig. 5.11. Because of the symmetry (glide mirror) along o -[010], only half of a unit cell was investigated.

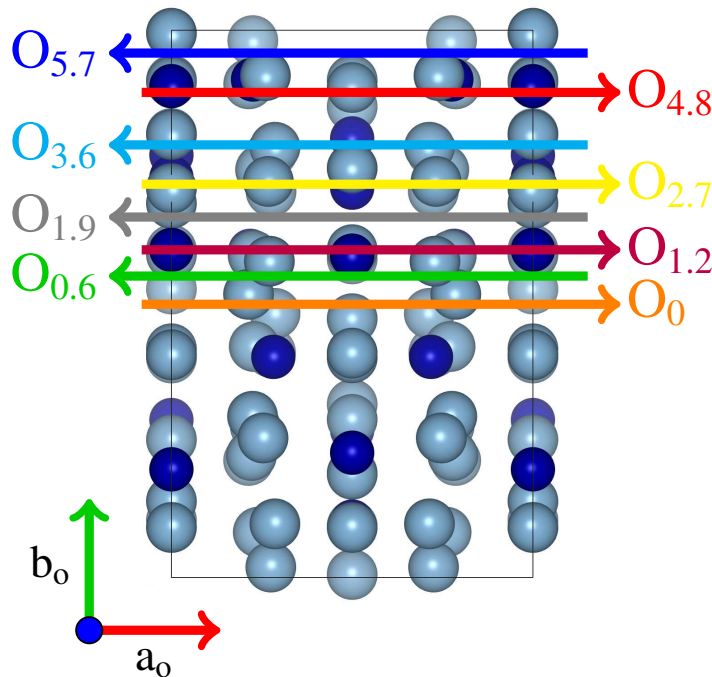


Figure 5.10: $o\text{-Al}_{13}\text{Co}_4(010)$ bulk truncation models that were considered.

The surface energies of the considered models are summarized in Fig. 5.12. Less stable models, *i.e.* $O_{1.2}^3$ and $O_{3.6}$, with the largest surface energies (between 2.2 and 2.38 J/m²), as well as $O_{1.2}^1$, $O_{1.2}^2$, $O_{1.2}^4$ and $O_{2.7}$, with surface energies ranging from 1.86 to 2.24 J/m², present low atomic density terminations combined with the presence of isolated Co. The surface energies for models with higher surface atomic density ($O_{0.6}$, $O_{0.6}^i$, $O_{1.9}$, $O_{4.8}$ and $O_{5.7}$) are smaller: they range from 1.72 to 2.02 J/m². Several models keep intact at their sur-

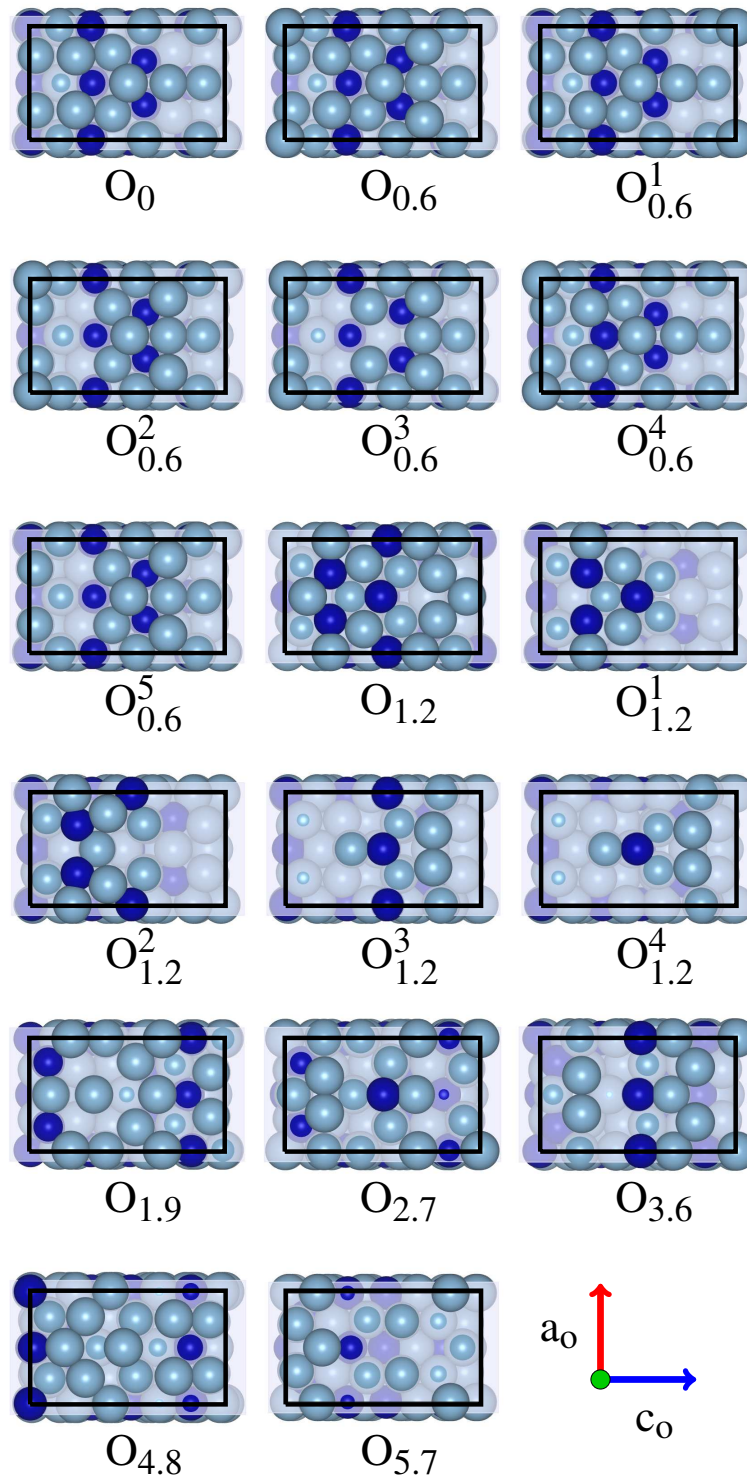


Figure 5.11: Surface structure models O_0 to $O_{5.7}$. Unit cells, Al and Co atoms are drawn in black, light blue and dark blue, respectively.

face the strong covalent-like Co–Al–Co linear molecular groups : O_0 , $O_{0.6}^1$, $O_{0.6}^4$, $O_{1.2}$, $O_{1.2}^1$ and $O_{1.2}^2$. They are found to be amongst the 8 most stable surface models for the whole range of allowed chemical potentials. The surface energy of the most stable model (O_0) is quite lower than the other considered models. It does not depend on the chemical potentials (1.66 J/m^2), since the stoichiometry of the slab used for the calculation is the one of the bulk crystal. It is described as a flat termination consisting of rows of protruding triangular motifs made of aluminum atoms separated by a 6.5 \AA gap, while maintaining intact the strongly bound Co–Al–Co molecular group at the surface.

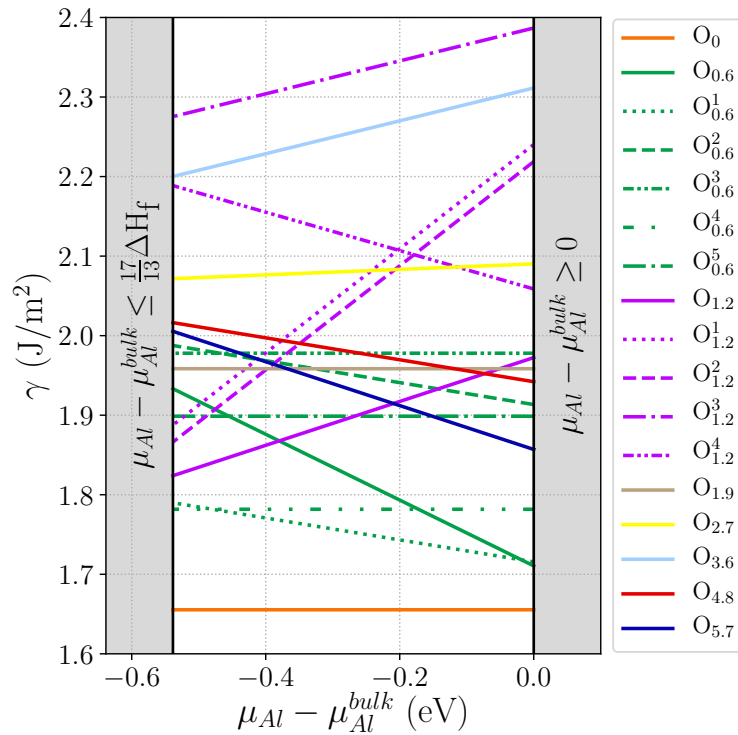


Figure 5.12: Surface energies of 17 surface models for $o\text{-Al}_{13}\text{Co}_4(010)$ as a function of $\mu_{\text{Al}} - \mu_{\text{Al}}^{\text{bulk}}$.

Five models (O_0 , $O_{0.6}^3$, $O_{0.6}^5$, $O_{1.2}^3$ and $O_{1.2}^4$) present a similar three-atoms triangular motif (either three Al atoms or one Co and two Al atoms). Among them, the three O_0 , $O_{0.6}^3$, $O_{0.6}^5$ models are the most stable. The surface energy of the most stable model (O_0) does not depend on the chemical potentials (1.66 J/m^2), since the stoichiometry of the slab used for the calculation is the one of the bulk crystal. All of the other models presents higher surface energies. Models $O_{1.2}^3$ and $O_{3.6}$ have the highest surface energies (between 2.2 and 2.38 J/m^2) and present both a low atomic surface density as well as isolated Co atoms. This is also the case for models $O_{1.2}^1$, $O_{1.2}^2$, $O_{1.2}^4$ and $O_{2.7}$ which have low atomic surface densities and relatively isolated Co atoms. Their surface energies range from 1.86 to 2.24 J/m^2 . Other models

which present higher atomic surface density (models $O_{0.6}$, $O_{0.6}^i$, $O_{1.9}$, $O_{4.8}$ and $O_{5.7}$) have surface energies ranging from 1.72 to 2.02 J/m². Overall, a low atomic surface density combined with the presence of isolated Co atoms give rise to high surface energies. However the surface energy of $O_{1.2}^4$ is higher than the one of O_0 . Complementary analysis is needed to discriminate between those two models.

As presented in Fig. 5.9, the twofold surface of $\text{Al}_{13}\text{Co}_4$ consists in flat terraces of $o\text{-Al}_{13}\text{Co}_4(010)$ and facets, identified as $m\text{-Al}_{13}\text{Co}_4(\bar{2}01)$. Focusing on the $o\text{-Al}_{13}\text{Co}_4(010)$ surface, the O_0 has been identified as a stable surface model with a rather low surface energy (1.66 J/m²). To complete the thermodynamic approach, STM images (Fig. 5.13) and SXRD rods (Fig. 5.14, Tab. 5.1) are simulated using stable surface models.

STM images of the most stable models (O_0 , $O_{0.6}$, $O_{0.6}^i$, $O_{1.2}$, $O_{1.2}^i$ and $O_{5.7}$) have been simulated (Fig. 5.13) and compared to both the experimental measurements and their filtered (2D FFT) counterparts. On the 2D FFT filtered image, rows of triangular motifs separated by a 0.65 nm gap are observed. Only five models reproduce relatively well this feature : O_0 , $O_{0.6}^3$, $O_{0.6}^5$, $O_{1.2}^3$ and $O_{1.2}^4$, because the atomic arrangement at the surface include a triplet made of either Al_3 or CoAl_2 atomic ensembles. In most cases – the O_0 , $O_{0.6}^3$ and $O_{0.6}^5$ are good examples – the bright/dark protrusions are due to atoms slightly above/below the mean position of the termination plane. So far, the STM image simulated using the O_0 or $O_{1.2}^4$ models show the best agreement with the experimental one.

The structure factors of the 34 inequivalent CTRs extracted from the X-ray diffraction measurements were simulated using the DFT-relaxed surface models. Four models were tested (O_0 , $O_{0.6}$, $O_{0.6}^1$ and $O_{1.2}^4$) based on the surface energy calculations and the STM image simulations. As shown in Tab. 5.1, O_0 is overall the best fitting surface model having the lowest χ^2 and R-factor values (Fig. 5.14) and reproduce quite well a lot of observed features. This model consists in a flat termination with rows along the [100] (pseudo-tenfold) direction, made of protruding triangular motifs of aluminum atoms separated by a 6.5 Å gap. The strong anisotropy in the surface plane may reflect the one observed on twofold surfaces of decagonal quasicrystals, spanned by perpendicular periodic and aperiodic axes.

Table 5.1: X-ray diffraction results – ROD analysis.

Surface Model	O_0	$O_{0.6}$	$O_{0.6}^1$	$O_{1.2}^4$
Scale factor	0.0197	0.0199	0.0198	0.0189
χ^2	6.107	6.137	7.145	7.269
R-factor	0.466	0.469	0.505	0.504

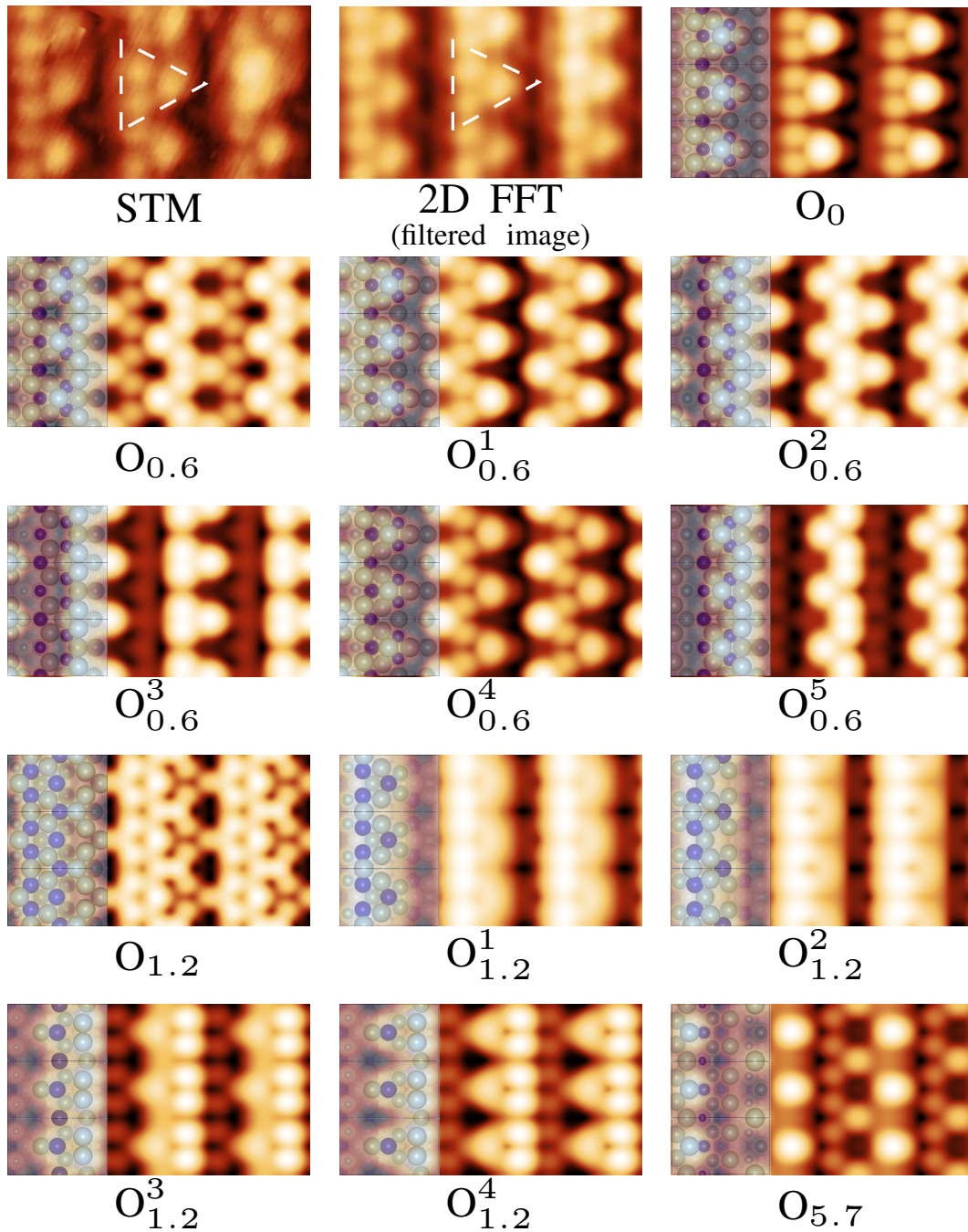


Figure 5.13: STM image simulations (models O_0 , $O_{0.6}$, $O_{1.2}$ and $O_{5.7}$) and comparison to experimental images ($V_b = 0.6$ V, 4.3×2.45 nm² area, 3×3 surface cells).

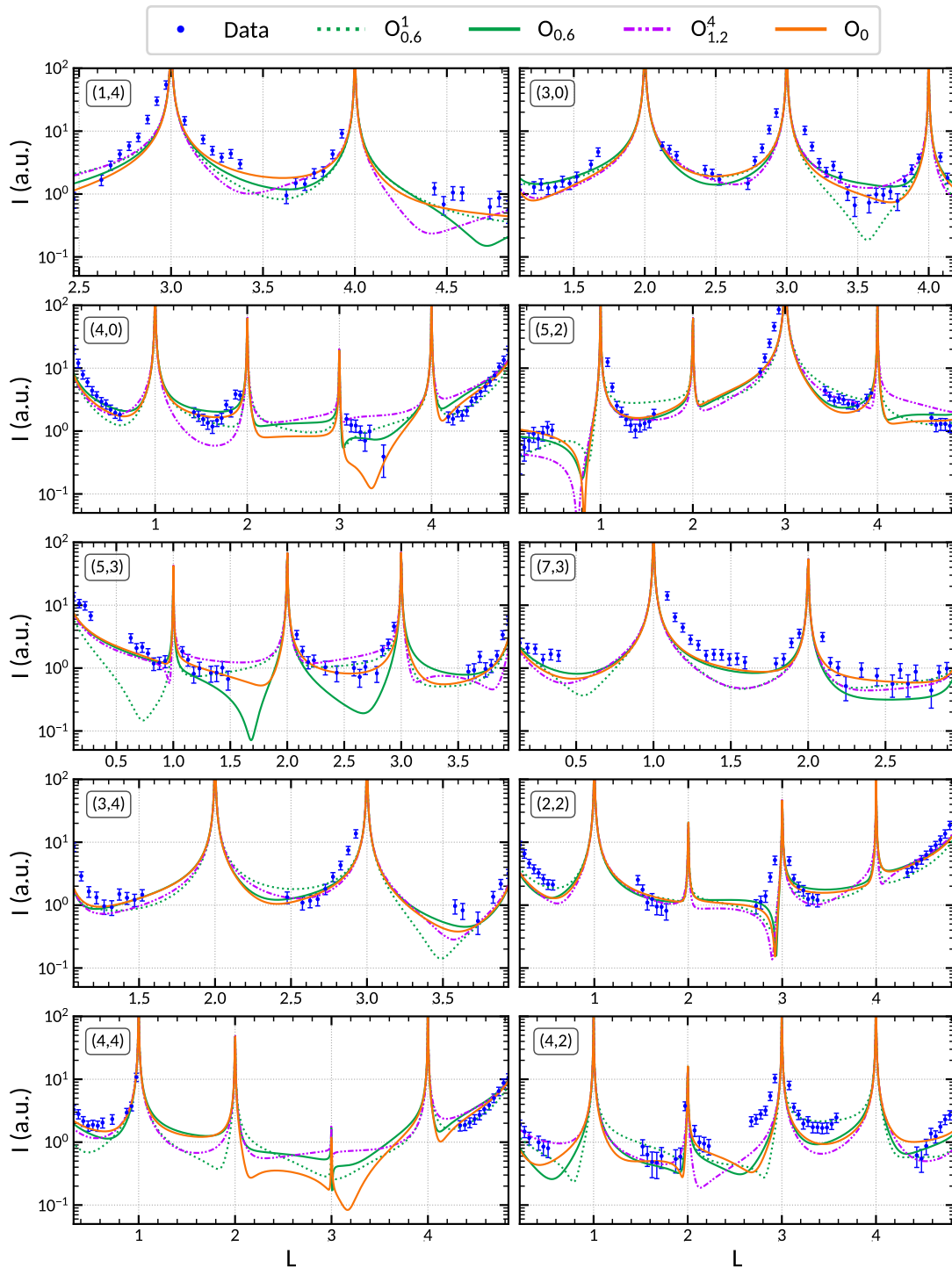


Figure 5.14: Example of six extracted CTRs of $o\text{-Al}_{13}\text{Co}_4(010)$ and their related DFT-based ROD simulation.

5.4.2 $m\text{-Al}_{13}\text{Co}_4(\bar{2}01)$ – Facets

Experimental SXRD measurements identified facets as $m\text{-Al}_{13}\text{Co}_4(\bar{2}01)$. As previously, 17 bulk truncated models – Fig. 5.15 – were built, by progressively removing atoms at the surface (labeled M_0 to $M_{7.2}$ in Fig. 5.16, with a step of 0.45 \AA , depending on the distance in \AA to the center of the cell, e.g. 7.2 \AA). Due to the symmetry of the monoclinic lattice, only half of the cell was considered. Models M_0 to $M_{1.35}$ are Al-rich surface models with a progressively increasing surface atomic density. Models $M_{1.8}$ to $M_{3.15}$, as well as models $M_{6.75}$ and $M_{7.2}$ have dense Co-rich terminations, while models $M_{3.6}$ to $M_{6.3}$ are less dense with a few Co atoms in the surface plane. The strong Co–Al–Co covalent-like bond is kept intact at the surface in models $M_{2.7}$, $M_{3.15}$, $M_{4.95}$, $M_{5.4}$, $M_{5.85}$.

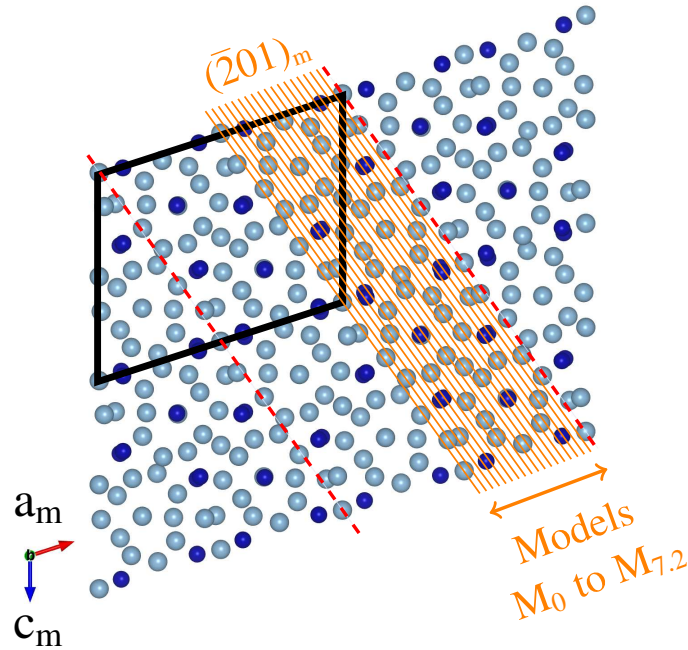


Figure 5.15: Bulk (monoclinic structure) truncation models considered in this work.

Surface energy calculations are summarized in Fig. 5.17. $M_{1.8}$ presents the highest surface energy (ranging from 1.91 to 2.39 J/m^2) due to a low atomic surface density combined with a Co-rich composition. In the Co-rich limit, the model $M_{3.15}$, which has a dense termination plane (highest surface atomic density 0.19 at/\AA^2) and keeps intact the strong Co–Al–Co covalent-like bond at the surface, clearly presents the lowest surface energy (1.19 J/m^2). In the Al-rich limit, four models present rather low surface energies: models $M_{5.85}$, $M_{3.15}$, $M_{1.35}$ and $M_{0.9}$. The most stable ones are the Al-rich models ($M_{1.35}$ and $M_{0.9}$), with

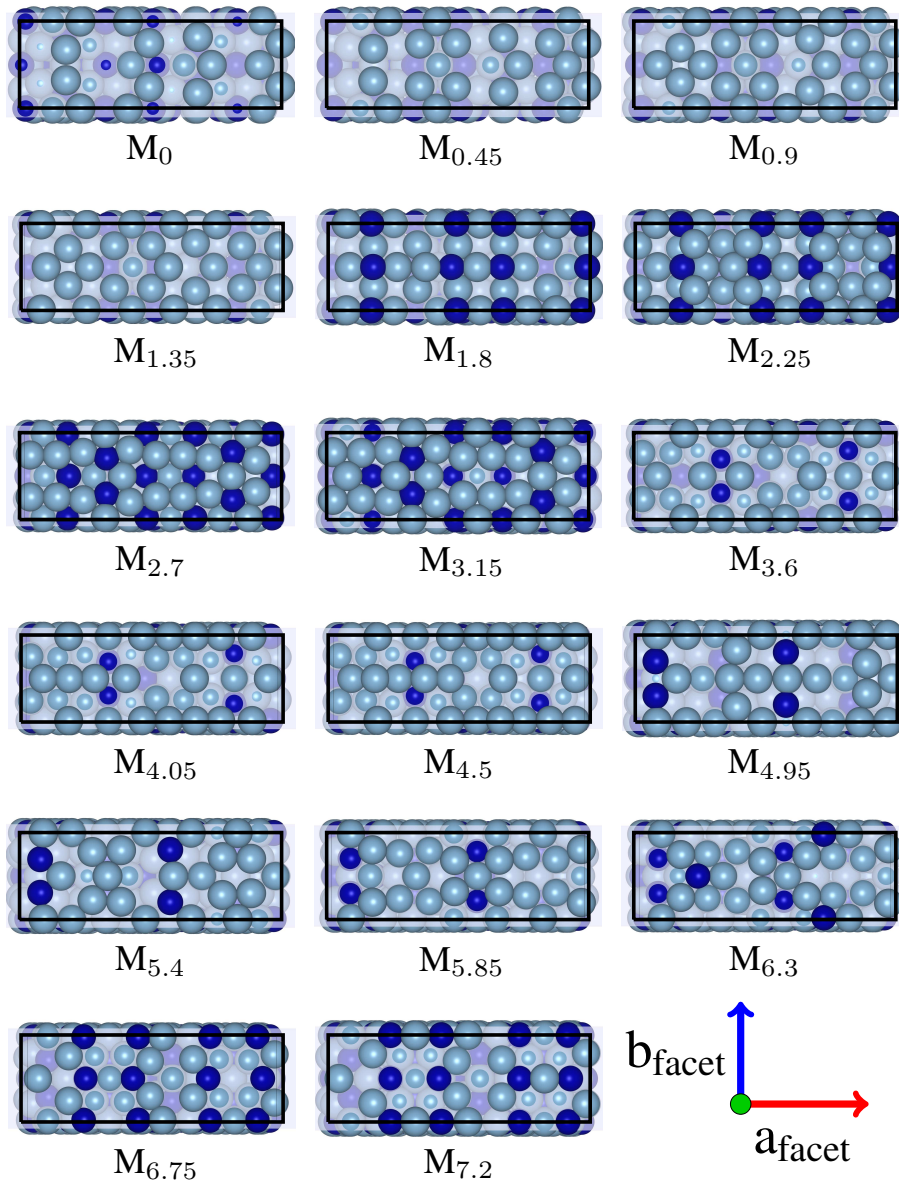


Figure 5.16: Surface structures of models M_0 and $M_{7.2}$. Unit cells, Al and Co atoms are drawn in black, light blue and dark blue, respectively. Here, $a_{\text{facet}} = 2c_m = 24.69 \text{ \AA}$ and $b_{\text{facet}} = b_m = 8.11 \text{ \AA}$.

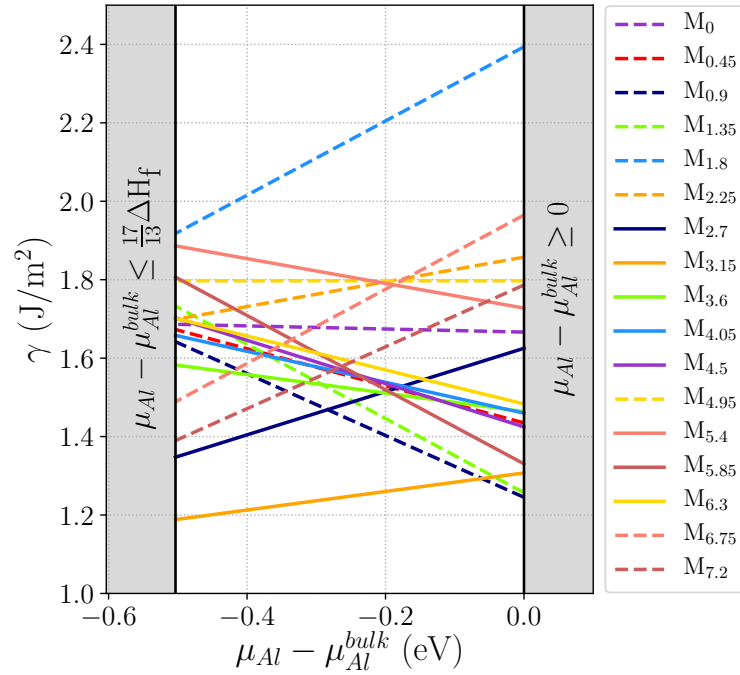


Figure 5.17: Surface energies of 17 surface models for $m-Al_{13}Co_4(\bar{2}01)$ as a function of $\mu_{Al} - \mu_{Al}^{bulk}$.

a similar surface energy (1.25 J/m^2). The $M_{3.15}$ surface model is the most stable one over the longest range of Al chemical potentials and therefore will be considered for further investigations.

5.5 Relative stability of $Al_{13}Co_4(010)$ and $Al_{13}Co_4(100)$

5.5.1 Surface energies

Now that the structure of the pseudo-twofold surface is known, it is of interest to compare its stability to the one of the pseudo-tenfold surface. Two surface models are available for the pseudo-tenfold surface: a dense Al-rich flat plane (Fig. 5.18a), identified by a combination of surface science studies and DFT calculations (P_{24}) [88, 177, 18], and a highly corrugated model (Fig. 5.18b), keeping intact the Henley-type clusters at the surface (P_{14}) [24, 34, 171], build by a theoretical cleavage. More details can be found in previous Chapters 1 and 4. Without considering the facets, the relative stabilities of the pseudo-twofold (O_0 model) and pseudo-tenfold surfaces rely on the Al chemical potential (Fig. 5.19).

In the Al-rich region ($-0.16 \text{ eV} < \mu_{Al} - \mu_{Al}^{bulk} < 0$), the pseudo-tenfold surface (P_{24} model) is more stable than the pseudo-twofold one (O_0 model). The situation is quite different

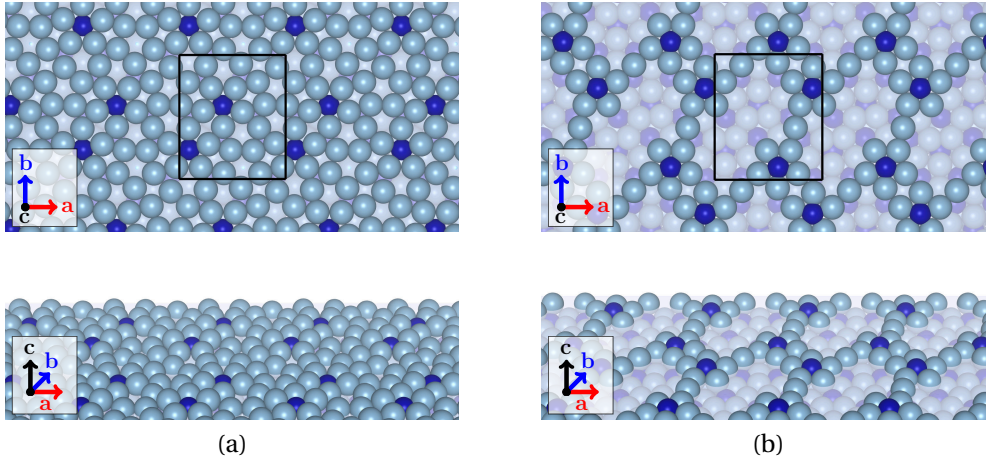


Figure 5.18: Surface structure of (a) model P₂₄ (flat surface) and (b) model P₁₄ (nanostructured surface). Al and Co atoms are drawn in light blue and dark blue, respectively.

in the Co-rich region, ($\frac{17}{13}\Delta H_f < \mu_{\text{Al}} - \mu_{\text{Al}}^{\text{bulk}} < -0.16$ eV), where the surface energies of the pseudo-twofold (O₀ model) and pseudo-tenfold (P₁₄ model) surfaces are very close, thus suggesting a similar stabilization. The surface energy anisotropy, without regarding the facets, is smaller than that of fcc Al and hcp Co ($0.81 < \frac{\gamma_{\text{Al}_{13}\text{Co}_4}^{\text{twofold}}}{\gamma_{\text{Al}_{13}\text{Co}_4}^{\text{tenfold}}} < 1.11$, while $\frac{\gamma_{\text{Al}(100)}}{\gamma_{\text{Al}(111)}} = 1.12$ and $\frac{\gamma_{\text{Co}(10\bar{1}0)}}{\gamma_{\text{Co}(0001)}} = 1.37$) [179, 180]. Focusing on the facets (M_{3,15} model), they turn up to be the most stable in the full range of allowed chemical potentials, with surface energies ranging from 1.19 J/m² (Co-rich potentials) to 1.31 J/m² (Al-rich potentials). Thus, they substantially contribute to stabilize the pseudo-twofold orientation over the pseudo-tenfold one.

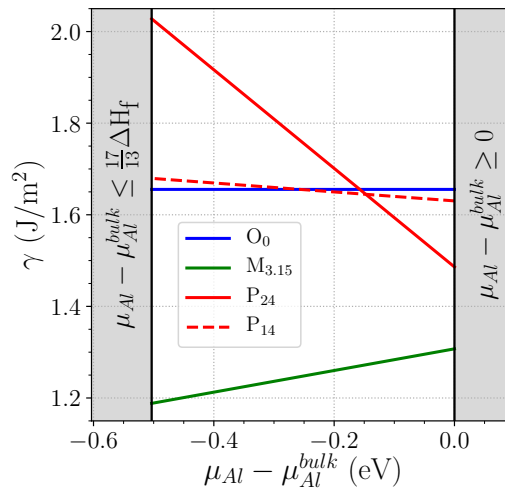


Figure 5.19: Comparison of $o\text{-Al}_{13}\text{Co}_4(100)$ (models P₂₄ and P₁₄), $o\text{-Al}_{13}\text{Co}_4(010)$ (model O₀) and $m\text{-Al}_{13}\text{Co}_4(\bar{2}01)$ (model M_{3,15}) surface energies as a function of $\mu_{\text{Al}} - \mu_{\text{Al}}^{\text{bulk}}$.

5.5.2 DOS

The contributions of s-, p- and d-states to the density of states (DOS) of $o-Al_{13}Co_4(100)$ (models P_{24} and P_{14}), $o-Al_{13}Co_4(010)$ (model O_0) and $m-Al_{13}Co_4(\bar{2}01)$ (model $M_{3.15}$) are plotted in Fig. 5.20. Both the surface and subsurface contributions to the DOS are calculated and compared to their bulk-like layer equivalents, except for the subsurface contribution to the DOS of $m-Al_{13}Co_4(\bar{2}01)$. A gap is present at the Fermi level for both p-states contributions. However this gap appears to be deeper in the case of $Al_{13}Co_4(100)$, thus suggesting a higher electronic stabilization of P_{24} compared to O_0 .

The electronic structure, exhibiting a free-electron like shape in the range $[-11.0 \text{ eV}, -3.5 \text{ eV}]$ with a main contribution from sp-states, as well as a strong contribution from d-states in the range $[-3.5 \text{ eV}, 0 \text{ eV}]$, is characterized by a pseudo-gap at the Fermi energy, similarly to what was observed for the twofold $(1\ 0\ 0\ 0)$ and $(1\ 2\ 1\ 1\ 0)$ surfaces of the decagonal quasicrystal $d-Al-Ni-Co$, which can be attributed to a combination of the Hume-Rothery stabilization mechanism and orbital hybridizations [181]. Focusing on the facets, the $M_{3.15}$ surface model is the most stable one over the longest range of Al chemical potentials. A deep pseudo-gap at the Fermi energy is also identified in the corresponding density of states, which shows similar features to that of the O_0 model.

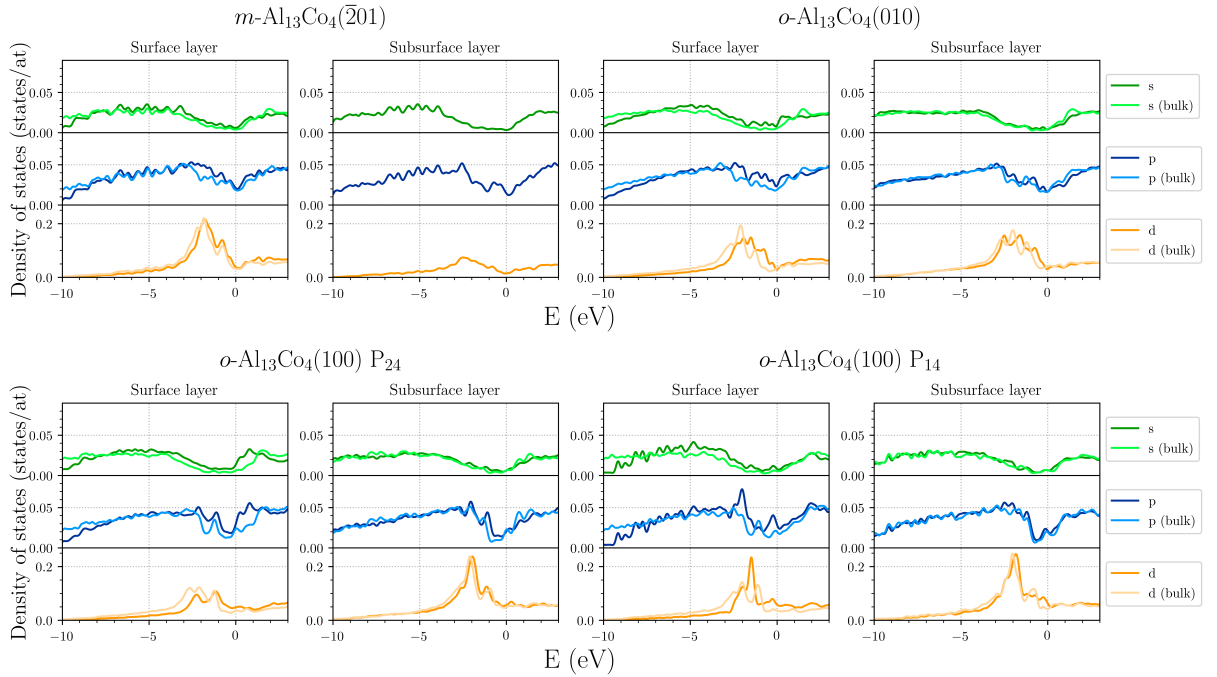


Figure 5.20: Comparison of $o-Al_{13}Co_4(100)$ (models P_{24} and P_{14}), $o-Al_{13}Co_4(010)$ (model O_0) and $m-Al_{13}Co_4(\bar{2}01)$ (model $M_{3.15}$) surface and subsurface density of states.

5.6 Hydrogen adsorption on Al₁₃Co₄

The gas-phase butadiene hydrogenation performances of the pseudo-twofold and pseudo-tenfold *o*-Al₁₃Co₄ surfaces have been recently compared [8]. The pseudo-twofold orientation is found to be the most active at 110°C, and even more selective to butene (100%) than previously investigated Al₁₃Fe₄(010) [7, 9].

Weak hydrogen binding and easy H₂ dissociation are key descriptors in hydrogenation catalysis. These factors are related to the atomic hydrogen adsorption properties of the different Al₁₃Co₄ surfaces, an overview of which is obtained through potential energy surfaces (Fig. 5.21). The adsorption has been computed on specific points of regular grids covering the surfaces, using point densities of 1.0 pts.Å⁻², 2.3 pts.Å⁻² and 1.6 pts.Å⁻², for the *o*-Al₁₃Co₄(010), *o*-Al₁₃Co₄(100) and *m*-Al₁₃Co₄($\bar{2}01$), respectively.

The energy landscape is quite contrasted on the different terminations considered here. Focusing on the pseudo-tenfold orientation – for which two surface models have been identified – the reaction conditions may indeed modify the Al-rich and relatively flat surface structure observed under ultra-high vacuum (P₂₄ model), in the form of highly cohesive clusters emerging from the bulk lattice (P₁₄ model)[171], to give rise to a nanostructured surface demonstrated to be more active [24, 171]. Hydrogen is calculated to be quite weakly bound on the P₂₄ model ($E_{\text{ads}} > -0.23$ eV), the most stable sites being located on Al-Al bridges above a subsurface Co atom, and slightly more strongly adsorbed on the P₁₄ model ($E_{\text{ads}} > -0.58$ eV), the more stable sites being located on top of the Al "glue" atoms that connects the bipentagonal Al motif, or in the vicinity of protruding Co atoms. On the P₂₄ model, the absence of protruding surface Co atom also lead to the H₂ dissociation with a rather high barrier (0.59 eV)[19], while a negligible barrier has been calculated on the P₁₄ model (0.18 eV) [24]. On both surface models, favorable hydrogen adsorption sites remain poorly connected.

The picture is slightly different on the pseudo-twofold surface. Firstly, on both the flat terraces and the facets, a spontaneous dissociation of hydrogen occurs on top of Co atoms. Atomic hydrogen is found to be strongly bound to the surface, either on top of Al atoms located above subsurface Co atoms (O₀ model, $E_{\text{ads}} > -0.59$ eV) or on top of Co atoms (M_{3,15} model, $E_{\text{ads}} > -0.53$ eV). This suggests that hydrogen dissociation is likely on this surface. Additional favorable adsorption sites are found on top or in the vicinity of surface Co atoms, but with weaker adsorption energies, *i.e.* likely active for hydrogenation steps. All these sites are well connected to one another and it is reasonable to assume that the diffusion of hydrogen atoms on this surface is facilitated.

Thus, the comparison of the hydrogen adsorption potential energy maps gives help-

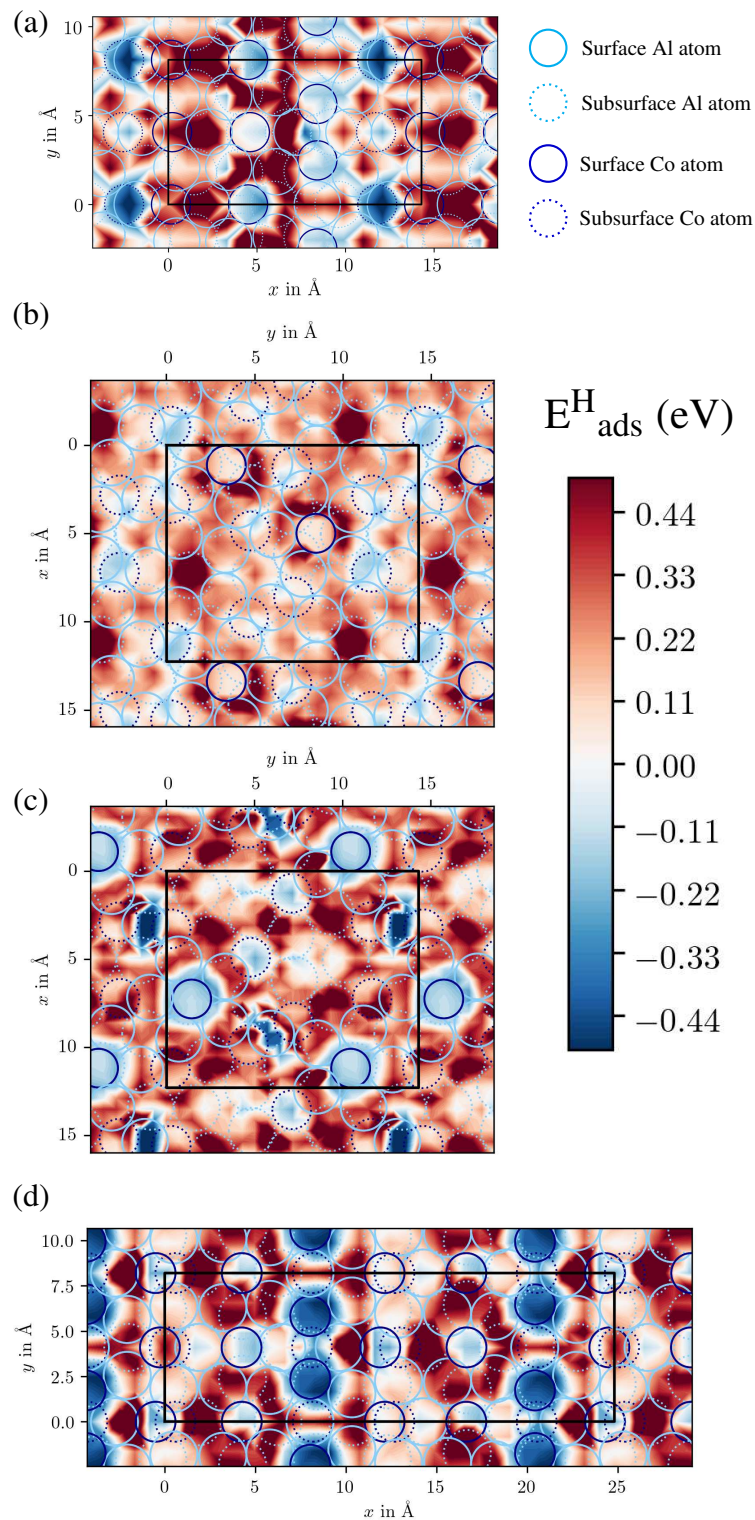


Figure 5.21: Adsorption energy maps of monoatomic hydrogen on (a) $o-Al_{13}Co_4(010)$ model O_0 , (b) $o-Al_{13}Co_4(100)$ model P_{24} , (c) $o-Al_{13}Co_4(100)$ model P_{14} and (d) $m-Al_{13}Co_4(\bar{2}01)$ model $M_{3.15}$.

ful insights to understand the better catalytic performances of the pseudo-twofold surface compared to the pseudo-tenfold one.

5.7 Conclusions and perspective

The structure, stability and hydrogen adsorption properties of the Al₁₃Co₄ pseudo-twofold surface have been investigated by a combination of experimental (LEED, AFM, STM and SXRD) and theoretical (DFT calculations) techniques. A highly faceted surface morphology has been identified (Fig. 5.22), similar to that of the *d*-Al-Ni-Co (1 2 1 1 0) and (1 0 0 0 0) twofold quasicrystalline surfaces.

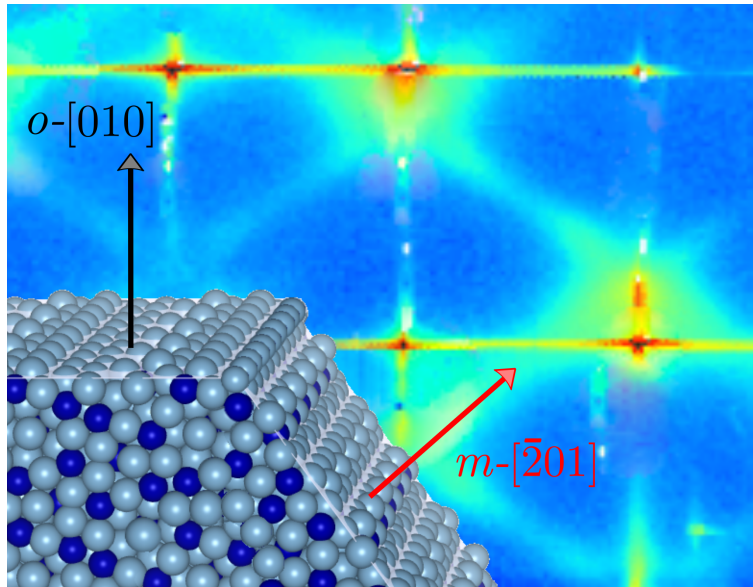


Figure 5.22: Artist's rendition of a flat terrace and a facet.

The surface model consists in a coexistence of both flat terraces (*o*-Al₁₃Co₄(010)), made of rows of triangular Al₃ motifs separated by a 0.65 nm gap (Fig. 5.23a), and facets (*m*-Al₁₃Co₄($\bar{2}$ 01)), with a fairly denser and Co-enriched atomic surface structure (Fig. 5.23b). The strong Co–Al–Co covalent-like molecular group identified in the bulk is kept intact at the surface in both the terraces and the facets.

The pseudo-twofold Al₁₃Co₄ surface is calculated to be less stable than the pseudo-tenfold surface in the Al-rich limit (1.66 J/m² vs 1.49 J/m² for $\mu_{\text{Al}} = \mu_{\text{Al}}^{\text{bulk}}$), while both orientations present similar surface energies in the Co-rich region (1.66–1.68 J/m²). Without considering the facets, the surface energy anisotropy is smaller than that of *fcc* Al and *hcp* Co ($0.81 < \frac{\gamma_{\text{Al}_{13}\text{Co}_4}^{\text{twofold}}}{\gamma_{\text{Al}_{13}\text{Co}_4}^{\text{tenfold}}} < 1.11$, while $\frac{\gamma_{\text{Al}(100)}}{\gamma_{\text{Al}(111)}} = 1.12$ and $\frac{\gamma_{\text{Co}(10\bar{1}0)}}{\gamma_{\text{Co}(0001)}} = 1.37$) [179, 180]. Facets

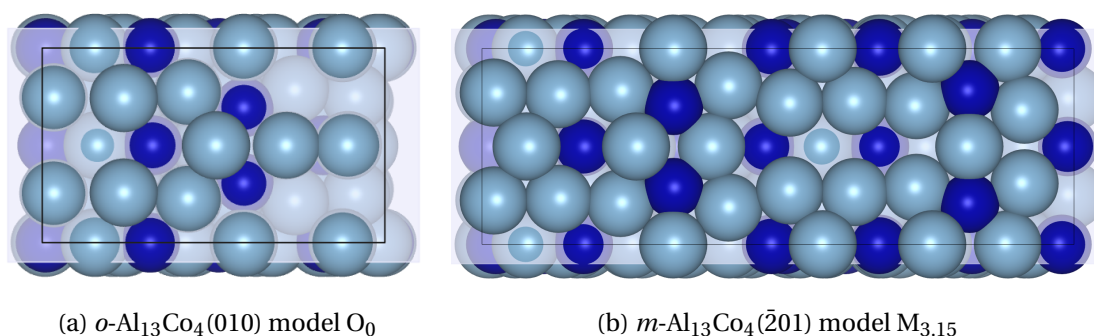


Figure 5.23: Surface structure of models (a) O_0 and (b) $M_{3.15}$. Al and Co atoms are drawn in light blue and dark blue, respectively.

substantially stabilize the pseudo-twofold surface orientation. Their surface energies are indeed calculated to be much lower than the previous ones ($[1.19 \text{ J/m}^2 : 1.31 \text{ J/m}^2]$).

Based on the surface model for the pseudo-twofold surface structure, potential energy maps for atomic hydrogen adsorption have been built. They show a wide diversity of favorable atomic hydrogen adsorption sites, some of them being quite strongly bound to the surface ($-0.60 < E_{\text{ads}}(\text{H}) < -0.50 \text{ eV}$), thus likely promoting H_2 dissociation, while others interact more weakly with the surface, and are possibly more active for hydrogenation steps. As already predicted for the pseudo-tenfold orientation [171], reaction conditions may modify the faceted structure of the pseudo-twofold surface identified under ultra-high vacuum conditions. Further experimental and theoretical works – under catalytic conditions – are therefore needed to fully understand the mechanism behind the catalytic properties of $\text{Al}_{13}\text{Co}_4(010)$.

Chapter 6

Surface structure and reactivity of *m*-Al₁₃Fe₄(010)

Contents

6.1	Introduction	132
6.2	Preliminary experimental and theoretical results	132
6.2.1	LEED measurements	132
6.2.2	STM images	133
6.2.3	Surface energy calculations	134
6.2.4	STM image simulation	135
6.2.5	Catalytic measurements	136
6.3	SXRD analysis	137
6.3.1	In-plane measurements	137
6.3.2	CTRs extraction	143
6.4	Adsorption calculations	145
6.4.1	Hydrogen adsorption	145
6.4.2	Butadiene and but-1-ene adsorptions	146
6.4.3	Coadsorption of hydrogen and butadiene/but-1-ene	147
6.5	Hydrogenation of butadiene : reaction pathways and kinetics	148
6.5.1	NEB calculations	148
6.5.2	Microkinetic modelling	152
6.6	Conclusion	155

6.1 Introduction

In this chapter, the (010) surface of $m\text{-Al}_{13}\text{Fe}_4$ is theoretically and experimentally investigated under both UHV and reaction conditions through the means of DFT and SXRD. The surface structure has already been studied by a combination of DFT and surface science techniques under UHV and a model had been proposed [26]. This model consists in an incomplete puckered layer built from the preservation of the cluster building blocks at the surface. These clusters are preserved thanks to the strong covalent interactions present in this compound [34]. This surface model is very similar to the P_{14} model of $\text{Al}_{13}\text{Co}_4(100)$ that was previously discussed in Chapter 5. $\text{Al}_{13}\text{Fe}_4$ and more particularly its (010) surface were shown to exhibit good performances – similar to Pd(100) – in the partial hydrogenation of acetylene [22] and butadiene [7, 9]. More details are to be found in Chapter 1 of this manuscript (*e.g.* crystallographic informations). The present work focuses on the butadiene hydrogenation reaction.

First, some preliminary experimental (LEED and STM analyses, as well as catalytic measurements) and theoretical (surface energy calculations) results will be presented. A detailed surface x-ray diffraction analysis will then give new insights on the surface structure under UHV conditions. Adsorption calculations of both hydrogen and alkenes will allow to establish a possible reaction path through the means of nudged elastic band (NEB) calculations. Finally, a microkinetic modelling of the reaction based on the NEB results will be presented and its results compared to experimental measurements.

6.2 Preliminary experimental and theoretical results

6.2.1 LEED measurements

The experiments were performed using $\text{Al}_{13}\text{Fe}_4$ single crystals cut parallel to the (010) planes. The different samples were taken from ingots grown from an Al-rich solution by Czochralski method (see Chapter 1 for more details) and oriented using back-scattered x-ray Laue diffraction technique, polished down to 0.25 μm using diamond paste and mounted onto a Ta plate. Because of its propensity to develop twins, it is difficult to obtain monodomain (no twin) single crystals of $\text{Al}_{13}\text{Fe}_4$ (as explained in Chapter 1).

The samples were prepared by cycles of 30 min 2 keV Ar^+ sputtering followed by 1 hour annealing at 873 K under UHV conditions. Neither oxygen, nor carbon surface contaminations were observed by AES prior to LEED analysis. Fig. 6.1a presents a LEED pattern (25 eV) taken in 2015 [26], showing a (1×1) surface and two twin domains (blue and red).

Fig. 6.1b is a LEED pattern (64 eV) obtained at SixS. The white dashed circle represents the same area of Fig. 6.1a for comparison. The same two domains (blue and red) are visible but another set of diffraction peaks can also be observed (green circles) which were previously absent. This new phase appears to be in epitaxy with the $\text{Al}_{13}\text{Fe}_4$ structure. Basic analysis would suggest this phase to be Al_5Fe_2 and more precisely its (001) surface. This will be ultimately confirmed by SXRD.

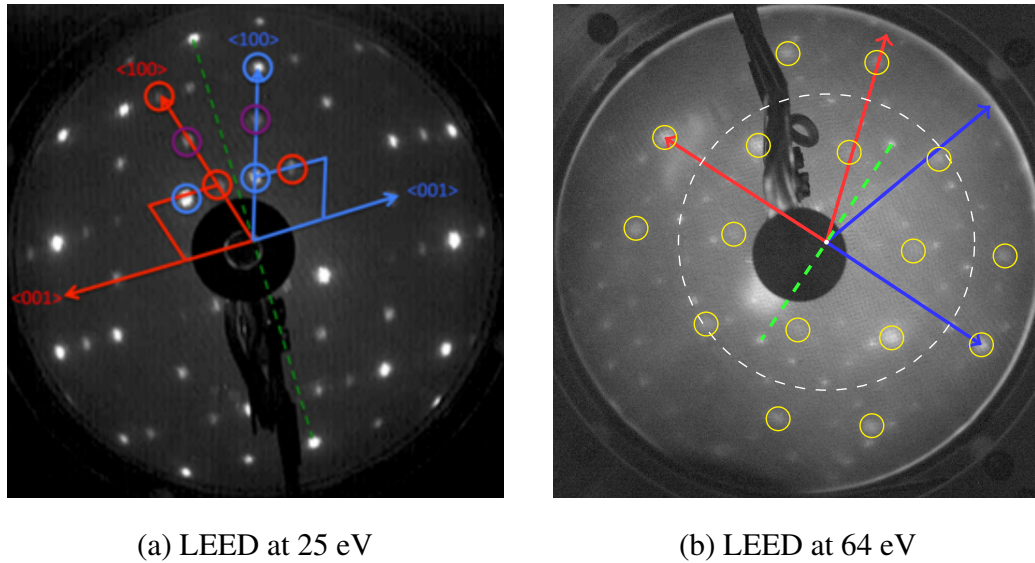


Figure 6.1: LEED patterns at (a) 25 eV [26] and (b) at 64 eV. The two twin domains are represented in blue and red. The Al_5Fe_2 diffraction peaks are circled in green. The white dashed circle in (b) represents the same area displayed in (a).

6.2.2 STM images

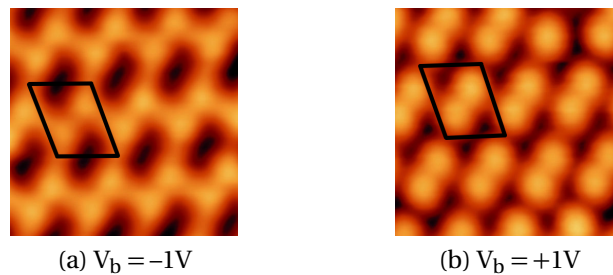


Figure 6.2: STM images ($5 \times 5 \text{ nm}^2$) of $\text{Al}_{13}\text{Fe}_4(010)$ [26].

STM analysis [26] shows the presence of terraces separated by a unique step height of $\frac{b}{2}$ meaning that only a flat or puckered termination is present at the surface. High resolution STM images (Fig. 6.2) show a bias-dependent surface, where pairs of bright spots dominate the unit cell. These high quality images will later be compared to DFT-based image simulation.

6.2.3 Surface energy calculations

The previous STM analysis suggest that the surface consists in a puckered termination. Based on this hypothesis, five surface models are considered : a complete puckered layer (model P, Fig. 6.3a), an incomplete puckered layer built from the preservation of the cluster building blocks which also have 2 Al glue atoms connecting the bipentagonal motifs (model P_2^{inc} , Fig. 6.3b), two models where only 1 Al glue is missing (P_{1a}^{inc} and P_{1b}^{inc} , Fig. 6.3c–d) and finally one model where no Al glue is present (P_0^{inc} , Fig. 6.3e).

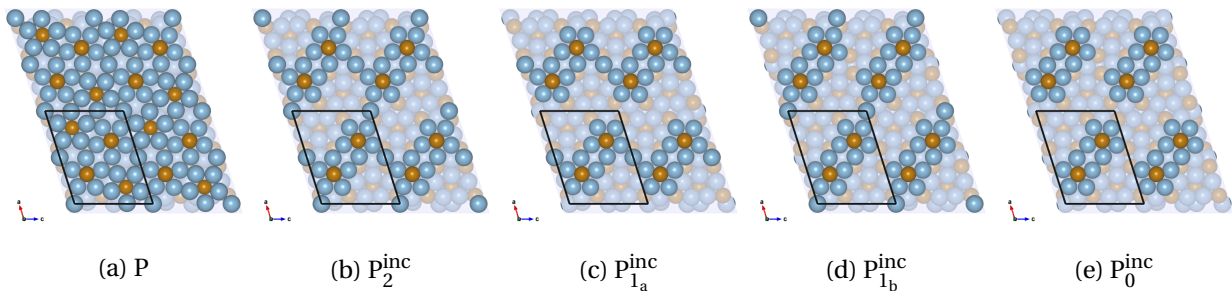


Figure 6.3: Considered surface models of $\text{Al}_{13}\text{Fe}_4(010)$. The surface unit cells, Al and Fe atoms are respectively drawn in black, light blue and brown.

Surface energies of the five considered models have been calculated (see Chapter 2 for more details). Here again, the DFT-D3 functional is used. The results are presented in Fig. 6.4 : in the Al chemical potential range $[-0.46 \text{ eV}; -0.05 \text{ eV}]$, P_2^{inc} is the most stable surface model with a surface energy ranging from 1.69 J/m^2 to 1.73 J/m^2 . In the range $[-0.05 \text{ eV}; 0 \text{ eV}]$, model P is the most stable one with a surface energy ranging from 1.67 J/m^2 to 1.69 J/m^2 . The three other models (P_{1a}^{inc} , P_{1b}^{inc} and P_0^{inc}) appear to be less stable in the full range of chemical potentials. The models with only one Al glue atom – P_{1a}^{inc} and P_{1b}^{inc} – present almost the same surface energy in the full range of $\mu_{\text{Al}} - \mu_{\text{Al}}^{\text{bulk}}$. P_0^{inc} (no Al glue atom) is even less stable over the same range of chemical potential.

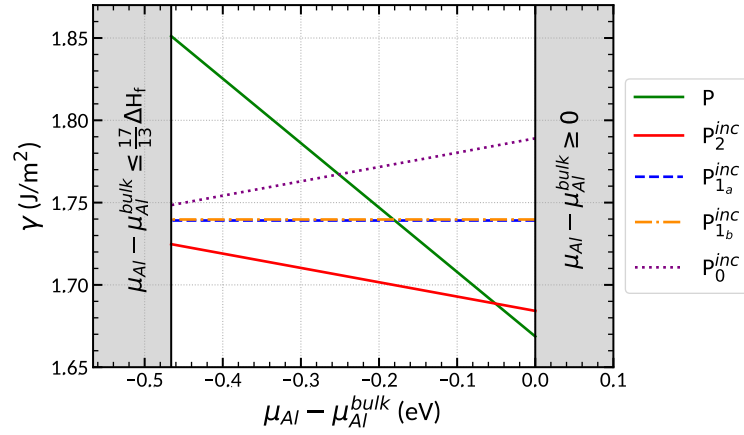


Figure 6.4: Calculated surface energies of $\text{Al}_{13}\text{Fe}_4(010)$ as a function of the Al chemical potential.

6.2.4 STM image simulation

Fig. 6.5a–b shows the STM image simulations of models P and P_2^{inc} for a bias of -1 V [26]. The simulation based on model P_2^{inc} is in good agreement with the experimental measurements. In Fig. 6.5a, the bright spots are due to the presence of protruding Fe atoms and Al pentagons. In Fig. 6.5b, the bright spots are also due to the protruding Fe atoms as well as the Al glue atoms.

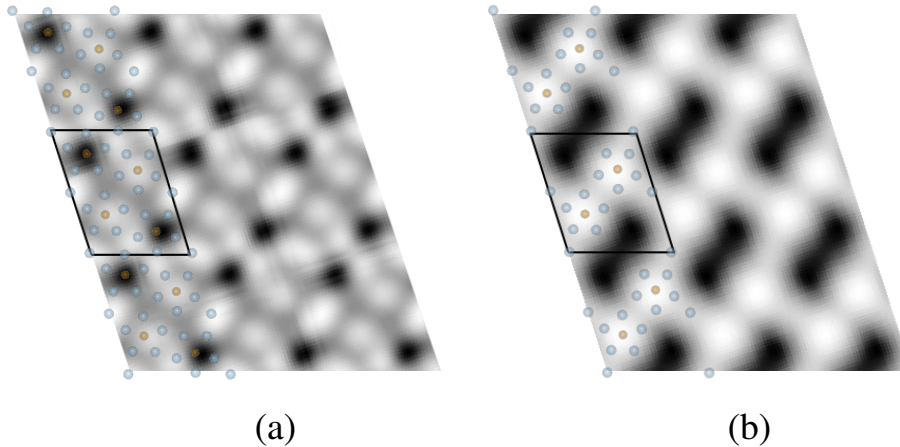


Figure 6.5: STM image simulations ($3a \times 3c$): (a) model P, $V_b = -1\text{V}$ and (b) model P_2^{inc} , $V_b = -1\text{V}$ [26]. The unit cell, Al and Fe atoms are drawn in black, light blue and brown, respectively.

6.2.5 Catalytic measurements

The reaction was performed in a dedicated static catalytic reactor coupled with UHV preparation and analysis chambers (LEED and AES). The sample was heated from the back by an infrared laser beam. The surface temperature was controlled using an infrared pyrometer (surface emissivity set to 0.3). A mixture of ultra pure gases (5 mbar hydrogen, 0.5 mbar butadiene and 0.5 mbar Ar for internal calibration) was prepared in a separate chamber before injection into the reactor. The reactants and products were monitored by mass spectroscopy and gas chromatography.

Fig. 6.6a shows the hydrocarbon partial pressures during butadiene hydrogenation on Pd(100) and Al₁₃Fe₄(010) at room temperature [7]. Butadiene is fully converted into butane in less than 50 minutes with Al₁₃Fe₄(010), which is also the time needed to do the conversion on Pd(100). Al₁₃Fe₄(010) appears to be more selective than Pd(100) towards the production of butene. An initial selectivity of 100% is observed (89% on average). The butane formation rate increases greatly after butadiene is fully converted.

Fig. 6.6b presents a comparison of the butene production of different intermetallic catalysts at room temperature. Al₁₃Fe₄(010) is the most active considered Al-based intermetallic catalysts. Only Al₁₃Co₄(010) and Al₁₃Ru₄(010) can also be considered as active at room temperature.

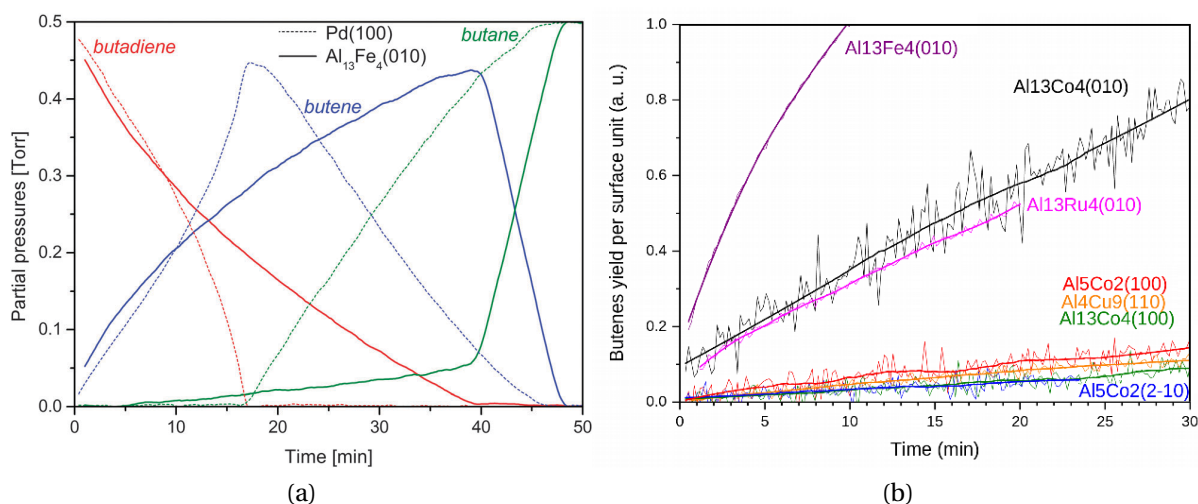


Figure 6.6: (a) Hydrocarbon partial pressures during butadiene hydrogenation on Al₁₃Fe₄(010) and Pd(100) at room temperature [7] and (b) butene production of different Al-based intermetallic catalysts at room temperature.

6.3 SXRD analysis

Before doing extensive DFT calculations in order to determine the adsorption and catalytic properties of $\text{Al}_{13}\text{Fe}_4(010)$, it is necessary to ascertain its surface model. Surface x-ray diffraction is the best tool to discriminate between the possible surface structures.

6.3.1 In-plane measurements

Fig. 6.7 shows the in-plane measurement (raw data) of the reciprocal space of $\text{Al}_{13}\text{Fe}_4(010)$. As expected (thanks to the LEED analysis) the complexity of the reciprocal space is quite high. A careful analysis is therefore needed to understand the different phases that are present in this sample. Miller indices will further be referred to as H, K, and L, given with respect to the (1×1) surface unit cell ($a_{\text{surf}} = 12.47 \text{ \AA}$, $b_{\text{surf}} = 15.49 \text{ \AA}$, $c_{\text{surf}} = 8.08 \text{ \AA}$ and $\beta = 107.7^\circ$).

Fig. 6.8a shows the in-plane measurement of the reciprocal space of $\text{Al}_{13}\text{Fe}_4(010)$ where the diffraction spots positions of the two mirror domains (red and black) are indicated (red and black circles). Additional in-plane SXRD data can be found in the Appendices (Figs. D.5 and D.6). The radii of the circles are proportional to the calculated intensity of the peaks. A script – that takes as inputs the lattice parameters and the atomic positions – allows for the determination of the peak positions and intensities. The observed pseudo 10-fold symmetry confirms the (010) surface orientation. The surface lattice parameters are consistent with the ones of $\text{Al}_{13}\text{Fe}_4(010)$ ($a_{\text{lit}} = 12.471 \text{ \AA}$, $b_{\text{lit}} = 15.492 \text{ \AA}$, $c_{\text{lit}} = 8.078 \text{ \AA}$ [91] and $a_{\text{SXRD}} = 12.48(6) \text{ \AA}$, $b_{\text{SXRD}} = 15.53(3) \text{ \AA}$, $c_{\text{SXRD}} = 8.10(3) \text{ \AA}$). Extinction conditions are $K+L=2n+1$ with $n \in \mathbb{N}$. For even values of K ($K=2$, *i.e.* $Q_y \simeq 0.8 \text{ \AA}^{-1}$; $K=4$, *i.e.* $Q_y \simeq 1.6 \text{ \AA}^{-1}$, *etc*), the peaks of both twin domains are superimposed. This is an issue for the measurements of CTRs because of the difficult deconvolution of the two superimposed CTRs. In the case where K is odd, the CTRs are distincts (not superimposed). Therefore, only these CTRs are measured.

To sum up, the expected pseudo 10-fold symmetry is observed and the presence of two mirrors domains is confirmed. However, another phase is present. The in-plane lattice parameters of the latter are consistent with the ones of $\text{Al}_5\text{Fe}_2(001)$ ($a_{\text{lit}} = 7.65(6) \text{ \AA}$, $b_{\text{lit}} = 6.41(5) \text{ \AA}$ [82] and $a_{\text{SXRD}} = 7.66(1) \text{ \AA}$, $b_{\text{SXRD}} = 6.44(2) \text{ \AA}$). Fig. 6.8b shows the in-plane map with the indication of the $\text{Al}_5\text{Fe}_2(001)$ peaks (using a similar script as before). For each $\text{Al}_{13}\text{Fe}_4(010)$ twin domain, there is also a $\text{Al}_5\text{Fe}_2(001)$ related domain who appears to have an epitaxial relationship : the green (respectively yellow) $\text{Al}_5\text{Fe}_2(001)$ domain is related to the black (respectively red) $\text{Al}_{13}\text{Fe}_4(010)$ domain.

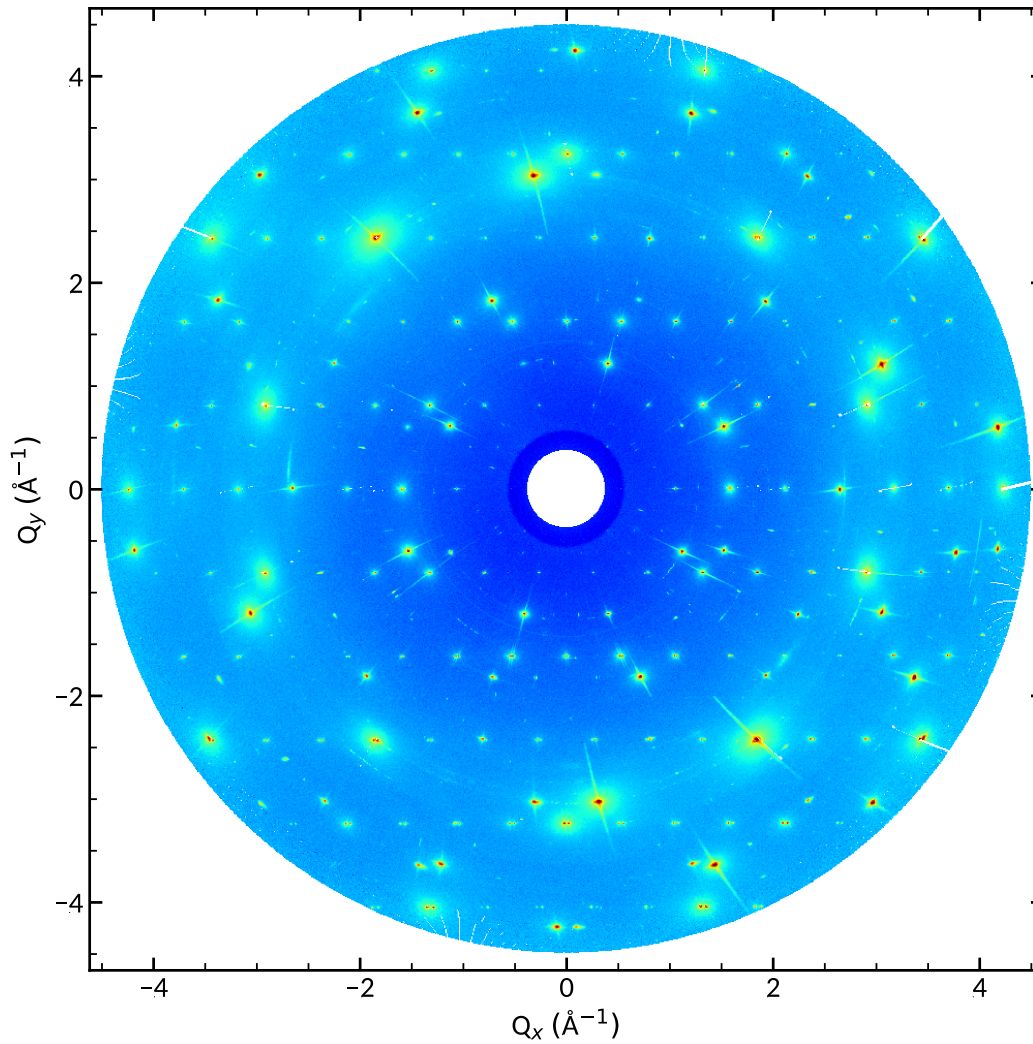
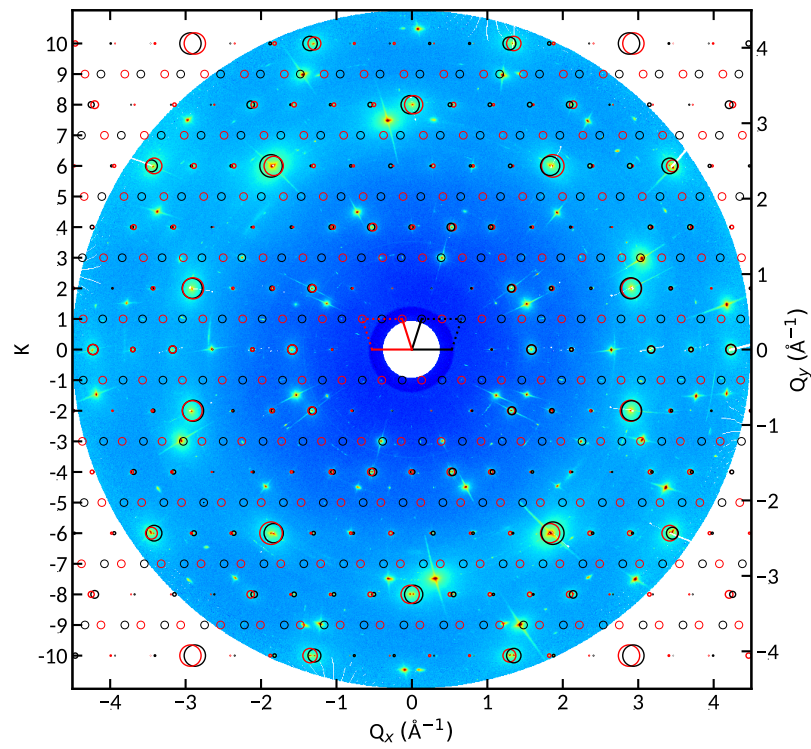
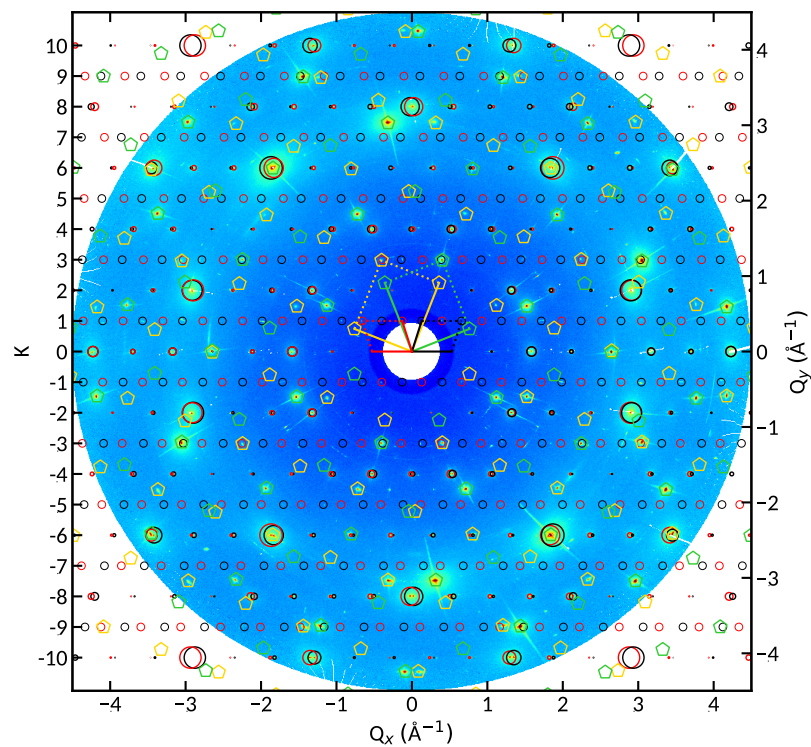

 Figure 6.7: In-plane reciprocal space map (raw data) of $\text{Al}_{13}\text{Fe}_4(010)$

Fig. 6.9 shows reciprocal space maps (in-plane and at $L_{\text{Al}_5\text{Fe}_2} = 1$) where the $\text{Al}_5\text{Fe}_2(001)$ peaks are indexed (positions and intensities). This confirms the epitaxial relationship between $\text{Al}_{13}\text{Fe}_4(010)$ and $\text{Al}_5\text{Fe}_2(001)$: $[010]_{\text{Al}_{13}\text{Fe}_4}$ is equivalent to $[001]_{\text{Al}_5\text{Fe}_2}$. Fig. 6.10 presents four CTRs of $\text{Al}_5\text{Fe}_2(001)$ with one of them $-(1,1)_{\text{Al}_5\text{Fe}_2}$ – superimposed to one of $\text{Al}_{13}\text{Fe}_4(010)$ CTR (5,3). The out-of-plane lattice parameter is also consistent with the one of $\text{Al}_5\text{Fe}_2(001)$ ($c_{\text{lit}} = 4.21(8) \text{ \AA}$ [82] and $c_{\text{SXRD}} = 4.23(1) \text{ \AA}$). Satellite peaks are present around integer values of $L_{\text{Al}_5\text{Fe}_2} (\pm 0.16)$ and are supposedly correlated to the partially occupied Al sites that form a disordered chain confined within the pentagonal Al channels (see Chapter 1 for more details on the crystal structure). On top of that, a splitting of the principal peaks occurs (e.g. $L_{\text{Al}_5\text{Fe}_2} = 2$ and $L_{\text{Al}_5\text{Fe}_2} = 2.03$, corresponding to a lattice parameter of $4.16(1) \text{ \AA}$). This could also be linked to this disordered chains.



(a)



(b)

Figure 6.8: In-plane reciprocal space maps of $\text{Al}_{13}\text{Fe}_4(010)$: (a) the position of the $\text{Al}_{13}\text{Fe}_4(010)$ in-plane spots are highlighted in red and black circles ((001) twin). The radii of the circles are proportional to the calculated intensity of the peaks, and (b) the position of the $\text{Al}_5\text{Fe}_2(001)$ spots are highlighted in yellow and green pentagons.

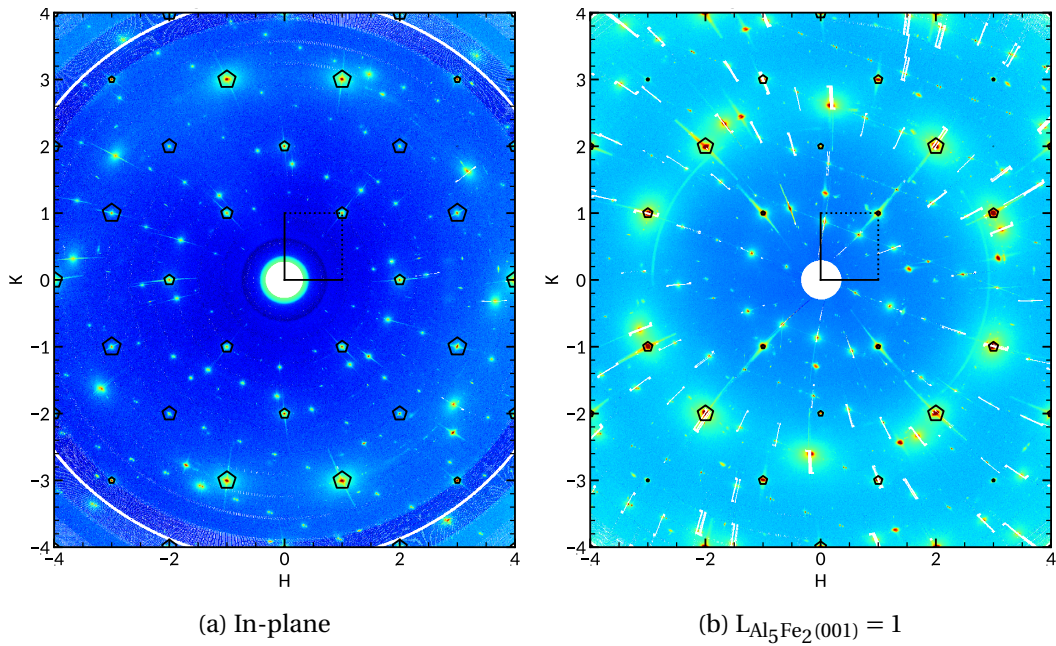


Figure 6.9: Reciprocal space maps : (a) in-plane and (b) $L_{\text{Al}_5\text{Fe}_2(001)} = 1$ where the diffraction peaks of $\text{Al}_5\text{Fe}_2(001)$ are indexed (positions and intensities). H, K and L are given with respect to the surface lattice parameters of $\text{Al}_5\text{Fe}_2(001)$.

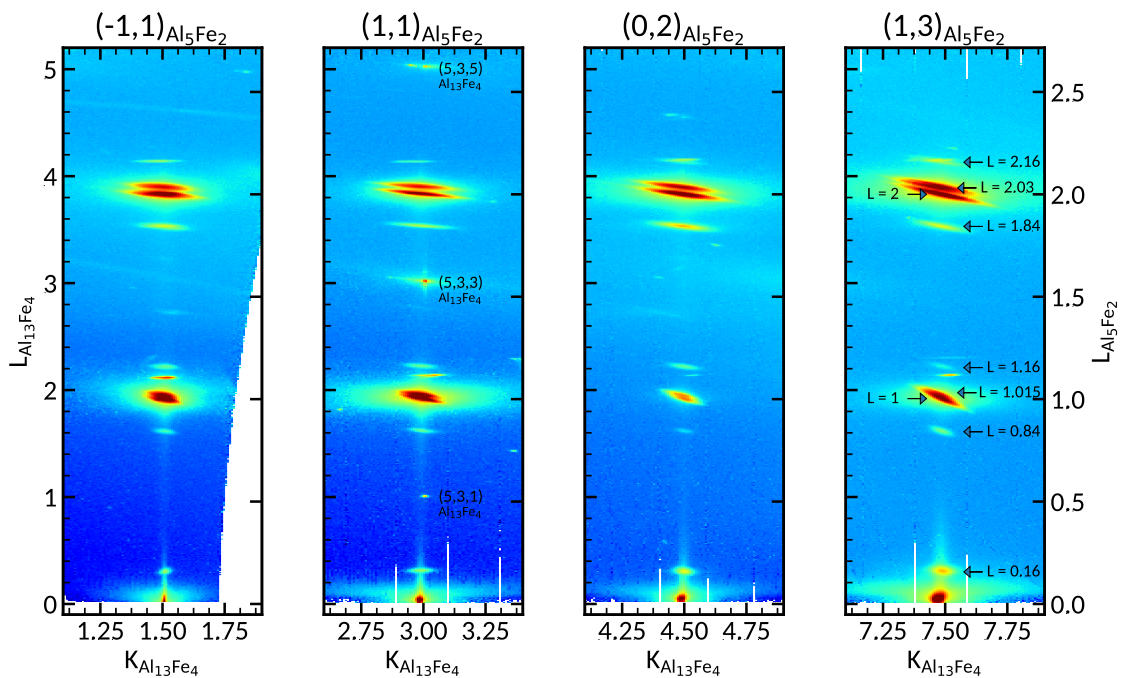


Figure 6.10: Examples of 4 CTRs of $\text{Al}_5\text{Fe}_2(001)$. $(1,1)_{\text{Al}_5\text{Fe}_2}$ and $(5,3)_{\text{Al}_{13}\text{Fe}_4}$ are superimposed.

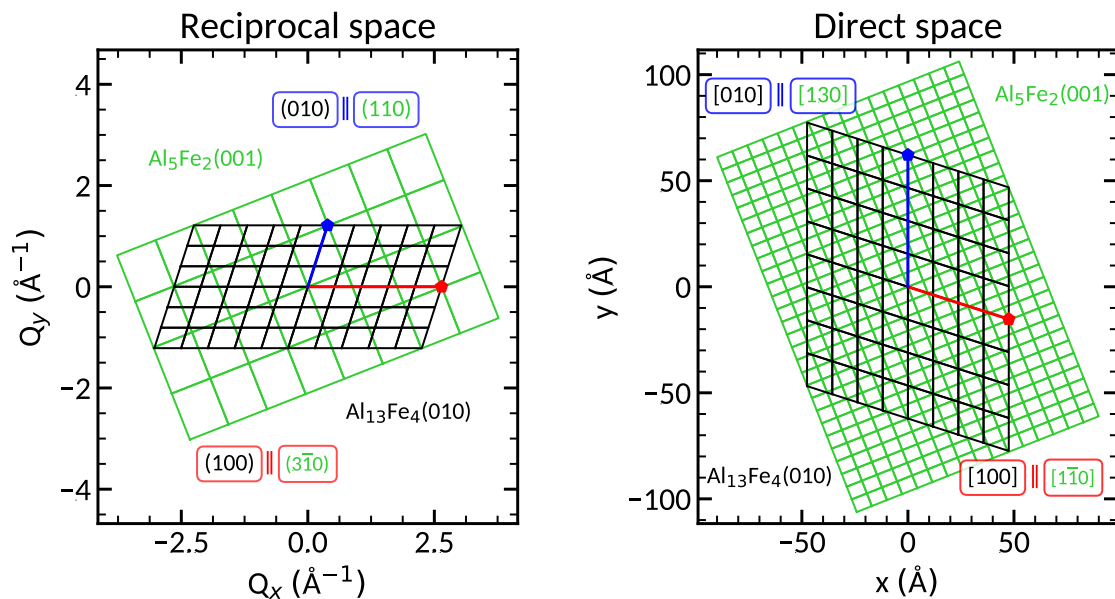


Figure 6.11: Epitaxial relationship between $\text{Al}_{13}\text{Fe}_4(010)$ and $\text{Al}_5\text{Fe}_2(001)$ in both the reciprocal space and the direct space.

All the peaks are therefore indexed, no other phase is present. Nevertheless, it is of interest to understand properly the epitaxial relationship of the two phases, in order to select the right CTRs to measure. Fig. 6.11 shows the epitaxial relationship between $\text{Al}_{13}\text{Fe}_4(010)$ and $\text{Al}_5\text{Fe}_2(001)$ in both the reciprocal space and the direct space. In the reciprocal space the common (hkl) planes are the following : $(110)_{\text{Al}_5\text{Fe}_2} \parallel (010)_{\text{Al}_{13}\text{Fe}_4}$ and $(3\bar{1}0)_{\text{Al}_5\text{Fe}_2} \parallel (100)_{\text{Al}_{13}\text{Fe}_4}$. This can be written using a transformation matrix between the primary (P) phase $\text{Al}_{13}\text{Fe}_4$ and the secondary (S) phase Al_5Fe_2 :

$$\begin{cases} 5\mathbf{p}_1^* = 3\mathbf{s}_1^* - 1\mathbf{s}_2^* \\ 3\mathbf{p}_2^* = \mathbf{s}_1^* + \mathbf{s}_2^* \end{cases} \iff \begin{pmatrix} \mathbf{p}_1^* \\ \mathbf{p}_2^* \end{pmatrix} = \begin{pmatrix} \frac{3}{5} & \frac{-1}{5} \\ \frac{1}{3} & \frac{1}{3} \end{pmatrix} \begin{pmatrix} \mathbf{s}_1^* \\ \mathbf{s}_2^* \end{pmatrix} \iff \mathbf{P}^* = \mathbf{M}\mathbf{S}^*$$

which can be inverted in order to describe the relationship in the direct space :

$$\mathbf{P} = {}^t\mathbf{M}^{-1}\mathbf{S} \iff \begin{pmatrix} \mathbf{p}_1 \\ \mathbf{p}_2 \end{pmatrix} = \begin{pmatrix} \frac{5}{4} & \frac{-5}{4} \\ \frac{3}{4} & \frac{9}{4} \end{pmatrix} \begin{pmatrix} \mathbf{s}_1 \\ \mathbf{s}_2 \end{pmatrix} \iff \begin{cases} 4\mathbf{p}_1 = 5\mathbf{s}_1 - 5\mathbf{s}_2 \\ 4\mathbf{p}_2 = 3\mathbf{s}_1 + 9\mathbf{s}_2 \end{cases}$$

In the direct space, the common $[abc]$ directions are therefore the following :

$$[130]_{\text{Al}_5\text{Fe}_2} \parallel [010]_{\text{Al}_{13}\text{Fe}_4} \quad \text{and} \quad [1\bar{1}0]_{\text{Al}_5\text{Fe}_2} \parallel [100]_{\text{Al}_{13}\text{Fe}_4}$$

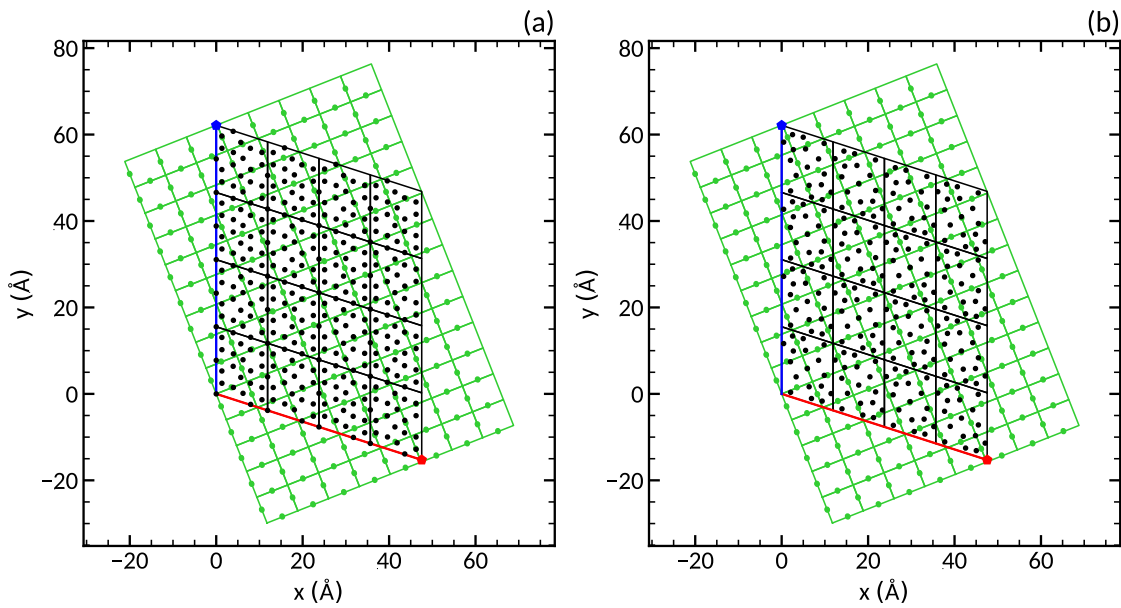


Figure 6.12: Possible superposition between $\text{Al}_{13}\text{Fe}_4(010)$ and $\text{Al}_5\text{Fe}_2(001)$ highlighting a preferential coincidence with the Al atoms of the disordered channels : relationships between (a) a P layer of $\text{Al}_{13}\text{Fe}_4$ and Al_5Fe_2 and (b) a F layer of $\text{Al}_{13}\text{Fe}_4$ and Al_5Fe_2 . Al atoms are drawn in black for $\text{Al}_{13}\text{Fe}_4$ and green for Al_5Fe_2 .

Fig. 6.12a presents a possible superposition of a P layer of $\text{Al}_{13}\text{Fe}_4$ on the Al disordered channels of Al_5Fe_2 . Some of the Al atoms of the P layer coincide with the Al atoms of Al_5Fe_2 along the $[100]_{\text{Al}_{13}\text{Fe}_4}$. The same situation occurs with a F layer (Fig. 6.12b). This may thus explain why this epitaxial relationship is favorable. Further DFT calculations (interfacial energy) are needed to better understand the structure of the interface. This could be of interest for surface coating applications.

On a more practical level, the Al_5Fe_2 peaks width along the K direction (Fig. 6.10) suggests small domains such as particles embedded in the $\text{Al}_{13}\text{Fe}_4$ matrix or near-2D objects that were formed at the surface. One possible explanation could be a phase transformation that occurred during the sputtering/annealing cycles. Looking at the phase diagram (in Chapter 1), one can notice a coexistence region of $\text{Al}_{13}\text{Fe}_4$ and Al_5Fe_2 .

In summary, when extracting the relevant CTRs, one has to be careful not to select a rod close to any Al_5Fe_2 peak in order to have a clean $\text{Al}_{13}\text{Fe}_4(010)$ signal. Knowing the relationship between the two helps finding out the best CTR candidates.

6.3.2 CTRs extraction

As mentioned before, only (H,K) CTRs with odd value of K have to be measured to make sure only one domain is investigated. The structure factors of eight inequivalent CTRs were measured for L ranging from 0 to 4.8. The structure factors of the five considered models were simulated using their DFT-relaxed surface structure and the ROD program and compared to the experimental data.

This is shown in Fig. 6.13. Some of the simulations reproduce very well most of the observed features (for example the (1,1) CTR for L ranging from 0 to 2 is strikingly well simulated using the P^{inc} models). Overall, the P^{inc} models are visually better fitting the experimental measurements. A χ^2 analysis is yet necessary to discriminate between all the models.

Tab. 6.1 sums up the ROD fitting results (only one fitting parameter, the scale factor). P and P_{1b}^{inc} models appear to be the worst fitting ones. P_{1a}^{inc} seems to be overall the best model with a χ^2 value of 4.445 and a R-factor of 0.460. Nevertheless, the discrepancy between P_{1a}^{inc} and $P_2^{\text{inc}}/P_0^{\text{inc}}$ is quite low (around 5% for the χ^2 value and 2% for the R-factor) and therefore maybe not significant.

A combination of these three models might also lead to a good agreement. This could lead to a partial desorption of Al glue atoms due to a too high annealing temperature. It was indeed previously observed that above 873 K, Al glue atoms were starting to desorb leading progressively to a P_0^{inc} surface structure [26] despite its higher surface energy.

Table 6.1: X-ray diffraction results – ROD analysis.

Surface Model	P	P_2^{inc}	P_{1a}^{inc}	P_{1b}^{inc}	P_0^{inc}
Scale factor	0.0126	0.00943	0.00954	0.00913	0.00969
χ^2	5.735	4.669	4.445	5.168	4.543
R-factor	0.485	0.469	0.460	0.496	0.463

The P_2^{inc} model will be kept as the main surface model in the following theoretical study since it was mainly observed using STM, having the lowest surface energy and fitting fairly well the SXR D data.

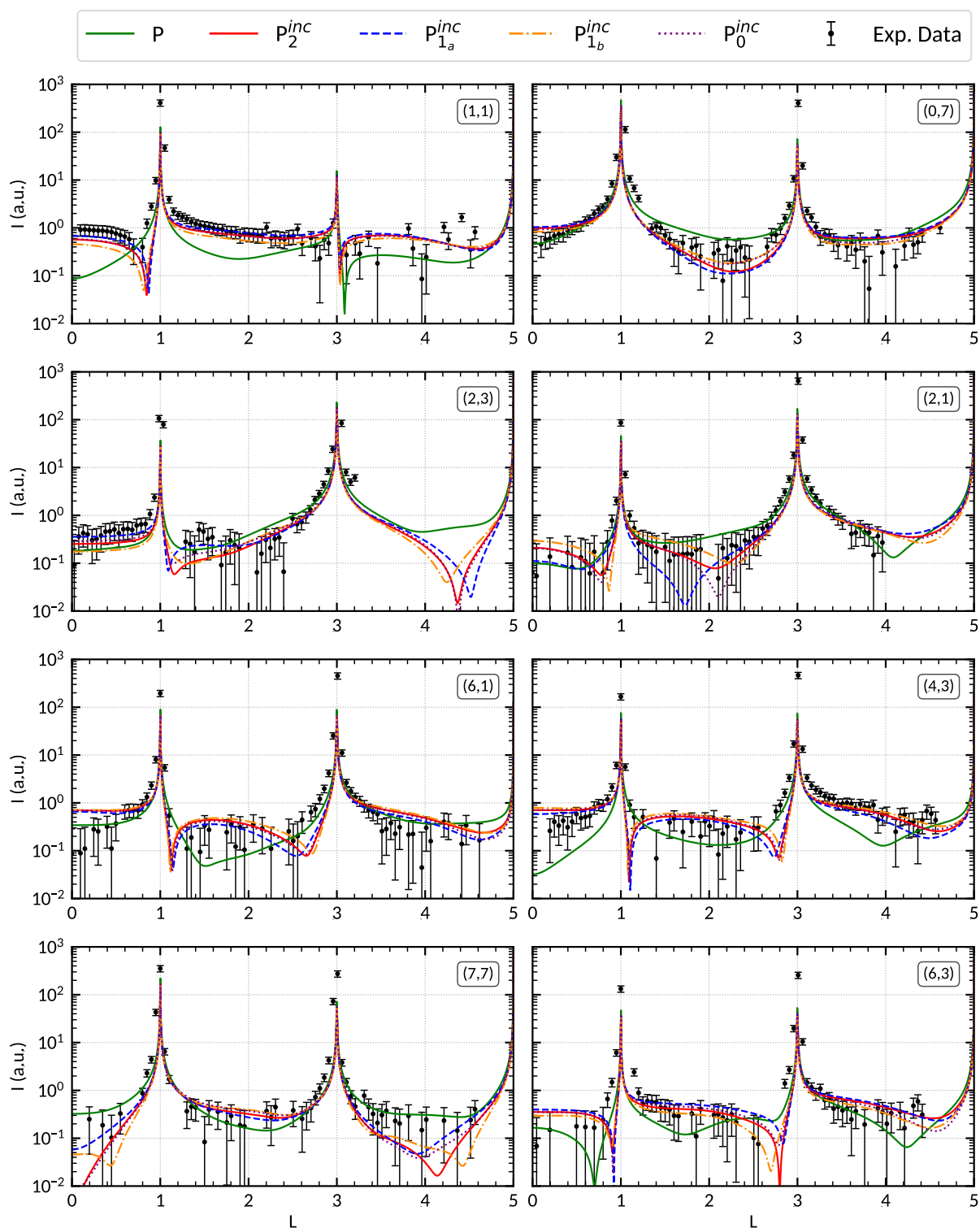


Figure 6.13: CTRs of $m\text{-Al}_{13}\text{Fe}_4(010)$ and their related DFT-based ROD simulation.

6.4 Adsorption calculations

Using the P_2^{inc} surface model for $\text{Al}_{13}\text{Fe}_4(010)$, one can move on to adsorption calculations of hydrogen, butadiene, and butene molecules. The DFT results will then allow for the determination of a possible hydrogenation reaction path.

6.4.1 Hydrogen adsorption

As stated in previous Chapters, weak hydrogen binding and easy dissociation are key descriptors in hydrogenation catalysis. These factors are related to the atomic hydrogen adsorption properties of $\text{Al}_{13}\text{Fe}_4(010)$. The right-hand map of Fig. 6.14 presents the potential energy surface of hydrogen adsorption energies on $\text{Al}_{13}\text{Fe}_4(010)$ P_2^{inc} . The adsorption has been computed on specific points of a regular grid covering the surface using a point density of $2.17 \text{ pts}/\text{\AA}^2$ (total of 400 adsorption positions).

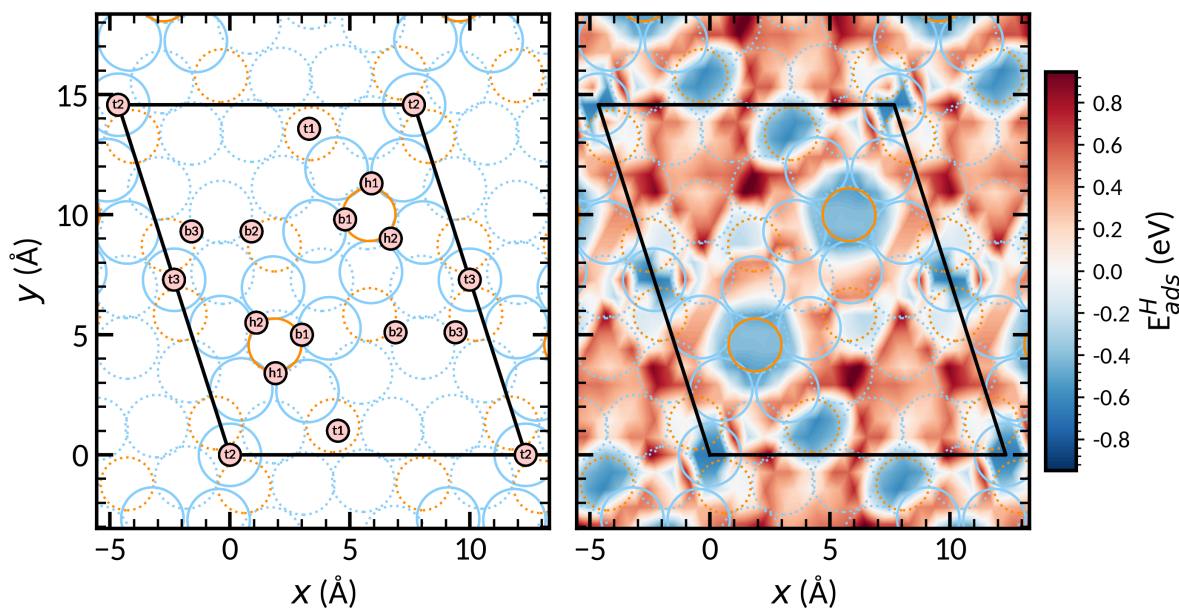


Figure 6.14: Hydrogen adsorption energy maps on P_2^{inc} . Al and Fe atoms are drawn in light blue and orange, respectively.

The left-hand map of Fig. 6.14 shows particular and stable adsorption sites (top, bridge and hollow sites) for which the adsorption energies are displayed in Tab. 6.2.

In total, 14 sites are considered to be stable (considering symmetry and steric hindrance). They are labelled $t1$ to $t3$ for top sites, $b1$ to $b3$ for bridge sites and $h1/h2$ for hollow sites. As for $\text{Al}_{13}\text{Co}_4(100)$ P^{14} , the most stable adsorption sites appear to be one of the subsurface

Table 6.2: Hydrogen adsorption energies on P_2^{inc}

Adsorption energies (eV)					
top		bridge		hollow	
t1	-0.61	b1	-0.44	h1	-0.53
t2	-0.57	b2	-0.28	h2	-0.47
t3	-0.55	b3	-0.19	-	-

Fe atom (site $t1$) and the Al glue atoms (sites $t2$ and $t3$) that link the bipentagonal Al motifs ($E_{\text{ads}}^{\text{H}} = [-0.61 \text{ eV}; -0.55 \text{ eV}]$). The second most stable sites are the protruding Fe atoms (hollow sites $h1$ and $h2$ with two Al atoms).

These results are further used as input to build hydrogenated surface models with hydrogen coverage ranging from 1 to 12 hydrogen atoms per surface unit cell. A maximum of 12 atoms will be adsorbed because of the coadsorption with an alkene molecule.

6.4.2 Butadiene and but-1-ene adsorptions

Following the same method that was applied to $\text{Al}_{13}\text{Co}_4$ the next step is to find the stable adsorption sites of butadiene and but-1-ene on $\text{Al}_{13}\text{Fe}_4(010)$. As previously stated, the *trans* configuration of butadiene is always preferred.

Fig. 6.15 displays the most stable adsorption sites for butadiene and butene and Tab. 6.3 their adsorption energies. Other sites are presented in reference [171]. Butadiene adsorption site involves primarily a protruding surface Fe atom and neighboring Al atoms (Fig. 6.15a, $E_{\text{ads}}^{\text{H}} = -1.90 \text{ eV}$). Butadiene is adsorbed within a $\pi_{\text{Fe}}(\text{C}=\text{C})\sigma_{\text{Al}}(\text{C})$ mode.

There are two ways to hydrogenate butadiene into butene. The first one consists in the hydrogenation of the $\text{C}=\text{C}$ bond that is adsorbed within a σ_{Al} mode (Fig. 6.15b, $E_{\text{ads}}^{\text{H}} = -1.38 \text{ eV}$). Butene is therefore adsorbed within a π_{Fe} mode. The second way consists in the hydrogenation of the $\text{C}=\text{C}$ bonded to the protruding Fe atom (Fig. 6.15c, $E_{\text{ads}}^{\text{H}} = -1.31 \text{ eV}$). In this case, butene is adsorbed within a $\sigma_{\text{Fe}}\sigma_{\text{Al}}$ mode, which weakens the adsorption.

Table 6.3: Butadiene and but-1-ene adsorption energies on P_2^{inc} .

Molecule	C_4H_6 ($\pi_{\text{Fe}}\sigma_{\text{Al}}$ mode)	C_4H_8 (π_{Fe} mode)	C_4H_8 ($\sigma_{\text{Fe}}\sigma_{\text{Al}}$ mode)
E_{ads} (eV)	-1.90	-1.38	-1.31

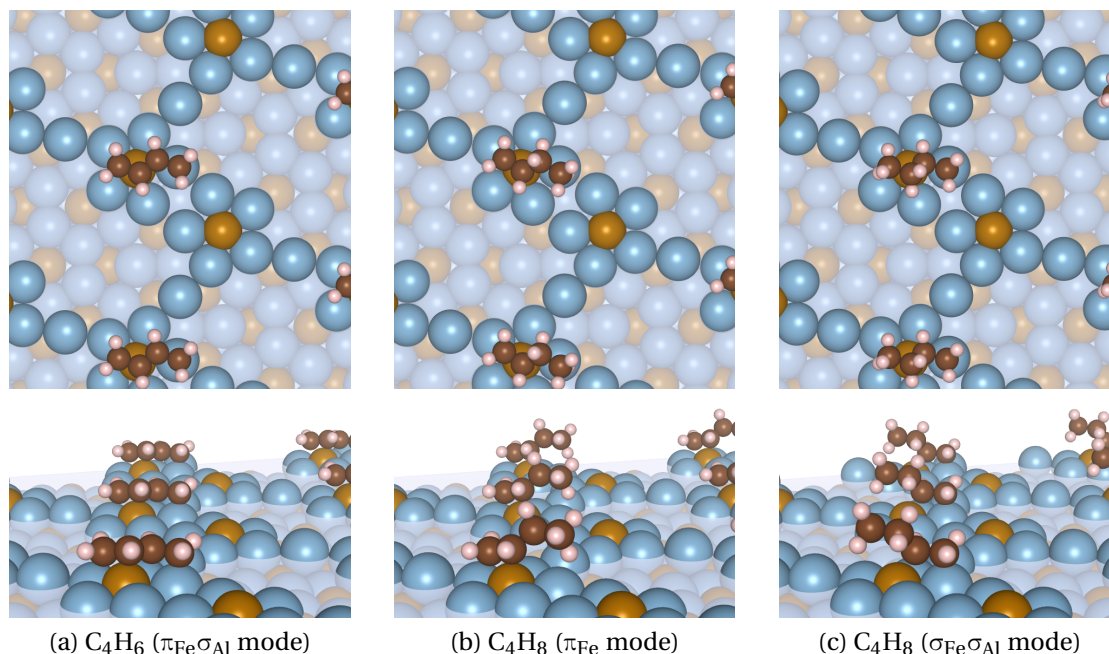


Figure 6.15: Adsorption sites of butadiene and but-1-ene on P_2^{inc} (top and perspective views). Al and Fe atoms are drawn in light blue and orange, respectively.

6.4.3 Coadsorption of hydrogen and butadiene/but-1-ene

It was shown that the optimum hydrogen coverage on $Al_{13}Fe_4(010)$ was eight hydrogen atoms per surface unit cell [171]. The next step is then the comparison between the adsorption energies of butadiene and butene under operating conditions. The thermodynamic model that was presented in Chapter 2 is therefore used.

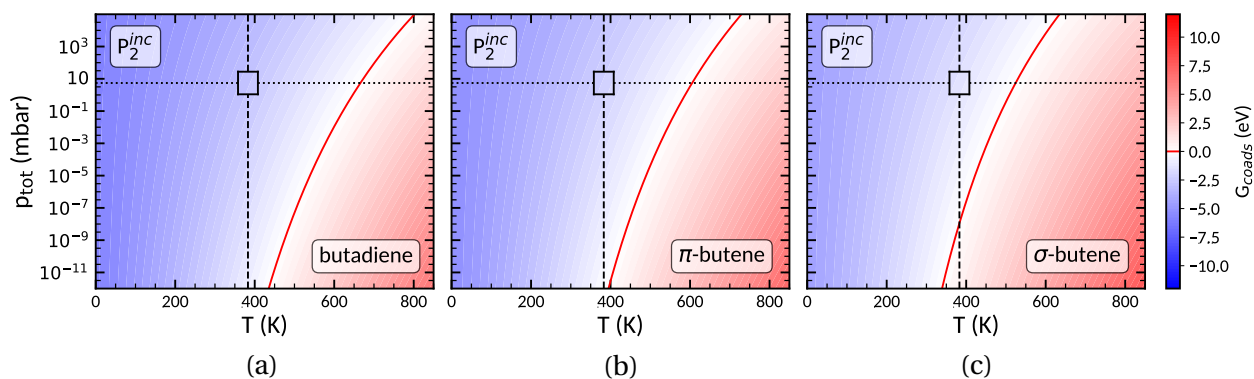


Figure 6.16: Adsorption free enthalpies (G_{coads} in eV) as a function of p and T for butadiene and butene (π and σ modes) on P_2^{inc} for a H coverage of 8.

The coadsorption (eight hydrogen atoms and one butadiene molecule) free enthalpy as a function of pressure and temperature (ratio 10:1) is plotted in Fig. 6.16a. Butadiene appears to be adsorbed on the surface for the reaction conditions ($T = 297\text{ K}$ or $T = 383\text{ K}$, $p = 5\text{ mbar}$). The coadsorption free enthalpy as a function of pressure and temperature is plotted in Fig. 6.16b and Fig. 6.16c for butene molecules adsorbed in π mode and σ mode, respectively. Both molecules appear to be adsorbed on the surface for the reaction conditions ($T = 297\text{ K}$ or $T = 383\text{ K}$, $p = 5\text{ mbar}$). However, as one could have expected, σ -butene is less strongly adsorbed than π -butene.

To summarize, the hydrogenation reaction is calculated to be thermodynamically feasible. Nevertheless, unlike $\text{Al}_{13}\text{Co}_4(100)$, it is not possible to state that the Fe centers are highly selective sites because of the close adsorption properties of σ -butene and π -butene. In both cases, but-1-ene is well adsorbed and could further be hydrogenated into butane.

6.5 Hydrogenation of butadiene : reaction pathways and kinetics

At this point, the surface structure is known and the adsorption properties (sites, energies, reaction feasibility) are determined for both hydrogen and alkene molecules on the pseudo 10-fold surface of $\text{Al}_{13}\text{Fe}_4$. As developed in Chapter 2, the Nudged Elastic Band method is a good one for the calculation of a possible reaction path. The results of the NEB calculations will be taken as inputs of a microkinetic model that aims to predict the activity of the catalyst as a function of the reaction conditions (p , T).

6.5.1 NEB calculations

The reaction path could be divided into three main parts following the adsorption of hydrogen and butadiene : the hydrogen molecule dissociation into two adsorbed hydrogen atoms, the partial hydrogenation of butadiene into butene, and finally the complete hydrogenation of butene into butane. All the calculations were done at the Γ point ($1 \times 1 \times 1$ k-points grid) only to speed up the investigation.

6.5.1.1 H_2 dissociation

All the stable adsorption sites of hydrogen were considered for the H_2 dissociation. However, only the protruding Fe atoms allows for the dissociation. Neither the Al glue atoms

nor the subsurface Fe atoms were able to adsorb H_2 and dissociate it. The calculated barrier is low for $Al_{13}Fe_4(010)$ with an activation energy of 0.06 eV (three times lower than $Al_{13}Co_4(100)$, $E_a = 0.18$ eV [24]). For this step only, the barrier was also calculated using a $9 \times 7 \times 1$ k-points mesh. The results (0.06 eV) is similar to the one calculated at the Γ point.

6.5.1.2 Partial hydrogenation

A possible partial hydrogenation reaction path is presented in Fig. 6.17. After the dissociation of H_2 , one hydrogen atom can react with the first C=C bond that is adsorbed on an Al atom. It was chosen to aim for the formation of π -butene rather than σ -butene, because of their adsorption energies.

The barrier of this first step is quite low ($E_a = 0.53$ eV), it is not the limiting step of the partial hydrogenation. In order to complete the hydrogenation of this first bond, the remaining H atom has to migrate onto an Al glue atom with a migration barrier of 0.75 eV. This higher value suggest that this step is the limiting one. Finally, this hydrogen atom can react with the second carbon of the bond to form butene. This last step has a rather low activation energy of 0.21 eV (not a limiting step).

The newly form butene molecules can either desorb ($E_{des} = 1.38$ eV) or stay adsorbed at the surface for further hydrogenation reactions.

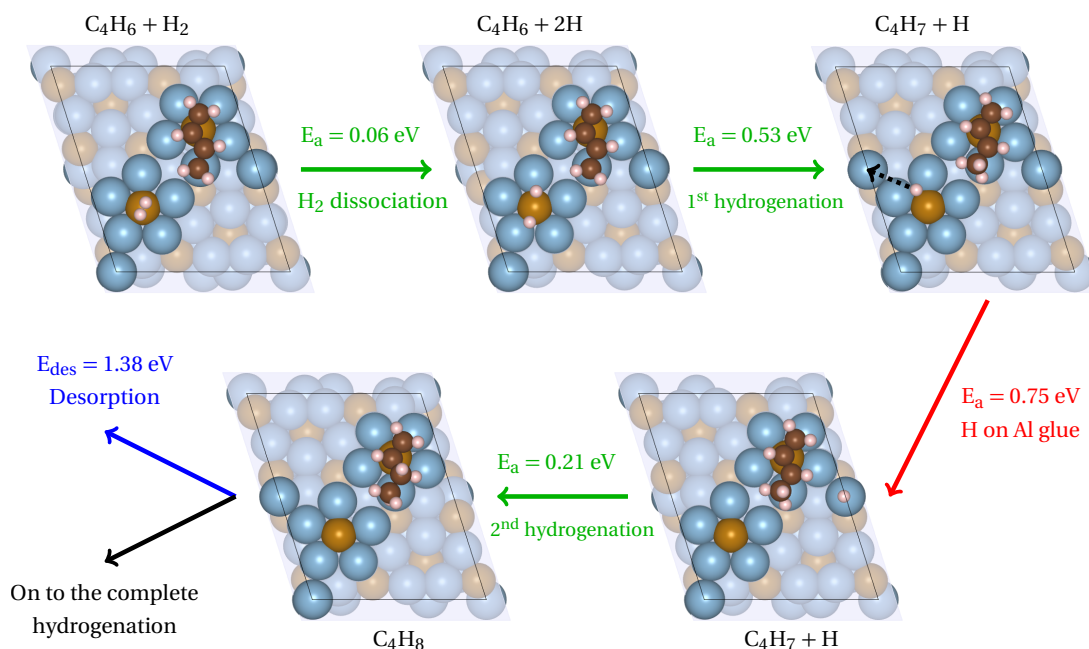


Figure 6.17: A possible reaction pathway on $Al_{13}Fe_4(010)$ for the partial hydrogenation of butadiene into butene.

6.5.1.3 Complete hydrogenation

A possible complete hydrogenation reaction path is presented in Fig. 6.18. After the dissociation of H_2 , one hydrogen atom can react with the last $\text{C}=\text{C}$ bond that is adsorbed on an Fe atom. To do so, the hydrogen atom has to migrate to an Al glue atom with a migration barrier of 0.78 eV. Only then the third hydrogenation can occur (hydrogenation of the outer carbon atom). This intermediate step has the highest energy barrier of 0.86 eV. This could explain the good selectivity of $\text{Al}_{13}\text{Fe}_4(010)$ towards the production of butene rather than butane.

Before completing the hydrogenation into butane, the remaining hydrogen atom has also to migrate towards a closer site to the molecule, *i.e.* a subsurface Fe atom, with an energy barrier of 0.86 eV. Finally, the fourth and last hydrogenation forms butane with an activation energy of 0.31 eV.

The newly form butane molecules can either desorb ($E_{\text{des}} = 0.42$ eV) or stay physisorbed at the surface (depending on the pressure and temperature conditions).

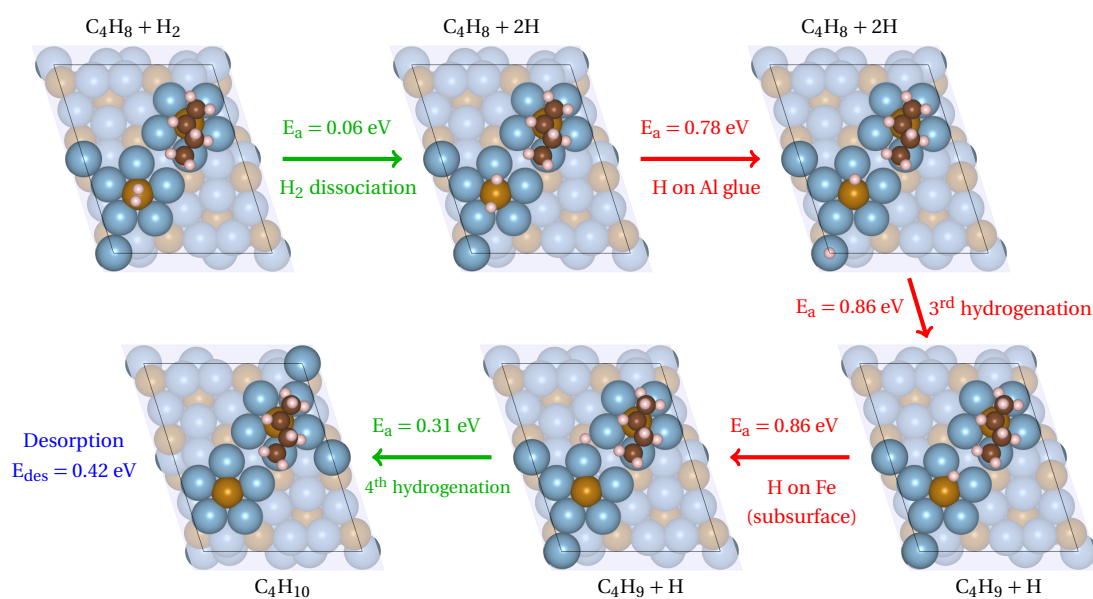


Figure 6.18: A possible reaction pathway on $\text{Al}_{13}\text{Fe}_4(010)$ for the complete hydrogenation of butene into butane.

6.5.1.4 Rate constants calculations

Using the Transition State Theory developed in Chapter 2, one can estimate the rate constants k for each elementary reaction steps of the reaction process (also detailed in Chapter

2). The NEB calculations coupled with vibrational calculations provide all the necessary input for the determination of k (activation energies and vibration frequencies). Table 6.4 presents the different values of the pre-exponential factors and activation energies for each elementary steps at 300K.

Table 6.4: Pre-exponential factors and activation energies of the different elementary steps.

Elementary step	A_0 (s^{-1}) at 300K	E_a (kJ/mol)
$H_2^* \rightarrow 2 H^*$	1.7×10^{15}	5.4
$2 H^* \rightarrow H_2^*$	4.8×10^{12}	13.6
$C_4H_6^* + H^* \rightarrow C_4H_7^* + *$	1.1×10^9	51.6
$C_4H_7^* + * \rightarrow C_4H_6^* + H^*$	3.8×10^{12}	37.5
$C_4H_7^* + H^* \rightarrow C_4H_8^* + *$	1.3×10^8	20.7
$C_4H_8^* + * \rightarrow C_4H_7^* + H^*$	4.1×10^{11}	0.3
$C_4H_8^* + H^* \rightarrow C_4H_9^* + *$	4.8×10^7	83
$C_4H_9^* + * \rightarrow C_4H_8^* + H^*$	2×10^{11}	0.1
$C_4H_9^* + H^* \rightarrow C_4H_{10}^* + *$	3×10^7	29.9
$C_4H_{10}^* + * \rightarrow C_4H_9^* + H^*$	4.2×10^{10}	90.1

6.5.1.5 Summary of the reaction path

Fig. 6.19 presents a summary of a possible reaction path. It is clear that the partial hydrogenation is easier to do (only one barrier higher than 0.7 eV) than the complete hydrogenation into butane (3 barriers higher than 0.7 eV). This suggests a high selectivity towards the formation of butene as observed experimentally.

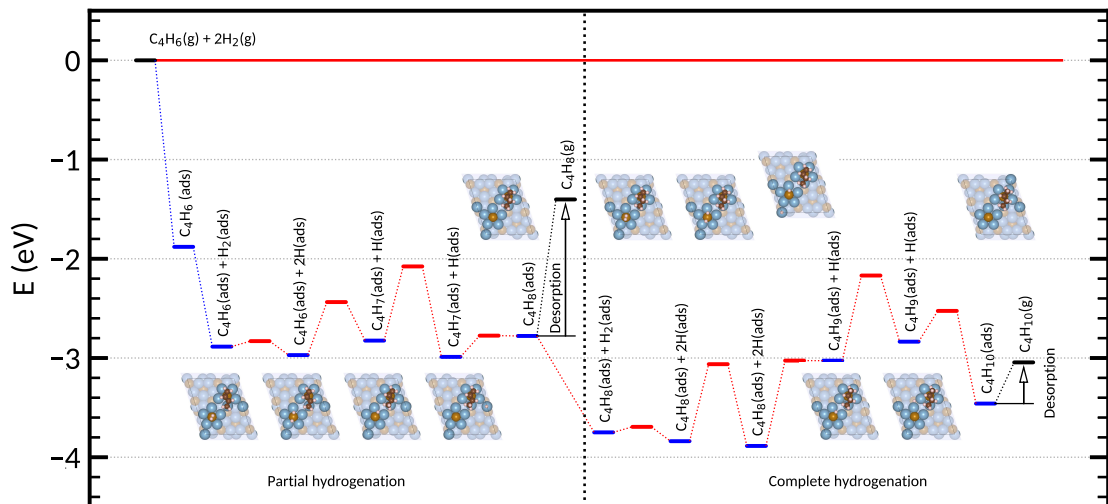


Figure 6.19: Summary of a possible reaction path of butadiene hydrogenation on $Al_{13}Fe_4(010)$.

6.5.2 Microkinetic modelling

The following section presents the results of the microkinetic modelling of the hydrogenation reaction of butadiene on Al₁₃Fe₄(010). The complete physical and mathematical descriptions of the microkinetic model are presented in Chapter 2.

The overall modelling is based on the reaction pathways that was previously determined (mechanism, activation energies, pre-exponential factors values). However, a few hypotheses and adjustments had to be made in order to reach convergence for the resolution of the ordinary differential equations (ODE) system and to fit the experimental measurements. They are detailed as follow :

1. The intermediate steps where hydrogen atoms migrate from one site to another are not considered in the microkinetic modelling. This decision had been made for two main reasons. First, the mathematical implementation of the diffusion mechanism is too demanding for the simple purpose of that model. It is therefore a matter of space and time coupling, bringing out partial differential equations (PDE) that need more advanced tools to get solved. Second, the diffusion of hydrogen atoms is considered to be easier than any other intermediate steps – despite high energy barriers – because of high pre-exponential factor values (higher than 10^{12} [182]).
2. The activation energies were determined through the means of NEB calculations using the DFT-D3 functional at the Γ point ($1 \times 1 \times 1$ k-points grid). In order to reach convergence and fit the experimental data, a multiplicative coefficient of **0.667** was applied to all the energy barriers. This coefficient allows for the adjustment of the temperature in the model (thermodynamic adjustment). This value tends to correct the DFT approximations.
3. The pre-exponential factors were determined thanks to the transition state theory (described in Chapter 2). In order to reach convergence and fit the experimental data, a coefficient of **0.475** was applied to all the factors : in the case of a dissociation (H₂ dissociation or C₄H_n losing a H atom), the factor 10^x becomes the factor $10^{x-0.475}$; in the case of a recombination or hydrogenation, the factor 10^x becomes the factor $10^{x+0.475}$. This coefficient allows for the adjustment of the production rates of the different considered species (kinetic adjustment).

The script of the microkinetic modelling is detailed in the Appendices of the present manuscript. It includes the definition of the different ordinary differential equations that model the hydrogenation reaction as well as the numerical resolution of the aforementioned ODE system.

6.5. Hydrogenation of butadiene : reaction pathways and kinetics

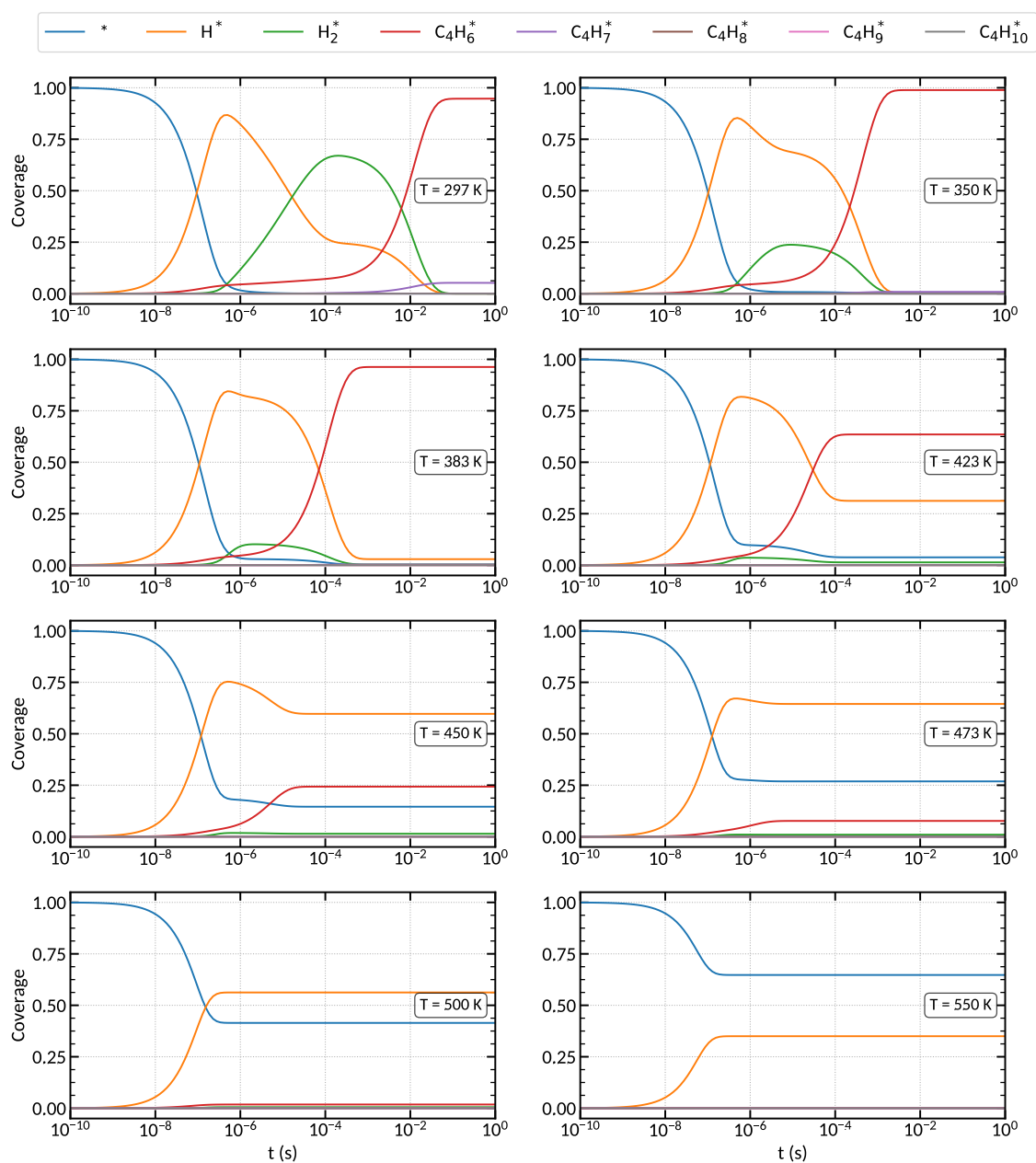


Figure 6.20: Coverage over time of different adsorbed molecules at given temperatures.

Given a set of activation energies, pre-exponential factors, as well as initial conditions (hydrogen and butadiene partial pressures – here is kept the previously studied 10:1 ratio for $\text{H}_2:\text{C}_4\text{H}_6$ – and reaction temperature), the model predicts the adsorption coverage over time of the different adsorbed species (indicated with a \star symbol : H_2^* , H^* , C_4H_6^* , C_4H_7^* , C_4H_8^* , C_4H_9^* , $\text{C}_4\text{H}_{10}^*$). Fig. 6.20 presents the results of the microkinetic modelling for eight different temperatures (297–550 K). In the considered range of temperatures, the system

always converges and reaches a stationary state (no more evolution of the chemical reaction). As expected, one can notice that the higher the temperature, the faster the reaction kinetic (shorter time to reach a stationary state).

Looking at the first few nanoseconds ($t < 10^{-7}\text{s}$), the main reaction appears to be the dissociation of hydrogen on top of Fe protruding atoms, followed by the low adsorption of butadiene and hydrogen molecules. This first step seems to be independent of the reaction temperature (for the considered temperature range). In the range 297–350K, the stationary coverage of butadiene increases, while all the other species get less adsorbed. In the range 350–473K it is the opposite scenario : the butadiene stationary coverage decreases progressively while the one of hydrogen increases. Above 473K, all the species start to get less and less adsorbed (more and more unoccupied sites).

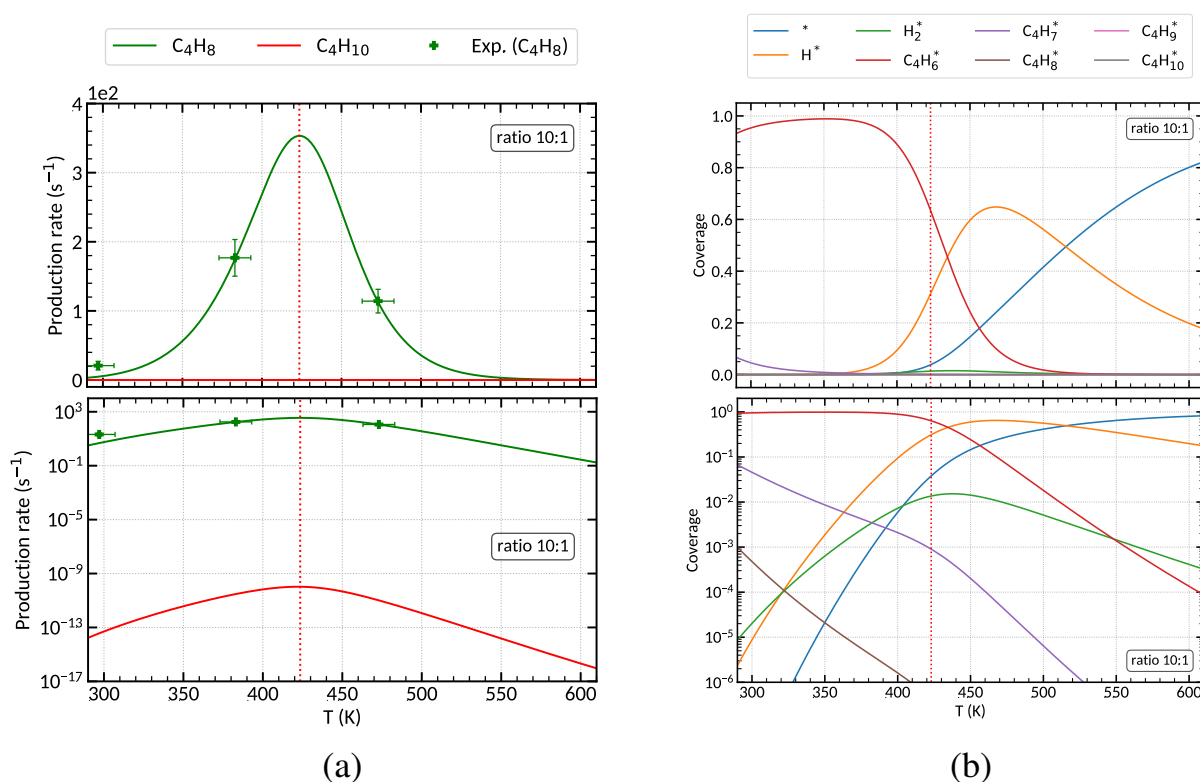


Figure 6.21: (a) Experimental and simulated production rates of butene and butane as a function of temperature. (b) Coverage (stationary state) of the different adsorbed molecules as a function of temperature. The red dotted line indicates the temperature of maximum butene production rate ($T = 423$ K $\approx 150^\circ\text{C}$).

Knowing all the stationary-state coverages of each adsorbed species, it is possible to determine the production rates of but-1-ene and butane as a function of temperature (see Chapter 2 for more details). The results are presented in Fig. 6.21a. The experimental data

points come from [7]. Although only three data points are available, the simulation shows a rather good agreement with the experiment. A maximum but-1-ene production rate ($r_{\max} = 353$ molecules/site/s) is calculated for $T = 423$ K. The butane production is insignificant (below 10^{-7} molecules/site/s) compared to the one of but-1-ene. This result is in agreement with the high selectivity towards butenes that has been experimentally observed. This is due to the fact that butene cannot stay adsorbed and be further hydrogenated into $C_4H_9^*$.

Fig. 6.21b shows the stationary-state coverages of the different adsorbed molecules as a function of temperature. At low temperatures (below 350 K), the two main adsorbed species are $C_4H_6^*$ and $C_4H_7^*$. This explains the rather low production rate of butene on this temperature range : not enough hydrogen atoms can react with $C_4H_7^*$ to produce C_4H_8 . In the range 350–423 K, $C_4H_6^*$ and H^* are the two dominant adsorbates and a increase of the production rate of butene is observed.

At 423 K (maximum production rate of butene), the $H^*:C_4H_6^*$ ratio is 0.31:0.62. This means that a maximum production rate of butene is reached out only when there are twice as many adsorbed butadiene molecules than hydrogen atoms at the surface. Based on the NEB calculations, the most difficult step of the partial hydrogenation is the first hydrogenation of $C_4H_6^*$ into $C_4H_7^*$. Therefore, this particular 1:2 ratio might be favorable because it would statistically allow to maximize the production of this intermediate state C_4H_7 .

In the range 423–520 K, only the coverages of hydrogen atoms and hydrogen molecules increase. Above 520 K, all the adsorbates start to desorb giving rise to a progressively insignificant butene production rate.

Additional experimental measurements (different pressure ratios and reaction temperatures) could improve the simulation tunings and the model implementation.

6.6 Conclusion

The study presented in this Chapter sums up the entire approach that was undertaken in this research project : going from UHV surface characterization and *ab initio* calculations to catalytic performances and reaction kinetic simulations.

Surface X-ray diffraction analysis confirms the surface structure that was previously reported, *i.e.* an incomplete puckered layer built from the preservation of the clusters building blocks. The presence of Al glue atoms that connect the clusters together is still controversial and certainly dependant on the annealing temperature and sputtering conditions. SXRD measurements also bring new light on a possible epitaxial relationship be-

tween Al₁₃Fe₄(010) and Al₅Fe₂(001). This result could be of interest for surface coating applications.

Adsorption calculations allow for the mapping of the hydrogen potential energy landscape as well as for the evaluation of stable butadiene and butene adsorption sites. The hydrogenation reaction of butadiene into butene is calculated to be thermodynamically feasible but no clear selectivity towards the semi-hydrogenation reaction can be deduced from this basic modelling.

All the previous results provide enough insights in order to build a microkinetic modelling of the hydrogenation of butadiene on Al₁₃Fe₄(010). A good agreement is found between the simulated and measured butene production rate as a function of the temperature. For a 10:1 ratio (5 Torr of H₂, 0.5 Torr of butadiene), a maximum production rate occurs at 423 K. The model predicts a 100% selectivity towards butene. This result is also in agreement with the catalytic performances of Al₁₃Fe₄(010).

Further theoretical (change of functional, increased precision of k-points grids, more accurate vibration calculations) and experimental (different pressure ratios and reaction temperatures) investigations are needed to finely tune the microkinetic modelling of the hydrogenation of butadiene on Al₁₃Fe₄(010).

Conclusions and Future Works

Conclusions

Through the different analyses and results presented in this manuscript, it is shown that the experimental-theoretical coupling (STM, SXRD, catalytic measurements and DFT calculations) is a powerful tool to get the full picture, from the surface atomic structure to the catalytic performances, vis-a-vis the butadiene hydrogenation reaction. Only then one can get a detailed picture of the surface structures of Al-based complex intermetallics, where are the active sites, what are the possible reaction conditions and mechanisms, and finally what are the reaction kinetics.

The surface structure and adsorption properties of $\text{Al}_5\text{Co}_2(2\bar{1}0)$ have been investigated in Chapter 3. This compound presents catalytic properties, attributed to protruding Co atoms at the surface. The analysis leads to the conclusion that surface Co atoms are well isolated from each other at the surface, the distance between two closest Co atoms being 7.6 Å. The consideration of atomic hydrogen and butadiene co-adsorption, in agreement with the Langmuir-Hinshelwood mechanism, as well as the influence of operating conditions (p,T), weaken the adsorption energies of butadiene and butene. Both chemisorbed and physisorbed butene molecules are adsorbed at reaction conditions, but less strongly than butadiene. The hydrogenation leading to physisorption of butene seems more realistic when comparing to experimental results. The study clearly show that although $\text{Al}_{13}\text{Fe}_4(010)$ and $\text{Al}_5\text{Co}_2(2\bar{1}0)$ present similar surface structures under UHV, with the presence of well isolated transition metal atoms protruding at the surface, and show analogous adsorption properties, their catalytic performances are rather different. Further theoretical and experimental investigations, including the determination of the surface structure under reaction condition, and of a possible reaction path, have to be conducted to fully get the catalytic properties of $\text{Al}_5\text{Co}_2(2\bar{1}0)$.

In Chapter 4, the catalytic behavior of the $\text{Al}_{13}\text{Co}_4(100)$ surface towards butadiene partial hydrogenation was rationalized. On the basis of surface phase diagrams determined through DFT calculations, it is shown that the (p, T, μ_{Al}) conditions where the $\text{Al}_{13}\text{Co}_4(100)$ dense Al-rich flat termination is the most stable narrow as the pressure increases and the temperature decreases. The dense Al-rich flat termination of $\text{Al}_{13}\text{Co}_4(100)$ is unlikely under hydrogenation conditions, and the adsorption of butadiene inhibits any further adsorption of hydrogen at the surface, which prevents butadiene hydrogenation. According to atomistic thermodynamics, the reaction conditions promote a nanostructured surface termination, in the form of highly cohesive clusters emerging from the bulk lattice. The comparison of butadiene and butene adsorption modes and energies under thermodynamic conditions give insights of the catalytic behavior of $\text{Al}_{13}\text{Co}_4(100)$. According to the calculations, butene may not desorb when chemisorbed through a π bonding involving a Co atom protruding at the surface. A better agreement with the experimental observation is obtained with the hydrogenation of the butadiene C=C fragment adsorbed on the protruding Co atom. The calculations thus suggest the hydrogenation of the π -bonded C=C fragment on the protruding Co atom first. Reaction conditions are also expected to influence the kinetics, for which further investigation is required. Experimental verification of the predicted nanostructuring requires *in situ/operando* characterization (e.g. surface X-ray diffraction) to identify the actual working surface under gas pressure conditions.

The surface structure of the pseudo 2-fold surface of $\text{Al}_{13}\text{Co}_4$ was investigated in Chapter 5. Based on a combination of experimental (LEED, AFM, STM, SXRD) and theoretical (DFT calculations) results, *o*- $\text{Al}_{13}\text{Co}_4(010)$ was shown to present a highly faceted surface structure similar to its quasicrystal counterpart *d*- AlNiCo 2-fold surface. The surface model consists of a coexistence of both flat terraces (orthorhombic structure) made of triangular Al motifs, and facets (*m*- $\text{Al}_{13}\text{Co}_4(\bar{2}01)$) with a fairly denser and Co-enriched atomic surface structure. Facets substantially stabilize the pseudo-2-fold surface orientation. Their surface energies are indeed calculated to be much lower than the flat terraces. The hydrogen adsorption investigation shows a wide diversity of favorable atomic hydrogen adsorption sites, some of them being quite strongly bound to the surface ($E_{\text{ads}} \simeq -0.5$ eV). This promotes the dissociation of H_2 , whereas others interact more weakly with the surface and are possibly more active for hydrogenation steps. Further experimental and theoretical works, under catalytic conditions, are therefore needed to fully understand the mechanism behind the catalytic properties of *o*- $\text{Al}_{13}\text{Co}_4(010)$.

In Chapter 6, surface X-ray diffraction analysis confirmed the surface structure that was

previously reported, *i.e.* an incomplete puckered layer built from the preservation of the clusters building blocks. The presence of Al glue atoms that connect the clusters together is still controversial and certainly dependant on the annealing temperature and sputtering conditions. SXR measurements also bring new light on a possible epitaxial relationship between $\text{Al}_{13}\text{Fe}_4(010)$ and $\text{Al}_5\text{Fe}_2(001)$. This result could be of interest for surface coating applications. On a theoretical point of view, the hydrogenation reaction of butadiene into butene is calculated to be thermodynamically feasible but no clear selectivity towards the semi-hydrogenation reaction can be deduced from this basic modelling. All the previous results provide enough insights in order to build a microkinetic modelling of the hydrogenation of butadiene. A good agreement is found between the simulated and measured butene production rate as a function of the temperature. For a 10:1 ratio (5 Torr of H_2 , 0.5 Torr of butadiene), a maximum production rate occurs at 423 K. The model predicts a 100% selectivity towards butene which is in agreement with the catalytic performances of $\text{Al}_{13}\text{Fe}_4(010)$. Further theoretical (change of functional, increased precision of k-points grids) and experimental (different pressure ratios and reaction temperatures) investigations are needed to finely tune the microkinetic modelling of the hydrogenation of butadiene on $\text{Al}_{13}\text{Fe}_4(010)$.



Several surfaces of Al-based approximants to decagonal quasicrystals have been identified as possible catalysts for butadiene hydrogenation. It is the case for $\text{Al}_{13}\text{Co}_4(100)$, $\text{Al}_{13}\text{Co}_4(010)$, $\text{Al}_{13}\text{Fe}_4(010)$ and $\text{Al}_5\text{Co}_2(2\bar{1}0)$ as developed previously. While these surfaces present structural similarities (apart from $\text{Al}_{13}\text{Co}_4(010)$) – pentagonal arrangement of Al atoms embedding a transition metal atom – their adsorption properties and catalytic performances are quite different. The adsorption energies of butadiene and butene increase when considering successively the $\text{Al}_{13}\text{Co}_4(100)$, $\text{Al}_{13}\text{Fe}_4(010)$ and $\text{Al}_5\text{Co}_2(2\bar{1}0)$ surfaces, with values ranging from -1.59 eV, -1.80 eV to -1.92 eV for butadiene and from -1.13 eV, -1.38 eV to -1.52 eV for butene. Hydrogen adsorption energies are similar on $\text{Al}_{13}\text{Fe}_4(010)$ and $\text{Al}_5\text{Co}_2(2\bar{1}0)$ – they are -0.41 eV and -0.39 eV, respectively – and slightly differ from the ones and $\text{Al}_{13}\text{Co}_4(100)$ (-0.24 eV). Focusing on catalytic performances, $\text{Al}_5\text{Co}_2(2\bar{1}0)$, like $\text{Al}_{13}\text{Co}_4(100)$, presents a lower activity at 383 K than $\text{Al}_{13}\text{Fe}_4(010)$, which is very active even at room temperature. Nevertheless, $\text{Al}_{13}\text{Co}_4(010)$ remains the most active one at 383 K.

Adsorption energies are a key element of any theoretical search for new catalyst materials, the Sabatier principle setting a correlation between the catalytic activity and the catalyst/molecular interactions. Here it was demonstrated that although they are similarities between the $\text{Al}_{13}\text{Fe}_4(010)$ and $\text{Al}_5\text{Co}_2(2\bar{1}0)$ surface structures investigated under

ultra-high vacuum and between their corresponding adsorption properties calculated using DFT, their catalytic performances are rather different. This different catalytic behaviour may come from kinetic factors, or from the emergence of a different surface structure under reaction conditions.

In the world of catalysis, conventional catalysts tend to follow a thermochemical linear scaling, the Brønsted-Evans-Polanyi relationship (linear correlation between the activation energy and the adsorption energy). It is the case for catalytic metals as well as alloys. However, it has recently been shown that single-atom alloys (highly dilute bimetallic alloys) have the ability to deviate from that linear scaling while exhibiting excellent catalytic properties [183, 184]. The Al-based intermetallics that were studied in this work seem to also break this conventional linear scaling (based on the calculated adsorption energies of both butadiene and butene, and their catalytic activities). Nevertheless, just a few of these complex intermetallics were investigated. This class of materials deserves then to be more in depth studied.

Perspectives

In this work, the surface structures (under ultra-high vacuum and reaction conditions) and the reaction properties of Al-based intermetallics were determined. New insights were then provided on the surface structures of such compounds as well as on their catalytic (adsorption and reactivity) properties. This work is far to be entirely completed, but it was brought a step further.

A few perspectives can be considered in order to improve the systematic study of Al-based complex intermetallics as potential catalysts for hydrogenation reactions. Considering the Al-Fe system for example, a few surface orientations of Al_5Fe_2 (that have yet to be studied) could be of interest. The (001) and (100) surfaces might present interesting active and selective sites. The $(02\bar{1})$ surface might also present interesting features – close to the one of $\text{Al}_5\text{Co}_2(2\bar{1}0)$ – and catalytic properties. On the other hand, one has to keep in mind that the Al-based intermetallics have one drawback that could be a problem under industrial conditions: they have a propensity to deactivate because of oxygen contamination [9], which is the main issue for practical use of non-noble metal catalysts. Others materials could be less sensitive to oxygen contamination such as Ga-based intermetallics. Replacing aluminium by its gallium counterpart may be – though expensive – a solution. Nevertheless, changing the materials is one thing. Another one would be to adapt the synthesis of the materials and go from centimeter-sized single-crystal to thin films [29] or even nanoparticles of complex intermetallics. The latter could benefit from the recent advances

of *in situ* and *operando* imaging using for example coherent x-ray diffraction imaging [30].

On a more theoretical side, thermodynamic and kinetic models could be improved by a systematic investigation of the impact of different functionals and *ab initio* parameters such as the discretization of the reciprocal space (k-points mesh). This approach could help to determine what kind of input parameters are the most suited to model particular chemical reactions. Moreover, the coupling between DFT calculations and SXRD measurements is the foundation of the work that was presented in this thesis. The surface models that are determined thanks to this powerful combination are further used to predict the thermodynamic feasibility and the kinetic of chemical reactions. The scientific community would greatly benefit from a computational tool that can couple SXRD data refinement and DFT structural relaxation. Such tool already exists for the refinement of bulk structures. This kind of tools uses for example machine learning to predict reaction barriers and first-principles-assisted genetic algorithms to automatically determine crystal structures from powder diffraction data [27, 28]. The transfer to the surface science field is just a step further.

Appendix A

Publications

The publications and communications that are associated with the present thesis can be found (among others) on the following *Google Scholar* account (regularly updated) :

https://scholar.google.fr/citations?hl=en&user=JMdqN-sAAAAJ&view_op=list_works&sortby=pubdate

Appendix B

Crystallographic data

Contents

B.1	Al₅Co₂	166
B.2	Al₅Fe₂	166
B.3	<i>o</i>-Al₁₃Co₄	167
B.4	<i>m</i>-Al₁₃Co₄	168
B.5	<i>m</i>-Al₁₃Fe₄	169

The crystallographic data (equivalent positions and Wyckoff numbers) are presented in the following tables.

B.1 Al₅Co₂

Al ₅ Co ₂ (Space group <i>P6₃/mmc</i> , group number 194) [11]					
Lattice parameters					
a (Å)	b(Å)	c(Å)	alpha	beta	gamma
7.656	7.656	7.539	90	90	120
	x	y	z	Wyckoff number	
Al1	0.00000	0.00000	0.00000	2a	
Al2	0.93400	0.46700	0.75000	6h	
Al3	0.39200	0.19600	0.06100	12k	
Co1	0.66667	0.33333	0.25000	2d	
Co2	0.25600	0.12800	0.75000	6h	

B.2 Al₅Fe₂

Al ₅ Fe ₂ (Space group <i>Cmcm</i> , group number 63) [82]					
Lattice parameters					
a (Å)	b(Å)	c(Å)	alpha	beta	gamma
7.6559	6.4154	4.2184	90	90	90
	x	y	z	Wyckoff number	
Al1	0.1880	0.1467	0.2500	8g	
Al2	0.0000	0.5000	0.0000	4b	
Al3	0.5000	0.0340	0.8300	8f	
Fe	0.0000	0.8277	0.2500	4c	

B.3 *o*-Al₁₃Co₄

The Al atoms that are present in the center of the Henley clusters are **Al16** and **Al17** for *o*-Al₁₃Co₄.

<i>o</i> -Al ₁₃ Co ₄ (Space group <i>Pmn</i> 2 ₁ , group number 31) [20]					
Lattice parameters					
a (Å)	b (Å)	c (Å)	alpha	beta	gamma
8.15800	12.34200	14.45200	90	90	90
	x	y	z	Wyckoff number	
Al25	0.22440	0.29460	0.73520	4b	
Co4	0.00000	0.77200	0.31670	2a	
Al16	0.00000	0.10470	0.23800	2a	
Al14	0.00000	0.59860	0.21490	2a	
Al17	0.00000	0.41790	0.58810	2a	
Al6	0.00000	0.81130	0.15640	2a	
Co9	0.22570	0.90990	0.73460	4b	
Al22	0.22510	0.98100	0.09350	4b	
Al4	0.00000	0.90850	0.44310	2a	
Al24	0.22590	0.58850	0.54220	4b	
Al19	0.21380	0.90200	0.28310	4b	
Co3	0.00000	0.19770	0.82500	2a	
Al7	0.00000	0.80920	0.83600	2a	
Al3	0.00000	0.90530	0.62260	2a	
Co2	0.00000	0.09010	0.51140	2a	
Co1	0.00000	0.89780	0.00000	2a	
Al18	0.21350	0.21380	0.09960	4b	
Co5	0.00000	0.59860	0.82480	2a	
Al15	0.00000	0.71110	0.96680	2a	
Al9	0.00000	0.40700	0.85200	2a	
Co7	0.00000	0.73090	0.51800	2a	
Al26	0.22910	0.42200	0.42520	4b	
Al21	0.25340	0.25500	0.91720	4b	
Al13	0.00000	0.52710	0.00540	2a	
Al10	0.00000	0.40100	0.14910	2a	
Al20	0.24010	0.08290	0.40880	4b	
Al1	0.00000	0.99450	0.81510	2a	
Al2	0.00000	0.09140	0.95690	2a	
Al5	0.00000	0.13940	0.67280	2a	
Co8	0.00000	0.28770	0.00760	2a	
Al11	0.00000	0.68370	0.67490	2a	
Al27	0.21330	0.51740	0.73380	4b	
Al12	0.00000	0.59000	0.39600	2a	
Co6	0.00000	0.41190	0.31370	2a	
Al28	0.23190	0.27630	0.28490	4b	
Co10	0.21810	0.59690	0.09840	4b	
Al8	0.00000	0.25200	0.41400	2a	
Al23	0.22140	0.22290	0.55000	4b	

B.4 $m\text{-Al}_{13}\text{Co}_4$

The Al atoms that are present in the center of the Henley clusters are **Al15** for $m\text{-Al}_{13}\text{Co}_4$.

$m\text{-Al}_{13}\text{Co}_4$ (Space group $C2/m$, group number 12) [16]					
Lattice parameters					
a (Å)	b (Å)	c (Å)	alpha	beta	gamma
15.18300	8.12200	12.34000	90	107.9	90
	x	y	z	Wyckoff number	
Al11	0.13671	0.21951	0.52149	8j	
Al10	0.17829	0.27988	0.33435	8j	
Al7	0.18555	0.28240	0.11092	8j	
Co5	0.31973	0.20658	0.27779	8j	
Al13	0.36793	0.28805	0.10985	8j	
Al14	0.49182	0.26717	0.32987	8j	
Al4	0.02071	0.00000	0.17091	4i	
Co4	0.09742	0.00000	0.01426	4i	
Co2	0.09808	0.00000	0.37654	4i	
Al15	0.17695	0.00000	0.71842	4i	
Al12	0.19447	0.00000	0.22725	4i	
Al3	0.25909	0.00000	0.03874	4i	
Al5	0.26256	0.00000	0.46521	4i	
Co3	0.40945	0.00000	0.01148	4i	
Al6	0.41360	0.00000	0.21180	4i	
Al2	0.42642	0.00000	0.41972	4i	
Al1	0.56605	0.00000	0.17393	4i	
Co1	0.58547	0.00000	0.38244	4i	
Al9	0.00000	0.24950	0.00000	4g	
Al8	0.00000	0.00000	0.50000	2c	

B.5 $m\text{-Al}_{13}\text{Fe}_4$

$m\text{-Al}_{13}\text{Fe}_4$ (Space group $C2/m$, group number 12) [91]					
Lattice parameters					
a (Å)	b (Å)	c (Å)	alpha	beta	gamma
15.492	8.078	12.471	90	107.69	90
	x	y	z	Wyckoff number	
Al11	0.13671	0.21951	0.52149	8j	
Al10	0.17829	0.27988	0.33435	8j	
Al7	0.18555	0.28240	0.11092	8j	
Fe5	0.31973	0.20658	0.27779	8j	
Al13	0.36793	0.28805	0.10985	8j	
Al14	0.49182	0.26717	0.32987	8j	
Al4	0.02071	0.00000	0.17091	4i	
Fe4	0.09742	0.00000	0.01426	4i	
Fe2	0.09808	0.00000	0.37654	4i	
Al15	0.17695	0.00000	0.71842	4i	
Al12	0.19447	0.00000	0.22725	4i	
Al3	0.25909	0.00000	0.03874	4i	
Al5	0.26256	0.00000	0.46521	4i	
Fe3	0.40945	0.00000	0.01148	4i	
Al6	0.41360	0.00000	0.21180	4i	
Al2	0.42642	0.00000	0.41972	4i	
Al1	0.56605	0.00000	0.17393	4i	
Fe1	0.58547	0.00000	0.38244	4i	
Al9	0.00000	0.24950	0.00000	4g	
Al8	0.00000	0.00000	0.50000	2c	

Appendix C

Python scripts

Contents

C.1 Thermodynamic modelling	171
C.2 Pre-exponential factors	172
C.3 Microkinetic modelling	187
C.4 Reciprocal space simulation	191

C.1 Thermodynamic modelling

```
1 #!/usr/bin/env python3
2 # -*- coding: utf-8 -*-
3 """
4 @author: Corentin Chatelier, PhD Student, IJL-SOLEIL-CNRS
5 Thermodynamic modelling
6 """
7 import numpy as np
8
9 def Gads(T, logPsurP0, Etot, Eslab, EH2, Emol, nH2, molecule):
10
11     GadsTP = Etot - Eslab - nH2*EH2 - Emol
12
13     mH = 1.6737210e-27; # kg
14     kB = 1.38064852e-23; # m2 kg s-2 K-1
15     h = 6.62607e-34; # m2 kg s-1
16     z_trans_star_H2 = ((2.0*np.pi*2.0*mH*kB*T)/(h**2))**(3.0/2.0);
17
18     P0 = 1.0e5; #
19     sigma_r = 2.0;
20     R = 0.739e-10;
21     I = mH*R**2.0/2.0;
22     z_rot_H2 = (1.0/sigma_r)*(8.0*(np.pi**2)*I*kB*T)/(h**2);
23
24     GadsTP += nH2*kB*T*np.log(z_trans_star_H2*z_rot_H2)/(1.60218e-19)
25
26     GadsTP += -kB*T*nH2*(logPsurP0 + np.log(P0/(kB*T)))/(1.60218e-19)
27
28     if molecule == 'butadiene':
```

```

29     amu = 1.660539e-27
30     Ia = amu*12.12444e-20 # en kg m2
31     Ib = amu*113.99086e-20
32     Ic = amu*126.09124e-20
33     sigma_butadiene = 2.0 # C2h
34     nC4H6 = 1
35     mC4H6 = 4*12*amu + 6*mH
36
37     z_trans_star_butadiene = ((2.0*np.pi*mC4H6*kB*T)/(h**2))**(3.0/2.0);
38
39     z_rot_butadiene = np.pi**(1.0/2.0)/sigma_butadiene*T**(3.0/2.0)
40     *8**(3.0/2.0)*np.pi**3*kB**(3.0/2.0)*(Ia*Ib*Ic)**(1.0/2.0)/h**3
41
42     GadsTP += nC4H6*kB*T*np.log(z_trans_star_butadiene*z_rot_butadiene)
43             /(1.60218e-19)
44
45     GadsTP += -kB*T*nC4H6*(logPsurP0 - 0 + np.log(P0/(kB*T)))
46             /(1.60218e-19)
47
48     if molecule == 'butene':
49         amu = 1.660539e-27
50         Ia = amu*33.3615745178189e-20
51         Ib = amu*92.8651038861518e-20
52         Ic = amu*119.995841513786e-20
53         sigma_butene = 1.0
54         nC4H8 = 1
55         mC4H8 = 4*12*amu + 8*mH
56
57         z_trans_star_butene = ((2.0*np.pi*mC4H8*kB*T)/(h**2))**(3.0/2.0);
58
59         z_rot_butene = np.pi**(1.0/2.0)/sigma_butene*T**(3.0/2.0)
60         *8**(3.0/2.0)*np.pi**3*kB**(3.0/2.0)*(Ia*Ib*Ic)**(1.0/2.0)/h**3
61
62         GadsTP += nC4H8*kB*T*np.log(z_trans_star_butene*z_rot_butene)
63             /(1.60218e-19)
64
65         GadsTP += -kB*T*nC4H8*(logPsurP0 - 0 + np.log(P0/(kB*T)))
66             /(1.60218e-19)
67
68     return GadsTP

```

C.2 Pre-exponential factors

```

1  #!/usr/bin/env python3
2  # -*- coding: utf-8 -*-
3  """
4  @author: Corentin Chatelier, PhD Student, IJL-SOLEIL-CNRS
5  Preexponential factor calculations
6  """
7  import numpy as np
8
9  # lecture frequences de vibration
10
11  dataraw = open('freq_vibrations', 'r')
12  dataraw.readline() #ligne de commentaire
13  rawdata = dataraw.readlines()
14
15  c1 = 0 #compteur d'etapes
16  for i in range(len(rawdata)):
17      rawdata[i] = rawdata[i].split(' ')
18      if '=' in rawdata[i]:
19          rawdata[i].remove('=')
20      while '' in rawdata[i]:
21          rawdata[i].remove('')
22

```



```

23     if rawdata[i][0] == '#':
24         c1 += 1
25
26     if rawdata[i][0] != '#':
27         rawdata[i] = float(rawdata[i][2]) # THz
28
29 steps = dict()
30 for i in range(1,c1+1):
31     steps[str(i)] = []
32
33 c2 = 0
34 for i in range(len(rawdata)):
35     if type(rawdata[i]) != float:
36         c2 += 1
37         j = 1
38         while type(rawdata[i+j]) == float:
39             steps[str(c2)].append(rawdata[i+j])
40             j += 1
41             if i+j == len(rawdata):
42                 break
43
44 # Calcul du preexp factor
45
46 def preexp(T,nH,nH2,nC4H6,nC4H7,nC4H8,nC4H9,nC4H10,f_TS,f_LM):
47     # volume boite pour une molecule
48     a = 12.32537e-10
49     b = 15.29928e-10
50     c = 36.88369*0.78e-10
51     alpha = np.deg2rad(90.0000)
52     beta = np.deg2rad(90.0000)
53     gamma = np.deg2rad(107.7025)
54     V = a*b*c*np.sqrt(1-np.cos(alpha)**2-np.cos(beta)**2-np.cos(gamma)**2
55         +2*np.cos(alpha)*np.cos(beta)*np.cos(gamma)) # m3
56
57     # constantes
58     amu = 1.660539e-27 # kg
59     kB = 1.38064852e-23; # m2 kg s-2 K-1
60     h = 6.62607e-34; # m2 kg s-1
61     hbar = h/(2*np.pi)
62
63     # H
64     mH = 1.6737210e-27; # kg
65
66     r = 53e-12
67     I_H = 2*mH*r**2/3
68     sigma_H = 3.0;
69
70     R = 0.739e-10;
71     I_H2 = 2*mH*R**2.0/2.0;
72     sigma_H2 = 2.0;
73
74     mC4H6 = 4*12*amu + 6*mH
75     Ia_C4H6 = amu*12.12444e-20 # en kg m2
76     Ib_C4H6 = amu*113.99086e-20
77     Ic_C4H6 = amu*126.09124e-20
78     sigma_C4H6 = 2.0
79
80     mC4H7 = 4*12*amu + 7*mH
81     Ia_C4H7 = amu*13.7951139000101e-20 # en kg m2
82     Ib_C4H7 = amu*123.048388217608e-20
83     Ic_C4H7 = amu*133.790707823907e-20
84     sigma_C4H7 = 1.0 # C2h
85
86     mC4H8 = 4*12*amu + 8*mH
87     Ia_C4H8 = amu*33.3615745178189e-20 # en kg m2
88     Ib_C4H8 = amu*92.8651038861518e-20
89     Ic_C4H8 = amu*119.995841513786e-20
90     sigma_C4H8 = 1.0 # C2h

```

Appendix C. Python scripts

```

91
92     mC4H9 = 4*12*amu + 9*mH
93     Ia_C4H9 = amu*18.835339872416e-20 # en kg m2
94     Ib_C4H9 = amu*133.790707823907e-20
95     Ic_C4H9 = amu*144.082300733439e-20
96     sigma_C4H9 = 1.0 # C2h
97
98     mC4H10 = 4*12*amu + 10*mH
99     Ia_C4H10 = amu*22.2103151328226e-20 # en kg m2
100    Ib_C4H10 = amu*134.861033486499e-20
101    Ic_C4H10 = amu*144.082300733439e-20
102    sigma_C4H10 = 1.0 # C2h
103
104    # https://cccbdb.nist.gov/rotcalc2.asp
105
106    z_trans_H = ((2.0*np.pi*mH*kB*T)/(h**2))**(3.0/2.0)*V;
107    z_rot_H = (1.0/sigma_H)*(8.0*(np.pi**2)*I_H*kB*T)/(h**2);
108
109    z_trans_H2 = ((2.0*np.pi*2.0*mH*kB*T)/(h**2))**(3.0/2.0)*V;
110    z_rot_H2 = (1.0/sigma_H2)*(8.0*(np.pi**2)*I_H2*kB*T)/(h**2);
111
112    z_trans_C4H6 = ((2.0*np.pi*mC4H6*kB*T)/(h**2))**(3.0/2.0)*V;
113    z_rot_C4H6 = np.pi**(1.0/2.0)/sigma_C4H6*T**(3.0/2.0)*8**(3.0/2.0)
114                *np.pi**3*kB**(3.0/2.0)*(Ia_C4H6*Ib_C4H6*Ic_C4H6)**(1.0/2.0)/h**3
115
116    z_trans_C4H7 = ((2.0*np.pi*mC4H7*kB*T)/(h**2))**(3.0/2.0)*V;
117    z_rot_C4H7 = np.pi**(1.0/2.0)/sigma_C4H7*T**(3.0/2.0)*8**(3.0/2.0)
118                *np.pi**3*kB**(3.0/2.0)*(Ia_C4H7*Ib_C4H7*Ic_C4H7)**(1.0/2.0)/h**3
119
120    z_trans_C4H8 = ((2.0*np.pi*mC4H8*kB*T)/(h**2))**(3.0/2.0)*V;
121    z_rot_C4H8 = np.pi**(1.0/2.0)/sigma_C4H8*T**(3.0/2.0)*8**(3.0/2.0)
122                *np.pi**3*kB**(3.0/2.0)*(Ia_C4H8*Ib_C4H8*Ic_C4H8)**(1.0/2.0)/h**3
123
124    z_trans_C4H9 = ((2.0*np.pi*mC4H9*kB*T)/(h**2))**(3.0/2.0)*V;
125    z_rot_C4H9 = np.pi**(1.0/2.0)/sigma_C4H9*T**(3.0/2.0)*8**(3.0/2.0)
126                *np.pi**3*kB**(3.0/2.0)*(Ia_C4H9*Ib_C4H9*Ic_C4H9)**(1.0/2.0)/h**3
127
128    z_trans_C4H10 = ((2.0*np.pi*mC4H10*kB*T)/(h**2))**(3.0/2.0)*V;
129    z_rot_C4H10 = np.pi**(1.0/2.0)/sigma_C4H10*T**(3.0/2.0)*8**(3.0/2.0)
130                *np.pi**3*kB**(3.0/2.0)*(Ia_C4H10*Ib_C4H10*Ic_C4H10)**(1.0/2.0)/h**3
131
132    z_vib_TS = 1
133    for i in range(len(f_TS)):
134        z_vib_TS = z_vib_TS/(1-np.exp(-hbar*f_TS[i]*1e12/kB/T))
135
136    z_vib_LM = 1
137    for i in range(len(f_LM)):
138        z_vib_LM = z_vib_LM/(1-np.exp(-hbar*f_LM[i]*1e12/kB/T))
139
140    A = kB*T/h \
141        * (z_vib_TS)/(z_vib_LM) \
142        * (z_trans_H*z_rot_H)**nH \
143        * (z_trans_H2*z_rot_H2)**nH2 \
144        * (z_trans_C4H6*z_rot_C4H6)**nC4H6 \
145        * (z_trans_C4H7*z_rot_C4H7)**nC4H7 \
146        * (z_trans_C4H8*z_rot_C4H8)**nC4H8 \
147        * (z_trans_C4H9*z_rot_C4H9)**nC4H9 \
148        * (z_trans_C4H10*z_rot_C4H10)**nC4H10
149
150    return A
151
152    T = 300
153    ##### Dissociation H2
154    f_TS,f_LM = steps['4'], steps['3']
155    nH,nH2,nC4H6,nC4H7,nC4H8,nC4H9,nC4H10 = 2, -1, 1-1, 0, 0, 0, 0
156    A_3_4 = preexp(T,nH,nH2,nC4H6,nC4H7,nC4H8,nC4H9,nC4H10,f_TS,f_LM)
157
158    f_TS,f_LM = steps['4'], steps['5']

```

```

159 nH,nH2,nC4H6,nC4H7,nC4H8,nC4H9,nC4H10 = 2-2, 0, 1-1, 0, 0, 0, 0
160 A_5_4 = preexp(T,nH,nH2,nC4H6,nC4H7,nC4H8,nC4H9,nC4H10,f_TS,f_LM)
161
162 ##### 1ere hydrogenation
163 f_TS,f_LM = steps['6'], steps['5']
164 nH,nH2,nC4H6,nC4H7,nC4H8,nC4H9,nC4H10 = 1-2, 0, -1, 1, 0, 0, 0
165 A_5_6 = preexp(T,nH,nH2,nC4H6,nC4H7,nC4H8,nC4H9,nC4H10,f_TS,f_LM)
166
167 f_TS,f_LM = steps['6'], steps['7']
168 nH,nH2,nC4H6,nC4H7,nC4H8,nC4H9,nC4H10 = 1-1, 0, 0, 1-1, 0, 0, 0
169 A_7_6 = preexp(T,nH,nH2,nC4H6,nC4H7,nC4H8,nC4H9,nC4H10,f_TS,f_LM)
170
171 ##### 2eme hydrogenation
172 f_TS,f_LM = steps['10'], steps['9']
173 nH,nH2,nC4H6,nC4H7,nC4H8,nC4H9,nC4H10 = -1, 0, 0, -1, 1, 0, 0
174 A_9_10 = preexp(T,nH,nH2,nC4H6,nC4H7,nC4H8,nC4H9,nC4H10,f_TS,f_LM)
175
176 f_TS,f_LM = steps['10'], steps['11']
177 nH,nH2,nC4H6,nC4H7,nC4H8,nC4H9,nC4H10 = 0, 0, 0, 0, 1-1, 0, 0
178 A_11_10 = preexp(T,nH,nH2,nC4H6,nC4H7,nC4H8,nC4H9,nC4H10,f_TS,f_LM)
179
180 ##### Dissociation H2
181 f_TS,f_LM = steps['14'], steps['13']
182 nH,nH2,nC4H6,nC4H7,nC4H8,nC4H9,nC4H10 = 2, -1, 0, 0, 1-1, 0, 0
183 A_13_14 = preexp(T,nH,nH2,nC4H6,nC4H7,nC4H8,nC4H9,nC4H10,f_TS,f_LM)
184
185 f_TS,f_LM = steps['14'], steps['15']
186 nH,nH2,nC4H6,nC4H7,nC4H8,nC4H9,nC4H10 = 2-2, 0, 0, 0, 1-1, 0, 0
187 A_15_14 = preexp(T,nH,nH2,nC4H6,nC4H7,nC4H8,nC4H9,nC4H10,f_TS,f_LM)
188
189 ##### 3eme hydrogenation
190 f_TS,f_LM = steps['18'], steps['17']
191 nH,nH2,nC4H6,nC4H7,nC4H8,nC4H9,nC4H10 = 1-2, 0, 0, 0, -1, 1, 0
192 A_17_18 = preexp(T,nH,nH2,nC4H6,nC4H7,nC4H8,nC4H9,nC4H10,f_TS,f_LM)
193
194 f_TS,f_LM = steps['18'], steps['19']
195 nH,nH2,nC4H6,nC4H7,nC4H8,nC4H9,nC4H10 = 1-1, 0, 0, 0, 0, 1-1, 0
196 A_19_18 = preexp(T,nH,nH2,nC4H6,nC4H7,nC4H8,nC4H9,nC4H10,f_TS,f_LM)
197
198 ##### 4eme hydrogenation
199 f_TS,f_LM = steps['22'], steps['21']
200 nH,nH2,nC4H6,nC4H7,nC4H8,nC4H9,nC4H10 = -1, 0, 0, 0, 0, -1, 1
201 A_21_22 = preexp(T,nH,nH2,nC4H6,nC4H7,nC4H8,nC4H9,nC4H10,f_TS,f_LM)
202
203 f_TS,f_LM = steps['22'], steps['23']
204 nH,nH2,nC4H6,nC4H7,nC4H8,nC4H9,nC4H10 = 0, 0, 0, 0, 0, 0, 1-1
205 A_23_22 = preexp(T,nH,nH2,nC4H6,nC4H7,nC4H8,nC4H9,nC4H10,f_TS,f_LM)

```

1	#	Vibration frequencies - C4H6 hydrogenation on Al13Fe4(010)
2	#	3 C4H6 ads H2 ads H2 g # C4H6 et H2 ads
3	1	f = 94.290942 THz 592.447463 2PiTHz 3145.207188 cm-1 389.956132 meV
4	2	f = 93.845580 THz 589.649171 2PiTHz 3130.351510 cm-1 388.114262 meV
5	3	f = 93.405550 THz 586.884378 2PiTHz 3115.673675 cm-1 386.294442 meV
6	4	f = 92.702874 THz 582.469337 2PiTHz 3092.234941 cm-1 383.388408 meV
7	5	f = 91.856217 THz 577.149631 2PiTHz 3063.993488 cm-1 379.886913 meV
8	6	f = 90.618984 THz 569.375870 2PiTHz 3022.723854 cm-1 374.770129 meV
9	7	f = 67.849179 THz 426.308963 2PiTHz 2263.204925 cm-1 280.601749 meV
10	8	f = 56.543566 THz 355.273706 2PiTHz 1886.090300 cm-1 233.845478 meV
11	9	f = 44.013691 THz 276.546178 2PiTHz 1468.138665 cm-1 182.026061 meV
12	10	f = 42.280453 THz 265.655922 2PiTHz 1410.324069 cm-1 174.857962 meV
13	11	f = 40.899486 THz 256.979050 2PiTHz 1364.259963 cm-1 169.146739 meV
14	12	f = 37.852633 THz 237.835109 2PiTHz 1262.627896 cm-1 156.545964 meV
15	13	f = 36.215380 THz 227.547943 2PiTHz 1208.015007 cm-1 149.774826 meV
16	14	f = 34.929480 THz 219.468394 2PiTHz 1165.121994 cm-1 144.456768 meV
17	15	f = 33.427655 THz 210.032150 2PiTHz 1115.026513 cm-1 138.245718 meV
18	16	f = 31.537080 THz 198.153318 2PiTHz 1051.963727 cm-1 130.426926 meV
19	17	f = 29.252469 THz 183.798685 2PiTHz 975.757315 cm-1 120.978532 meV
20	18	f = 28.473774 THz 178.905996 2PiTHz 949.782825 cm-1 117.758104 meV

Appendix C. Python scripts

21	19 f =	26.885329 THz	168.925507	2PiTHz	896.798033	cm-1	111.188825	meV
22	20 f =	26.422400 THz	166.016837	2PiTHz	881.356376	cm-1	109.274303	meV
23	21 f =	25.181121 THz	158.217649	2PiTHz	839.951755	cm-1	104.140782	meV
24	22 f =	24.324596 THz	152.835944	2PiTHz	811.381161	cm-1	100.598479	meV
25	23 f =	22.634312 THz	142.215579	2PiTHz	754.999371	cm-1	93.608025	meV
26	24 f =	17.010314 THz	106.878953	2PiTHz	567.402972	cm-1	70.349028	meV
27	25 f =	16.234530 THz	102.004561	2PiTHz	541.525618	cm-1	67.140644	meV
28	26 f =	14.424595 THz	90.632400	2PiTHz	481.152667	cm-1	59.655349	meV
29	27 f =	13.268532 THz	83.368647	2PiTHz	442.590581	cm-1	54.874258	meV
30	28 f =	11.757172 THz	73.872487	2PiTHz	392.177016	cm-1	48.623770	meV
31	29 f =	10.131382 THz	63.657351	2PiTHz	337.946518	cm-1	41.900043	meV
32	30 f =	9.849511 THz	61.886301	2PiTHz	328.544303	cm-1	40.734317	meV
33	31 f =	9.375066 THz	58.905279	2PiTHz	312.718542	cm-1	38.772172	meV
34	32 f =	7.496626 THz	47.102692	2PiTHz	250.060527	cm-1	31.003565	meV
35	33 f =	6.472312 THz	40.666739	2PiTHz	215.893099	cm-1	26.767342	meV
36	# 4 C4H6 ads	H ads H ads H2	g # TS disso	H2				
37	1 f =	94.273784 THz	592.339652	2PiTHz	3144.634836	cm-1	389.885169	meV
38	2 f =	93.839690 THz	589.612164	2PiTHz	3130.155044	cm-1	388.089903	meV
39	3 f =	93.440526 THz	587.104141	2PiTHz	3116.840359	cm-1	386.439092	meV
40	4 f =	92.705810 THz	582.487782	2PiTHz	3092.332860	cm-1	383.400548	meV
41	5 f =	91.834176 THz	577.011147	2PiTHz	3063.258298	cm-1	379.795761	meV
42	6 f =	90.611138 THz	569.326571	2PiTHz	3022.462134	cm-1	374.737679	meV
43	7 f =	59.382913 THz	373.113846	2PiTHz	1980.800700	cm-1	245.588075	meV
44	8 f =	56.103842 THz	352.510834	2PiTHz	1871.422665	cm-1	232.026922	meV
45	9 f =	44.012710 THz	276.540014	2PiTHz	1468.105941	cm-1	182.022004	meV
46	10 f =	42.270417 THz	265.592862	2PiTHz	1409.989292	cm-1	174.816455	meV
47	11 f =	40.901418 THz	256.991188	2PiTHz	1364.324402	cm-1	169.154728	meV
48	12 f =	37.842573 THz	237.771901	2PiTHz	1262.292335	cm-1	156.504359	meV
49	13 f =	36.213400 THz	227.535504	2PiTHz	1207.948969	cm-1	149.766638	meV
50	14 f =	34.914535 THz	219.374495	2PiTHz	1164.623503	cm-1	144.394963	meV
51	15 f =	33.424291 THz	210.011012	2PiTHz	1114.914295	cm-1	138.231805	meV
52	16 f =	29.248976 THz	183.776737	2PiTHz	975.640793	cm-1	120.964085	meV
53	17 f =	28.484409 THz	178.972820	2PiTHz	950.137584	cm-1	117.802089	meV
54	18 f =	26.928781 THz	169.198519	2PiTHz	898.247409	cm-1	111.368525	meV
55	19 f =	26.409149 THz	165.933578	2PiTHz	880.914366	cm-1	109.219501	meV
56	20 f =	25.192642 THz	158.290037	2PiTHz	840.336051	cm-1	104.188429	meV
57	21 f =	24.373493 THz	153.143174	2PiTHz	813.012192	cm-1	100.800701	meV
58	22 f =	22.612457 THz	142.078259	2PiTHz	754.270360	cm-1	93.517640	meV
59	23 f =	17.025783 THz	106.976149	2PiTHz	567.918972	cm-1	70.413004	meV
60	24 f =	16.232443 THz	101.991449	2PiTHz	541.456006	cm-1	67.132013	meV
61	25 f =	14.443488 THz	90.751114	2PiTHz	481.782898	cm-1	59.733488	meV
62	26 f =	13.259419 THz	83.311389	2PiTHz	442.286609	cm-1	54.836570	meV
63	27 f =	11.088066 THz	69.668371	2PiTHz	369.858044	cm-1	45.856570	meV
64	28 f =	10.134324 THz	63.675835	2PiTHz	338.044649	cm-1	41.912210	meV
65	29 f =	9.396413 THz	59.039403	2PiTHz	313.430583	cm-1	38.860454	meV
66	30 f =	7.747342 THz	48.677985	2PiTHz	258.423501	cm-1	32.040442	meV
67	31 f =	7.502516 THz	47.139696	2PiTHz	250.256975	cm-1	31.027922	meV
68	32 f =	5.737314 THz	36.048607	2PiTHz	191.376188	cm-1	23.727632	meV
69	# 5 C4H6 ads	H ads H ads H2	g # C4H6 et 2H ads					
70	1 f =	94.230900 THz	592.070204	2PiTHz	3143.204380	cm-1	389.707815	meV
71	2 f =	93.823035 THz	589.507517	2PiTHz	3129.599494	cm-1	388.021024	meV
72	3 f =	93.529630 THz	587.664000	2PiTHz	3119.812561	cm-1	386.807598	meV
73	4 f =	92.750790 THz	582.770401	2PiTHz	3093.833242	cm-1	383.586572	meV
74	5 f =	91.789829 THz	576.732506	2PiTHz	3061.779039	cm-1	379.612356	meV
75	6 f =	90.644475 THz	569.536031	2PiTHz	3023.574125	cm-1	374.875549	meV
76	7 f =	50.387388 THz	316.593299	2PiTHz	1680.742312	cm-1	208.385563	meV
77	8 f =	48.220747 THz	302.979891	2PiTHz	1608.470948	cm-1	199.425053	meV
78	9 f =	44.015731 THz	276.558991	2PiTHz	1468.206687	cm-1	182.034495	meV
79	10 f =	42.254466 THz	265.492639	2PiTHz	1409.457225	cm-1	174.750487	meV
80	11 f =	40.905914 THz	257.019439	2PiTHz	1364.474385	cm-1	169.173324	meV
81	12 f =	37.827959 THz	237.680079	2PiTHz	1261.804869	cm-1	156.443921	meV
82	13 f =	36.208863 THz	227.506999	2PiTHz	1207.797640	cm-1	149.747876	meV
83	14 f =	34.903013 THz	219.302098	2PiTHz	1164.239157	cm-1	144.347310	meV
84	15 f =	33.444977 THz	210.140988	2PiTHz	1115.604315	cm-1	138.317356	meV
85	16 f =	29.241919 THz	183.732398	2PiTHz	975.405407	cm-1	120.934901	meV
86	17 f =	28.480908 THz	178.950820	2PiTHz	950.020789	cm-1	117.787608	meV
87	18 f =	26.969958 THz	169.457243	2PiTHz	899.620933	cm-1	111.538820	meV
88	19 f =	26.382667 THz	165.767188	2PiTHz	880.031031	cm-1	109.109981	meV

C.2. Pre-exponential factors

89	20 f =	25.222757 THz	158.479259	2PiTHz	841.340602	cm-1	104.312978 meV
90	21 f =	24.458106 THz	153.674815	2PiTHz	815.834589	cm-1	101.150634 meV
91	22 f =	22.558450 THz	141.738919	2PiTHz	752.468859	cm-1	93.294282 meV
92	23 f =	18.508930 THz	116.295036	2PiTHz	617.391423	cm-1	76.546808 meV
93	24 f =	17.075429 THz	107.288087	2PiTHz	569.574996	cm-1	70.618325 meV
94	25 f =	16.239784 THz	102.037572	2PiTHz	541.700870	cm-1	67.162372 meV
95	26 f =	15.100773 THz	94.880955	2PiTHz	503.707554	cm-1	62.451800 meV
96	27 f =	14.472818 THz	90.935400	2PiTHz	482.761242	cm-1	59.854787 meV
97	28 f =	13.259654 THz	83.312865	2PiTHz	442.294443	cm-1	54.837542 meV
98	29 f =	10.706330 THz	67.269857	2PiTHz	357.124725	cm-1	44.277839 meV
99	30 f =	10.148228 THz	63.763199	2PiTHz	338.508451	cm-1	41.969714 meV
100	31 f =	9.409100 THz	59.119121	2PiTHz	313.853793	cm-1	38.912925 meV
101	32 f =	8.016183 THz	50.367163	2PiTHz	267.391072	cm-1	33.152280 meV
102	33 f =	7.502999 THz	47.142731	2PiTHz	250.273088	cm-1	31.029919 meV
103	# 6 C4H6 ads H ads H ads H2	g # TS C4H7 et HadsFe					
104	1 f =	94.611742 THz	594.463108	2PiTHz	3155.907920	cm-1	391.282854 meV
105	2 f =	93.933325 THz	590.200485	2PiTHz	3133.278350	cm-1	388.477144 meV
106	3 f =	93.577600 THz	587.965402	2PiTHz	3121.412657	cm-1	387.005985 meV
107	4 f =	93.069318 THz	584.771770	2PiTHz	3104.458184	cm-1	384.903898 meV
108	5 f =	91.777355 THz	576.654129	2PiTHz	3061.362947	cm-1	379.560767 meV
109	6 f =	91.006064 THz	571.807965	2PiTHz	3035.635450	cm-1	376.370963 meV
110	7 f =	46.632607 THz	293.001311	2PiTHz	1555.496285	cm-1	192.857029 meV
111	8 f =	43.748415 THz	274.879398	2PiTHz	1459.290003	cm-1	180.928966 meV
112	9 f =	42.645797 THz	267.951447	2PiTHz	1422.510636	cm-1	176.368904 meV
113	10 f =	41.186156 THz	258.780252	2PiTHz	1373.822254	cm-1	170.332312 meV
114	11 f =	38.103705 THz	239.412642	2PiTHz	1271.002763	cm-1	157.584315 meV
115	12 f =	36.303383 THz	228.100882	2PiTHz	1210.950472	cm-1	150.138777 meV
116	13 f =	36.138706 THz	227.066184	2PiTHz	1205.457425	cm-1	149.457726 meV
117	14 f =	34.636360 THz	217.626666	2PiTHz	1155.344562	cm-1	143.244521 meV
118	15 f =	33.447573 THz	210.157298	2PiTHz	1115.690900	cm-1	138.328092 meV
119	16 f =	29.555583 THz	185.703205	2PiTHz	985.868103	cm-1	122.232110 meV
120	17 f =	28.726824 THz	180.495956	2PiTHz	958.223666	cm-1	118.804636 meV
121	18 f =	26.819644 THz	168.512791	2PiTHz	894.606988	cm-1	110.917170 meV
122	19 f =	26.598648 THz	167.124234	2PiTHz	887.235367	cm-1	110.003205 meV
123	20 f =	25.544885 THz	160.503247	2PiTHz	852.085622	cm-1	105.645191 meV
124	21 f =	25.290164 THz	158.902789	2PiTHz	843.589051	cm-1	104.591750 meV
125	22 f =	23.887231 THz	150.087900	2PiTHz	796.792240	cm-1	98.789683 meV
126	23 f =	23.220675 THz	145.899803	2PiTHz	774.558318	cm-1	96.033027 meV
127	24 f =	21.533860 THz	135.301235	2PiTHz	718.292244	cm-1	89.056920 meV
128	25 f =	17.688846 THz	111.142300	2PiTHz	590.036388	cm-1	73.155215 meV
129	26 f =	16.544521 THz	103.952292	2PiTHz	551.865805	cm-1	68.422664 meV
130	27 f =	16.373353 THz	102.876810	2PiTHz	546.156247	cm-1	67.714769 meV
131	28 f =	13.868950 THz	87.141180	2PiTHz	462.618348	cm-1	57.357386 meV
132	29 f =	13.831375 THz	86.905093	2PiTHz	461.364999	cm-1	57.201990 meV
133	30 f =	13.591519 THz	85.398034	2PiTHz	453.364266	cm-1	56.210025 meV
134	31 f =	10.304079 THz	64.742438	2PiTHz	343.707071	cm-1	42.614261 meV
135	32 f =	9.130889 THz	57.371066	2PiTHz	304.573655	cm-1	37.762334 meV
136	# 7 C4H7 ads H ads H2	g # C4H7 HadsFe					
137	1 f =	94.304570 THz	592.533090	2PiTHz	3145.661769	cm-1	390.012493 meV
138	2 f =	93.646720 THz	588.399697	2PiTHz	3123.718257	cm-1	387.291843 meV
139	3 f =	93.187313 THz	585.513159	2PiTHz	3108.394094	cm-1	385.391888 meV
140	4 f =	92.560721 THz	581.576163	2PiTHz	3087.493227	cm-1	382.800510 meV
141	5 f =	91.485044 THz	574.817482	2PiTHz	3051.612489	cm-1	378.351864 meV
142	6 f =	91.278717 THz	573.521091	2PiTHz	3044.730160	cm-1	377.498564 meV
143	7 f =	89.075101 THz	559.675368	2PiTHz	2971.225467	cm-1	368.385140 meV
144	8 f =	44.677875 THz	280.719369	2PiTHz	1490.293455	cm-1	184.772906 meV
145	9 f =	43.957707 THz	276.194420	2PiTHz	1466.271240	cm-1	181.794530 meV
146	10 f =	42.885913 THz	269.460139	2PiTHz	1430.520034	cm-1	177.361943 meV
147	11 f =	42.570107 THz	267.475872	2PiTHz	1419.985885	cm-1	176.055875 meV
148	12 f =	42.329753 THz	265.965682	2PiTHz	1411.968533	cm-1	175.061850 meV
149	13 f =	40.471105 THz	254.287453	2PiTHz	1349.970716	cm-1	167.375097 meV
150	14 f =	38.280235 THz	240.521813	2PiTHz	1276.891169	cm-1	158.314385 meV
151	15 f =	36.223578 THz	227.599453	2PiTHz	1208.288463	cm-1	149.808730 meV
152	16 f =	34.663121 THz	217.794812	2PiTHz	1156.237220	cm-1	143.355196 meV
153	17 f =	32.706550 THz	205.501314	2PiTHz	1090.973039	cm-1	135.263466 meV
154	18 f =	30.039441 THz	188.743371	2PiTHz	1002.007850	cm-1	124.233185 meV
155	19 f =	29.188354 THz	183.395836	2PiTHz	973.618653	cm-1	120.713372 meV
156	20 f =	28.615795 THz	179.798340	2PiTHz	954.520132	cm-1	118.345456 meV

Appendix C. Python scripts

157	21 f =	27.094918 THz	170.242391	2PiTHz	903.789155	cm-1	112.055614	meV
158	22 f =	25.352565 THz	159.294862	2PiTHz	845.670507	cm-1	104.849818	meV
159	23 f =	24.043105 THz	151.067286	2PiTHz	801.991641	cm-1	99.434326	meV
160	24 f =	23.354001 THz	146.737519	2PiTHz	779.005612	cm-1	96.584421	meV
161	25 f =	20.504323 THz	128.832463	2PiTHz	683.950585	cm-1	84.799095	meV
162	26 f =	17.021664 THz	106.950272	2PiTHz	567.781594	cm-1	70.395971	meV
163	27 f =	13.696721 THz	86.059039	2PiTHz	456.873434	cm-1	56.645107	meV
164	28 f =	10.533054 THz	66.181132	2PiTHz	351.344863	cm-1	43.561227	meV
165	29 f =	10.329796 THz	64.904020	2PiTHz	344.564883	cm-1	42.720616	meV
166	30 f =	9.579210 THz	60.187949	2PiTHz	319.528031	cm-1	39.616441	meV
167	31 f =	7.765459 THz	48.791815	2PiTHz	259.027808	cm-1	32.115367	meV
168	32 f =	6.559253 THz	41.213000	2PiTHz	218.793113	cm-1	27.126898	meV
169	33 f =	5.240873 THz	32.929377	2PiTHz	174.816705	cm-1	21.674517	meV
170	# 8 C4H7 ads	H ads H2 g # TS	C4H7 HadsAlglue					
171	1 f =	94.301508 THz	592.513848	2PiTHz	3145.559615	cm-1	389.999827	meV
172	2 f =	93.612689 THz	588.185869	2PiTHz	3122.583080	cm-1	387.151099	meV
173	3 f =	93.173758 THz	585.427984	2PiTHz	3107.941918	cm-1	385.335826	meV
174	4 f =	92.549828 THz	581.507720	2PiTHz	3087.129873	cm-1	382.755460	meV
175	5 f =	91.434142 THz	574.497658	2PiTHz	3049.914594	cm-1	378.141352	meV
176	6 f =	91.270514 THz	573.469554	2PiTHz	3044.456559	cm-1	377.464642	meV
177	7 f =	89.175232 THz	560.304510	2PiTHz	2974.565479	cm-1	368.799249	meV
178	8 f =	43.944236 THz	276.109778	2PiTHz	1465.821888	cm-1	181.738817	meV
179	9 f =	42.894740 THz	269.515598	2PiTHz	1430.814457	cm-1	177.398447	meV
180	10 f =	42.518855 THz	267.153844	2PiTHz	1418.276292	cm-1	175.843912	meV
181	11 f =	42.320047 THz	265.904698	2PiTHz	1411.644779	cm-1	175.021709	meV
182	12 f =	40.506580 THz	254.510345	2PiTHz	1351.154014	cm-1	167.521807	meV
183	13 f =	38.268973 THz	240.451052	2PiTHz	1276.515510	cm-1	158.267809	meV
184	14 f =	36.218434 THz	227.567131	2PiTHz	1208.116871	cm-1	149.787456	meV
185	15 f =	34.662745 THz	217.792450	2PiTHz	1156.224683	cm-1	143.353642	meV
186	16 f =	32.715960 THz	205.560442	2PiTHz	1091.286941	cm-1	135.302385	meV
187	17 f =	31.260067 THz	196.412796	2PiTHz	1042.723578	cm-1	129.281293	meV
188	18 f =	30.021637 THz	188.631511	2PiTHz	1001.413998	cm-1	124.159556	meV
189	19 f =	29.192524 THz	183.422038	2PiTHz	973.757759	cm-1	120.730618	meV
190	20 f =	28.624466 THz	179.852823	2PiTHz	954.809373	cm-1	118.381317	meV
191	21 f =	27.116415 THz	170.377459	2PiTHz	904.506208	cm-1	112.144517	meV
192	22 f =	25.343343 THz	159.236922	2PiTHz	845.362912	cm-1	104.811681	meV
193	23 f =	24.092800 THz	151.379527	2PiTHz	803.649279	cm-1	99.639847	meV
194	24 f =	23.398528 THz	147.017289	2PiTHz	780.490867	cm-1	96.768569	meV
195	25 f =	23.347415 THz	146.696137	2PiTHz	778.785923	cm-1	96.557183	meV
196	26 f =	17.033439 THz	107.024255	2PiTHz	568.174355	cm-1	70.444667	meV
197	27 f =	13.700520 THz	86.082906	2PiTHz	457.000143	cm-1	56.660817	meV
198	28 f =	10.335951 THz	64.942698	2PiTHz	344.770217	cm-1	42.746074	meV
199	29 f =	9.575806 THz	60.166565	2PiTHz	319.414506	cm-1	39.602366	meV
200	30 f =	7.769896 THz	48.819695	2PiTHz	259.175815	cm-1	32.133717	meV
201	31 f =	6.443257 THz	40.484175	2PiTHz	214.923896	cm-1	26.647177	meV
202	32 f =	5.241215 THz	32.931523	2PiTHz	174.828100	cm-1	21.675930	meV
203	# 9 C4H7 ads	H ads H2 g # C4H7 HadsAlglue						
204	1 f =	94.137330 THz	591.482287	2PiTHz	3140.083226	cm-1	389.320841	meV
205	2 f =	93.591903 THz	588.055269	2PiTHz	3121.889746	cm-1	387.065137	meV
206	3 f =	93.353543 THz	586.557607	2PiTHz	3113.938902	cm-1	386.079357	meV
207	4 f =	92.572083 THz	581.647552	2PiTHz	3087.872220	cm-1	382.847499	meV
208	5 f =	91.420548 THz	574.412242	2PiTHz	3049.461137	cm-1	378.085130	meV
209	6 f =	91.382304 THz	574.171953	2PiTHz	3048.185478	cm-1	377.926969	meV
210	7 f =	89.424164 THz	561.868594	2PiTHz	2982.868947	cm-1	369.828748	meV
211	8 f =	53.451660 THz	335.846688	2PiTHz	1782.955422	cm-1	221.058378	meV
212	9 f =	43.881608 THz	275.716275	2PiTHz	1463.732846	cm-1	181.479809	meV
213	10 f =	42.910981 THz	269.617645	2PiTHz	1431.356208	cm-1	177.465616	meV
214	11 f =	42.549302 THz	267.345150	2PiTHz	1419.291903	cm-1	175.969832	meV
215	12 f =	42.307393 THz	265.825193	2PiTHz	1411.222697	cm-1	174.969378	meV
216	13 f =	40.525410 THz	254.628663	2PiTHz	1351.782145	cm-1	167.599686	meV
217	14 f =	38.265762 THz	240.430872	2PiTHz	1276.408379	cm-1	158.254527	meV
218	15 f =	36.190437 THz	227.391220	2PiTHz	1207.182988	cm-1	149.671669	meV
219	16 f =	34.696160 THz	218.002405	2PiTHz	1157.339298	cm-1	143.491837	meV
220	17 f =	32.678136 THz	205.322783	2PiTHz	1090.025246	cm-1	135.145955	meV
221	18 f =	30.077266 THz	188.981039	2PiTHz	1003.269587	cm-1	124.389620	meV
222	19 f =	29.227116 THz	183.639386	2PiTHz	974.911622	cm-1	120.873679	meV
223	20 f =	28.627608 THz	179.872563	2PiTHz	954.914173	cm-1	118.394311	meV
224	21 f =	27.272445 THz	171.357828	2PiTHz	909.710831	cm-1	112.789809	meV

C.2. Pre-exponential factors

225	22 f =	25.465482 THz	160.004340	2PiTHz	849.437010	cm-1	105.316805	meV
226	23 f =	24.097252 THz	151.407503	2PiTHz	803.797797	cm-1	99.658261	meV
227	24 f =	23.404795 THz	147.056663	2PiTHz	780.699899	cm-1	96.794486	meV
228	25 f =	17.100085 THz	107.443001	2PiTHz	570.397409	cm-1	70.720291	meV
229	26 f =	13.729003 THz	86.261871	2PiTHz	457.950238	cm-1	56.778614	meV
230	27 f =	13.143160 THz	82.580907	2PiTHz	438.408598	cm-1	54.355758	meV
231	28 f =	10.337651 THz	64.953378	2PiTHz	344.826916	cm-1	42.753104	meV
232	29 f =	10.041803 THz	63.094511	2PiTHz	334.958492	cm-1	41.529575	meV
233	30 f =	9.556223 THz	60.043521	2PiTHz	318.761284	cm-1	39.521376	meV
234	31 f =	7.754351 THz	48.722026	2PiTHz	258.657308	cm-1	32.069431	meV
235	32 f =	6.421268 THz	40.346016	2PiTHz	214.190435	cm-1	26.556239	meV
236	33 f =	5.245499 THz	32.958440	2PiTHz	174.970997	cm-1	21.693647	meV
237	# 10 C4H8 ads H ads H2 g # TS C4H8							
238	1 f =	93.076083 THz	584.814278	2PiTHz	3104.683850	cm-1	384.931877	meV
239	2 f =	92.540775 THz	581.450840	2PiTHz	3086.827907	cm-1	382.718021	meV
240	3 f =	91.960808 THz	577.806796	2PiTHz	3067.482271	cm-1	380.319467	meV
241	4 f =	90.773192 THz	570.344788	2PiTHz	3027.867685	cm-1	375.407882	meV
242	5 f =	90.412838 THz	568.080616	2PiTHz	3015.847560	cm-1	373.917576	meV
243	6 f =	88.976102 THz	559.053340	2PiTHz	2967.923222	cm-1	367.975714	meV
244	7 f =	87.868091 THz	552.091497	2PiTHz	2930.963930	cm-1	363.393344	meV
245	8 f =	87.032390 THz	546.840634	2PiTHz	2903.087956	cm-1	359.937162	meV
246	9 f =	42.467414 THz	266.830634	2PiTHz	1416.560422	cm-1	175.631171	meV
247	10 f =	42.406919 THz	266.450530	2PiTHz	1414.542510	cm-1	175.380982	meV
248	11 f =	42.052526 THz	264.223813	2PiTHz	1402.721234	cm-1	173.915330	meV
249	12 f =	41.597891 THz	261.367260	2PiTHz	1387.556261	cm-1	172.035112	meV
250	13 f =	40.315693 THz	253.310972	2PiTHz	1344.786738	cm-1	166.732366	meV
251	14 f =	40.050127 THz	251.642369	2PiTHz	1335.928394	cm-1	165.634070	meV
252	15 f =	37.992009 THz	238.710831	2PiTHz	1267.276961	cm-1	157.122375	meV
253	16 f =	36.682380 THz	230.482194	2PiTHz	1223.592469	cm-1	151.706186	meV
254	17 f =	34.879083 THz	219.151743	2PiTHz	1163.440946	cm-1	144.248345	meV
255	18 f =	34.283230 THz	215.407886	2PiTHz	1143.565420	cm-1	141.784093	meV
256	19 f =	31.152375 THz	195.736144	2PiTHz	1039.131342	cm-1	128.835913	meV
257	20 f =	30.119982 THz	189.249431	2PiTHz	1004.694440	cm-1	124.566279	meV
258	21 f =	29.072971 THz	182.670862	2PiTHz	969.769887	cm-1	120.236185	meV
259	22 f =	28.710737 THz	180.394882	2PiTHz	957.687079	cm-1	118.738107	meV
260	23 f =	24.906925 THz	156.494826	2PiTHz	830.805568	cm-1	103.006799	meV
261	24 f =	24.305420 THz	152.715458	2PiTHz	810.741520	cm-1	100.519174	meV
262	25 f =	23.074577 THz	144.981840	2PiTHz	769.685001	cm-1	95.428812	meV
263	26 f =	21.597030 THz	135.698139	2PiTHz	720.399340	cm-1	89.318167	meV
264	27 f =	14.080023 THz	88.467394	2PiTHz	469.659003	cm-1	58.230316	meV
265	28 f =	13.152983 THz	82.642627	2PiTHz	438.736261	cm-1	54.396383	meV
266	29 f =	10.467208 THz	65.767408	2PiTHz	349.148469	cm-1	43.288909	meV
267	30 f =	8.318771 THz	52.268379	2PiTHz	277.484322	cm-1	34.403684	meV
268	31 f =	5.695082 THz	35.783256	2PiTHz	189.967483	cm-1	23.552975	meV
269	32 f =	4.145268 THz	26.045484	2PiTHz	138.271238	cm-1	17.143455	meV
270	# 11 C4H8 ads H2 g # C4H8 ads							
271	1 f =	93.609667 THz	588.166884	2PiTHz	3122.482288	cm-1	387.138602	meV
272	2 f =	92.834023 THz	583.293369	2PiTHz	3096.609594	cm-1	383.930796	meV
273	3 f =	92.488868 THz	581.124697	2PiTHz	3085.096467	cm-1	382.503350	meV
274	4 f =	91.356599 THz	574.010442	2PiTHz	3047.328044	cm-1	377.820660	meV
275	5 f =	90.642055 THz	569.520829	2PiTHz	3023.493421	cm-1	374.865543	meV
276	6 f =	90.452213 THz	568.328014	2PiTHz	3017.160957	cm-1	374.080417	meV
277	7 f =	88.665974 THz	557.104743	2PiTHz	2957.578440	cm-1	366.693124	meV
278	8 f =	87.293887 THz	548.483669	2PiTHz	2911.810561	cm-1	361.018628	meV
279	9 f =	42.875320 THz	269.393578	2PiTHz	1430.166673	cm-1	177.318132	meV
280	10 f =	42.688091 THz	268.217188	2PiTHz	1423.921409	cm-1	176.543818	meV
281	11 f =	42.272045 THz	265.603090	2PiTHz	1410.043590	cm-1	174.823187	meV
282	12 f =	41.902008 THz	263.278084	2PiTHz	1397.700512	cm-1	173.292840	meV
283	13 f =	40.600555 THz	255.100809	2PiTHz	1354.288692	cm-1	167.910458	meV
284	14 f =	39.903146 THz	250.718864	2PiTHz	1331.025654	cm-1	165.026208	meV
285	15 f =	38.064550 THz	239.166621	2PiTHz	1269.696676	cm-1	157.422381	meV
286	16 f =	36.737046 THz	230.825670	2PiTHz	1225.415927	cm-1	151.932266	meV
287	17 f =	35.078445 THz	220.404369	2PiTHz	1170.090932	cm-1	145.072838	meV
288	18 f =	34.512462 THz	216.848194	2PiTHz	1151.211778	cm-1	142.732121	meV
289	19 f =	31.118931 THz	195.526009	2PiTHz	1038.015767	cm-1	128.697599	meV
290	20 f =	30.102228 THz	189.137880	2PiTHz	1004.102229	cm-1	124.492855	meV
291	21 f =	29.239283 THz	183.715832	2PiTHz	975.317463	cm-1	120.923997	meV
292	22 f =	28.599822 THz	179.697983	2PiTHz	953.987356	cm-1	118.279400	meV

Appendix C. Python scripts

293	23 f =	25.295772 THz	158.938020	2PiTHz	843.776089	cm-1	104.614940	meV
294	24 f =	24.903887 THz	156.475738	2PiTHz	830.704235	cm-1	102.994236	meV
295	25 f =	23.461137 THz	147.410670	2PiTHz	782.579264	cm-1	97.027498	meV
296	26 f =	22.201466 THz	139.495927	2PiTHz	740.561178	cm-1	91.817917	meV
297	27 f =	14.023807 THz	88.114179	2PiTHz	467.783840	cm-1	57.997825	meV
298	28 f =	13.238699 THz	83.181201	2PiTHz	441.595461	cm-1	54.750879	meV
299	29 f =	10.423982 THz	65.495812	2PiTHz	347.706611	cm-1	43.110141	meV
300	30 f =	8.183882 THz	51.420844	2PiTHz	272.984896	cm-1	33.845826	meV
301	31 f =	5.466020 THz	34.344014	2PiTHz	182.326784	cm-1	22.605648	meV
302	32 f =	4.216354 THz	26.492135	2PiTHz	140.642434	cm-1	17.437446	meV
303	33 f =	2.501562 THz	15.717776	2PiTHz	83.443115	cm-1	10.345631	meV
304	# 13 C4H8 ads H2 ads # C4H8 H2adsFe							
305	1 f =	93.609551 THz	588.166153	2PiTHz	3122.478411	cm-1	387.138122	meV
306	2 f =	92.776602 THz	582.932580	2PiTHz	3094.694221	cm-1	383.693320	meV
307	3 f =	92.451018 THz	580.886878	2PiTHz	3083.833921	cm-1	382.346814	meV
308	4 f =	91.374734 THz	574.124387	2PiTHz	3047.932961	cm-1	377.895661	meV
309	5 f =	90.663929 THz	569.658265	2PiTHz	3024.223042	cm-1	374.956004	meV
310	6 f =	90.416759 THz	568.105250	2PiTHz	3015.978339	cm-1	373.933791	meV
311	7 f =	88.637028 THz	556.922869	2PiTHz	2956.612900	cm-1	366.573412	meV
312	8 f =	87.241797 THz	548.156377	2PiTHz	2910.073018	cm-1	360.803200	meV
313	9 f =	68.142970 THz	428.154909	2PiTHz	2273.004749	cm-1	281.816773	meV
314	10 f =	56.405811 THz	354.408165	2PiTHz	1881.495287	cm-1	233.275769	meV
315	11 f =	42.879636 THz	269.420696	2PiTHz	1430.310641	cm-1	177.335982	meV
316	12 f =	42.696018 THz	268.266995	2PiTHz	1424.185827	cm-1	176.576601	meV
317	13 f =	42.270923 THz	265.596040	2PiTHz	1410.006162	cm-1	174.818546	meV
318	14 f =	41.927283 THz	263.436891	2PiTHz	1398.543590	cm-1	173.397368	meV
319	15 f =	40.608498 THz	255.150721	2PiTHz	1354.553663	cm-1	167.943310	meV
320	16 f =	39.863658 THz	250.470749	2PiTHz	1329.708454	cm-1	164.862896	meV
321	17 f =	38.078029 THz	239.251314	2PiTHz	1270.146302	cm-1	157.478128	meV
322	18 f =	36.771557 THz	231.042505	2PiTHz	1226.567068	cm-1	152.074989	meV
323	19 f =	35.067437 THz	220.335203	2PiTHz	1169.723744	cm-1	145.027313	meV
324	20 f =	34.518630 THz	216.886950	2PiTHz	1151.417527	cm-1	142.757630	meV
325	21 f =	31.501759 THz	197.931390	2PiTHz	1050.785544	cm-1	130.280850	meV
326	22 f =	31.110281 THz	195.471661	2PiTHz	1037.727242	cm-1	128.661826	meV
327	23 f =	30.132011 THz	189.325006	2PiTHz	1005.095654	cm-1	124.616024	meV
328	24 f =	29.232948 THz	183.676029	2PiTHz	975.106154	cm-1	120.897798	meV
329	25 f =	28.598206 THz	179.687825	2PiTHz	953.933426	cm-1	118.272714	meV
330	26 f =	25.275644 THz	158.811554	2PiTHz	843.104700	cm-1	104.531698	meV
331	27 f =	24.907354 THz	156.497519	2PiTHz	830.819867	cm-1	103.008572	meV
332	28 f =	23.477793 THz	147.515321	2PiTHz	783.134838	cm-1	97.096380	meV
333	29 f =	22.222012 THz	139.625020	2PiTHz	741.246514	cm-1	91.902888	meV
334	30 f =	14.074240 THz	88.431061	2PiTHz	469.466112	cm-1	58.206401	meV
335	31 f =	13.221679 THz	83.074262	2PiTHz	441.027740	cm-1	54.680490	meV
336	32 f =	11.771924 THz	73.965179	2PiTHz	392.669103	cm-1	48.684781	meV
337	33 f =	10.481393 THz	65.856535	2PiTHz	349.621631	cm-1	43.347573	meV
338	34 f =	9.756395 THz	61.301237	2PiTHz	325.438292	cm-1	40.349220	meV
339	35 f =	8.211405 THz	51.593781	2PiTHz	273.902987	cm-1	33.959654	meV
340	36 f =	6.804142 THz	42.751682	2PiTHz	226.961725	cm-1	28.139678	meV
341	37 f =	5.449730 THz	34.241660	2PiTHz	181.783403	cm-1	22.538278	meV
342	38 f =	4.181128 THz	26.270801	2PiTHz	139.467410	cm-1	17.291761	meV
343	39 f =	2.477056 THz	15.563803	2PiTHz	82.625695	cm-1	10.244284	meV
344	# 14 C4H8 ads H ads H ads # TS C4H8 2HadsFe							
345	1 f =	93.639403 THz	588.353721	2PiTHz	3123.474177	cm-1	387.261581	meV
346	2 f =	92.803752 THz	583.103172	2PiTHz	3095.599867	cm-1	383.805606	meV
347	3 f =	92.445774 THz	580.853930	2PiTHz	3083.659006	cm-1	382.325127	meV
348	4 f =	91.404276 THz	574.310007	2PiTHz	3048.918383	cm-1	378.017837	meV
349	5 f =	90.665701 THz	569.669401	2PiTHz	3024.282161	cm-1	374.963334	meV
350	6 f =	90.406570 THz	568.041231	2PiTHz	3015.638475	cm-1	373.891653	meV
351	7 f =	88.702192 THz	557.332311	2PiTHz	2958.786561	cm-1	366.842912	meV
352	8 f =	87.208303 THz	547.945929	2PiTHz	2908.955785	cm-1	360.664681	meV
353	9 f =	60.175919 THz	378.096448	2PiTHz	2007.252525	cm-1	248.867685	meV
354	10 f =	56.372323 THz	354.197755	2PiTHz	1880.378251	cm-1	233.137274	meV
355	11 f =	42.874751 THz	269.390007	2PiTHz	1430.147718	cm-1	177.315782	meV
356	12 f =	42.700748 THz	268.296715	2PiTHz	1424.343607	cm-1	176.596164	meV
357	13 f =	42.274027 THz	265.615547	2PiTHz	1410.109724	cm-1	174.831387	meV
358	14 f =	41.930847 THz	263.459281	2PiTHz	1398.662459	cm-1	173.412106	meV
359	15 f =	40.599719 THz	255.095556	2PiTHz	1354.260799	cm-1	167.907000	meV
360	16 f =	39.871866 THz	250.522324	2PiTHz	1329.982256	cm-1	164.896843	meV

C.2. Pre-exponential factors

361	17 f =	38.077832 THz	239.250075	2PiTHz	1270.139719	cm-1	157.477311	meV
362	18 f =	36.765279 THz	231.003061	2PiTHz	1226.357664	cm-1	152.049027	meV
363	19 f =	35.065865 THz	220.325328	2PiTHz	1169.671316	cm-1	145.020813	meV
364	20 f =	34.510577 THz	216.836352	2PiTHz	1151.148913	cm-1	142.724326	meV
365	21 f =	31.117285 THz	195.515669	2PiTHz	1037.960875	cm-1	128.690793	meV
366	22 f =	30.124995 THz	189.280925	2PiTHz	1004.861634	cm-1	124.587009	meV
367	23 f =	29.227985 THz	183.644845	2PiTHz	974.940604	cm-1	120.877273	meV
368	24 f =	28.591591 THz	179.646265	2PiTHz	953.712791	cm-1	118.245358	meV
369	25 f =	25.272064 THz	158.789059	2PiTHz	842.985276	cm-1	104.516891	meV
370	26 f =	24.899530 THz	156.448363	2PiTHz	830.558905	cm-1	102.976217	meV
371	27 f =	23.462192 THz	147.417298	2PiTHz	782.614448	cm-1	97.031860	meV
372	28 f =	22.215423 THz	139.583619	2PiTHz	741.026725	cm-1	91.875637	meV
373	29 f =	14.067852 THz	88.390920	2PiTHz	469.253011	cm-1	58.179979	meV
374	30 f =	13.214964 THz	83.032067	2PiTHz	440.803735	cm-1	54.652717	meV
375	31 f =	11.033815 THz	69.327505	2PiTHz	368.048442	cm-1	45.632207	meV
376	32 f =	10.483293 THz	65.868473	2PiTHz	349.685007	cm-1	43.355431	meV
377	33 f =	9.821597 THz	61.710915	2PiTHz	327.613207	cm-1	40.618875	meV
378	34 f =	8.206921 THz	51.565604	2PiTHz	273.753403	cm-1	33.941108	meV
379	35 f =	7.391258 THz	46.440646	2PiTHz	246.545832	cm-1	30.567798	meV
380	36 f =	5.460940 THz	34.312100	2PiTHz	182.157355	cm-1	22.584642	meV
381	37 f =	4.189418 THz	26.322893	2PiTHz	139.743955	cm-1	17.326048	meV
382	38 f =	2.504132 THz	15.733927	2PiTHz	83.528858	cm-1	10.356262	meV
383	# 15	C4H8 ads H ads H ads #	C4H8 2HadsFe					
384	1 f =	93.583519 THz	588.002589	2PiTHz	3121.610074	cm-1	387.030462	meV
385	2 f =	92.795617 THz	583.052057	2PiTHz	3095.328504	cm-1	383.771961	meV
386	3 f =	92.490353 THz	581.134027	2PiTHz	3085.145998	cm-1	382.509491	meV
387	4 f =	91.339904 THz	573.905542	2PiTHz	3046.771148	cm-1	377.751614	meV
388	5 f =	90.661999 THz	569.646143	2PiTHz	3024.158689	cm-1	374.948025	meV
389	6 f =	90.417797 THz	568.111774	2PiTHz	3016.012974	cm-1	373.938085	meV
390	7 f =	88.777236 THz	557.803825	2PiTHz	2961.289750	cm-1	367.153268	meV
391	8 f =	87.116923 THz	547.371774	2PiTHz	2905.907687	cm-1	360.286764	meV
392	9 f =	50.357961 THz	316.408403	2PiTHz	1679.760732	cm-1	208.263863	meV
393	10 f =	48.128312 THz	302.399100	2PiTHz	1605.387621	cm-1	199.042769	meV
394	11 f =	42.872466 THz	269.375650	2PiTHz	1430.071496	cm-1	177.306332	meV
395	12 f =	42.697350 THz	268.275365	2PiTHz	1424.230262	cm-1	176.582111	meV
396	13 f =	42.261131 THz	265.534514	2PiTHz	1409.679534	cm-1	174.778050	meV
397	14 f =	41.912802 THz	263.345901	2PiTHz	1398.060539	cm-1	173.337477	meV
398	15 f =	40.599922 THz	255.096833	2PiTHz	1354.267580	cm-1	167.907841	meV
399	16 f =	39.884252 THz	250.600147	2PiTHz	1330.395408	cm-1	164.948067	meV
400	17 f =	38.065873 THz	239.174931	2PiTHz	1269.740796	cm-1	157.427851	meV
401	18 f =	36.742220 THz	230.858175	2PiTHz	1225.588488	cm-1	151.953661	meV
402	19 f =	35.056279 THz	220.265100	2PiTHz	1169.351579	cm-1	144.981170	meV
403	20 f =	34.516890 THz	216.876019	2PiTHz	1151.359496	cm-1	142.750435	meV
404	21 f =	31.116512 THz	195.510811	2PiTHz	1037.935086	cm-1	128.687596	meV
405	22 f =	30.113526 THz	189.208866	2PiTHz	1004.479084	cm-1	124.539579	meV
406	23 f =	29.232578 THz	183.673705	2PiTHz	975.093814	cm-1	120.896268	meV
407	24 f =	28.617092 THz	179.806493	2PiTHz	954.563415	cm-1	118.350822	meV
408	25 f =	25.290487 THz	158.904815	2PiTHz	843.599806	cm-1	104.593083	meV
409	26 f =	24.908652 THz	156.505674	2PiTHz	830.863161	cm-1	103.013940	meV
410	27 f =	23.492114 THz	147.605306	2PiTHz	783.612555	cm-1	97.155609	meV
411	28 f =	22.204186 THz	139.513013	2PiTHz	740.651888	cm-1	91.829164	meV
412	29 f =	18.809687 THz	118.184747	2PiTHz	627.423591	cm-1	77.790639	meV
413	30 f =	15.140998 THz	95.133698	2PiTHz	505.049326	cm-1	62.618158	meV
414	31 f =	14.083957 THz	88.492115	2PiTHz	469.790239	cm-1	58.246587	meV
415	32 f =	13.225901 THz	83.100785	2PiTHz	441.168545	cm-1	54.697948	meV
416	33 f =	10.681739 THz	67.115346	2PiTHz	356.304450	cm-1	44.176137	meV
417	34 f =	10.487856 THz	65.897145	2PiTHz	349.837223	cm-1	43.374303	meV
418	35 f =	8.221622 THz	51.657974	2PiTHz	274.243782	cm-1	34.001908	meV
419	36 f =	8.041572 THz	50.526690	2PiTHz	268.237977	cm-1	33.257282	meV
420	37 f =	5.460938 THz	34.312088	2PiTHz	182.157294	cm-1	22.584634	meV
421	38 f =	4.224006 THz	26.540210	2PiTHz	140.897658	cm-1	17.469089	meV
422	39 f =	2.545736 THz	15.995329	2PiTHz	84.916597	cm-1	10.528320	meV
423	# 16	C4H8 ads H ads H ads #	TS C4H8 HadsFe HadsAlglue					
424	1 f =	93.607735 THz	588.154747	2PiTHz	3122.417856	cm-1	387.130614	meV
425	2 f =	92.829297 THz	583.263677	2PiTHz	3096.451964	cm-1	383.911252	meV
426	3 f =	92.349228 THz	580.247312	2PiTHz	3080.438572	cm-1	381.925844	meV
427	4 f =	91.369809 THz	574.093440	2PiTHz	3047.768664	cm-1	377.875290	meV
428	5 f =	90.640333 THz	569.510006	2PiTHz	3023.435963	cm-1	374.858419	meV

Appendix C. Python scripts

429	6 f =	90.252084 THz	567.070569	2PiTHz	3010.485387	cm-1	373.252751	meV
430	7 f =	88.650035 THz	557.004600	2PiTHz	2957.046794	cm-1	366.627208	meV
431	8 f =	87.341079 THz	548.780183	2PiTHz	2913.384704	cm-1	361.213797	meV
432	9 f =	45.900009 THz	288.398263	2PiTHz	1531.059457	cm-1	189.827248	meV
433	10 f =	42.863543 THz	269.319583	2PiTHz	1429.773845	cm-1	177.269428	meV
434	11 f =	42.667644 THz	268.088717	2PiTHz	1423.239378	cm-1	176.459257	meV
435	12 f =	42.259022 THz	265.521267	2PiTHz	1409.609204	cm-1	174.769330	meV
436	13 f =	41.915393 THz	263.362181	2PiTHz	1398.146970	cm-1	173.348193	meV
437	14 f =	40.582041 THz	254.984486	2PiTHz	1353.671148	cm-1	167.833892	meV
438	15 f =	39.877358 THz	250.556828	2PiTHz	1330.165433	cm-1	164.919554	meV
439	16 f =	38.054263 THz	239.101989	2PiTHz	1269.353558	cm-1	157.379840	meV
440	17 f =	36.738258 THz	230.833282	2PiTHz	1225.456337	cm-1	151.937276	meV
441	18 f =	35.069006 THz	220.345060	2PiTHz	1169.776074	cm-1	145.033801	meV
442	19 f =	34.488220 THz	216.695880	2PiTHz	1150.403167	cm-1	142.631866	meV
443	20 f =	32.720211 THz	205.587151	2PiTHz	1091.428737	cm-1	135.319966	meV
444	21 f =	31.109834 THz	195.468851	2PiTHz	1037.712329	cm-1	128.659977	meV
445	22 f =	30.121224 THz	189.257232	2PiTHz	1004.735853	cm-1	124.571414	meV
446	23 f =	29.208613 THz	183.523127	2PiTHz	974.294422	cm-1	120.797156	meV
447	24 f =	28.591754 THz	179.647290	2PiTHz	953.718233	cm-1	118.246033	meV
448	25 f =	25.133101 THz	157.915933	2PiTHz	838.349998	cm-1	103.942190	meV
449	26 f =	24.895238 THz	156.421392	2PiTHz	830.415720	cm-1	102.958464	meV
450	27 f =	24.486289 THz	153.851893	2PiTHz	816.774670	cm-1	101.267189	meV
451	28 f =	23.435022 THz	147.246584	2PiTHz	781.708156	cm-1	96.919494	meV
452	29 f =	22.125981 THz	139.021639	2PiTHz	738.043260	cm-1	91.505735	meV
453	30 f =	20.775709 THz	130.537633	2PiTHz	693.003053	cm-1	85.921459	meV
454	31 f =	14.041849 THz	88.227539	2PiTHz	468.385648	cm-1	58.072440	meV
455	32 f =	13.210130 THz	83.001695	2PiTHz	440.642494	cm-1	54.632726	meV
456	33 f =	10.400288 THz	65.346939	2PiTHz	346.916268	cm-1	43.012151	meV
457	34 f =	8.159231 THz	51.265960	2PiTHz	272.162638	cm-1	33.743879	meV
458	35 f =	6.776983 THz	42.581039	2PiTHz	226.055809	cm-1	28.027358	meV
459	36 f =	5.487323 THz	34.477870	2PiTHz	183.037404	cm-1	22.693754	meV
460	37 f =	4.082581 THz	25.651611	2PiTHz	136.180228	cm-1	16.884203	meV
461	38 f =	2.477411 THz	15.566035	2PiTHz	82.637545	cm-1	10.245753	meV
462	# 17	C4H8 ads H ads H ads #	C4H8	HadsFe	HadsAlglue			
463	1 f =	93.428747 THz	587.030132	2PiTHz	3116.447462	cm-1	386.390379	meV
464	2 f =	92.695716 THz	582.424363	2PiTHz	3091.996182	cm-1	383.358806	meV
465	3 f =	92.397715 THz	580.551967	2PiTHz	3082.055935	cm-1	382.126372	meV
466	4 f =	91.232951 THz	573.233538	2PiTHz	3043.203585	cm-1	377.309293	meV
467	5 f =	90.773170 THz	570.344647	2PiTHz	3027.866933	cm-1	375.407789	meV
468	6 f =	90.027545 THz	565.659749	2PiTHz	3002.995571	cm-1	372.324132	meV
469	7 f =	88.598764 THz	556.682452	2PiTHz	2955.336564	cm-1	366.415166	meV
470	8 f =	87.341222 THz	548.781084	2PiTHz	2913.389485	cm-1	361.214390	meV
471	9 f =	53.721736 THz	337.543621	2PiTHz	1791.964163	cm-1	222.175320	meV
472	10 f =	44.819223 THz	281.607482	2PiTHz	1495.008305	cm-1	185.357473	meV
473	11 f =	42.848060 THz	269.222303	2PiTHz	1429.257402	cm-1	177.205397	meV
474	12 f =	42.651031 THz	267.984330	2PiTHz	1422.685209	cm-1	176.390548	meV
475	13 f =	42.218358 THz	265.265768	2PiTHz	1408.252805	cm-1	174.601158	meV
476	14 f =	41.869015 THz	263.070783	2PiTHz	1396.599982	cm-1	173.156391	meV
477	15 f =	40.563505 THz	254.868018	2PiTHz	1353.052842	cm-1	167.757232	meV
478	16 f =	39.821500 THz	250.205862	2PiTHz	1328.302212	cm-1	164.688544	meV
479	17 f =	38.037851 THz	238.998865	2PiTHz	1268.806090	cm-1	157.311963	meV
480	18 f =	36.661844 THz	230.353162	2PiTHz	1222.907458	cm-1	151.621255	meV
481	19 f =	34.919555 THz	219.406033	2PiTHz	1164.790929	cm-1	144.415721	meV
482	20 f =	34.504998 THz	216.801295	2PiTHz	1150.962802	cm-1	142.701252	meV
483	21 f =	31.097390 THz	195.390661	2PiTHz	1037.297229	cm-1	128.608512	meV
484	22 f =	30.090154 THz	189.062011	2PiTHz	1003.699455	cm-1	124.442917	meV
485	23 f =	29.306015 THz	184.135123	2PiTHz	977.543409	cm-1	121.199980	meV
486	24 f =	29.032444 THz	182.416227	2PiTHz	968.418069	cm-1	120.068581	meV
487	25 f =	25.057224 THz	157.439183	2PiTHz	835.819009	cm-1	103.628387	meV
488	26 f =	24.956173 THz	156.804261	2PiTHz	832.448310	cm-1	103.210473	meV
489	27 f =	23.596179 THz	148.259168	2PiTHz	787.083801	cm-1	97.585989	meV
490	28 f =	22.099285 THz	138.853906	2PiTHz	737.152793	cm-1	91.395331	meV
491	29 f =	20.298906 THz	127.541789	2PiTHz	677.098608	cm-1	83.949558	meV
492	30 f =	14.141714 THz	88.855007	2PiTHz	471.716778	cm-1	58.485448	meV
493	31 f =	13.571431 THz	85.271814	2PiTHz	452.694189	cm-1	56.126946	meV
494	32 f =	13.269159 THz	83.372586	2PiTHz	442.611494	cm-1	54.876851	meV
495	33 f =	10.734984 THz	67.449894	2PiTHz	358.080510	cm-1	44.396341	meV
496	34 f =	10.463616 THz	65.744836	2PiTHz	349.028636	cm-1	43.274051	meV

C.2. Pre-exponential factors

497	35 f =	10.375178	THz	65.189165	2PiTHz	346.078671	cm-1	42.908302	meV
498	36 f =	8.240888	THz	51.779026	2PiTHz	274.886426	cm-1	34.081585	meV
499	37 f =	5.443015	THz	34.199472	2PiTHz	181.559431	cm-1	22.510509	meV
500	38 f =	4.109491	THz	25.820696	2PiTHz	137.077875	cm-1	16.995497	meV
501	39 f =	2.409807	THz	15.141266	2PiTHz	80.382519	cm-1	9.966166	meV
502	# 18	C4H9 ads	H ads #	TS	C4H9	HadsFe			
503	1 f =	92.354465	THz	580.280218	2PiTHz	3080.613265	cm-1	381.947503	meV
504	2 f =	91.415695	THz	574.381749	2PiTHz	3049.299249	cm-1	378.065059	meV
505	3 f =	90.600840	THz	569.261869	2PiTHz	3022.118639	cm-1	374.695091	meV
506	4 f =	90.395437	THz	567.971281	2PiTHz	3015.267118	cm-1	373.845611	meV
507	5 f =	90.306897	THz	567.414970	2PiTHz	3012.313756	cm-1	373.479440	meV
508	6 f =	89.595611	THz	562.945830	2PiTHz	2988.587817	cm-1	370.537798	meV
509	7 f =	88.603987	THz	556.715270	2PiTHz	2955.510788	cm-1	366.436767	meV
510	8 f =	88.034805	THz	553.138991	2PiTHz	2936.524904	cm-1	364.082817	meV
511	9 f =	86.570688	THz	543.939677	2PiTHz	2887.687246	cm-1	358.027717	meV
512	10 f =	44.907750	THz	282.163717	2PiTHz	1497.961265	cm-1	185.723593	meV
513	11 f =	42.791096	THz	268.864388	2PiTHz	1427.357288	cm-1	176.969813	meV
514	12 f =	42.690296	THz	268.231040	2PiTHz	1423.994949	cm-1	176.552936	meV
515	13 f =	42.541444	THz	267.295778	2PiTHz	1419.029798	cm-1	175.937335	meV
516	14 f =	42.193126	THz	265.107230	2PiTHz	1407.411148	cm-1	174.496806	meV
517	15 f =	41.749877	THz	262.322214	2PiTHz	1392.625951	cm-1	172.663674	meV
518	16 f =	39.860225	THz	250.449182	2PiTHz	1329.593957	cm-1	164.848700	meV
519	17 f =	39.688472	THz	249.370022	2PiTHz	1323.864873	cm-1	164.138384	meV
520	18 f =	39.356058	THz	247.281406	2PiTHz	1312.776750	cm-1	162.763631	meV
521	19 f =	37.781519	THz	237.388286	2PiTHz	1260.255789	cm-1	156.251860	meV
522	20 f =	37.032874	THz	232.684412	2PiTHz	1235.283683	cm-1	153.155712	meV
523	21 f =	33.972971	THz	213.458469	2PiTHz	1133.216283	cm-1	140.500963	meV
524	22 f =	32.312903	THz	203.027958	2PiTHz	1077.842397	cm-1	133.635474	meV
525	23 f =	31.429265	THz	197.475899	2PiTHz	1048.367417	cm-1	129.981040	meV
526	24 f =	30.356131	THz	190.733193	2PiTHz	1012.571490	cm-1	125.542910	meV
527	25 f =	28.390543	THz	178.383044	2PiTHz	947.006558	cm-1	117.413891	meV
528	26 f =	28.011772	THz	176.003152	2PiTHz	934.372098	cm-1	115.847417	meV
529	27 f =	26.808816	THz	168.444761	2PiTHz	894.245832	cm-1	110.872392	meV
530	28 f =	24.044771	THz	151.077752	2PiTHz	802.047202	cm-1	99.441215	meV
531	29 f =	21.972179	THz	138.055275	2PiTHz	732.912992	cm-1	90.869662	meV
532	30 f =	20.698065	THz	130.049780	2PiTHz	690.413123	cm-1	85.600348	meV
533	31 f =	12.914784	THz	81.145980	2PiTHz	430.790806	cm-1	53.411272	meV
534	32 f =	12.330505	THz	77.474849	2PiTHz	411.301369	cm-1	50.994889	meV
535	33 f =	10.744021	THz	67.506678	2PiTHz	358.381969	cm-1	44.433717	meV
536	34 f =	8.937612	THz	56.156670	2PiTHz	298.126622	cm-1	36.963004	meV
537	35 f =	7.966371	THz	50.054184	2PiTHz	265.729520	cm-1	32.946273	meV
538	36 f =	6.522485	THz	40.981981	2PiTHz	217.566667	cm-1	26.974838	meV
539	37 f =	5.362086	THz	33.690978	2PiTHz	178.859918	cm-1	22.175812	meV
540	38 f =	4.953495	THz	31.123728	2PiTHz	165.230809	cm-1	20.486017	meV
541	# 19	C4H9 ads	H ads #	C4H9	HadsFe				
542	1 f =	92.357086	THz	580.296685	2PiTHz	3080.700684	cm-1	381.958342	meV
543	2 f =	91.682531	THz	576.058331	2PiTHz	3058.199952	cm-1	379.168606	meV
544	3 f =	90.766762	THz	570.304386	2PiTHz	3027.653196	cm-1	375.381289	meV
545	4 f =	90.419221	THz	568.120719	2PiTHz	3016.060460	cm-1	373.943973	meV
546	5 f =	90.324107	THz	567.523104	2PiTHz	3012.887821	cm-1	373.550615	meV
547	6 f =	89.630472	THz	563.164863	2PiTHz	2989.750627	cm-1	370.681968	meV
548	7 f =	88.695180	THz	557.288249	2PiTHz	2958.552644	cm-1	366.813910	meV
549	8 f =	88.064410	THz	553.325005	2PiTHz	2937.512421	cm-1	364.205254	meV
550	9 f =	86.563823	THz	543.896543	2PiTHz	2887.458253	cm-1	357.999325	meV
551	10 f =	44.828443	THz	281.665415	2PiTHz	1495.315863	cm-1	185.395605	meV
552	11 f =	42.832424	THz	269.124058	2PiTHz	1428.735835	cm-1	177.140731	meV
553	12 f =	42.740363	THz	268.545620	2PiTHz	1425.665006	cm-1	176.759996	meV
554	13 f =	42.568770	THz	267.467472	2PiTHz	1419.941289	cm-1	176.050346	meV
555	14 f =	42.209017	THz	265.207076	2PiTHz	1407.941215	cm-1	174.562526	meV
556	15 f =	41.732184	THz	262.211047	2PiTHz	1392.035788	cm-1	172.590503	meV
557	16 f =	39.898471	THz	250.689489	2PiTHz	1330.869711	cm-1	165.006874	meV
558	17 f =	39.698022	THz	249.430028	2PiTHz	1324.183437	cm-1	164.177881	meV
559	18 f =	39.344869	THz	247.211102	2PiTHz	1312.403521	cm-1	162.717357	meV
560	19 f =	37.786485	THz	237.419487	2PiTHz	1260.421427	cm-1	156.272396	meV
561	20 f =	37.079335	THz	232.976330	2PiTHz	1236.833429	cm-1	153.347856	meV
562	21 f =	33.997104	THz	213.610107	2PiTHz	1134.021302	cm-1	140.600773	meV
563	22 f =	32.312239	THz	203.023784	2PiTHz	1077.820236	cm-1	133.632726	meV
564	23 f =	31.427858	THz	197.467054	2PiTHz	1048.320462	cm-1	129.975219	meV

Appendix C. Python scripts

565	24 f =	30.335849 THz	190.605763	2PiTHz	1011.894982	cm-1	125.459033	meV
566	25 f =	28.407529 THz	178.489770	2PiTHz	947.573146	cm-1	117.484139	meV
567	26 f =	28.000803 THz	175.934235	2PiTHz	934.006227	cm-1	115.802055	meV
568	27 f =	26.820266 THz	168.516701	2PiTHz	894.627749	cm-1	110.919744	meV
569	28 f =	24.043633 THz	151.070600	2PiTHz	802.009235	cm-1	99.436508	meV
570	29 f =	21.993400 THz	138.188610	2PiTHz	733.620849	cm-1	90.957426	meV
571	30 f =	20.987003 THz	131.865228	2PiTHz	700.051042	cm-1	86.795298	meV
572	31 f =	12.930131 THz	81.242410	2PiTHz	431.302737	cm-1	53.474743	meV
573	32 f =	12.258471 THz	77.022247	2PiTHz	408.898575	cm-1	50.696980	meV
574	33 f =	11.046522 THz	69.407342	2PiTHz	368.472285	cm-1	45.684757	meV
575	34 f =	8.868835 THz	55.724535	2PiTHz	295.832492	cm-1	36.678568	meV
576	35 f =	7.996662 THz	50.244510	2PiTHz	266.739928	cm-1	33.071548	meV
577	36 f =	6.416915 THz	40.318667	2PiTHz	214.045245	cm-1	26.538238	meV
578	37 f =	5.350192 THz	33.616251	2PiTHz	178.463206	cm-1	22.126626	meV
579	38 f =	4.925076 THz	30.945167	2PiTHz	164.282859	cm-1	20.368486	meV
580	39 f =	1.464383 THz	9.200987	2PiTHz	48.846541	cm-1	6.056201	meV
581	# 20	C4H9 ads H ads #	TS	C4H9 HadsFeSub				
582	1 f =	92.473596 THz	581.028742	2PiTHz	3084.587057	cm-1	382.440191	meV
583	2 f =	91.841107 THz	577.054695	2PiTHz	3063.489487	cm-1	379.824425	meV
584	3 f =	90.770636 THz	570.328727	2PiTHz	3027.782416	cm-1	375.397310	meV
585	4 f =	90.478684 THz	568.494341	2PiTHz	3018.043958	cm-1	374.189895	meV
586	5 f =	90.389196 THz	567.932067	2PiTHz	3015.058942	cm-1	373.819800	meV
587	6 f =	89.754014 THz	563.941101	2PiTHz	2993.871548	cm-1	371.192897	meV
588	7 f =	88.627835 THz	556.865113	2PiTHz	2956.306279	cm-1	366.535396	meV
589	8 f =	88.106719 THz	553.590845	2PiTHz	2938.923724	cm-1	364.380233	meV
590	9 f =	86.416304 THz	542.969653	2PiTHz	2882.537544	cm-1	357.389235	meV
591	10 f =	42.905345 THz	269.582235	2PiTHz	1431.168222	cm-1	177.442309	meV
592	11 f =	42.764641 THz	268.698163	2PiTHz	1426.474831	cm-1	176.860402	meV
593	12 f =	42.608248 THz	267.715519	2PiTHz	1421.258134	cm-1	176.213614	meV
594	13 f =	42.272601 THz	265.606585	2PiTHz	1410.062147	cm-1	174.825488	meV
595	14 f =	41.680189 THz	261.884348	2PiTHz	1390.301395	cm-1	172.375466	meV
596	15 f =	39.965008 THz	251.107553	2PiTHz	1333.089141	cm-1	165.282048	meV
597	16 f =	39.720054 THz	249.568457	2PiTHz	1324.918332	cm-1	164.268996	meV
598	17 f =	39.339608 THz	247.178045	2PiTHz	1312.228025	cm-1	162.695598	meV
599	18 f =	37.810368 THz	237.569549	2PiTHz	1261.218082	cm-1	156.371169	meV
600	19 f =	37.020279 THz	232.605274	2PiTHz	1234.863553	cm-1	153.103623	meV
601	20 f =	34.077865 THz	214.117540	2PiTHz	1136.715181	cm-1	140.934771	meV
602	21 f =	32.304855 THz	202.977388	2PiTHz	1077.573926	cm-1	133.602187	meV
603	22 f =	31.737888 THz	199.415033	2PiTHz	1058.661967	cm-1	131.257402	meV
604	23 f =	31.482488 THz	197.810307	2PiTHz	1050.142733	cm-1	130.201152	meV
605	24 f =	30.290060 THz	190.318060	2PiTHz	1010.367616	cm-1	125.269664	meV
606	25 f =	28.448239 THz	178.745555	2PiTHz	948.931069	cm-1	117.652500	meV
607	26 f =	28.067750 THz	176.354872	2PiTHz	936.239320	cm-1	116.078923	meV
608	27 f =	27.765565 THz	174.456190	2PiTHz	926.159530	cm-1	114.829188	meV
609	28 f =	27.037969 THz	169.884572	2PiTHz	901.889553	cm-1	111.820093	meV
610	29 f =	24.055693 THz	151.146376	2PiTHz	802.411519	cm-1	99.486385	meV
611	30 f =	22.069822 THz	138.668781	2PiTHz	736.169999	cm-1	91.273480	meV
612	31 f =	12.985018 THz	81.587277	2PiTHz	433.133578	cm-1	53.701739	meV
613	32 f =	12.318930 THz	77.402122	2PiTHz	410.915271	cm-1	50.947019	meV
614	33 f =	8.857923 THz	55.655971	2PiTHz	295.468494	cm-1	36.633438	meV
615	34 f =	8.002859 THz	50.283445	2PiTHz	266.946630	cm-1	33.097176	meV
616	35 f =	6.298036 THz	39.571730	2PiTHz	210.079876	cm-1	26.046594	meV
617	36 f =	5.360637 THz	33.681876	2PiTHz	178.811600	cm-1	22.169821	meV
618	37 f =	4.901211 THz	30.795218	2PiTHz	163.486803	cm-1	20.269788	meV
619	38 f =	1.517490 THz	9.534671	2PiTHz	50.618016	cm-1	6.275836	meV
620	# 21	C4H9 ads H ads #	C4H9 HadsFeSub					
621	1 f =	92.347045 THz	580.233595	2PiTHz	3080.365752	cm-1	381.916816	meV
622	2 f =	91.518659 THz	575.028695	2PiTHz	3052.733785	cm-1	378.490887	meV
623	3 f =	90.647986 THz	569.558097	2PiTHz	3023.691266	cm-1	374.890072	meV
624	4 f =	90.413437 THz	568.084380	2PiTHz	3015.867545	cm-1	373.920054	meV
625	5 f =	90.334251 THz	567.586836	2PiTHz	3013.226162	cm-1	373.592564	meV
626	6 f =	89.498603 THz	562.336307	2PiTHz	2985.351961	cm-1	370.136603	meV
627	7 f =	88.602682 THz	556.707068	2PiTHz	2955.467245	cm-1	366.431369	meV
628	8 f =	88.107532 THz	553.595954	2PiTHz	2938.950846	cm-1	364.383595	meV
629	9 f =	86.550229 THz	543.811127	2PiTHz	2887.004795	cm-1	357.943104	meV
630	10 f =	53.052115 THz	333.336270	2PiTHz	1769.628023	cm-1	219.405991	meV
631	11 f =	42.844977 THz	269.202927	2PiTHz	1429.154541	cm-1	177.192644	meV
632	12 f =	42.748554 THz	268.597085	2PiTHz	1425.938222	cm-1	176.793871	meV

C.2. Pre-exponential factors

633	13 f =	42.562134 THz	267.425772	2PiTHz	1419.719913	cm-1	176.022899	meV
634	14 f =	42.194638 THz	265.116729	2PiTHz	1407.461579	cm-1	174.503058	meV
635	15 f =	41.687998 THz	261.933414	2PiTHz	1390.561879	cm-1	172.407762	meV
636	16 f =	39.945857 THz	250.987221	2PiTHz	1332.450318	cm-1	165.202844	meV
637	17 f =	39.724868 THz	249.598708	2PiTHz	1325.078929	cm-1	164.288908	meV
638	18 f =	39.345486 THz	247.214977	2PiTHz	1312.424090	cm-1	162.719907	meV
639	19 f =	37.773268 THz	237.336446	2PiTHz	1259.980574	cm-1	156.217738	meV
640	20 f =	37.044372 THz	232.756655	2PiTHz	1235.667211	cm-1	153.203264	meV
641	21 f =	33.981586 THz	213.512604	2PiTHz	1133.503677	cm-1	140.536595	meV
642	22 f =	32.326197 THz	203.111483	2PiTHz	1078.285819	cm-1	133.690451	meV
643	23 f =	31.447382 THz	197.589731	2PiTHz	1048.971731	cm-1	130.055966	meV
644	24 f =	30.380190 THz	190.884364	2PiTHz	1013.374030	cm-1	125.642412	meV
645	25 f =	28.438908 THz	178.686930	2PiTHz	948.619840	cm-1	117.613913	meV
646	26 f =	27.988052 THz	175.854115	2PiTHz	933.580883	cm-1	115.749319	meV
647	27 f =	26.771379 THz	168.209535	2PiTHz	892.997052	cm-1	110.717563	meV
648	28 f =	24.089123 THz	151.356421	2PiTHz	803.526615	cm-1	99.624639	meV
649	29 f =	21.946713 THz	137.895267	2PiTHz	732.063539	cm-1	90.764344	meV
650	30 f =	12.980755 THz	81.560490	2PiTHz	432.991370	cm-1	53.684107	meV
651	31 f =	12.233761 THz	76.866987	2PiTHz	408.074329	cm-1	50.594787	meV
652	32 f =	10.861899 THz	68.247325	2PiTHz	362.313946	cm-1	44.921220	meV
653	33 f =	8.919662 THz	56.043888	2PiTHz	297.527884	cm-1	36.888769	meV
654	34 f =	8.069313 THz	50.700989	2PiTHz	269.163304	cm-1	33.372008	meV
655	35 f =	6.439247 THz	40.458980	2PiTHz	214.790140	cm-1	26.630593	meV
656	36 f =	5.638078 THz	35.425087	2PiTHz	188.066024	cm-1	23.317224	meV
657	37 f =	5.334590 THz	33.518220	2PiTHz	177.942779	cm-1	22.062101	meV
658	38 f =	5.020833 THz	31.546825	2PiTHz	167.476963	cm-1	20.764504	meV
659	39 f =	1.427514 THz	8.969337	2PiTHz	47.616750	cm-1	5.903727	meV
660	# 22 C4H10 ads # TS C4H10							
661	1 f =	91.426024 THz	574.446652	2PiTHz	3049.643813	cm-1	378.107779	meV
662	2 f =	91.316583 THz	573.759013	2PiTHz	3045.993245	cm-1	377.655166	meV
663	3 f =	90.532303 THz	568.831239	2PiTHz	3019.832497	cm-1	374.411646	meV
664	4 f =	90.146255 THz	566.405625	2PiTHz	3006.955306	cm-1	372.815077	meV
665	5 f =	89.902868 THz	564.876382	2PiTHz	2998.836803	cm-1	371.808511	meV
666	6 f =	88.615418 THz	556.787091	2PiTHz	2955.892078	cm-1	366.484041	meV
667	7 f =	88.083667 THz	553.446000	2PiTHz	2938.154769	cm-1	364.284895	meV
668	8 f =	87.876381 THz	552.143584	2PiTHz	2931.240454	cm-1	363.427628	meV
669	9 f =	87.370626 THz	548.965836	2PiTHz	2914.370306	cm-1	361.335996	meV
670	10 f =	42.824309 THz	269.073071	2PiTHz	1428.465154	cm-1	177.107171	meV
671	11 f =	42.783679 THz	268.817782	2PiTHz	1427.109868	cm-1	176.939137	meV
672	12 f =	42.604740 THz	267.693476	2PiTHz	1421.141111	cm-1	176.199105	meV
673	13 f =	42.392592 THz	266.360508	2PiTHz	1414.064600	cm-1	175.321729	meV
674	14 f =	41.819567 THz	262.760089	2PiTHz	1394.950559	cm-1	172.951889	meV
675	15 f =	39.882275 THz	250.587724	2PiTHz	1330.329454	cm-1	164.939890	meV
676	16 f =	39.728083 THz	249.618910	2PiTHz	1325.186179	cm-1	164.302205	meV
677	17 f =	38.985847 THz	244.955302	2PiTHz	1300.427841	cm-1	161.232561	meV
678	18 f =	37.665616 THz	236.660043	2PiTHz	1256.389661	cm-1	155.772521	meV
679	19 f =	36.626126 THz	230.128738	2PiTHz	1221.716027	cm-1	151.473537	meV
680	20 f =	35.376473 THz	222.276934	2PiTHz	1180.032077	cm-1	146.305384	meV
681	21 f =	33.600432 THz	211.117738	2PiTHz	1120.789723	cm-1	138.960265	meV
682	22 f =	31.912824 THz	200.514189	2PiTHz	1064.497206	cm-1	131.980880	meV
683	23 f =	31.533891 THz	198.133283	2PiTHz	1051.857363	cm-1	130.413739	meV
684	24 f =	30.237554 THz	189.988152	2PiTHz	1008.616189	cm-1	125.052515	meV
685	25 f =	28.497107 THz	179.052602	2PiTHz	950.561132	cm-1	117.854602	meV
686	26 f =	28.240117 THz	177.437887	2PiTHz	941.988872	cm-1	116.791777	meV
687	27 f =	27.999801 THz	175.927937	2PiTHz	933.972792	cm-1	115.797910	meV
688	28 f =	26.089756 THz	163.926774	2PiTHz	870.260574	cm-1	107.898598	meV
689	29 f =	23.913783 THz	150.254728	2PiTHz	797.677902	cm-1	98.899491	meV
690	30 f =	21.238024 THz	133.442437	2PiTHz	708.424188	cm-1	87.833437	meV
691	31 f =	14.501682 THz	91.116756	2PiTHz	483.724034	cm-1	59.974158	meV
692	32 f =	12.854059 THz	80.764436	2PiTHz	428.765248	cm-1	53.160135	meV
693	33 f =	12.425220 THz	78.069958	2PiTHz	414.460702	cm-1	51.386596	meV
694	34 f =	8.631328 THz	54.232234	2PiTHz	287.910108	cm-1	35.696317	meV
695	35 f =	7.691490 THz	48.327056	2PiTHz	256.560480	cm-1	31.809457	meV
696	36 f =	6.187500 THz	38.877212	2PiTHz	206.392794	cm-1	25.589454	meV
697	37 f =	5.482451 THz	34.447256	2PiTHz	182.874876	cm-1	22.673603	meV
698	38 f =	3.145056 THz	19.760971	2PiTHz	104.907779	cm-1	13.006912	meV
699	# 23 C4H10 ads # C4H10 ads							
700	1 f =	92.695420 THz	582.422500	2PiTHz	3091.986291	cm-1	383.357579	meV

Appendix C. Python scripts

701	2 f =	92.053144 THz	578.386962	2PiTHz	3070.562277	cm-1	380.701339	meV
702	3 f =	91.992039 THz	578.003025	2PiTHz	3068.524019	cm-1	380.448627	meV
703	4 f =	91.484007 THz	574.810970	2PiTHz	3051.577916	cm-1	378.347578	meV
704	5 f =	90.940921 THz	571.398657	2PiTHz	3033.462503	cm-1	376.101552	meV
705	6 f =	90.666415 THz	569.673884	2PiTHz	3024.305964	cm-1	374.966285	meV
706	7 f =	89.958506 THz	565.225964	2PiTHz	3000.692678	cm-1	372.038610	meV
707	8 f =	89.404416 THz	561.744512	2PiTHz	2982.210216	cm-1	369.747076	meV
708	9 f =	89.286219 THz	561.001858	2PiTHz	2978.267589	cm-1	369.258252	meV
709	10 f =	80.922613 THz	508.451771	2PiTHz	2699.287724	cm-1	334.669145	meV
710	11 f =	43.090780 THz	270.747356	2PiTHz	1437.353661	cm-1	178.209205	meV
711	12 f =	42.983368 THz	270.072469	2PiTHz	1433.770798	cm-1	177.764987	meV
712	13 f =	42.933024 THz	269.756147	2PiTHz	1432.091494	cm-1	177.556780	meV
713	14 f =	42.772102 THz	268.745042	2PiTHz	1426.723702	cm-1	176.891258	meV
714	15 f =	42.180234 THz	265.026226	2PiTHz	1406.981115	cm-1	174.443488	meV
715	16 f =	40.409808 THz	253.902314	2PiTHz	1347.926076	cm-1	167.121594	meV
716	17 f =	40.333649 THz	253.423790	2PiTHz	1345.385666	cm-1	166.806623	meV
717	18 f =	39.997388 THz	251.311001	2PiTHz	1334.169216	cm-1	165.415960	meV
718	19 f =	39.513284 THz	248.269285	2PiTHz	1318.021240	cm-1	163.413866	meV
719	20 f =	38.186067 THz	239.930137	2PiTHz	1273.750060	cm-1	157.924937	meV
720	21 f =	37.555588 THz	235.968718	2PiTHz	1252.719531	cm-1	155.317483	meV
721	22 f =	34.750735 THz	218.345307	2PiTHz	1159.159709	cm-1	143.717539	meV
722	23 f =	34.019781 THz	213.752588	2PiTHz	1134.777714	cm-1	140.694556	meV
723	24 f =	33.363730 THz	209.630499	2PiTHz	1112.894211	cm-1	137.981346	meV
724	25 f =	31.419648 THz	197.415471	2PiTHz	1048.046616	cm-1	129.941266	meV
725	26 f =	30.385322 THz	190.916607	2PiTHz	1013.545206	cm-1	125.663635	meV
726	27 f =	28.254230 THz	177.526565	2PiTHz	942.459652	cm-1	116.850146	meV
727	28 f =	26.625192 THz	167.291016	2PiTHz	888.120788	cm-1	110.112983	meV
728	29 f =	24.573315 THz	154.398693	2PiTHz	819.677540	cm-1	101.627099	meV
729	30 f =	22.297176 THz	140.097291	2PiTHz	743.753723	cm-1	92.213742	meV
730	31 f =	19.186273 THz	120.550906	2PiTHz	639.985147	cm-1	79.348074	meV
731	32 f =	12.387894 THz	77.835434	2PiTHz	413.215657	cm-1	51.232230	meV
732	33 f =	7.635452 THz	47.974959	2PiTHz	254.691253	cm-1	31.577702	meV
733	34 f =	6.793516 THz	42.684920	2PiTHz	226.607295	cm-1	28.095734	meV
734	35 f =	5.609389 THz	35.244830	2PiTHz	187.109066	cm-1	23.198576	meV
735	36 f =	3.814437 THz	23.966814	2PiTHz	127.235919	cm-1	15.775249	meV
736	37 f =	2.571195 THz	16.155295	2PiTHz	85.765833	cm-1	10.633612	meV
737	38 f =	2.357612 THz	14.813314	2PiTHz	78.641473	cm-1	9.750303	meV
738	39 f =	0.908721 THz	5.709665	2PiTHz	30.311683	cm-1	3.758171	meV

C.3 Microkinetic modelling

```

1  #!/usr/bin/env python3
2  # -*- coding: utf-8 -*-
3  """
4  @author: Corentin Chatelier, Phd Student, IJL-SOLEIL-CNRS
5  Microkinetic modelling
6  """
7  import numpy as np
8  import scipy.integrate as spi
9  import matplotlib.pyplot as plt
10
11 # Activation energies and Preexp factors
12 vea = np.zeros(28)
13 va = np.zeros(28) # power of 10
14
15 #####
16 coeff = 0.667
17
18 vea[1] = 184*coeff # Desorption C4H6 old = 184
19 vea[3] = 97*coeff # Desorption H2 old = 97
20 vea[13] = 130*coeff # Desorption C4H8 old = 130
21 vea[15] = 94*coeff # Desorption H2 old = 94
22 vea[27] = 39*coeff # Desorption C4H10 old = 39
23
24 vea[4] = 5.4*coeff # Dissociation H2
25 vea[5] = 13.6*coeff # Recombinaison H2
26 vea[6] = 51.6*coeff # Hydrogenation 1
27 vea[7] = 37.5*coeff # Deshydrogenation 1
28
29 vea[10] = 20.7*coeff # Hydrogenation 2
30 vea[11] = 0.3*coeff # Deshydrogenation 2
31
32 vea[16] = 5.4*coeff # Dissociation H2
33 vea[17] = 13.6*coeff # Recombinaison H2
34
35 vea[20] = 83*coeff # Hydrogenation 3
36 vea[21] = 0.1*coeff # Deshydrogenation 3
37
38 vea[24] = 29.9*coeff # Hydrogenation 4
39 vea[25] = 90.1*coeff # Deshydrogenation 4
40
41 #####
42 coeff2 = 0.475
43 va[4] = 15.23 -coeff2# Dissociation H2
44 va[5] = 12.68 +coeff2# Recombinaison H2
45
46 va[6] = 9.03 +coeff2# Hydrogenation 1
47 va[7] = 12.58 -coeff2# Deshydrogenation 1
48
49 va[10] = 8.13 +coeff2# Hydrogenation 2
50 va[11] = 11.61 -coeff2# Deshydrogenation 2
51
52 va[16] = 15.05 -coeff2# Dissociation H2
53 va[17] = 12.50 +coeff2# Recombinaison H2
54
55 va[20] = 7.68 +coeff2# Hydrogenation 3
56 va[21] = 11.31 -coeff2# Deshydrogenation 3
57
58 va[24] = 7.47 +coeff2# Hydrogenation 4
59 va[25] = 10.62 -coeff2# Deshydrogenation 4
60
61 #####
62 # INITIAL PARAMETERS
63

```

Appendix C. Python scripts

```

64 T = 273 + 24 # in K
65 ratio = 'ratio 10:1'
66 pH2 = 133.3 * 5 # in Pa
67 pC4H6 = 133.3 * 0.5 # in Pa
68 pC4H8 = 133.3 * 0.0 # in Pa
69 pC4H10 = 133.3 * 0.0 # in Pa
70 tmax = 1e4 # in s
71 plot1 = True # Graph cov = f(t) at given T
72 #####
73 def K(T,Afi,Ari,Eafi,Eari):
74     R = 8.3144598 # J/(molK)
75     kfi = 10**Afi * np.exp(-Eafi*1e3/(R*T)) #Arrhenius' equation
76     kri = 10**Ari * np.exp(-Eari*1e3/(R*T))
77     return kfi, kri
78
79 def calc_kads(T, P, A, m):
80     """
81     Reaction rate constant for adsorption
82     T in K
83     P in Pa
84     A m2
85     m in kg
86     """
87     kb = 1.38064852E-23 # boltzmann constant
88     return P*A / np.sqrt(2 * np.pi * m * kb * T)
89
90 def calc_kdes(T, A, m, sigma, theta_rot, Edes):
91     """
92     Reaction rate constant for desorption
93     T in K
94     A in m2
95     m in kg
96     sigma- Symmetry number
97     theta_rot- Rotational temperature in K
98     Edes in J/mol
99     """
100     kb = 1.38064852e-23 # boltzmann constant
101     h = 6.62607004e-34 # planck constant
102     R = 8.3144598 # gas constant
103
104     return kb * T**3 / h**3 * A * (2 * np.pi * m * kb)
105         / (sigma * theta_rot) * np.exp(-Edes*1e3 / (R*T))
106
107 def Irot():
108     kb = 1.38064852e-23 # boltzmann constant
109     h = 6.62607004e-34 # planck constant
110     hbar = h/2/np.pi
111
112     amu = 1.660539e-27 # kg
113     mH = 1.6737210e-27; # kg
114
115     RH2 = 73.9e-12;
116     I_H2 = 2*mH*RH2**2.0/2.0;
117     sigma_H2 = 2.0;
118     theta_rot_H2 = hbar**2/2/kb/I_H2
119
120     mC4H6 = 4*12*amu + 6*mH
121     Ia_C4H6 = amu*12.12444e-20 # en kg m2
122     Ib_C4H6 = amu*113.99086e-20
123     Ic_C4H6 = amu*126.09124e-20
124     sigma_C4H6 = 2.0
125     I_C4H6 = np.sqrt(Ia_C4H6**2+Ib_C4H6**2+Ic_C4H6**2)
126     theta_rot_C4H6 = hbar**2/2/kb/I_C4H6
127
128     mC4H8 = 4*12*amu + 8*mH
129     Ia_C4H8 = amu*33.3615745178189e-20 # en kg m2
130     Ib_C4H8 = amu*92.8651038861518e-20
131     Ic_C4H8 = amu*119.995841513786e-20

```



```

132 sigma_C4H8 = 1.0 # C2h
133 I_C4H8 = np.sqrt(Ia_C4H8**2+Ib_C4H8**2+Ic_C4H8**2)
134 theta_rot_C4H8 = hbar**2/2/kb/I_C4H8
135
136 mC4H10 = 4*12*amu + 10*mH
137 Ia_C4H10 = amu*22.21031513282226e-20 # en kg m2
138 Ib_C4H10 = amu*134.861033486499e-20
139 Ic_C4H10 = amu*144.082300733439e-20
140 sigma_C4H10 = 1.0 # C2h
141 I_C4H10 = np.sqrt(Ia_C4H10**2+Ib_C4H10**2+Ic_C4H10**2)
142 theta_rot_C4H10 = hbar**2/2/kb/I_C4H10
143
144 return mH, mC4H6, mC4H8, mC4H10, sigma_H2, sigma_C4H6, sigma_C4H8,
145 sigma_C4H10, theta_rot_H2, theta_rot_C4H6, theta_rot_C4H8, theta_rot_C4H10
146
147 #####
148
149 def dydt(t, y, params):
150     """ Set of ODE """
151     T = params[0]
152     pH2 = params[1]
153     pC4H6 = params[2]
154     pC4H8 = params[3]
155     pC4H10 = params[4]
156
157     mH, mC4H6, mC4H8, mC4H10, sigma_H2, sigma_C4H6,
158     sigma_C4H8, sigma_C4H10, theta_rot_H2, theta_rot_C4H6,
159     theta_rot_C4H8, theta_rot_C4H10 = Irot()
160
161     # area ads C4Hx
162     AreaC = (130e-12+130e-12+145e-12+107e-12+107e-12)*(108e-12+108e-12+145e-12)
163     AreaH2 = np.pi*((74e-12+53e-12+53e-12)/2)**2 # aire d'ads H2
164
165     # C4H6
166     kf1 = calc_kads(T, pC4H6, AreaC, mC4H6)
167     kr1 = calc_kdes(T, AreaC, mC4H6, sigma_C4H6, theta_rot_C4H6, vea[1])
168     # H2
169     kf2 = calc_kads(T, pH2, AreaH2, mH*2)
170     kr2 = calc_kdes(T, AreaH2, mH*2, sigma_H2, theta_rot_H2, vea[3])
171     # C4H8
172     kf7 = calc_kdes(T, AreaC, mC4H8, sigma_C4H8, theta_rot_C4H8, vea[13])
173     kr7 = calc_kads(T, pC4H8, AreaC, mC4H8)
174     # H2
175     kf8 = calc_kads(T, pH2, AreaH2, mH*2)
176     kr8 = calc_kdes(T, AreaH2, mH*2, sigma_H2, theta_rot_H2, vea[15])
177     # C4H10
178     kf14 = calc_kdes(T, AreaC, mC4H10, sigma_C4H10, theta_rot_C4H10, vea[27])
179     kr14 = calc_kads(T, pC4H10, AreaC, mC4H10)
180
181     kf3, kr3 = K(T,va[4], va[5], vea[4], vea[5] ) # H2* + * <-> 2 H*
182     kf4, kr4 = K(T,va[6], va[7], vea[6], vea[7] ) # C4H6* + H* <-> C4H7* + *
183     kf6, kr6 = K(T,va[10],va[11],vea[10],vea[11]) # C4H7* + H* <-> C4H8* + *
184     kf9, kr9 = K(T,va[16],va[17],vea[16],vea[17]) # H2* + * <-> 2 H*
185     kf11, kr11 = K(T,va[20],va[21],vea[20],vea[21]) # C4H8* + H* <-> C4H9* + *
186     kf13, kr13 = K(T,va[24],va[25],vea[24],vea[25]) # C4H9* + H* <-> C4H10* + *
187
188     r1 = kf1*y[0]-kr1*y[3] # butadiene ads/des
189     r2 = kf2*y[0]-kr2*y[2] # dihydrogene ads/des
190     r3 = kf3*y[2]*y[0]-kr3*y[1]**2 # dissociation/association
191     r4 = kf4*y[3]*y[1]-kr4*y[4]*y[0] # C4H7
192     r6 = kf6*y[4]*y[1]-kr6*y[5]*y[0] # C4H8
193     r7 = kf7*y[5]*y[1]-kr7*y[0] # butene ads/des
194     r8 = kf8*y[0]-kr8*y[2] # dihydrogene ads/des
195     r9 = kf9*y[2]*y[0]-kr9*y[1]**2 # dissociation/association
196     r11 = kf11*y[5]*y[1]-kr11*y[6]*y[0] # C4H9
197     r13 = kf13*y[6]*y[1]-kr13*y[7]*y[0] # C4H10
198     r14 = kf14*y[7]-kr14*y[0] # butane ads/des
199

```

Appendix C. Python scripts

```
200 dydt = np.zeros(8)
201
202 dydt[0] = -r1-r2-r3+r4+r6+r7-r8-r9+r11+r13+r14 # *
203 dydt[1] = 2*r3-r4-r6+2*r9-r11-r13 # H*
204 dydt[2] = r2-r3+r8-r9 # H2*
205 dydt[3] = r1-r4 # C4H6*
206 dydt[4] = r4-r6 # C4H7*
207 dydt[5] = r6-r7-r11 # C4H8*
208 dydt[6] = r11-r13 # C4H9*
209 dydt[7] = r13-r14 # C4H10*
210
211 return dydt
212
213 def solve_odes(T,pH2,pC4H6,pC4H8,pC4H10,tmax):
214 # initial conditions
215 y0 = [1,0,0,0,0,0,0,0]
216 t0 = 0
217 t1 = tmax # total integration time
218
219 # construct ODE solver
220 r = spi.ode(dydt).set_integrator('vode', method='bdf', atol=1e-8,
221          rtol=1e-8, nsteps=1000, with_jacobian=True)
222 r.set_initial_value(y0, t0).set_f_params([T,pH2,pC4H6,pC4H8,pC4H10])
223
224 # integrate on a logarithmic scale
225 xx = np.linspace(-10.0, np.log10(t1), int((np.log10(t1) + 12.0) * 10))
226 yy = []
227 tt = []
228 for x in xx:
229     tnew = 10.0**x
230     tt.append(tnew)
231     yy.append(r.integrate(tnew))
232
233 return tt, np.matrix(yy)
234
235 #####
236
237 def main(T,pH2,pC4H6,pC4H8,pC4H10,tmax):
238 fig, ax = plt.subplots()
239 x,y = solve_odes(T,pH2,pC4H6,pC4H8,pC4H10,tmax)
240 labels = ['*', 'H$^*$', 'H$_2^*$', 'C$_4H$_6^*$', 'C$_4H$_7^*$',
241          'C$_4H$_8^*$', 'C$_4H$_9^*$', 'C$_4H$_{10}^*$']
242
243 for i in range(0, len(labels)):
244     plt.semilogx(x, y[:,i], label=labels[i])
245
246 plt.legend(loc='center', bbox_to_anchor=(1.15, 0.5))
247 plt.grid(True, linestyle=':')
248 plt.xlabel('t (s)')
249 plt.ylabel('Coverage')
250 ax.tick_params(which='major', width=1.5)
251 ax.tick_params(which='minor', width=1)
252 ax.tick_params(which='major', length=7)
253 ax.tick_params(which='minor', length=4)
254 ax.xaxis.set_tick_params(which='both', direction='in', top=True, labelbottom=True)
255 ax.yaxis.set_tick_params(which='both', direction='in', top=True, labelbottom=True)
256 plt.minorticks_on()
257 plt.xlim(1e-10, tmax)
258
259 plt.show()
260 plt.tight_layout()
261 fig.set_size_inches(8,4)
262
263 if plot1:
264     main(T,pH2,pC4H6,pC4H8,pC4H10,tmax)
265
266 #####
```

C.4 Reciprocal space simulation

```

1  #!/usr/bin/env python3
2  # -*- coding: utf-8 -*-
3  """
4  @author: Corentin Chatelier, Phd Student, IJL-SOLEIL-CNRS
5  Reciprocal space simulation
6  """
7  import time
8  import numpy as np
9  import math
10 from datetime import timedelta
11 from scipy.interpolate import interp1d
12 from multiprocessing import Pool
13
14 t0 = time.time()
15 #####
16 """ Some definition """
17 def dotproduct(v1, v2):
18     return sum((a*b) for a, b in zip(v1, v2))
19
20 def length(v):
21     return math.sqrt(dotproduct(v, v))
22
23 def angle(v1, v2):
24     return math.acos(dotproduct(v1, v2) / (length(v1) * length(v2)))
25
26 #####
27 """ How to read the POSCAR file to retrieve positions and parameters """
28
29 def lecture(filetoberead) :
30
31     data = open(filetoberead, 'r')
32     data.readline();
33     scale = data.readline()
34     scale = float(scale.split()[0])
35
36     vec_a = scale*np.array(list(map(float, data.readline().split())))
37     vec_b = scale*np.array(list(map(float, data.readline().split())))
38     vec_c = scale*np.array(list(map(float, data.readline().split())))
39
40     a = length(vec_a)
41     b = length(vec_b)
42     c = length(vec_c)
43     alpha = angle(vec_b, vec_c)*180/np.pi
44     beta = angle(vec_a, vec_c)*180/np.pi
45     gamma = angle(vec_a, vec_b)*180/np.pi
46
47     data.readline()
48
49     natoms = data.readline().split()
50     nAl = int(natoms[0]); nCo = int(natoms[1])
51
52     data.readline();
53
54     full_data = data.read().split()
55
56     n = len(full_data)
57
58     x = []; y = []; z = []
59
60     for i in range(int(round(n/3.0))):
61         x.append(float(full_data[3*i]))
62         y.append(float(full_data[3*i+1]))
63         z.append(float(full_data[3*i+2]))

```

```

64
65     x = np.array(x); y = np.array(y); z = np.array(z)
66     data.close()
67
68     return vec_a, vec_b, vec_c, a, b, c, alpha, beta, gamma, nAl, nCo, x, y, z
69
70 #####
71 """ Input DATA """
72
73 # BEWARE fractionnal coordinates are needed
74 file = input('File (ortho ou meta) : ')
75 if file == 'ortho':
76     fichier = 'Al13Co4_ortho.vasp'
77 if file == 'meta':
78     size = input('Size (NxMxK) : ')
79     file += '_' + size
80     fichier = 'POSCAR_meta_dislo_' + size + '_remdupli_biatom.vasp'
81
82 vec_a,vec_b,vec_c,a,b,c,alpha,beta,gamma,nAl,nCo, x, y, z = lecture(fichier)
83
84
85 def maillages(nAl,nCo,x,y,z,nx,ny,nz):
86     xA1 = x[:nAl]; yA1 = y[:nAl]; zA1 = z[:nAl];
87     xCo = x[nAl:]; yCo = y[nAl:]; zCo = z[nAl:];
88
89     xnxA11 = np.array([]); ynyA11 = np.array([]); znzA11 = np.array([]);
90     xnxCo1 = np.array([]); ynyCo1 = np.array([]); znzCo1 = np.array([]);
91
92     for i in range(nx):
93         xnxA11 = np.append(xnxA11,xA1+i); ynyA11 = np.append(ynyA11,yA1);
94         znzA11 = np.append(znzA11,zA1);
95         xnxCo1 = np.append(xnxCo1,xCo+i); ynyCo1 = np.append(ynyCo1,yCo);
96         znzCo1 = np.append(znzCo1,zCo);
97
98     xnxA12 = np.array([]); ynyA12 = np.array([]); znzA12 = np.array([]);
99     xnxCo2 = np.array([]); ynyCo2 = np.array([]); znzCo2 = np.array([]);
100
101     for i in range(ny):
102         xnxA12 = np.append(xnxA12,xnxA11); ynyA12 = np.append(ynyA12,ynyA11+i);
103         znzA12 = np.append(znzA12,znzA11);
104         xnxCo2 = np.append(xnxCo2,xnxCo1); ynyCo2 = np.append(ynyCo2,ynyCo1+i);
105         znzCo2 = np.append(znzCo2,znzCo1);
106
107     xnxA13 = np.array([]); ynyA13 = np.array([]); znzA13 = np.array([]);
108     xnxCo3 = np.array([]); ynyCo3 = np.array([]); znzCo3 = np.array([]);
109
110     for i in range(nz):
111         xnxA13 = np.append(xnxA13,xnxA12); ynyA13 = np.append(ynyA13,ynyA12);
112         znzA13 = np.append(znzA13,znzA12+i);
113         xnxCo3 = np.append(xnxCo3,xnxCo2); ynyCo3 = np.append(ynyCo3,ynyCo2);
114         znzCo3 = np.append(znzCo3,znzCo2+i);
115
116     xnx = np.append(xnxA13,xnxCo3); yny = np.append(ynyA13,ynyCo3);
117     znz = np.append(znzA13,znzCo3)
118     nA12 = xnxA13.shape[0]
119     nCo2 = xnxCo3.shape[0]
120
121     return xnx, yny, znz, nA12, nCo2
122
123 map_type = int(input('Map yz (0), xz (1) or xy (2) ? Enter 0, 1 or 2 : '))
124
125 if map_type == 0:
126     nx = 1; ny = int(input('ny = ')); nz = int(input('nz = '))
127 if map_type == 1:
128     nx = int(input('nx = ')); ny = 1; nz = int(input('nz = '))
129 if map_type == 2:
130     nx = int(input('nx = ')); ny = int(input('ny = ')); nz = 1
131

```

```

132 resx = 2*np.pi/(nx*a); resy = 2*np.pi/(ny*b); resz = 2*np.pi/(nz*c)
133
134 x, y, z, nAl, nCo = maillages(nAl,nCo,x,y,z,nx,ny,nz)
135
136 #recentrage de la maille
137 x -= nx/2; y -= ny/2; z -= nz/2
138
139 Ntot = nAl + nCo
140 #####
141 """ How to calculate the atomic scattering factors """
142 # at 18.41 keV
143 f1_Al = 13.06; f2_Al = 0.046
144 f1_Co = 27.35; f2_Co = 0.8749
145
146 f1 = [f1_Al for i in range(nAl)]+[f1_Co for i in range(nCo)]
147 f2 = [f2_Al for i in range(nAl)]+[f2_Co for i in range(nCo)]
148
149 f_Al = [6.4202 ,3.0387,1.9002,0.7426,1.5936,31.5472,1.9646 ,85.0886,1.1151]
150 f_Co = [12.2841,4.2791,7.3409,0.2784,4.0034,13.5359, 2.3488,71.1692,1.0118]
151 f_coeff = []
152
153 for i in range(nAl):
154     f_coeff.append(f_Al)
155 for i in range(nCo):
156     f_coeff.append(f_Co)
157
158 def f_atom(natom,f_coeff,q):
159     f = f_coeff[natom][8]
160     for i in range(4):
161         f += f_coeff[natom][i*2]*np.exp(-f_coeff[natom][i*2+1]*(q/4/np.pi)**2);
162     return f
163
164 #####
165 """ How to calculate F """
166
167 bm = False
168 matype = 'map'
169
170 blackman = int(input('Blackman windowing, no (0) or yes (1) ? Enter 0 or 1 :'))
171 if blackman == 1:
172     bm = True
173     matype = 'bm_map'
174
175 if bm:
176     limit= 0.8
177     rangex = np.arange(limit-(1-limit),1+(1.-limit)/100.,(1.-limit)/50.)
178     window = np.blackman(101)
179     f = interp1d(rangex,window,kind='linear')
180
181 def Fq(qx,qy,qz,Ntot,x,y,z,f_coeff,f1,f2):
182     Freal = 0
183     Fimag = 0
184     q = length(np.array([qx,qy,qz]))
185     for i in range(Ntot):
186         r = np.sqrt((a*x[i])**2+(b*y[i])**2+(c*z[i])**2)
187         coeff = 1
188         if bm and r/(a*nx/2) > limit and r/(a*nx/2) <= 1:
189             coeff = f(r/(a*nx/2))
190         if bm and r/(a*nx/2) > 1:
191             coeff = 0
192         phase = qx*x[i]*a+qy*y[i]*b+qz*z[i]*c
193         Freal+=coeff*((f_atom(i,f_coeff,q)+f1[i])*np.cos(phase)-f2[i]*np.sin(phase))
194         Fimag+=coeff*((f_atom(i,f_coeff,q)+f1[i])*np.sin(phase)+f2[i]*np.cos(phase))
195     F = Freal + Fimag*1j
196
197     return F
198
199 #####

```

Appendix C. Python scripts

```
200
201 Qx = np.arange(-5,5+resx,resx)
202 Qy = np.arange(-5,5+resy,resy)
203 Qz = np.arange(-5,5+resz,resz)
204
205 Q_value = float(input('Q = '))
206
207 if map_type == 0:
208     Q1 = Qy; Q2 = Qz; sQ1 = 'y'; sQ2 = 'z'; sQ3 = 'Qx'; res1 = resy; res2 = resz
209
210 if map_type == 1:
211     Q1 = Qx; Q2 = Qz; sQ1 = 'x'; sQ2 = 'z'; sQ3 = 'Qy'; res1 = resx; res2 = resz
212
213 if map_type == 2:
214     Q1 = Qx; Q2 = Qy; sQ1 = 'x'; sQ2 = 'y'; sQ3 = 'Qz'; res1 = resx; res2 = resy
215
216 map_Q1Q2, map_Q2Q1 = np.meshgrid(Q2,Q1)
217
218 #####
219
220 nproc = int(input('Number of processes : '))
221
222 listes_Q1 = []
223 rangeQ1 = len(Q1)
224 div = int(rangeQ1/nproc)
225 mod = int(rangeQ1%nproc)
226
227 for i in range(nproc):
228     if i < nproc-1:
229         listes_Q1 += [np.arange(i*div,(i+1)*div)]
230     else:
231         listes_Q1 += [np.arange(i*div,(i+1)*div+mod)]
232
233 #####
234 def paral(liste_Q1):
235     map_F = np.zeros_like(map_Q1Q2)
236     for i in liste_Q1:
237         for j in range(len(Q2)):
238             if map_type == 0:
239                 map_F[i,j]=np.abs(Fq(Q1[i],Q_value,Q2[j],Ntot,x,y,z,f_coeff,f1,f2))
240             if map_type == 1:
241                 map_F[i,j]=np.abs(Fq(Q_value,Q1[i],Q2[j],Ntot,x,y,z,f_coeff,f1,f2))
242             if map_type == 2:
243                 map_F[i,j]=np.abs(Fq(Q1[i],Q2[j],Q_value,Ntot,x,y,z,f_coeff,f1,f2))
244
245     return map_F
246
247 with Pool(nproc) as p:
248     maps_F = np.array(p.map(paral,listes_Q1))
249
250 map_F = maps_F.sum(axis=0)
251
252 np.save(mapttype+'_'+file+'_'+sQ1+sQ2+'_'+sQ3+'_'+str(Q_value)+'_'+str(nx)
253         +'_'+str(ny)+'_'+str(nz)+'_'+str(res1)+'_'+str(res2),map_F.T)
254
255 #####
256
257 t1 = time.time()
258 elapsedtime_sec = (t1-t0)
259
260 print('Duration : ',timedelta(seconds=elapsedtime_sec))
```

Appendix D

Diffraction data

Contents

D.1 SXR D data of $\text{Al}_{13}\text{Co}_4(010)$	195
D.2 Fourier transform of $\text{Al}_{13}\text{Co}_4$	195
D.3 SXR D data of $\text{Al}_{13}\text{Fe}_4(010)$	195

D.1 SXR D data of $\text{Al}_{13}\text{Co}_4(010)$

Figs. D.1 and D.2 present the SXR D out-of-plane data of $\text{Al}_{13}\text{Co}_4(010)$ for $K \in [0, 1, 2, 3, 4, 5]$. More details regarding $\text{Al}_{13}\text{Co}_4$ can be found in Chapters 1 and 5.

D.2 Fourier transform of $\text{Al}_{13}\text{Co}_4$

Figs. D.3 and D.4 present the simulations of the reciprocal space of $\text{Al}_{13}\text{Co}_4$ with and without a core metadislocation for $K = 2$ and $K = 3$ (with respect to the (010) orientation). More details regarding the metadislocations can be found in Chapters 1 and 5.

D.3 SXR D data of $\text{Al}_{13}\text{Fe}_4(010)$

Fig. D.5 and Fig. D.6 present the SXR D measurements of another sample of $\text{Al}_{13}\text{Fe}_4(010)$ that has four domains instead of two (first sample). More details regarding $\text{Al}_{13}\text{Fe}_4$ can be found in Chapter 1 and 6.

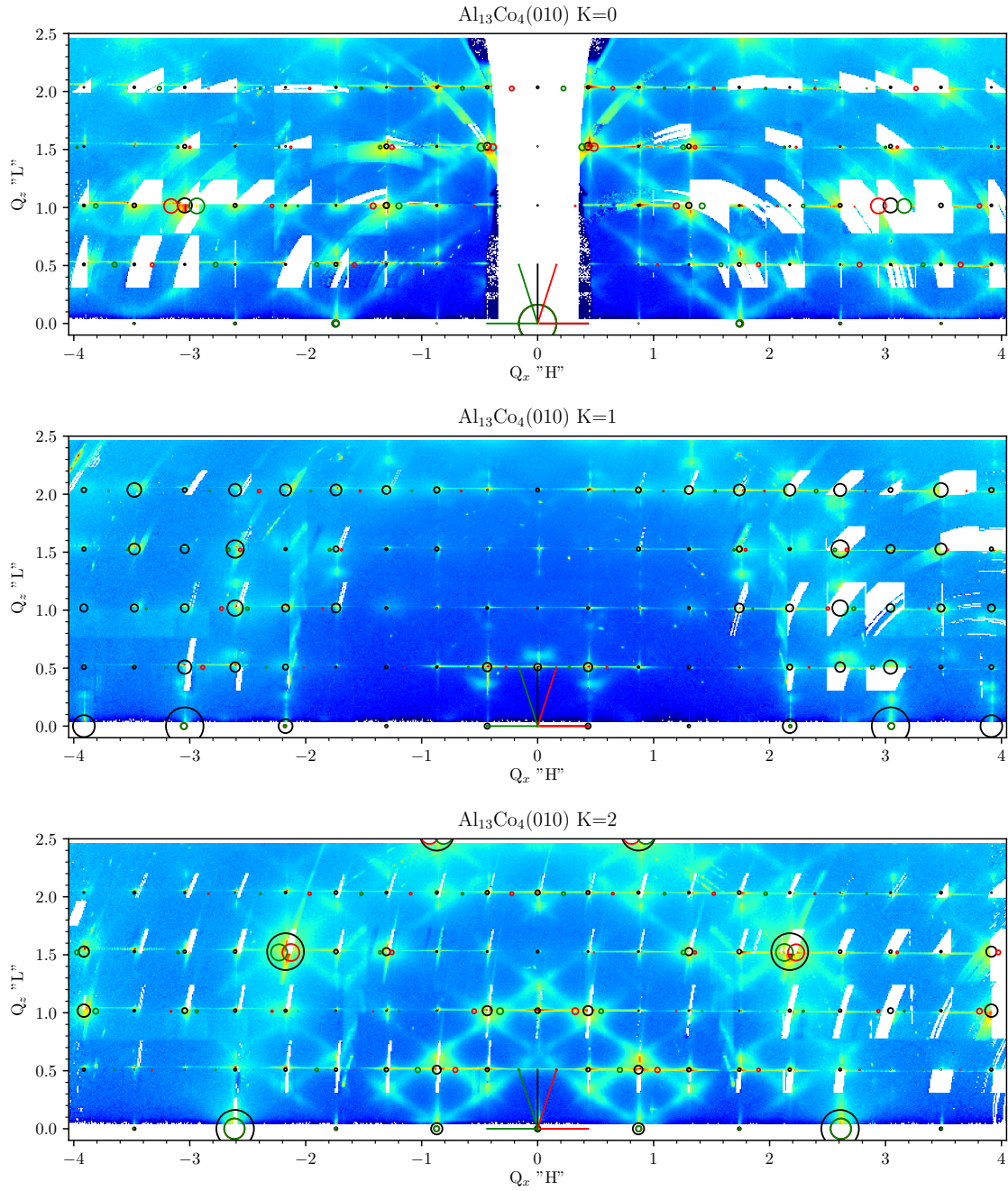


Figure D.1: SXR out-of-plane measurements of Al₁₃Co₄(010) ($K \in [0, 1, 2]$). Diffraction peaks of the orthorhombic structure are indicated using black circles, while peaks of the monoclinic structure are indicated using red and green circles (two domains).

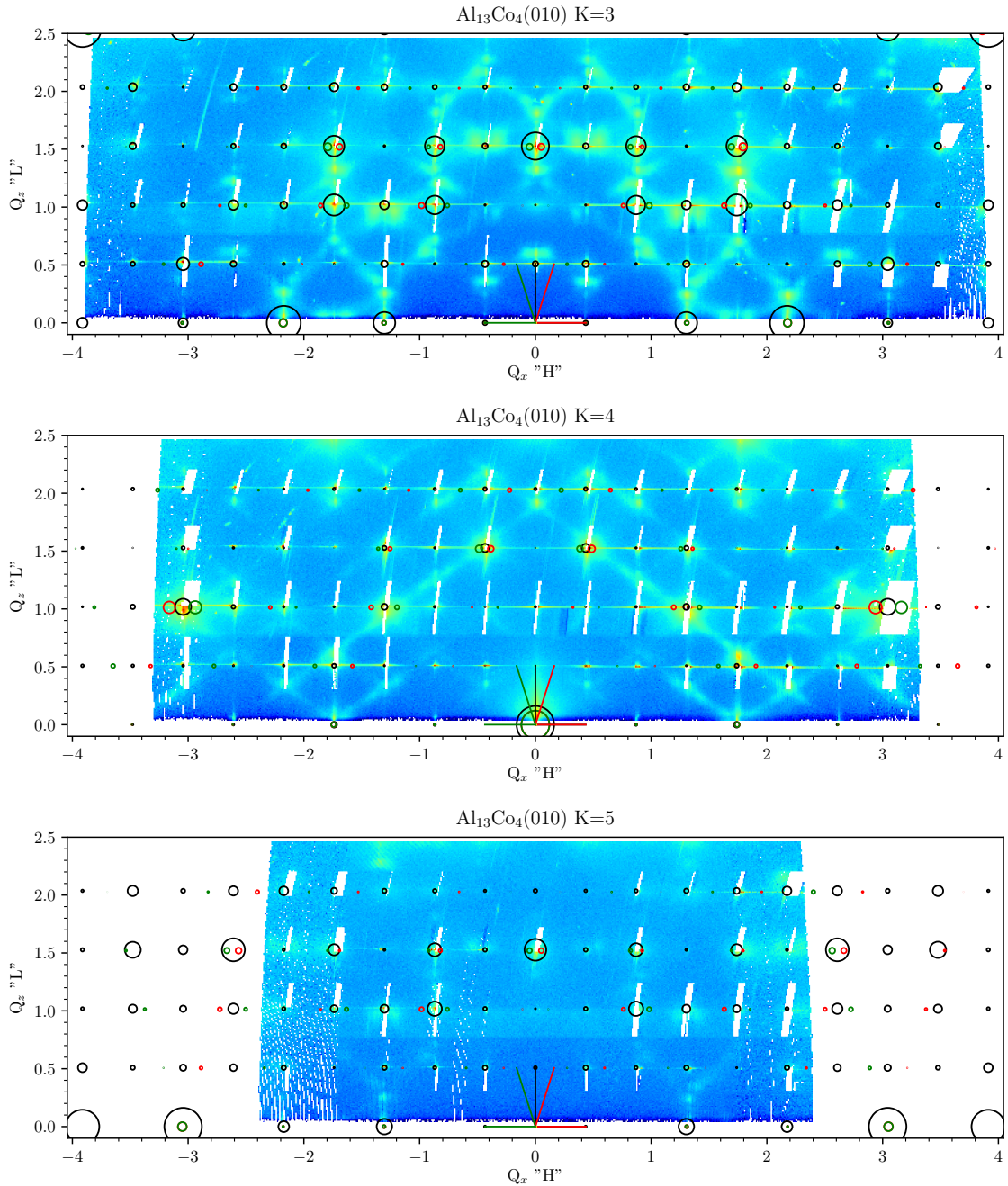


Figure D.2: SXR out-of-plane measurements of $Al_{13}Co_4(010)$ ($K \in [3, 4, 5]$). Diffraction peaks of the orthorhombic structure are indicated using black circles, while peaks of the monoclinic structure are indicated using red and green circles (two domains).

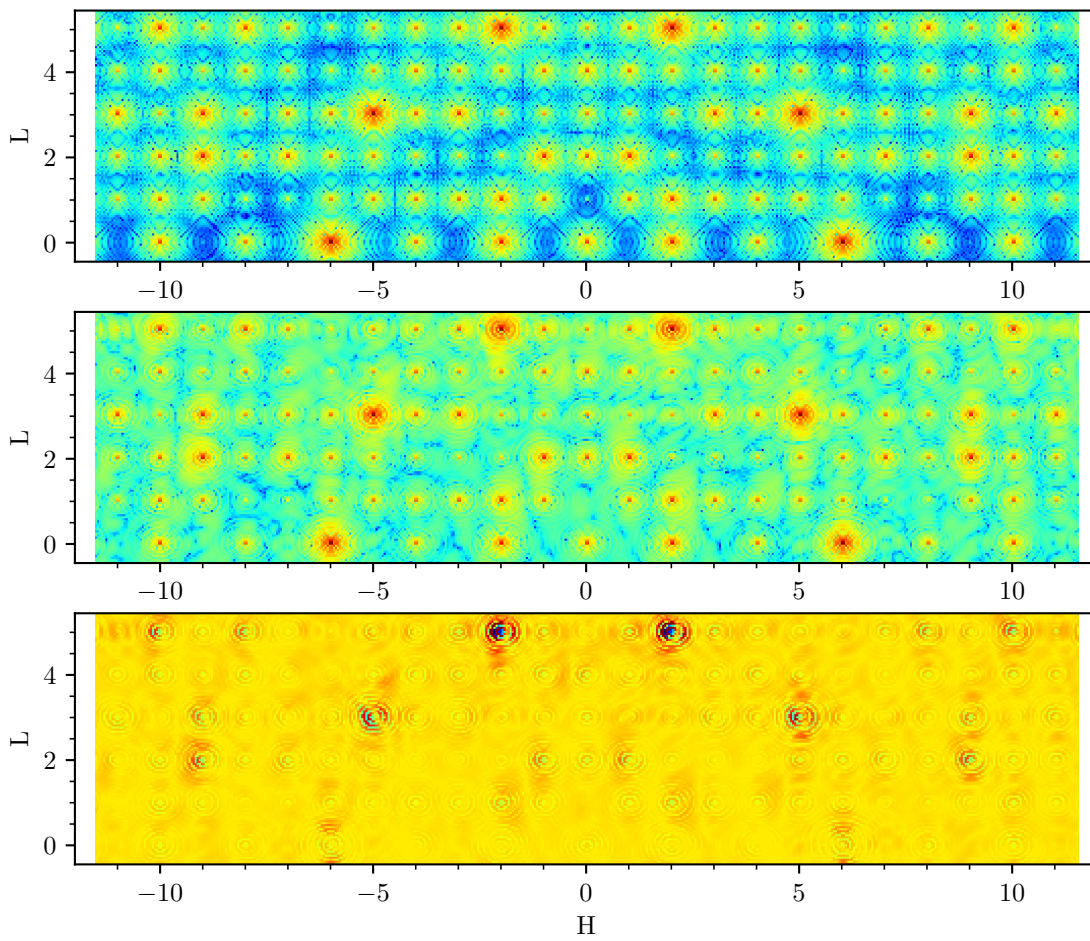


Figure D.3: Fourier transform of a metadislocation in $\text{Al}_{13}\text{Co}_4$ for $K = 2$: (top) simulation without the defect, (middle) with the defect, and (bottom) their difference.

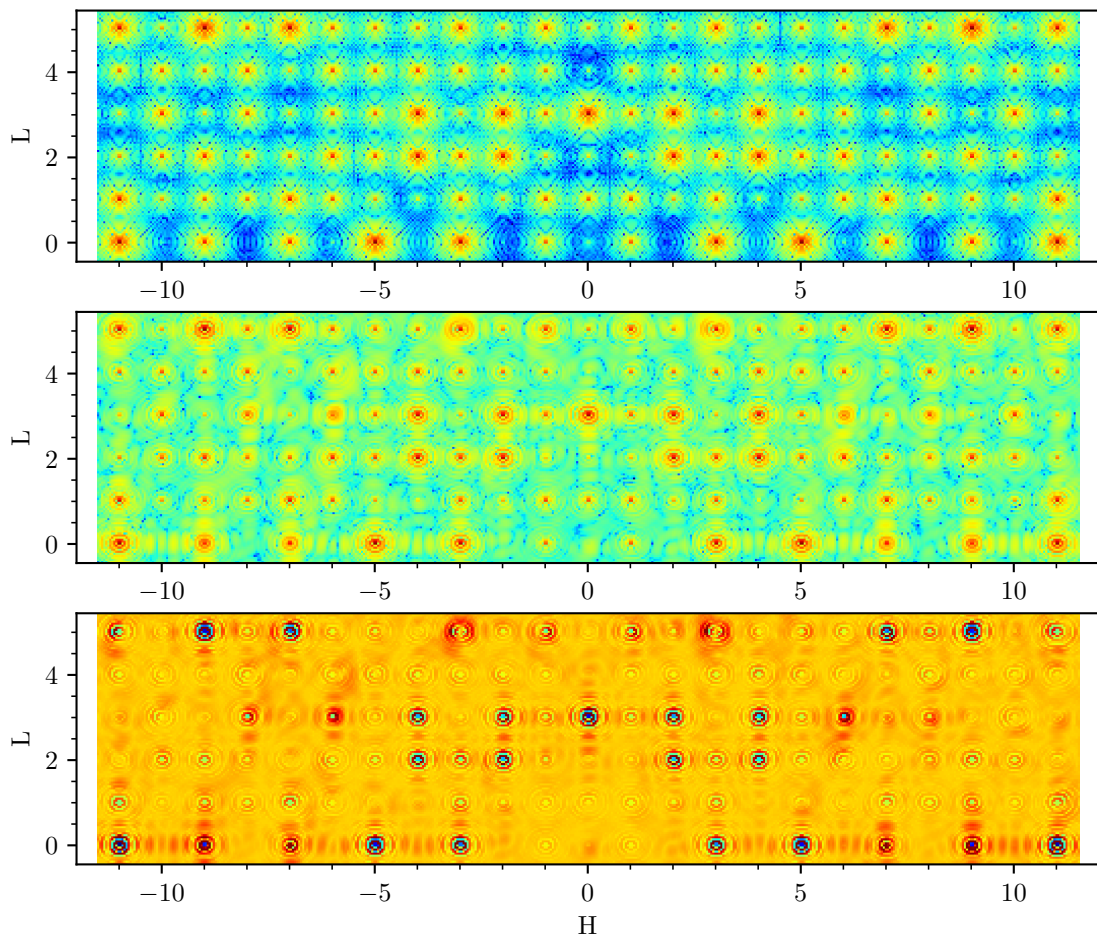
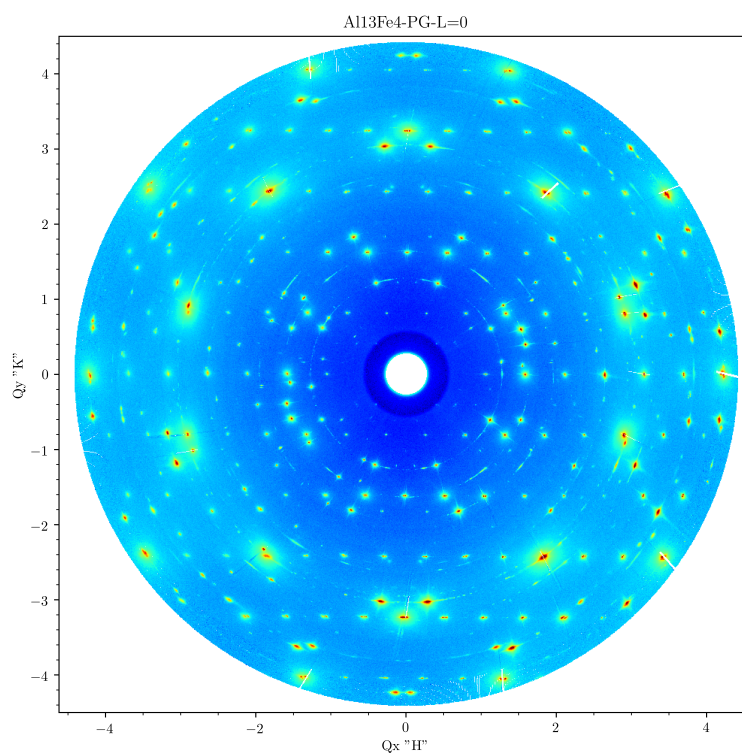
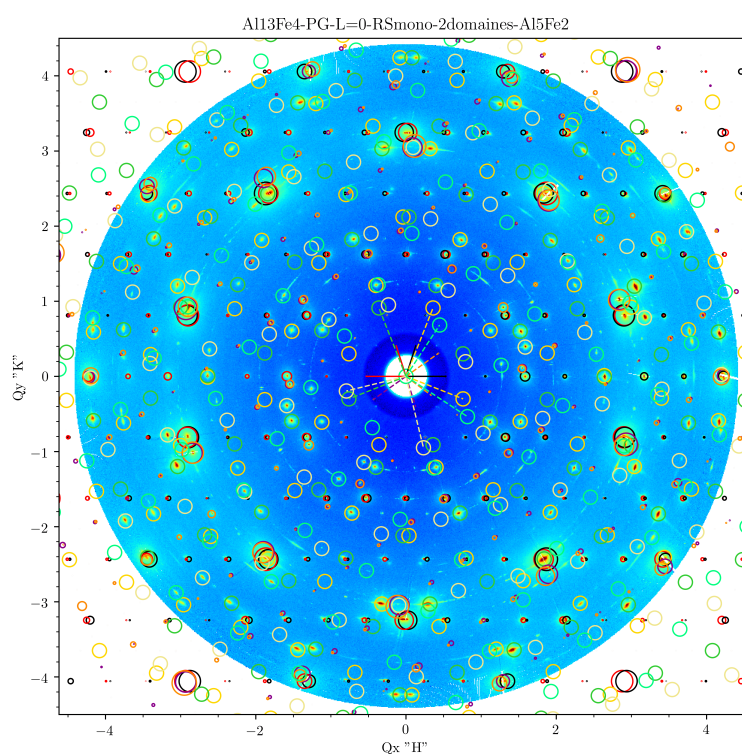


Figure D.4: Fourier transform of a metadislocation in $Al_{13}Co_4$ for $K = 3$: (top) simulation without the defect, (middle) with the defect, and (bottom) their difference.

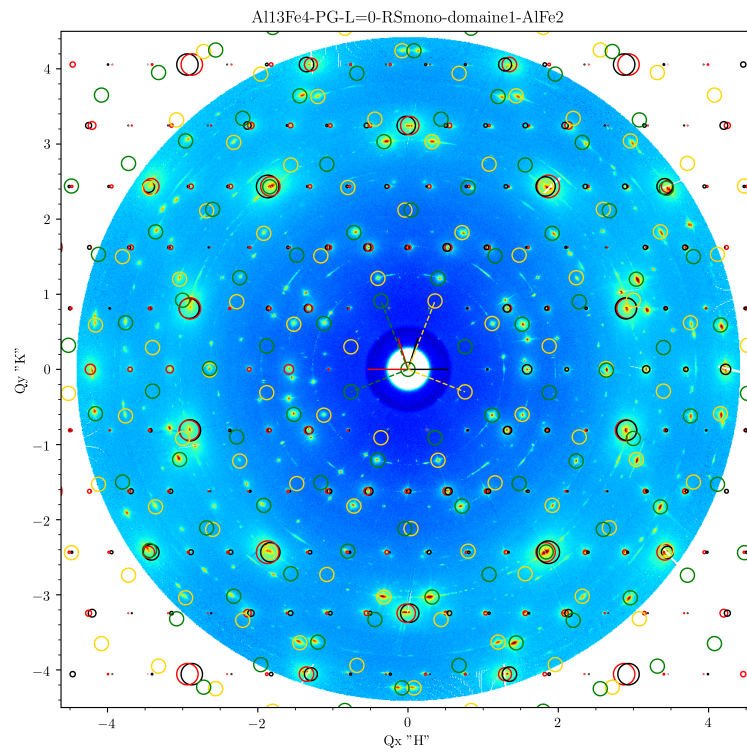


(a)

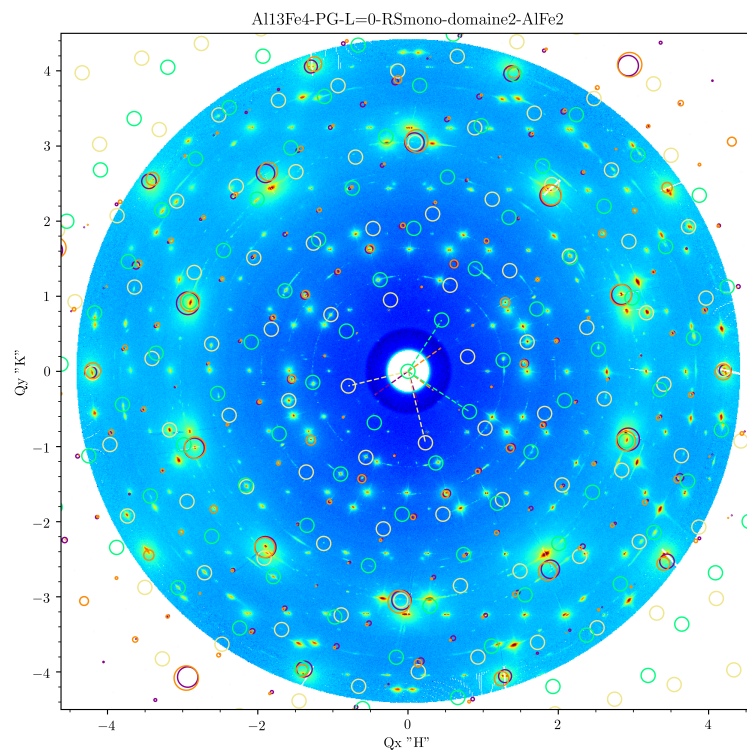


(b)

Figure D.5: In-plane reciprocal space maps of Al₁₃Fe₄(010) (sample with 4 domains): (a) raw data and (b) Al₁₃Fe₄(010) and Al₅Fe₂(001) spots are indicated with circles (4 domains).



(a)



(b)

Figure D.6: In-plane reciprocal space maps of $Al_{13}Fe_4(010)$ (sample with 4 domains): (a) 2 of the 4 domains are indicated with circles (b) the 2 other domains are indicated with circles of different colors.

Bibliography

- [1] E. Vignola, S. N. Steinmann, B. D. Vandegheuchte, D. Curulla, and P. Sautet. C_2H_2 -induced surface restructuring of Pd–Ag catalysts: insights from theoretical modeling. *J. Phys. Chem. C*, 120(46):26320–26327, 2016.
- [2] L. Piccolo, A. Piednoir, and J.C. Bertolini. Pd–Au single-crystal surfaces: Segregation properties and catalytic activity in the selective hydrogenation of 1,3-butadiene. *Surf. Sci.*, 592:169–81, 2005.
- [3] A. Hugon, L. Delannoy, J.-M. Krafft, and C. Louis. Selective hydrogenation of 1,3-butadiene in the presence of an excess of alkenes over supported bimetallic gold-palladium catalysts. *J. Phys. Chem. C*, 114(24):10823–10835, 2010.
- [4] A. Cooper, B. Bachiller-Baeza, J. A. Anderson, I. Rodriguez-Ramos, and A. Guerrero-Ruiz. Design of surface sites for the selective hydrogenation of 1,3-butadiene on Pd nanoparticles: Cu bimetallic formation and sulfur poisoning. *Catal. Sci. Technol.*, 4:1446–55, 2014.
- [5] W. M. H. Sachtler. Chemisorption complexes on alloy surfaces. *Catal. Rev. Sci. Eng.*, 14:193, 1976.
- [6] A. Borodzinski and G. C. Bond. Selective Hydrogenation of Ethyne in Ethene-Rich Streams on Palladium Catalysts, Part 2: Steady-State Kinetics and Effects of Palladium Particle Size, Carbon Monoxide, and Promoters. *Catal. Rev. Sci. Eng.*, 50:379–469, 2008.
- [7] L. Piccolo. $Al_{13}Fe_4$ selectively catalyzes the hydrogenation of butadiene at room temperature. *Chem. Comm.*, 49(80):9149–9151, 2013.
- [8] L. Piccolo, C. Chatelier, M.-C. de Weerd, F. Morfin, J. Ledieu, V. Fournée, P. Gille, and É. Gaudry. Catalytic properties of $Al_{13}TM_4$ complex intermetallics: influence of the

- transition metal and the surface orientation on butadiene hydrogenation. *Sci. Tech. Adv. Mat.*, 2019.
- [9] L. Piccolo and L. Kibis. The partial hydrogenation of butadiene over $\text{Al}_{13}\text{Fe}_4$: a surface-science study of reaction and deactivation mechanisms. *J. Catal.*, 332:112, 2015.
- [10] A. G. C. Gwyer. Uber die Legierungen des Aluminiums mit Kupfer, Eisen, Nickel, Kobalt, Blei und Cadmium. *Z. Anorg. Allg. Chem.*, 57(1):113–153, 1908.
- [11] A. J. Bradley and C. S. Cheng. The Crystal Structure of Co_2Al_5 . *Zeit. Kri. - Cryst. Mat.*, 99(1):480, 1938.
- [12] U. Burkhardt, M. Ellner, Y. Grin, and B. Baumgartner. Powder diffraction refinement of the Co_2Al_5 structure. *Powd. Diff.*, 13:159–162, 1998.
- [13] M. Meier, J. Ledieu, M.-C. De Weerd, Y.-T. Huang, G. J. P. Abreu, R.D. Diehl, T. Mazet, V. Fourné, and É. Gaudry. Interplay between bulk atomic clusters and surface structure in complex intermetallic compounds: the case study of the $\text{Al}_5\text{Co}_2(001)$ surface. *Phys. Rev. B*, 91:085414, 2015.
- [14] M. Meier, J. Ledieu, M.-C. De Weerd, V. Fournée, and É. Gaudry. Structural investigations of $\text{Al}_5\text{Co}_2(2\bar{1}0)$ and (100) surfaces: Influence of bonding strength and annealing temperature on surface terminations. *Phys. Rev. B*, 93:075412, 2016.
- [15] M. Meier, J. Ledieu, V. Fournée, and E. Gaudry. Semi-hydrogenation of acetylene on Al_5Co_2 surfaces. *J. Phys. Chem. C*, 121:4958–4969, 2017.
- [16] R.C. Hudd and W.H. Taylor. The structure of $\text{Co}_4\text{Al}_{13}$. *Acta Cryst. A*, 15:441, 1962.
- [17] J. Grin, U. Burkhardt, M. Ellner, and K. Peters. Crystal structure of orthorhombic Co_4Al_9 . *Z. Kristallogr.*, 209:479, 1994.
- [18] É. Gaudry, C. Chatelier, G. McGuirk, L. Serkovic Loli, M.-C. DeWeerd, J. Ledieu, V. Fournée, R. Felici, J. Drnec, G. Beutier, and M. de Boissieu. Structure of the $\text{Al}_{13}\text{Co}_4(100)$ surface: Combination of surface x-ray diffraction and ab initio calculations. *Phys. Rev. B*, 94:165406, 2016.
- [19] D. Kandaskalov, J. Ledieu, V. Fournée, and É. Gaudry. Catalytic Semihydrogenation of Acetylene on the (100) Surface of the $o\text{-Al}_{13}\text{Co}_4$ Quasicrystalline Approximant: Density Functional Theory Study. *J. Phys. Chem. C*, 2017.

-
- [20] J. Grin, U. Burkhardt, M. Ellner, and K. Peters. Crystal structure of orthorhombic $\text{Co}_4\text{Al}_{13}$. *J. Alloys Compd.*, 206:243–247, 1994.
- [21] M. Armbrüster, K. Kovnir, Yu. Grin, R. Schlögl, P. Gille, M. Heggen, and M. Feuerbacher. Ordered cobalt-aluminium and iron-aluminium intermetallic compounds as hydrogenation catalysts, 2009. European Patent 09157875.7.
- [22] M. Armbrüster, K. Kovnir, M. Friedrich, D. Teschner, G. Wowsnick, M. Hahne, P. Gille, L. Szentmiklosi, M. Feuerbacher, M. Heggen, F. Girgsdies, D. Rosenthal, R. Schlögl, and Y. Grin. $\text{Al}_{13}\text{Fe}_4$ as a low-cost alternative for palladium in heterogeneous hydrogenation. *Nat. Mater.*, 11:690–693, 2012.
- [23] C. Chatelier, Y. Garreau, L. Piccolo, A. Vlad, A. Resta, J. Ledieu, V. Fournée, M.-C. de Weerd, F.-E. Picca, M. de Boissieu, R. Felici, A. Coati, and É. Gaudry. From the Surface Structure to Catalytic Properties of $\text{Al}_5\text{Co}_2(2\bar{1}0)$: A Study Combining Experimental and Theoretical Approaches. *J. Phys. Chem. C*, 124(8):4552–4562, 2020.
- [24] M. Krajčí and J. Hafner. Complex intermetallic compounds as selective hydrogenation catalysts - a case study for the (100) surface of $\text{Al}_{13}\text{Co}_4$. *J. Catal.*, 278:200–207, 2011.
- [25] C. Chizallet, G. Bonnard, E. Krebs, L. Bisson, C. Thomazeau, and P. Raybaud. Thermodynamic Stability of Buta-1,3-diene and But-1-ene on Pd(111) and (100) Surfaces under H_2 Pressure: A DFT Study. *J. Phys. Chem. C*, 115:12135–12149, 2011.
- [26] J. Ledieu, É. Gaudry, L. N. Serkovic Loli, S. Alarcón Villaseca, M.-C. de Weerd, M. Hahne, P. Gille, Y. Grin, J.-M. Dubois, and V. Fournée. Structural investigation of the (010) surface of the $\text{Al}_{13}\text{Fe}_4$ catalyst. *Phys. Rev. Lett.*, 110:076102, 2013.
- [27] L. Ward, K. Michel, and C. Wolverton. Automated crystal structure solution from powder diffraction data: Validation of the first-principles-assisted structure solution method. *Phys. Rev. Mat.*, 1(6):063802, 2017.
- [28] K. Michel, B. Meredig, L. Ward, and C. Wolverton. *First-Principles-Assisted Structure Solution: Leveraging Density Functional Theory to Solve Experimentally Observed Crystal Structures*, pages 1–14. Springer International Publishing, 2019.
- [29] I.G. Aviziotis, T. Duguet, K. Soussi, M. Heggen, M.-C. Lafont, F. Morfin, S. Mishra, S. Daniele, A.G. Boudouvis, and C. Vahlas. Chemical Vapor Deposition of $\text{Al}_{13}\text{Fe}_4$ Highly Selective Catalytic Films for the Semi-Hydrogenation of Acetylene. *Phys. Stat. Solid. (a)*, 215(2):1700692, 2018.

- [30] M. Abuin, Young Y. Kim, H. Runge, S. Kulkarni, S. Maier, D. Dzhigaev, S. Lazarev, L. Gelisio, C. Seitz, M.-I. Richard, T. Zhou, V. Vonk, T.F. Keller, I.A. Vartanyants, and A. Stierle. Coherent x-ray imaging of co-adsorption-induced structural changes in pt nanoparticles: Implications for catalysis. *ACS App. Nano Mat.*, 2(8):4818–4824, 2019.
- [31] F. Studt, F. Abild-Pedersen, T. Bligaard, R. Z. Sorensen, C. H. Christensen, and Jens K. Norskov. Identification of non-precious metal alloy catalysts for selective hydrogenation of acetylene. *Science*, 320:1320–1322, 2008.
- [32] D. Kandaskalov, V. Fournée, J. Ledieu, and É. Gaudry. Adsorption properties of the o-Al₁₃Co₄(100) surface towards molecules involved in the semi-hydrogenation of acetylene. *J. Phys. Chem. C*, 118:23032–2304, 2014.
- [33] J.-M. Dubois and E. Belin-Ferré, editors. *Complex Metallic Alloys: Fundamentals and Applications*. Wiley-VCH, Weinheim, 2011.
- [34] Ph. Scheid, C. Chatelier, J. Ledieu, V. Fournée, and É. Gaudry. Bonding network and stability of clusters: the case study of the Al₁₃TM₄ pseudo-10fold surfaces. *Acta Crystallogr. A*, 2019.
- [35] S. Furukawa and T. Komatsu. Intermetallic Compounds: Promising Inorganic Materials for Well Structured and Electronically Modified Reaction Environments for Efficient Catalysis. *ACS Catal.*, 7:735–765, 2017.
- [36] K. Kovnir, M. Armbrüster, D. Teschner, T.V. Venkov, F.C. Jentoft, A. Knop-Gericke, Yu. Grin, and R. Schlögl. A new approach to well-defined, stable and site-isolated catalysts. *Scie. Tech. Adv. Mat.*, 8:420, 2007.
- [37] M. T. Greiner, T. E. Jones, S. Beeg, L. Zwiener, M. Scherzer, F. Girgsdies, S. Piccinin, M. Armbrüster, A. Knop-Gericke, and R. Schlögl. Free-atom-like d states in single-atom alloy catalysts. *Nat. Chem.*, 10:1008–1015, 2018.
- [38] J. R. Kitchin, J. K. Norskov, M. A. Barteau, and J. G. Chen. Role of Strain and Ligand Effects in the Modification of the Electronic and Chemical Properties of Bimetallic Surfaces. *Phys. Rev. Lett.*, 93:156801–1–14, 2004.
- [39] M. Mavrikakis, B. Hammer, and J. K. Norskov. Effect of Strain on the Reactivity of Metal Surfaces. *Phys. Rev. Lett.*, 81:2819–22, 1998.
- [40] A.P. Tsai, S. Kameoka, and Y. Ishii. PdZn=Cu: Can an Intermetallic Compound Replace an Element? *J. Phys. Soc. Jpn.*, 73:3270–3273, 2004.

-
- [41] A.P. Tsai, S. Kameoka, K. Nozawa, M. Shimoda, and Y. Ishii. Intermetallic: A pseudo-element for catalysis. *Acc. Chem. Research*, 50:2879–2885, 2017.
- [42] B. Hammer. Bond Activation at Monatomic Steps: NO Dissociation at Corrugated Ru(0001). *Phys. Rev. Lett.*, 83:3681–3684, 1999.
- [43] K.J. Laidler. A glossary of terms used in chemical kinetics, including reaction dynamics. *Pure App. Chem.*, 68(1):149–192, 1996.
- [44] I. Langmuir. Part II. Heterogeneous reactions. Chemical reactions on surfaces. *Trans. Faraday Soc.*, 17:607–620, 1922.
- [45] P.W. Atkins. *Physical Chemistry, Sixth edition*. Oxford University press, Oxford, 1998.
- [46] G. Ertl. Reactions at well-defined surfaces. *Surf. Sci.*, 299-300:742–754, 1994.
- [47] W. Henry Weinberg. Eley-Rideal Surface Chemistry: Direct Reactivity of Gas Phase Atomic Hydrogen with Adsorbed Species. *Acc. Chem. Res.*, 29:479–487, 1996.
- [48] R. J. Baxter and P. Hu. Insight into why the Langmuir–Hinshelwood mechanism is generally preferred. *J. Chem. Phys.*, 116(11):4379–4381, March 2002.
- [49] B. Hammer and J.K. Norskov. Theoretical surface science and catalysis – calculations and concepts. *Adv. Catal.*, 45:71–129, 2000.
- [50] T. Toyao, Z. Maeno, S. Takakusagi, T. Kamachi, I. Takigawa, and K. Shimizu. Machine Learning for Catalysis Informatics: Recent Applications and Prospects. *ACS Catal.*, 10(3):2260–2297, 2020.
- [51] W. Yang, T.T. Fidelis, and W.-H. Sun. Machine Learning in Catalysis, From Proposal to Practicing. *ACS Omega*, 5(1):83–88, 2020.
- [52] D. M. Newns. Self-consistent model of hydrogen chemisorption. *Phys. Rev.*, 178(3):1123, 1969.
- [53] M. P. Andersson, T. Bligaard, A. Kustov, K. E. Larsen, J. Greeley, T. Johannessen, C. H. Christensen, and J. K. Nørskov. Toward computational screening in heterogeneous catalysis: Pareto-optimal methanation catalysts. *J. Catal.*, 239(2):501–506, 2006.
- [54] W. Chen, W. F. Schneider, and C. Wolverton. Trends in Atomic Adsorption on Pt3M(111) Transition Metal Bimetallic Surface Overlayers. *J. Phys. Chem. C*, 118(16):8342–8349, 2014.

- [55] M. Tada and S. Muratsugu. *Heterogeneous Catalysts for Clean Technology. Chapter 7 : Site-Isolated Heterogeneous Catalysts*. Wiley, 2013.
- [56] N. Cheng, L. Zhang, K. Doyle-Davis, and X. Sun. Single-atom catalysts: From design to application. *Electrochem. Energ. Rev.*, 2:539–573, 2019.
- [57] O.G. Piringer and A.L. Baner, editors. *Plastic Packaging: Interactions with Food and Pharmaceuticals*. Wiley, 2008.
- [58] Sarah Gautier. *Réactivité catalytique à haut recouvrement : une approche théorique*. PhD thesis, École Normale Supérieure de Lyon - ENS LYON, 2015.
- [59] J.-M. Dubois and E. Belin-Ferré. *Complex metallic alloys*. Willey, 2010.
- [60] K. Sugiyama, S. Nishimura, and K. Hiraga. Structure of a W–(AlCoNi) crystalline phase related to Al–Co–Ni decagonal quasicrystals, studied by single crystal X-ray diffraction. *J. Alloys Compnd.*, 342(1):65–71, August 2002.
- [61] T. Ishimasa, Y. Tanaka, and S. Kashimoto. Icosahedral quasicrystal and 1/1 cubic approximant in Au–Al–Yb alloys. *Phil. Mag.*, 91(33):4218–4229, November 2011.
- [62] W. Steurer and S. Deloudi, editors. *Crystallography of Quasicrystals*. Springer, 2009.
- [63] L. Bindi, N. Yao, C. Lin, L. S. Hollister, C. L. Andronicos, V. V. Distler, M. P. Eddy, A. Kostin, V. Kryachko, G. J. MacPherson, W. M. Steinhardt, M. Yudovskaya, and P. J. Steinhardt. Natural quasicrystal with decagonal symmetry. *Sci. Rep.*, 5:1–5, 2015.
- [64] S. Kameoka, T. Tanabe, and A.P. Tsai. Al-Cu-Fe quasicrystals for steam reforming of methanol: a new form of copper catalysts. *Catal. Today*, 93-5:23–26, 2004.
- [65] T. Toyokazu, S. Kameoka, and A. P. Tsai. A novel catalyst fabricated from Al-Cu-Fe quasicrystal for steam reforming of methanol. *Catal. Today*, 111:153–157, 2006.
- [66] T. Janssen, G. Chapuis, and M. de Boissieu, editors. *Aperiodic Crystals From Modulated Phases to Quasicrystals*. Oxford University Press, 2007.
- [67] J. Dolinsek, M. Komelj, P. Jeglic, S. Vrtnik, D. Stanic, P. Popcevic, J. Ivkov, A. Smontara, Z. Jaglicic, P. Gille, and Y. Grin. Anisotropic magnetic and transport properties of orthorhombic Al₁₃Co₄. *Phys. Rev. B*, 79:184201, 2009.
- [68] U. Köster, W. Liu, H. Liebertz, and M. Michel. Mechanical properties of quasicrystalline and crystalline phases in AlCuFe alloys. *J. Non-Cryst. Solids*, 153-154:466–452, 1993.

-
- [69] R. O. Suzuki and H. Kozasa. Thermoelectric properties of $Zr_3Mn_4Si_6$ and $TiMnSi_2$. *J. Electron. Mat.*, 39:2017–2022, 2010.
- [70] T. Weber, J. Dshemuchadse, M. Kobas, M. Conrad, B. Harbrecht, and W. Steurer. Large, larger, largest ... a family of cluster-based tantalum copper aluminides with giant unit cells. I. Structure solution and refinement . *Acta Crystallogr. B*, 65:308–317, 2009.
- [71] M. Conrad, B. Harbrecht, T. Weber, D. Y. Jung, and W. Steurer. Large, larger, largest ... a family of cluster-based tantalum copper aluminides with giant unit cells. II. The cluster structure . *Acta Crystallograph. B*, 65:308–317, 2009.
- [72] J. Dshemuchadse, S. Bigler, A. Simonov, T. Weber, and W. Steurer. A new complex intermetallic phase in the system Al-Cu-Ta with familiar clusters and packing principles. *Acta Crystallograph. B*, 69:238–248, 2013.
- [73] U. Mizutani. Introduction to the Electron Theory of Metals, June 2001.
- [74] U. Mizutani. *Hume-Rothery Rules for Structurally Complex Alloy Phases*. Taylor Francis US, 2010.
- [75] U. Mizutani, M. Inukai, H. Sato, and E. S. Zijlstra. *Physical metallurgy*, volume 1, chapter Electron theory of complex metallic alloys. Elsevier, d.e. laughlin and k. hono edition, 2014.
- [76] U. Mizutani and H. Sato. The Physics of the Hume-Rothery Electron Concentration Rule. *Crystals*, 7:9, 2017.
- [77] G. Trambly de Laissardière, D. Nguyen Manh, and D. Mayou. Electronic structure of complex Hume-Rothery phases and quasicrystals in transition metal aluminides. *Prog. Mater. Sci.*, 50:679–788, 2005.
- [78] V. J. Yannello and D. C. Fredrickson. Generality of the 18- n Rule: Intermetallic Structural Chemistry Explained through Isolobal Analogies to Transition Metal Complexes. *Inorg. Chem.*, 54(23):11385–11398, 2015.
- [79] K. Miyazaki, V. Yannello, and D. Fredrickson. Electron-counting in intermetallics made easy: the 18- n rule and isolobal bonds across the Os-Al system. *Zeit. Krist. - Cryst. Mat.*, 232:487–496, 2017.
- [80] K. Momma and F. Izumi. VESTA 3 for three-dimensional visualization of crystal, volumetric and morphology data. *J. Appl. Cryst.*, 44(6):1272–1276, 2011.

- [81] A. Ormeci and Y. Grin. Chemical bonding in Al_5Co_2 : the electron localizability - electron density approach. *Israel J. Chem.*, 51:1349, 2011.
- [82] U. Burkhardt, Y. Grin, M. Ellner, and K. Peters. Structure refinement of the iron-aluminium phase with the approximate composition Al_5Fe_2 . *Acta Crystallogr. B*, 50:313–316, 1994.
- [83] M. Ellner and J. Mayer. X-ray and electron diffraction investigations of the liquid-quenched Al_5Fe_2 . *Script. Metall. Mat.*, 26:501–504, 1992.
- [84] P. Priputen, M. Kusý, M. Drienovský, D. Janičkovič, R. Čička, I. Černíčková, and J. Janovec. Experimental reinvestigation of al-co phase diagram in vicinity of $\text{Al}_{13}\text{Co}_4$ family of phases. *J. Alloys Compnd.*, 647:486–497, 2015.
- [85] V. Elser and C.L. Henley. Crystal and quasicrystal structures in Al-Mn-Si alloys. *Phys. Rev. Lett.*, 55(26):2883–2886, 1985.
- [86] C. Dong, Q. Wang, J. B. Qiang, Y. M. Wang, N. Jiang, G. Han, Y. H. Li, J. Wu, and J. H. Xia. From clusters to phase diagrams: composition rules of quasicrystals and bulk metallic glasses. *J. Phys. D: Appl. Phys.*, 40:R273–R291, 2007.
- [87] R. Addou, É. Gaudry, T. Deniozou, M. Heggen, M. Feuerbacher, P. Gille, Y. Grin, R. Widmer, O. Groening, V. Fournée, J.-M. Dubois, and J. Ledieu. Investigation of the (100) surface of the orthorhombic $\text{Al}_{13}\text{Co}_4$ crystal. *Phys. Rev. B*, 80:014203, 2009.
- [88] H. Shin, K. Pussi, É. Gaudry, J. Ledieu, V. Fournée, S. Alarcón-Villaseca, J.-M. Dubois, Yu. Grin, P. Gille, W. Moritz, and R.D. Diehl. Structure of the orthorhombic $\text{Al}_{13}\text{Co}_4(100)$ surface using LEED, STM and ab initio studies. *Phys. Rev. B*, 84:085411, 2011.
- [89] M. Krajčí and J. Hafner. Surface structures of complex intermetallic compounds: An ab-initio dft study for the (100) surface of o- $\text{Al}_{13}\text{Co}_4$. *Phys. Rev. B*, 84:115410, Sep 2011.
- [90] É. Gaudry, C. Chatelier, G. M. McGuirk, L. N. Serkovic-Loli, M.-C. de Weerd, J. Ledieu, V. Fournée, R. Felici, J. Drnec, G. Beutier, and M. de Boissieu. Structure of the $\text{Al}_{13}\text{Co}_4(100)$ surface: Combination of surface x-ray diffraction and ab initio calculations. *Phys. Rev. B*, 94(16):165406, 2016.

-
- [91] J. Grin, U. Burkhardt, M. Ellner, and K. Peters. Refinement of the $\text{Fe}_4\text{Al}_{13}$ structure and its relationship to the quasihomological homeotypical structures. *Zeit. Krist.*, 209:479–487, 1994.
- [92] A. Matilainen, K. Pussi, R. D. Diehl, J. Ledieu, M. Hahne, P. Gille, E. Gaudry, L.N. Serkovic Loli, G. McGuirk, M.-C. de Weerd, V. Fournée, and J. Ledieu. Structure of the monoclinic $\text{Al}_{13}\text{Fe}_4(010)$ complex metallic alloy surface determined by low-energy electron diffraction. *Phys. Rev. B*, 92:014109, 2015.
- [93] M. Mihalkovič and M. Widom. First-principles calculations of cohesive energies in the Al-Co binary alloy system. *Phys. Rev. B*, 75:014207, 2007.
- [94] C. L. Henley, M. De Boissieu, and W. Steurer. Discussion on clusters, phasons and quasicrystal stabilisation. *Phil. Mag.*, 86:1131–1151, 2006.
- [95] K. Saito, K. Sugiyama, and K. Hiraga. Al_{13}M_4 -type structures and atomic models of their twins. *Mat. Sci. Eng. A*, 294-296:279–282, 2000.
- [96] X. L. Ma, H. Liebertz, and U. Koster. Multiple Twins of Monoclinic $\text{Al}_{13}\text{Fe}_4$ Showing Pseudo-Orthorhombic and Fivefold Symmetries. *Phys. Stat. Sol. (a)*, 158:359–367, 1996.
- [97] M. Feuerbacher and M. Heggen. On the concept of metadislocations in complex metallic alloys. *Phil. Mag.*, 86:935–944, 2006.
- [98] M. Heggen, L. Houben, and M. Feuerbacher. Metadislocations in the structurally complex orthorhombic alloy $\text{Al}_{13}\text{Co}_4$. *Phil. Mag.*, 88:2333–2338, 2008.
- [99] M. Heggen, L. Houben, and M. Feuerbacher. Plastic-deformation mechanism in complex solids. *Nat. Mater.*, 9:332–336, 2010.
- [100] M. Heidelmann, Marc Heggen, Christian Dwyer, and Michael Feuerbacher. Comprehensive model of metadislocation movement in $\text{Al}_{13}\text{Co}_4$. *Script. Mater.*, 98:24–27, 2015.
- [101] J. Czochralski. Ein neues Verfahren zur Messung der Kristallisationsgeschwindigkeit der Metalle. *Zeits. Phys. Chem.*, 92:219–221, 1918.
- [102] P.W. Bridgman. Certain Physical Properties of Single Crystals of Tungsten, Antimony, Bismuth, Tellurium, Cadmium, Zinc, and Tin. *Proc. Am. Acad. Art. Sci.*, 60(6):305–383, 1925.

- [103] P. Gille and B. Bauer. Single crystal growth of $\text{Al}_{13}\text{Co}_4$ and $\text{Al}_{13}\text{Fe}_4$ from al-rich solutions by the Czochralski method. *Cryst. Res. Technol.*, 43:1161, 2008.
- [104] P. Gille, B. Bauer, M. Hahne, A. Smontara, and J. Dolinsek. Single crystal growth of Al-based intermetallic phases being approximants to quasicrystals. *J. of Cryst. Growth*, 318:1016–1020, 2011.
- [105] T. Goedecke and M. Ellner. Phase equilibria in the aluminium-rich portion of the binary system Co-Al and in the cobalt/aluminium-rich portion of the ternary system Co-Ni-Al. *Z. Metallkd.*, 87:854, 1996.
- [106] Matthias Meier. *Influence de la liaison chimique sur la structure des surfaces d'alliages métalliques complexes*. PhD thesis, Université de Lorraine, 2015.
- [107] F. Morfin and L. Piccolo. A versatile elevated-pressure reactor combined with an ultrahigh vacuum surface setup for efficient testing of model and powder catalysts under clean gas-phase conditions. *Rev. Sci. Instr.*, 84:094101, 2013.
- [108] D. R. Hartree. The Wave Mechanics of an Atom with a Non-Coulomb Central Field. Part II. Some Results and Discussion. *Math. Proc. Camb. Phil. Soc.*, 24(1):111–132, 1928.
- [109] V. Fock. Näherungsmethode zur Lösung des quantenmechanischen Mehrkörperproblems. *Zeit. Phys.*, 61:126–148, 1930.
- [110] P. Hohenberg and W. Kohn. Inhomogeneous Electron Gas. *Phys. Rev.*, 136(3B):864–871, 1964.
- [111] W. Kohn and L. J. Sham. Self-Consistent Equations Including Exchange and Correlation Effects. *Phys. Rev.*, 140(4A):1133–1138, 1965.
- [112] J. C. Slater. The Self Consistent Field and the Structure of Atoms. *Phys. Rev.*, 32(3):339, 1928.
- [113] L.H. Thomas. The calculation of atomic fields. *Proc. Camb. Phil. Soc.*, 23(5):542–548, 1927.
- [114] E. Fermi. Un Metodo Statistico per la Determinazione di alcune Prioprietà dell'Atomo. *Rend. Accad. Naz. Lincei.*, 6:602–607, 1927.

-
- [115] J. P. Perdew, J. A. Chevary, S. H. Vosko, K. A. Jackson, M. R. Pederson, D. J. Singh, and C. Fiolhais. Atoms, molecules, solids, and surfaces: Applications of the generalized gradient approximation for exchange and correlation. *Phys. Rev. B*, 46:6671, 1992.
- [116] J. P. Perdew, K. Burke, and M. Ernzerhof. Generalized gradient approximation made simple. *Phys. Rev. Lett.*, 77:3865, 1996.
- [117] J. P. Perdew, K. Burke, and M. Ernzerhof. Erratum: Generalized gradient approximation made simple. *Phys. Rev. Lett.*, 78:1396, 1997.
- [118] S. Grimme. Semiempirical gga-type density functional constructed with a long-range dispersion correction. *J. Comp. Chem.*, 27:1787, 2006.
- [119] S. Grimme, J. Antony, S. Ehrlich, and H. Krieg. A consistent and accurate ab initio parametrization of density functional dispersion correction (DFT-D) for the 94 elements H-Pu. *J. Chem. Phys.*, 132:154104, 2010.
- [120] S. Grimme, S. Ehrlich, and L. Goerigk. Effect of the damping function in dispersion corrected density functional theory. *J. Comput. Chem.*, 32:1456, 2011.
- [121] A. Patra, J. E. Bates, J. Sun, and J. P. Perdew. Properties of real metallic surfaces: Effects of density functional semilocality and van der waals nonlocality. *Proc. Nat. Acad. Sci.*, 114: E91, 2017.
- [122] G. Kresse and J. Hafner. Ab initio molecular dynamics for liquid metals. *Phys. Rev. B*, 47:558–561, 1993.
- [123] G. Kresse and J. Hafner. Ab initio molecular-dynamics simulation of the liquid-metal-amorphous-semiconductor transition in germanium. *Phys. Rev. B*, 49:14251–14269, 1994.
- [124] G. Kresse and J. Furthmüller. Efficiency of ab-initio total energy calculations for metals and semiconductors using a plane-wave basis set. *Comp. Mat. Sci.*, 6(1):15–50, 1996.
- [125] G. Kresse and J. Furthmüller. Efficient iterative schemes for ab initio total-energy calculations using a plane-wave basis set. *Phys. Rev. B*, 54(16):11169–11186, 1996.
- [126] G. Kresse and D. Joubert. From ultrasoft pseudopotentials to the projector augmented-wave method. *Phys. Rev. B*, 59:1758, 1999.

- [127] F. Bloch. Über die Quantenmechanik der Elektronen in Kristallgittern. *Zeit. Phys.*, 52:555–600, 1929.
- [128] P. E. Blochl. Projector augmented-wave method. *Phys. Rev. B*, 50:17953, 1994.
- [129] J. Tersoff and D. R. Hamann. Theory and application for the scanning tunneling microscope. *Phys. Rev. Lett.*, 50:1998–2001, 1983.
- [130] J. Tersoff and D. R. Hamann. Theory of the scanning tunneling microscope. *Phys. Rev. B*, 31:805–813, 1985.
- [131] W. Sun and G. Ceder. Efficient creation and convergence of surface slabs. *Surface Science*, 617:53 – 59, 2013.
- [132] C. Kittel. *Introduction to Solid State Physics*. John Wiley & Sons, USA, 7 edition, 1996.
- [133] F. Fleischer, T. Weber, D. Y. Jung, and W. Steurer. α - $\text{Al}_{13}\text{Co}_4$, a new quasicrystal approximant. *J. Alloys Compnd.*, 500:153–160, 2010.
- [134] F. Vigne, J. Haubrich, D. Loffreda, Ph. Sautet, and F. F. Delbecq. Highly selective hydrogenation of butadiene on Pt/Sn alloy elucidated by first-principles calculations. *J. Catal.*, 275:129–139, 2010.
- [135] N.C. Craig, P. Groner, and D.C. McKean. Equilibrium Structures for Butadiene and Ethylene: Compelling Evidence for Pi-Electron Delocalization in Butadiene. *J. Phys. Chem. A*, 110:7461–7469, 2006.
- [136] A. Bouchy, G. Roussy, M.J. Ledoux, and F.G. Gault. Interpretation of the rotational spectra of multideuteriated species of but-1-ene for the study of catalytic mechanisms by microwave spectroscopy. *J. de Chim. Physique*, 76:357–363, 1979.
- [137] S. Gautier and P. Sautet. Coadsorption of Butadiene and Hydrogen on the (111) Surfaces of Pt and Pt₂Sn Surface Alloy: Understanding the Cohabitation from First-Principles Calculations. *J. Phys. Chem. C*, 121:25152–25163, 2017.
- [138] G. Henkelman, B. P. Uberuaga, and H. Jónsson. A climbing image nudged elastic band method for finding saddle points and minimum energy paths. *J. Chem. Phys.*, 113:9901, 2000.
- [139] G. Henkelman and H. Jónsson. Improved tangent estimate in the nudged elastic band method for finding minimum energy paths and saddle points. *J. Chem. Phys.*, 113:9978, 2000.

-
- [140] University of Texas VTST. *Nudged Elastic Bands*, 2020 (accessed October 3, 2020). <https://theory.cm.utexas.edu/vtsttools/neb.html>.
- [141] D. Sheppard, R. Terrell, and G. Henkelman. Optimization methods for finding minimum energy paths. *J. Chem. Phys.*, 128:134106, 2008.
- [142] Svante Arrhenius. Über die Dissociationswärme und den Einfluss der Temperatur auf den Dissociationsgrad der Elektrolyte. *Zeit. Phys. Chem.*, 4(1):96–116, 1889.
- [143] Svante Arrhenius. Über die Reaktionsgeschwindigkeit bei der Inversion von Rohrzucker durch Säuren. *Zeit. Phys. Chem.*, 4:226–248, 1889.
- [144] H. Eyring. The Activated Complex in Chemical Reactions. *J. Chem. Phys.*, 3:107–115, 1935.
- [145] K.J. Laidler and M.C. King. Development of transition-state theory. *J. Phys. Chem.*, 87:2657–2664, 1983.
- [146] S. Glasstone, K.J. Laidler, and H. Eyring. *The Theory of Rate Processes*. McGraw-Hill Book Company, Inc., New York and London, 1940.
- [147] I.A.W Filot. *Introduction to microkinetic modeling*. Technische Universiteit Eindhoven, 2018.
- [148] P.W. Atkins and J. Paula. *Physical Chemistry, 9th edition*. Oxford University press, Oxford, 2010.
- [149] The SciPy Community. *ODE Solver in SciPy*, 2020 (accessed October 3, 2020). <https://docs.scipy.org/doc/scipy/reference/generated/scipy.integrate.ode.html>.
- [150] Synchrotron SOLEIL. *Surfaces and interfaces x-ray scattering Beamline*, 2020 (accessed October 3, 2020). <https://www.synchrotron-soleil.fr/en/beamlines/sixs>.
- [151] I.K. Robinson and D.J. Tweet. Surface X-ray diffraction. *Rep. Prog. Phys.*, 55(5):599, 1992.
- [152] J. Als-Nielsen and D. McMorrow. *Elements of Modern X-ray Physics. Chapter 5: Kinematical scattering II: crystalline order*. Wiley, 2011.
- [153] P. Willmott. *A Introduction To Synchrotron Radiation*. Wiley, 2011.

- [154] S. Roobol, W. Onderwaater, J. Drnec, R. Felici, and J. Frenken. BINoculars : data reduction and analysis software for two-dimensional detectors in surface x-ray diffraction. *J. Appl. Cryst.*, 48(4):1324–1329, 2015.
- [155] E. Vlieg. Integrated intensities using a six-circle surface x-ray diffractometer. *J. Appl. Cryst.*, 30:532–543, 1997.
- [156] E. Vlieg. A (2+3)-type surface diffractometer: Mergence of the z-axis and (2+2)-type geometries. *J. Appl. Cryst.*, 31:198–203, 1998.
- [157] E. Vlieg. Rod: a program for surface x-ray crystallography. *J. Appl. Cryst.*, 33:401–405, 2000.
- [158] Cynthia Fourmental. *Étude structurale d'interfaces organiques/métalliques aux propriétés magnétiques*. PhD thesis, Université Paris Diderot, 2018.
- [159] A. Dawiec, Y. Garreau, J. Bisou, S. Hustache, B. Kanoute, F. Picca, G. Renaud, and A. Coati. Real-time control of the beam attenuation with XPAD hybrid pixel detector. *J. Instr.*, 11:12018, 2016.
- [160] J.T. Grant and D. Briggs. *Surface Analysis by Auger and X-ray Photoelectron Spectroscopy*. Chichester: IM Publications, 2003.
- [161] M.A. Van Hove, W.H. Weinberg, and C. M. Chan. *Low-energy electron diffraction*. Springer-Verlag, 1986.
- [162] F. Ohnesorge and G. Binnig. True atomic resolution by atomic force microscopy through repulsive and attractive forces. *Science*, 260(5113):1451–1456, 1993.
- [163] R. van Rijn, M. D. Ackermann, O. Balmes, T. Dufrane, A. Geluk, H. Gonzalez, H. Is-ern, E. de Kuyper, L. Petit, V.A. Sole, D. Wermeille, R. Felici, and J. W. M. Frenken. Ultrahigh vacuum/high-pressure flow reactor for surface x-ray diffraction and grazing incidence small angle x-ray scattering studies close to conditions for industrial catalysis. *Rev. Sci. Instr.*, 81:014101, 2010.
- [164] A. Benali, C. Lacaze-Dufaure, and J. Morillo. Density functional study of copper segregation in aluminum. *Surf. Sci.*, 605:341–350, 2011.
- [165] J.R. Kitchin, K. Reuter, and M. Scheffler. Alloy surface segregation in reactive environments: First-principles atomistic thermodynamics study of Ag₃Pd(111) in oxygen atmospheres. *Phys. Rev. B*, 77:075437, 2008.

-
- [166] V. Blum, L. Hammer, Ch. Schmidt, O. Wieckhorst, S. Müller, and K. Heinz. Segregation in strongly ordering compounds: a key role of constitutional defects. *Phys. Rev. Lett.*, 89:266102, 2002.
- [167] P. Villars and L. D. Calvert. *Pearson's Handbook of Crystallographic Data for Intermetallic Phases*. ASM International, Metals Park, Ohio, USA, 1998.
- [168] M. Krajčí and J. Hafner. Intermetallic compound AlPd as a selective hydrogenation catalyst: a DFT study. *J. Phys. Chem. C*, 116:6307–6319, 2012.
- [169] M. Krajčí and J. Hafner. The (210) surface of intermetallic B20 compound GaPd as a selective hydrogenation catalyst: a DFT study. *J. Catal.*, 295:70–80, 2012.
- [170] E. Vajda, J. Tremmel, B. Rozsondai, I. Hargittai, A.K. Maltsev, N.D. Kagramanov, and O.M. Nefedov. Molecular structure of allyl radical from electron diffraction. *J. Am. Chem. Soc.*, 108:4352, 1986.
- [171] É. Gaudry, C. Chatelier, D. Loffreda, D. Kandaskalov, A. Coati, and L. Piccolo. Catalytic activation of a non-noble intermetallic surface through nanostructuring under hydrogenation conditions revealed by atomistic thermodynamics. *J. Mater. Chem. A*, 8:7422–7431, 2020.
- [172] B. Mattson, W. Foster, J. Greimann, T. Hoette, N. Le, A. Mirich, S. Wankum, A. Cabri, C. Reichenbacher, and E. Schwanke. Heterogeneous Catalysis: The Horiuti–Polanyi Mechanism and Alkene Hydrogenation. *J. Chem. Educ.*, 90:613–619, 2013.
- [173] K. Reuter, C. Stampfl, M.V. Ganduglia-Pirovano, and M. Scheffler. Atomistic description of oxide formation on metal surfaces: the example of ruthenium. *Chem. Phys. Letters*, 352:311, 2002.
- [174] K. Reuter and M. Scheffler. Composition and structure of the RuO₂(110) surface in an O₂ and CO environment: Implications for the catalytic formation of CO₂. *Phys. Rev. B*, 68:045407, 2003.
- [175] S. Posada-Pérez, F. Vinesa, R. Valero, J. A. Rodríguez, and Francesc Illas. Adsorption and dissociation of molecular hydrogen on orthorhombic β -Mo₂C and cubic δ -MoC (001) surfaces. *Surface Science*, 656:24–32, 2017.
- [176] D.C.A. Ivarsson, I.G. Aviziotis, T. Keilhauer, and M. Armbrüster. Fixed-bed reactor for catalytic studies on low-surface area materials. *Rev. Sci. Inst.*, 90(1):014101, 2019.

- [177] J. Ledieu, É. Gaudry, M.-C. de Weerd, R. D. Diehl, and V. Fournée. The (100) surface of the $\text{Al}_{13}\text{Co}_4$ quasicrystalline approximant. *Mater. Res. Soc. Symp. Proc.*, 1517: 2012.
- [178] R. Mader, R. Widmer, P. Groning, S. Deloudi, W. Steurer, M. Heggen, P. Schall, M. Feuerbacher, and O. Groning. High-resolution scanning tunneling microscopy investigation of the (12110) and (10000) two-fold symmetric d-Al-Ni-Co quasicrystalline surfaces. *Phys. Rev. B*, 80:035433, 2009.
- [179] L. Vitos, A.V. Ruban, H.L. Skriver, and J. Kollár. The surface energy of metals. *Surf. Sci.*, 411:186, 1998.
- [180] R. Tran, Z. Xu, B. Radhakrishnan, D. Winston, W. Sun, K.A. Persson, and S. Ping-Ong. Surface energies of elemental crystals. *Sci. Data*, 3:160080, 2016.
- [181] R. Mäder, R. Widmer, B. Bauer, P. Gille, P. Gröning, W. Steurer, , and O. Gröning. Revealing the atomic surface structure of the (100) Y-Al-Ni-Co approximant by low-energy electron diffraction and scanning tunneling microscopy. *Phys. Rev. B*, 81:064201:1–8, 2010.
- [182] R.C. Baetzold and G.A. Somorjai. Preexponential Factors in Surface Reactions. *J. Catal.*, 45:94–105, 1976.
- [183] M. T. Darby, R. Réocreux, E. C. H. Sykes, A. Michaelides, and M. Stamatakis. Elucidating the Stability and Reactivity of Surface Intermediates on Single-Atom Alloy Catalysts. *ACS Catal.*, 8(6):5038–5050, 2018.
- [184] M. T. Darby, M. Stamatakis, A. Michaelides, and E. C. H. Sykes. Lonely Atoms with Special Gifts: Breaking Linear Scaling Relationships in Heterogeneous Catalysis with Single-Atom Alloys. *J. Phys. Chem. Lett.*, 9(18):5636–5646, 2018.

Résumé

Remplacer les catalyseurs à base de métaux nobles (Pd, Pt, Au) par des substituts peu coûteux, stables, sélectifs et actifs est un grand défi pour l'industrie chimique. Plusieurs intermétalliques complexes à base d'aluminium se sont révélés prometteurs pour les réactions d'hydrogénation d'alcynes et d'alcènes, importantes dans l'industrie des polymères. C'est le cas des approximants quasicristallins Al_5Co_2 , $\text{Al}_{13}\text{Co}_4$ et $\text{Al}_{13}\text{Fe}_4$. L'étude des propriétés catalytiques de ces derniers nécessite plusieurs approches, théoriques et expérimentales, afin de déterminer les structures de surface hors et sous conditions de réaction, première étape avant la détermination des propriétés d'adsorption et des mécanismes de réaction. La combinaison d'expériences de sciences de surface (microscopie à effet tunnel, diffraction de surface des rayons X) et de calculs de chimie théorique (énergies de surface, énergies d'adsorption, chemins de réaction) a permis d'établir des modèles de surface détaillés, leurs propriétés d'adsorption et de mieux comprendre les facteurs clés à l'origine des propriétés catalytiques prometteuses de ces matériaux.

Mots-clés: catalyse, surfaces, aluminium, intermétalliques, butadiène, DFT, SXRD.

Abstract

Replacing noble metal (Pd, Pt, Au) catalysts with inexpensive, environmentally harmless, active, selective, and stable substitutes is a big challenge for the chemical industry. Several aluminium-based complex intermetallic compounds have shown promises for alkynes and alkenes hydrogenation reactions, which are of interest in the chemical industry. It is the case for Al_5Co_2 , $\text{Al}_{13}\text{Co}_4$ and $\text{Al}_{13}\text{Fe}_4$ quasicrystalline approximants. The study of their catalytic properties demands different approaches, both theoretical and experimental, in order to determine first their surface structures under ultra-high vacuum or reaction conditions, then their catalytic properties. The combination of surface science experiments (scanning tunneling microscopy, surface X-ray diffraction) and theoretical chemistry calculations (surface energies, adsorption energies and reaction pathways) allows for a better understanding of the key parameters behind the promising catalytic properties of these materials.

Keywords: catalysis, surfaces, aluminium, intermetallics, butadiene, DFT, SXRD.